

Estimation of Methane and Carbon Dioxide Surface Fluxes using a 3-D Global Atmospheric Chemical Transport Model

Yu-Han Chen

Center for Global Change Science
Department of Earth, Atmospheric and Planetary Sciences
MIT, Cambridge, MA 02139-4307 USA



**Report No. 73
December 2003**

The Earth's unique environment for life is determined by an interactive system comprising the atmosphere, ocean, land, and the living organisms themselves. Scientists studying the Earth have long known that this system is not static but changing. As scientific understanding of causal mechanisms for environmental change has improved in recent years there has been a concomitant growth in public awareness of the susceptibility of the present environment to significant regional and global change. Such change has occurred in the past, as exemplified by the ice ages, and is predicted to occur over the next century due to the continued rise in the atmospheric concentrations of carbon dioxide and other greenhouse gases.

The *Center for Global Change Science* at MIT was established to address long-standing scientific problems that impede our ability to accurately predict changes in the global environment. The Center is interdisciplinary and involves both research and education.

This report is one of a series of preprints and reprints from the Center intended to communicate new results or provide useful reviews and commentaries on the subject of global change. See the inside back cover of this report for a complete list of the titles in this series.

Ronald G. Prinn, *Director*
Rafael L. Bras, *Associate Director*
MIT Center for Global Change Science

For more information contact the Center office.

LOCATION:
Center for Global Change Science
Massachusetts Institute of Technology
Building 54, Room 1312
77 Massachusetts Avenue
Cambridge, MA 02139-4307 USA

ACCESS:
Tel: (617) 253-4902
Fax: (617) 253-0354
E-mail: cgcs@mit.edu
Website: <http://mit.edu/cgcs/>

**Estimation of Methane and Carbon Dioxide Surface Fluxes
using a 3-D Global Atmospheric Chemical Transport Model**

by

Yu-Han Chen

B.S. Chemistry, 1995
Stanford University

Submitted to the Department of Earth, Atmospheric, and Planetary Sciences
in partial fulfillment of the requirements for the degree of

Doctor of Philosophy in Climate Physics and Chemistry

at the

MASSACHUSETTS INSTITUTE OF TECHNOLOGY

February 2004

© Massachusetts Institute of Technology 2004. All rights reserved.

Author.....
Department of Earth, Atmospheric, and Planetary Sciences
November 6, 2003

Certified by.....
Ronald G. Prinn
TEPCO Professor of Atmospheric Chemistry
Thesis Supervisor

Accepted by.....
Maria T. Zuber
Head, Department of Earth, Atmospheric, and Planetary Sciences

**Estimation of Methane and Carbon Dioxide Surface Fluxes
using a 3-D Global Atmospheric Chemical Transport Model**

by

Yu-Han Chen

Submitted to the Department of Earth, Atmospheric, and Planetary Sciences
on November 6, 2003 in partial fulfillment
of the requirements for the degree of

Doctor of Philosophy in Climate Physics and Chemistry

Abstract

Methane (CH₄) and carbon dioxide (CO₂) are the two most radiatively important greenhouse gases attributable to human activity. Large uncertainties in their source and sink magnitudes currently exist. We estimate global methane surface emissions between 1996 and 2001, using a top-down approach that combines observed and simulated atmospheric CH₄ concentrations. As a secondary study, we describe our participation in a CO₂ inverse-modeling intercomparison.

The available methane time-series data used in this work include observations from 13 high-frequency stations (in-situ) and 74 low-frequency sites (flask). We also construct an annually-repeating reference emissions field from pre-existing datasets of individual methane processes. For our forward simulations, we use the 3-D global chemical transport model MATCH driven by NCEP meteorology. A prescribed, annually-repeating OH field scaled to fit methyl chloroform observations is used as the methane sink. A total methane source of approximately 600 Tg yr⁻¹ best reproduces the methane growth rate between 1993-2001. Using the reference emissions, MATCH can reproduce the observed methane variations at many sites. Interannual variations in transport, including those associated with ENSO and the NAO, are found to be important at certain locations.

We adapt the Kalman Filter to estimate methane flux magnitudes and uncertainties between 1996 and 2001. Seven seasonal processes (3 wetland, rice, and 3 biomass burning) are optimized at each month, while three aseasonal processes (animals/waste, coal, and gas) are optimized as constant emissions. These optimized emissions represent adjustments to the reference emissions. For the entire period, the inversion reduces coal and gas emissions, and increases rice and biomass burning emissions. The optimized seasonal emission has a strong peak in July, largely due to increased emissions from rice producing regions. The inversion also attributes the large 1998 increase in atmospheric CH₄ to global wetland emissions, consistent with a bottom-up study based on a wetland process model. The current observational network can significantly constrain northern emitting regions, but is less effective at constraining tropical emitting regions due to limited observations. We further assessed the inversion

sensitivity to different observing sites and model sampling strategies. Better estimates of global OH fluctuations are also necessary to fully describe the interannual behavior of methane observations.

Carbon dioxide inversions were conducted as part of the Transcom 3 (Level 1) modeling intercomparison. We further explored the sensitivity of our CO₂ inversion results to different parameters.

Thesis Supervisor: Ronald G. Prinn

Title: TEPCO Professor of Atmospheric Chemistry

Acknowledgements

I must first thank my advisor Ron Prinn for his support and advice over these many years. Ron provided the necessary direction to start my research project, and then gave me the freedom to follow my own specific interests. He also helped me to maintain perspective on the overall scientific picture. Phil Rasch was always available for MATCH support, and provided specific help at critical times. Ed Boyle advised me during the early years, when my research interests were less well-defined. Alan Plumb and Mario Molina provided insights into my work as I was finishing. I am also grateful to Brian Eaton for introducing me to the nitty-gritty aspects of MATCH. Further thanks goes to the members of AGAGE, on whose data this work relies. I also learned a great deal about atmospheric inversions from the members of the TRANSCOM experiment.

The best part of MIT is how fellow students can help one another out, even when projects are highly independent. Don Lucas provided constant scientific and technical insights; without his help, my work would be less than what is presented here. It was also good having a solid friend and classmate from the very start. Donnan Steele, Stephanie Shaw, Jin Huang, and Jake Gebbie also provided many valuable discussions which improved my work. I enjoyed the camaraderie and support of the Prinn group members, both students and staff. I also became good friends with fellow classmates Pablo Zurita and Juli Atherton, especially through our many dinners and pints together. Matt Hungerford, Josh Briggs, and Arup De are old friends whom I must mention, as they helped me through.

My final thanks is for my family, whose constant love and support kept me going over the years. Wen-Wen, Richard, and Aliya provided much needed diversions during my time here. Finally, I dedicate this thesis to Mom and Dad.

This thesis work was funded at different times by the National Defense Science and Engineering Graduate Fellowship, NSF, DOE, and the PAOC Houghton Fund.

Contents

Chapter 1	Introduction	15
1.1	Methane.....	16
1.2	Carbon Dioxide	19
1.3	Forward and Inverse Modeling Approach.....	21
1.4	Chapter Descriptions	23
Chapter 2	The MATCH Model	25
2.1	Model Description and Previous Studies	25
2.2	Emission Redistribution	26
2.3	Planetary boundary layer dynamics	29
Chapter 3	Forward Modeling of Atmospheric Methane	33
3.1	Methane Observations.....	33
3.1.1	High-Frequency (In-situ) Observations.....	38
3.1.2	Low-Frequency (Flask) Observations	40
3.1.3	Other Observations	41
3.2	Sources	41
3.2.1	Seasonal Emissions	42
3.2.2	Aseasonal Emissions	48
3.2.3	Other Sources	49
3.3	Sinks.....	50
3.3.1	OH Fields.....	50
3.3.2	Other Sinks	51
3.4	Modeled versus Observed Methane	54
3.4.1	Comparison to High-Frequency (In-Situ) Observations.....	56
3.4.2	Comparison to Low-Frequency (Flask) Observations.....	63
3.4.3	Flask monthly averages from high and low-frequency MATCH sampling	66
3.5	Impact of Transport IAV on Methane Seasonality	67
3.6	Sensitivity to specific processes	71
3.7	Conclusions	77
Chapter 4	Inverse Modeling of Atmospheric Methane: Methodology	79
4.1	Kalman Filter Equations.....	80
4.1.1	Measurement Equation.....	80
4.1.2	State-Space Equation.....	84
4.1.3	Kalman Filter for Time-Dependent Inversions.....	87
4.2	Observational Errors	91
4.3	Inversion Check.....	97

4.4	Summary	103
Chapter 5	Inverse Modeling of Atmospheric Methane: Results	105
5.1	Inversion Description	105
5.2	Average Seasonal Results	115
5.3	Average Annual Results.....	118
5.3.1	Comparison to Bottom-up Estimates.....	121
5.3.2	Errors	123
5.4	Interannual Results.....	123
5.4.1	Global Methane Increase in 1998.....	129
5.4.2	Model Errors.....	131
5.5	Summary and Conclusions.....	132
Chapter 6	Annual Mean Carbon Dioxide Inversions	135
6.1	Control Inversion.....	135
6.1.1	Observations	135
6.1.2	Transcom 3 Protocol and Surface Flux Description.....	136
6.1.3	Inversion Methodology.....	140
6.2	MATCH versus other model results.....	143
6.2.1	Difference between MATCH.NCEP and MATCH.CCM3	147
6.3	Inversion Sensitivity Experiments.....	150
6.4	Summary	156
Chapter 7	Conclusions	159
7.1	Summary	159
7.2	Further conclusions	162
Appendices	166
Appendix A.....	166
Appendix B.....	168
Appendix C.....	170
References	172

List of Figures

Figure 1.1. Globally averaged methane mole fractions (top) and corresponding growth rate (bottom) (NOAA (2003)).	17
Figure 1.2. Time series of globally (surface) averaged CO ₂ mole fractions (top) and growth rate (bottom) (NOAA (2003)).	20
Figure 1.3. General schematic describing the forward (LHS) and inverse optimal estimation (RHS) of surface fluxes.	22
Figure 2.1. MATCH at T42 resolution with model land (green) and ocean/sea ice (blue) designations.	27
Figure 2.2 Match land/ocean redistribution near Barrow, Alaska.	28
Figure 2.3 Barrow Detrended Monthly Mean values: Observed (Black) versus Modeled (Red) Seasonal Cycle.	28
Figure 2.4. PBL Heights from MATCH for January (left) and July (right) in 1990.	30
Figure 2.5. Effect of Changing PBL on simulated CO ₂ using a fossil-fuel source at a grid in central Europe during December.	31
Figure 3.1: Location of methane time-series data used in this study.	35
Figure 3.2: Time series of CH ₄ mole fractions at 5 AGAGE stations,	39
Figure 3.3: Annual Mean Distribution of Methane Emissions at 2.8° x 2.8° (T42) resolution.	45
Figure 3.4. Annual Average Distributions of Seasonal Processes.	46
Figure 3.5. Aseasonal Emission.	47
Figure 3.6: Methyl Chloroform evolution over the past 20 years using annually repeating OH field (monthly varying).	53
Figure 3.7: Left: comparison between JPL (2003) 2 parameter (red) and 3 parameter (green) rate constant expressions and Gierczak et al. (1997) (blue) rate constants for CH ₄ + OH over a range of temperatures.	53
Figure 3.8. Reference model (red) versus observed (black) methane growth rate.	55
Figure 3.9: Reference model (red) versus Observed (black) Interhemispheric Gradient.	55
Figure 3.10. Observed (Black) and Modeled (Red) High-Frequency In-Situ values.	58
Figure 3.11: Effect of transport IAV at Samoa. Top: Observed and modeled (inverted) mole fractions.	60
Figure 3.12: Effect of transport IAV at Mace Head. Top: Observations (black, left hand side) and MATCH (red, right hand inverted scale).	62
Figure 3.13. Observed (Black) and Modeled (Red) Flask values at representative locations.	65
Figure 3.14. Top: Monthly means at Barrow.	67
Figure 3.15: The effect of model transport IAV on methane surface seasonality.	70
Figure 3.16. Same information as Figure 3.15 but at CH ₄ observing stations.	70
Figure 3.17. Sensitivity of Alert and Cape Grim to an August emission pulse from Western Hemispheric Bogs (as shown in Figure 3.4).	73
Figure 3.18: Sensitivity of Alert to an August month-pulse from Bogs West using 1997 (Blue) and 1998 (Red) meteorology.	73
Figure 4.1. Test of the linearity of pulsed emissions.	83
Figure 4.2 The evolution of a methane emissions for a single month (September, 1999) with the addition of new monthly data (horizontal).	90

Figure 4.3. Kalman state-vector for 3 aseasonal sources.	91
Figure 4.4. Seasonal Inversion Results.	98
Figure 4.5. Comparisons between reference (top) and inversion optimized (bottom) MATCH runs with observations at the AGAGE sites.	101
Figure 4.6. Modeled mixing ratios from reference (blue) and inversion optimized (red) MATCH runs, , as compared to flask observations (black).	102
Figure 4.7. Comparison between MATCH and inversion-predicted monthly means at Alert and Barrow.	102
Figure 5.1. Seasonal Inversion Results for the Flask LF case (see Table 1.1). The reference (blue) and optimized (red) monthly methane fluxes are shown in the left plots.	107
Figure 5.2. Monthly mean observations at high-frequency inversion sites, arranged by latitude and numbered according to Table 4.2.	109
Figure 5.3. Same case as described in Figure 5.2, but showing flask sites which have monthly means for at least 70% of the inversion months (see Table 4.2).	110
Figure 5.4. Same case as described in Figure 5.2, but showing flask sites which have monthly means for less than 70% of the inversion months.	113
Figure 5.5. Average seasonal results using high and low-frequency measurements (Flask LF) and high-frequency only (In-situ only).	117
Figure 5.6 Annual Average Methane Emissions.	119
Figure 5.7 Monthly Mean Anomalies (from the 5 year mean value) for Flask LF (Red) and In-situ only (Green).	125
Figure 5.8. Same as Figure 5.7, but with the same vertical range for all processes to emphasize contributions to the total change.	125
Figure 5.9 Flask LF vs. Flask HF interannual results.	126
Figure 5.10. Flask LF vs. Flask LF All.	126
Figure 5.11. Flask LF (red) vs. Flask HF (green) interannual variability inversions for Bogs East and West (expanded from Figure 5.10).	127
Figure 5.12. Observed high-frequency mole fractions (Black), and MATCH runs with reference (Blue) and optimized (Red) emissions at Samoa.	129
Figure 6.1. CO ₂ flask observing sties used for the Transcom 3 experiment.	136
Figure 6.2. Background (prior) fluxes from the Transcom 3 Intercomparison.	138
Figure 6.3. Fossil Fuel and Neutral Biosphere Tracer responses for all model.	138
Figure 6.4. 11 Land and 11 Ocean regions optimized in the Transcom 3 intercomparison.	140
Figure 6.5. Observed (black diamonds), background (blue +’s), and optimized (red x’s) CO ₂ mole fractions from MATCH.	143
Figure 6.6. Transcom 3 Inversion results for the 11 land (green) and 11 ocean (blue) regions shown in Figure 6.4.	145
Figure 6.7. MATCH versus model mean for aggregated regions.	146
Figure 6.8. Differences in the simulated CO ₂ mole fractions at the 76 control sites from the FF, BIO, and OCN background fluxes.	147
Figure 6.9. December surface flux differences between different MATCH runs.	149
Figure 6.10. December difference (CCM – NCEP18) between the Planetary Boundary Layer Height and the bottom level KvH.	150
Figure 6.11. Aggregated values for MATCH control (red) and 15 Model Mean (black).	152

Figure 6.12. Aggregated Regions for different sensitivity cases.....152
Figure 6.13. Comparison between OCN distribution and 11 ocean regions used for ocean uptake.153
Figure 6.14. Aggregated Regions for additional sensitivity tests.....156

List of Tables

Table 1.1 Methane Emission Ranges (IPCC (2001)) in Tg yr ⁻¹	17
Table 1.2. IPCC (2001) carbon budget driven by anthropogenic emissions (all values in Gt C yr ⁻¹)	20
Table 3.1. List of Methane observing sites used in this study*	36
Table 3.2. Methane sources ranked by emission contribution.	44
Table 3.3. List of sensitivities to seasonal methane emissions for High-Frequency and Flask Sites. Units are in ppb (Tg yr ⁻¹) multiplied by 0.1.....	76
Table 4.1. Monthly Observational Error Ranges: High-Frequency versus Flask (ppb).....	95
Table 4.2. Monthly mean observational errors (as standard deviations in ppb) averaged over 1996-2001. The total error represents the quadratic sum of the 4 separate errors.	95
Table 5.1. Inversion Case Descriptions.....	108
Table 5.2. Five-year averaged inversion emission values and errors for aggregated regions (units of Tg yr ⁻¹)	120
Table 5.3. Five-year averaged individual inversion values and errors for Energy, Wetland, and Biomass Burning in Table 5.2. All values in Tg yr ⁻¹	120
Table 5.4 In-situ only annual anomalies (Tg yr ⁻¹)	128
Table 5.5. Flask LF annual anomalies (Tg yr ⁻¹)	128
Table 5.6. Flask LF ALL annual anomalies (Tg yr ⁻¹)	128

List of Acronyms

AES	Atmospheric Environment Service (Canada)
AGAGE	Advanced Global Atmospheric Gases Experiment
ALE	Atmospheric Lifetime Experiment
CCM3	Community Climate Model 3
CGER	Commission on Geosciences, Environment and Resources
CMDL	Climate Monitoring and Diagnostics Laboratory
CSIRO	Commonwealth Scientific and Industrial Research Organization (Australia)
EDGAR	Emission Database for Global Atmospheric Research
ENSO	El Niño Southern Oscillation
FAO	Food and Agricultural Organization
GAGE	Global Atmospheric Gases Experiment
GC-FID	Gas Chromatography - Flame Ionization Detection
GEIA	Global Emission Inventory Activity
HBL	Hudson Bay Lowland
IAV	Interannual Variability
IEA	International Energy Agency
IFU	Fraunhofer Institute for Atmospheric Environmental Research (Germany)
INM	Instituto Nacional de Meteorología (Spain)
ITCZ	Intertropical-Convergence Zone
JMA	Japan Meteorological Agency
KMA	Laboratorium voor Luchtonderzoek (the Netherlands)
LLO	Korea Meteorological Administration
MATCH	Model for Atmospheric Chemistry and Transport
MRI	Meteorological Research Institute (Korea)
MSW	Municipal Solid Waste
NAO	North Atlantic Oscillation
NCAR	National Center for Atmospheric Research
NCEP	National Centers for Environmental Research
NH	Northern Hemisphere
NIES	National Institute for Environmental Studies (Japan)
NIWA	National Institute of Water and Atmospheric Research (NIWA)
OECD	Organisation for Economic Cooperation and Development
PBL(H)	Planetary Boundary Layer (Height)
RIVM	National Institute of Public Health and the Environment (the Netherlands)
SAWB	South African Weather Bureau
SH	Southern Hemisphere
SOI	Southern Oscillation Index
SPITFIRE	Split Implementation of Transport using Flux Integral Representation
TRANSCOM	Atmospheric Tracer Transport Model Intercomparison Project

Chapter 1

Introduction

Methane (CH_4) and carbon dioxide (CO_2) are the two most radiatively important greenhouse gases attributable to human activity. Together they account for approximately 80% of the total 2.5 W m^{-2} increase in radiative forcing caused by the anthropogenic release of greenhouse gases in the industrial age according to *IPCC* (2001). Direct atmospheric measurements indicate that the total burdens of atmospheric methane and carbon dioxide have been increasing over the past several decades. Ice-core measurements further record their rapid growth since the onset of the industrial revolution. These increases are caused predominately by human activities, which are known to produce CH_4 from agriculture, livestock, energy production, and waste management, and CO_2 from fossil-fuel combustion and deforestation. Biomass burning is also a significant source for both of these gases. Although most emission processes have been identified, significant uncertainties exist in their magnitudes and variability. Both the methane and carbon dioxide cycles have significant natural components, which complicate the quantification of their total budgets. Better constraints on their current budgets are important for an improved understanding of their roles in the global climate system. The requirements for climate studies include predicting future changes in their sources and sinks due to climate feedbacks. Mitigation strategies that seek to reduce atmospheric concentrations of CH_4 and CO_2 will also require better estimates of their sources and sinks.

Estimates of methane and carbon dioxide surface fluxes have relied on three broad, and often overlapping, approaches. The first are global extrapolations from direct flux (or proxy flux) measurements. For example, emissions of CH_4 from rice can be made using a flux chamber; these point measurements can then be extrapolated to a large area. The errors in this approach arise from the scaling of a few measurements to much larger space and time domains. The second approach uses process models which seek to represent the actual physical and biological process that produce CH_4 and CO_2 . A wetland model based on climatological microbial and soil variables can, for example, be used to estimate methane emissions. This approach suffers from modeling uncertainties, especially those equations and parameters linking climate variables to actual fluxes. The first and second methods are considered to be “bottom-up” approaches, and are often hybridized and interrelated through the use of flux measurements to test the process models. The third method is the “top-down” approach, which includes atmospheric inverse modeling. This method relies on worldwide observations of CH_4 and CO_2 that have been taken over the past few decades. These observations implicitly contain information about surface fluxes, which can be extracted and quantified through the use of atmospheric models. Forward modeling involves the direct comparison between actual and simulated observations. Inverse modeling combines real and modeled observations to produce an optimized set of values for unknown fluxes or flux model parameters. In this work, the values of interest are current CH_4 and CO_2 surface flux magnitudes.

We conduct forward and inverse studies of CH_4 and CO_2 fluxes over the past decade, using a state-of-the-art chemical transport model. The primary focus is on methane, beginning with the description of new high-frequency observational data-sets that are simulated for the first time using a global model. The

competing influences of atmospheric transport and emissions on the observations are also explored. For the inversions, we adapt the Kalman Filter to solve for both constant and time-varying methane fluxes. The time-varying fluxes are optimized at higher temporal resolution than previously attempted in a global CH₄ inversion. The inversion also quantifies the ability of the observational network to constrain methane emissions. As a secondary focus, carbon dioxide inversions were conducted as part of a modeling intercomparison, allowing us to test our model against approximately 15 other models. We further explored the sensitivity of the CO₂ inversion results to different inversion parameters.

1.1 Methane

Methane is the second most important anthropogenic greenhouse gas, contributing approximately 20% of the 2.5 W m⁻² increase in radiative forcing due to human activities (*IPCC* (2001)). CH₄ also plays a central role in global atmospheric chemistry, affecting tropospheric OH concentrations and acting as a source of stratospheric water vapor. The increase in the total methane burden can be linked qualitatively to increases in human activities that emit methane. Using air trapped in ice-cores, *Etheridge et al.* (1998) measured increases over the past 1000 years from pre-industrial values of ~695 ppb to current levels of ~1700 ppb. Most of the increase occurred in the last 200 years, concurrently with the industrial revolution and consequent population growth. High precision time-series CH₄ measurements have been made since the mid-1980s; currently, about 70 of these sites operate worldwide. These observations describe the spatial distribution and temporal behavior of CH₄ within the atmosphere. Figure 1.1 (top) shows the global average of the NOAA flask network surface sites over the past two decades (*NOAA* (2003)). The red line represents the annually averaged change in the global burden; it has increased because methane sources have exceeded sinks. Global mole fractions have increased over the past 20 years by approximately 0.5 % yr⁻¹. More recently, the growth rate has slowed, reflecting the convergence of methane sources and sinks. The more variable blue curve in Figure 1.1 (top) shows the seasonal cycle in methane, which is due to the seasonality of certain sources (wetlands, rice, biomass burning) and the sink (OH destruction). Changes in the global growth rate are shown at the bottom of Figure 1.1, corresponding to the time derivative of the red curve. Although the growth rate has shown a gradual decline over the past 20 years, large year-to-year fluctuations are evident.

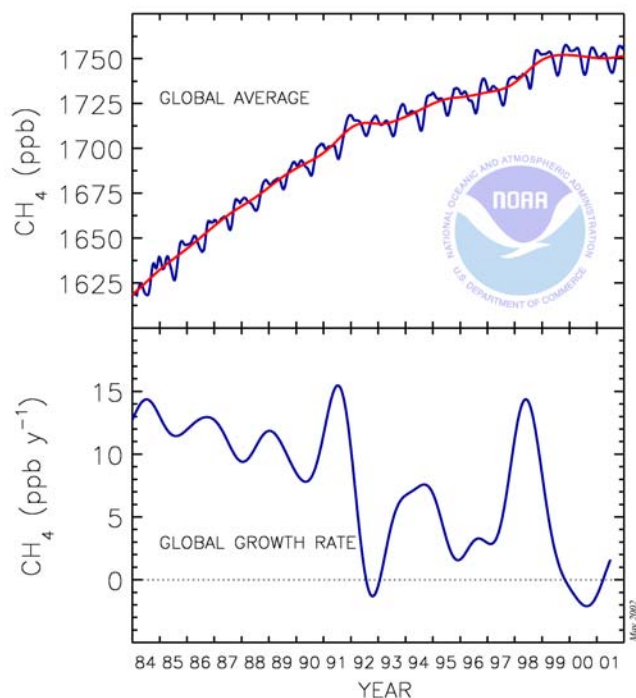


Figure 1.1. Globally averaged methane mole fractions (top) and corresponding growth rate (bottom) (NOAA (2003)).

Table 1.1 Methane Emission Ranges (IPCC (2001)) in Tg yr⁻¹

Process	IPCC Range
Wetlands	92-237
Animals	80-115
Waste	35-73
Rice	25-100
Energy	75-110
Biomass Burning	23-55
Other (Termites, Geologic, etc.)	variable
Total	500 – 600

The emission ranges for several major methane-producing processes are shown in Table 1.1 (IPCC (2001)). The range of emission estimates reflect bottom-up and top-down values that can be found in the literature. Anthropogenic processes (shaded) account for about 80% of the total methane budget. The global emission total is largely determined by the global concentration of the atmospheric hydroxyl radical (OH), which destroys about 90% of the total methane input into the atmosphere. The size of the global OH sink cannot be measured directly but can, however, be estimated using methyl chloroform measurements (Prinn *et al.* (2001)). Stratospheric destruction and terrestrial surface uptake contribute as

smaller CH₄ sinks. The large emission ranges in Table 1.1 show the room for significant improvement in constraining individual methane emissions. Methane reductions have been examined (*Reilly et al. (2002)*, *Hansen et al. (2000)*) as a strategy to mitigate anthropogenically induced climate change. Acceptance of these proposed policies will require better estimates of individual budget terms in order to determine possible reductions, as well as verification of any future mitigation policy. In addition to multi-year average emission values, there is also the need to better quantify interannual changes in emissions. The large growth rate fluctuations shown in Figure 1.1 (bottom) suggest strong methane emission variability. Was the large increase in 1998, for example, isolated to a single process or due perhaps to a worldwide phenomenon related to the El Niño?

Atmospheric studies which combine atmospheric observations and a chemical transport model can be used to constrain CH₄ emission processes. Forward methane modeling studies have tested possible methane emissions scenarios by direct comparisons to observed mole fractions (*Fung et al. (1991)*, *Lelieveld et al. (1998)*). Inversions of atmospheric methane have generally focused on average methane emissions applicable over many years (e.g. *Houweling et al. (1999)*, *Hein et al. (1997)*). *Dentener et al. (2003)* recently used a semi-inverse technique to examine for anthropogenic emission trends between 1979-1993. *Cunnold et al. (2002)* analyzed changes in global emissions between 1985-1997. Except for the latter work, these studies have relied on low-frequency (flask) observations, taken about once a week. However, since the mid-1990s, more than 13 high-frequency observational stations have measured CH₄ in-situ approximately once per hour. These observations contain potentially much more information on methane emissions than the low-frequency flask samples. However, the effective use of these new datasets requires a global transport model driven by realistic meteorology.

In this thesis we incorporate high-frequency observations into a global 3-D methane inversion for the first time. These observations potentially offer strong constraints on methane emissions, especially for estimating both intraannual and interannual methane flux changes. As a first step, we compare directly observed and simulated CH₄ mole fractions, using a current best-guess emissions field. This forward modeling study allows the following questions to be addressed:

- How well can a CTM driven by realistic meteorology and a current best-guess CH₄ emissions field reproduce high and low frequency CH₄ observations?
- How large is the impact of interannual transport variability (as opposed to emission variability) on observed methane mole-fractions?

Once the general characteristics of modeled and observed CH₄ mole fractions have been analyzed, emission fluxes can be adjusted optimally in order to achieve a best fit to the observations. We adapt the Kalman Filter to solve for both constant and time-varying (monthly) methane emissions. The following questions can then be tackled:

- How well can we constrain methane fluxes using a state-of-the-art transport model and all available observations?
- Can the inversion attribute interannual changes in observed methane growth rates to specific processes?

- How do our top-down results compare to previous bottom-up estimates?

We also test the sensitivity of the inversion results to the use of different observational networks and model sampling strategies. Possible errors and limitations of the overall top-down approach are also discussed.

1.2 Carbon Dioxide

Observations of atmospheric carbon dioxide have been made at Mauna Loa, Hawaii since the late 1950's. Figure 1.2 shows the global increase in the atmospheric burden of CO₂ over the past 2 decades from the current observational network, which overlaps with the CH₄ network at most sites (NOAA (2003)). The observed global growth rate results primarily from anthropogenic fossil fuel combustion. The gradual increase ($\sim 0.5\% \text{ yr}^{-1}$, red curve) is superimposed on top of a natural seasonal cycle (blue curve), which occurs because of the large seasonal exchange of carbon between the atmosphere and biosphere. This seasonal cycle is dominated by net uptake of atmospheric CO₂ in the Northern Hemispheric summer due to increased photosynthesis relative to respiration, with the opposite occurring in winter leading to a net release. For our CO₂ inversions, we focus on recent atmospheric increases driven by anthropogenic activity. Table 1.2 shows the IPCC (2001) carbon budget for the 1980's and 1990's. The global atmospheric increase is very well constrained by global measurements. Total anthropogenic emissions are also known to better than 10% from economic data of fossil fuel consumption. Note that the well-observed atmospheric increase is only about 50% of the total emissions. The remainder must be taken up by some combination of the oceans and continents because there is no atmospheric sink for CO₂. The ocean uptake values in Table 1.2 represent estimates from ocean carbon modeling (which implicitly or explicitly incorporate oceanic observations), and atmospheric tracers (such as O₂ and ¹³CO₂) which provide information on the partitioning between ocean and land uptake. Estimates of land uptake have been more difficult to constrain, and have been historically quantified as the difference (residual) necessary to balance the budget. Tans *et al.* (1990) used the difference between modeled and observed CO₂ to infer the need for a substantial northern hemispheric land sink.

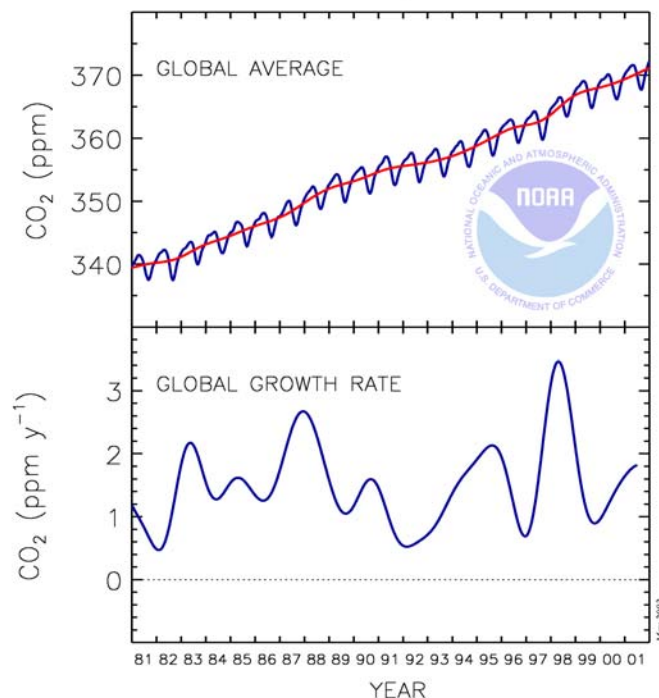


Figure 1.2. Time series of globally (surface) averaged CO₂ mole fractions (top) and growth rate (bottom) (NOAA (2003)).

Table 1.2. IPCC (2001) carbon budget driven by anthropogenic emissions (all values in Gt C yr⁻¹)

	1980-1989	1990-1999
Atmospheric Increase	3.3 ± 0.1	3.2 ± 0.1
Anthropogenic Emissions	5.4 ± 0.3	6.3 ± 0.4
Ocean-atmosphere flux	-1.9 ± 0.6	-1.7 ± 0.5
Land-atmosphere flux	-0.2 ± 0.7	-1.4 ± 0.7

$$\text{Atmospheric Increase} = \text{Emissions} + \text{Ocean-atmosphere flux} + \text{Land atmosphere flux}$$

More recent efforts have focused on regional estimates of carbon exchange. Estimates of regional fluxes are important not only for better understanding the carbon cycle, but for the potential monitoring of emissions by countries under a climate policy. Using historical data of land use change, *Houghton et al.* (1999) estimated a land sink for the United States equivalent to 10 – 30% of its total fossil fuel emissions (0.15 – 0.40 Gt yr⁻¹). *Pacala et al.* (2001) conducted an extensive budgeting of the US carbon sink to estimate a 0.30 – 0.58 Gt yr⁻¹ uptake for the 1980s. Such detailed inventory studies can be done where abundant carbon source/sink data exists. This data is, however, lacking for most of the world, such as for the large boreal forests in Siberia. Atmospheric inversions using 3-D transport models and global observations provide a way to estimate carbon fluxes regionally across the world. *Fan et al.* (1998) estimated a North American uptake of 1.7 Gt yr⁻¹, which is nearly equivalent to the total U.S. fossil fuel input. Subsequent inversions show smaller sinks of less than 1 Tg yr⁻¹ (*Pacala et al.* (2001), *Gurney et al.* (2002)). In addition to the average mean fluxes described above, more recent inversions have estimated

the interannual variability for specific land and ocean regions (*Bousquet et al. (2000)*, *Rodenbeck et al. (2003)*). Carbon dioxide inversions are potentially more difficult than methane inversions because carbon exchange involves strong 2-way fluxes due to photosynthesis and respiration. In addition, both land and ocean surface fluxes must be considered; separating their influence from atmospheric mole fractions alone can be difficult. In contrast, land emissions dominate the CH₄ flux.

The results from any inversion will be sensitive to the atmospheric model used. Model advection and physics, as well as resolution, vary considerably across current global atmospheric models. In addition, a single model can usually accept more than one driving set of meteorological inputs. *Mahowald (1996)* showed that different sets of analyzed observed winds can result in very different tracer behavior in MATCH. The Atmospheric Tracer Transport Model Intercomparison Project (Transcom) examined the sensitivity of forward and inverse modeling to different transport models (*Law et al. (1996b)*, *Denning et al. (1999)*). We participated in the third installment (Transcom 3), which focused on inter-model comparisons of CO₂ inversions as described by *Gurney et al. (2002)*. Using a common set of observations and a standard inversion technique for all models, Transcom 3 allowed us to address the following questions:

- How do the MATCH CO₂ inversion results compare to other models?
- Which aspects of MATCH transport lead to these model differences in the inversion?

Comparison to other models also led to a more detailed examination of the planetary boundary layer scheme (PBL) in MATCH. This scheme is particularly important for CO₂, because local carbon exchange occurs almost everywhere that observations are taken. Using the MATCH results, we conducted further sensitivity studies of our Transcom 3 inversion using different sets of observations and model inputs.

1.3 Forward and Inverse Modeling Approach

The top-down approach used to address the aforementioned questions for methane and carbon dioxide is described in Figure 1.3. Both forward and inverse approaches require observations and modeled inputs. The emission fields that are input into the model consist of flux patterns which are based on bottom-up information. The 3-D chemical transport model MATCH is used throughout this study. NCEP meteorology at a resolution of approximately 2.8° x 2.8° drives the model. The observations include CH₄ and CO₂ time-series at different locations worldwide. For methane, we have collected all available high-frequency (in-situ) data in addition to low-frequency (flask) measurements. The forward modeling studies compare observations and model simulations directly, using a “best guess” emission field based on current knowledge. This approach is useful as a starting point for any study of the fluxes, since it provides a preliminary sense of how well the model can simulate available observations. Forward modeling can also provide insight into the physics and chemistry controlling the observations, especially when there is good agreement between the model and observations. Moreover, differences between modeled and observed values can suggest how the initial emissions can be improved.

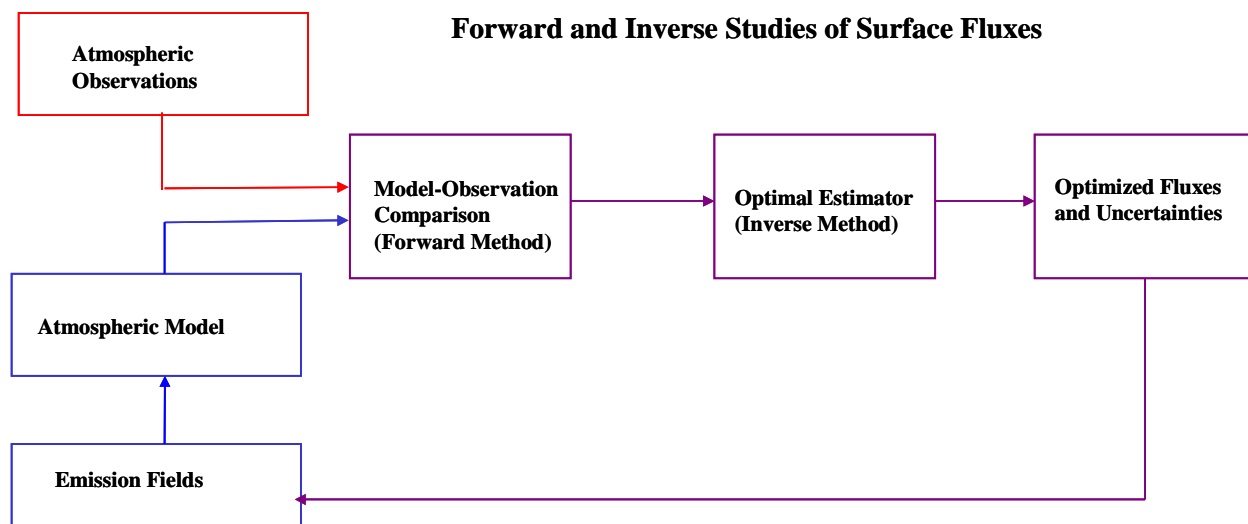


Figure 1.3. General schematic describing the forward and inverse technique for the study of surface fluxes.

Inverse modeling produces a set of surface flux magnitudes that improve the model fit to observations. The optimal estimator combines observations and modeled values to produce a set of optimized fluxes. Many such optimal estimation schemes exist, as described in *Kasibhatla et al. (2000)* and *Enting (2002)*. These include batch inversions which use all observational information simultaneously. Recursive inversions, such as the Kalman Filter, use time-series observations in a step-wise fashion. For methane, we use the Kalman Filter to solve for both monthly and constant fluxes. For carbon dioxide, a standard batch inversion method is used. The inverse modeling used in this study requires that each process/region of interest be modeled independently by MATCH. This requires many more model runs compared to forward model studies, and can lead to computational limitations on how many processes/regions can be optimized.

The optimized values can be considered to be improvements to the bottom-up values using the information contained in atmospheric measurements. The inversion, when properly formulated, can also produce objective uncertainties for the optimized fluxes, which quantify the ability of the observations to constrain emissions from different regions. Regions that are well sampled by the observations will have a large uncertainty reduction; poorly sampled regions will have small uncertainty reductions. The inversion methodology can also be extended to identify the optimal locations for new observations that can further constrain regional fluxes. Atmospheric inversions can suffer from ill-posing, if the observational network cannot distinguish between the regions of interest. Thus, the choice of processes/regions to investigate is a very important element of the inversion process. The inversion process generally ignores model errors and biases. Thus, a more complete study of the uncertainty would be to explore sensitivity to model uncertainties and thus expand the flux uncertainty to include model uncertainties. A full accounting of model uncertainties is difficult, given the expense of running a 3-D atmospheric model multiple times for many years.

1.4 Chapter Descriptions

The following describes the chapter organization of this thesis. The main work is contained in Chapters 3 – 6.

Chapter 2 describes the chemical transport model (MATCH) used throughout this thesis. As a finite resolution model, MATCH needs to be sampled carefully when making comparisons with point observations. We also examine the planetary boundary layer (PBL) scheme, which is important because most CH₄ and CO₂ observations are taken at the earth's surface.

Chapter 3 contains the methane forward modeling work, which compares observed and modeled CH₄ mole fractions using a reference (best-guess) emissions field. The first part of the chapter describes the observations, focusing on high-frequency measurements, some of which are examined for the first time using a global model. The forward comparisons allowed us to study the impact of interannually varying transport on CH₄ observations. We also examined the sensitivity of the current CH₄ observational networks to specific methane emission processes and geographic patterns.

Chapter 4 develops the inversion methodology used to optimally estimate methane fluxes. The Kalman Filter is adapted to produce both constant and time-varying (monthly) flux estimates. The observational errors, which determine the weighting of different observations, are also described. We test the inversion results by running the optimized emissions forward in MATCH, followed by a comparison to the observations. This shows the modeled-observational CH₄ mole fraction improvement when using the optimized emissions compared to the reference.

Chapter 5 presents the seasonal, annual, and interannual CH₄ inversion results. We discuss these results in sequence, along with comparisons to previous estimates. The emission uncertainty reduction due to use of measurements from the current observational network is also assessed. We further test the sensitivity of the inversion using different sets of observations.

Chapter 6 contains the CO₂ annual mean inversion results from the Transcom 3 experiment. The MATCH (NCEP) results are compared to the average and standard deviation results from all 15 participating models. Differences from the model average are discussed from a transport perspective. We conduct additional sensitivity studies by varying different inversion parameters.

Chapter 7 summarizes the main findings and contributions of this thesis. It includes some ideas for further constraining methane emissions.

Chapter 2

The MATCH Model

This chapter describes the Model of Atmospheric Transport and Chemistry (MATCH) used throughout this work. MATCH has been used to examine global behavior of many different atmospheric constituents. Of particular interest to this study are previous simulations of long-lived gases with emission patterns similar to CH₄ and CO₂. As a global model with a high but finite resolution, MATCH must be sampled carefully when comparing to observational point measurements. Surface flux data sets which have different resolutions than MATCH also require careful conversion onto the MATCH grid. The planetary boundary layer (PBL) scheme in MATCH is a particularly important aspect of transport because the majority of CH₄ and CO₂ observations are taken at the earth's surface. The final section reviews how MATCH parameterizes mixing within the PBL. We also perform a simple test showing how changing the PBL height can affect simulated tracers.

2.1 Model Description and Previous Studies

The MATCH model was developed to realistically simulate atmospheric constituents using observed analyzed meteorology (*Rasch et al. (1997), Mahowald (1996)*). Throughout this work, MATCH is driven by NCEP reanalysis meteorology at T42 resolution, approximately 2.8° x 2.8°. We have not used the full NCEP horizontal resolution of T62, approximately 1.8° x 1.8°, due to the number of simulations required for inverse modeling. As computational power increases, future work will use the full T62 resolution. In the vertical, NCEP has 28 sigma levels between ~1000 and 2.9 mb. The surface (bottom) layer varies between 50 – 100 meters in height. The planetary boundary layer determined by MATCH contains several of the bottommost layers. Eight meteorological inputs drive MATCH in our configuration: horizontal winds (U, V), temperature (T), surface pressure (PS), surface heat and water vapor fluxes (SHFLX, WVFLX), and surface stresses (TAUX, TAUY). These inputs are available at a time resolution of 6 hours from the NCEP archived meteorology. MATCH linearly interpolates this data to the 40 minute model time-step used for T42 resolution. The water vapor field (Q) is initialized using NCEP data at the first time step, after which MATCH predicts its own hydrological cycle. *Rasch et al. (1998)* implemented the mass-conserving SPITFIRE advection scheme, replacing the original semi-Lagrangian (SLT) advection scheme. *Mahowald (1996)* examined the sensitivity of transport to different moist convection schemes within MATCH. Our version uses convection schemes based on *Zhang et al. (1995)* and *Hack (1994)*. The planetary boundary layer (PBL) parameterization is based on *Holtslag et al. (1993)* and is similar to the NCAR CCM3 scheme (*Kiehl et al. (1996)*). MATCH has been used in the study of numerous gases, including radon, CFC1₃, CH₃Br, SF₆, (*Mahowald (1996), Mahowald et al. (1997b), Jensen (1999), Roger Dargaville (personal communication)*). It has also been used in studies of the sulfur cycle and aerosols (*Lucas (2003), Rasch et al. (2000)*). *Lawrence et al. (1999)* added a comprehensive

photochemical module into MATCH. *Kuhlmann et al.* (2003) have recently modeled ozone using an updated version of this model. The OH fields used in our methane and methyl chloroform (CH_3CCl_3) simulations were produced by this latest version.

A useful test of transport involves the comparison between modeled and observed values of long-lived, anthropogenic tracers that have relatively well-known emission magnitudes and distributions. These comparisons are useful before the simulation of complex biogenic tracers such as CH_4 and CO_2 , which also have long-lifetimes compared to global mixing, but have much more uncertain emissions. *Mahowald et al.* (1997a) compared simulated and observed interhemispheric gradients of CCl_3F , using MATCH with NCEP winds at T42 resolution between 1990-1991. CCl_3F (CFC-11) is produced anthropogenically for refrigerant and foam-blowing applications, has a lifetime of ~50 years, and like CH_4 and CO_2 , is dominated by Northern Hemispheric emissions. *Mahowald et al.* (1997a) found that the simulated interhemispheric gradient (IHG) of 14 ppt compared well with the observed IHG of 13 ppt, within the observational errors. Another long-lived tracer of anthropogenic origin, sulfur hexafluoride (SF_6), has been simulated using the same MATCH version as ours at T62 (Roger Dargaville, personal communication) and T21 resolution (*Jockel* (2000)). This compound is emitted by leakage from electrical switching equipment; its global emissions are based on electrical power usage and population distributions. The magnitude and distribution of its emissions are considered to be fairly well known. For both studies, multi-year simulations followed the Transcom 2 protocol and were compared to SF_6 observations for 1993 (*Denning et al.* (1999)). In general, both simulations reproduce the SF_6 IHG defined by approximately 20 stations. *Jockel* (2000) shows a correspondence of model to observed IHG to within 10%. The ability to reproduce the observed IHGs of these anthropogenic compounds adds confidence to the accuracy of MATCH transport when simulating more complex tracers such as CH_4 and CO_2 .

2.2 Emission Redistribution

The following describes how the MATCH orography is used to redistribute surface fluxes after they have been interpolated onto the MATCH resolution. The horizontal resolution of MATCH is shown in Figure 2.1, with corresponding land and ocean orographic cells. An initial interpolation process converts primary surface flux datasets, which are typically at high resolution (e.g. $1^\circ \times 1^\circ$), to the MATCH grid ($2.8^\circ \times 2.8^\circ$). This process results in small misallocations of land fluxes into MATCH ocean grids, and the vice-versa. For example, nearly all methane emissions are located on the continents; the initial interpolation process places a small amount of flux into ocean designated grid cells near the coasts. A land/ocean redistribution procedure is then used to transfer these misallocated fluxes to nearby land grids. The reverse redistribution procedure is used for ocean CO_2 flux regions, i.e. misallocated fluxes on land are transferred to ocean grids. This redistribution procedure is important for the following reasons. Many anthropogenic fluxes represent localized emissions. The land/ocean redistribution concentrates the more diffuse emissions from the initial interpolation into more localized emissions. Another reason is that many coastal sites sample air of marine origin, and are typically located in a MATCH ocean grid. Misallocation of land emissions to these ocean grids may lead to elevated mole fractions that are inconsistent with the observations. The final reason is that orography can affect transport based on surface roughness, temperature, and other parameters. Although we have not explicitly explored

land/ocean transport differences in this study, we keep land and ocean fluxes in consistent orographic grid cells within MATCH.

Figure 2.2 shows the effect of redistributing methane emissions on simulated CH₄ mole fractions at Barrow, Alaska. The Barrow site is situated directly adjacent to the Arctic Ocean, with prevailing winds from the ocean (*Dlugokencky et al. (1995)*). The MATCH grid containing Barrow Station in Figure 2.2 is designated ocean, but the initial regridding procedure misallocates land-based emissions to this grid cell

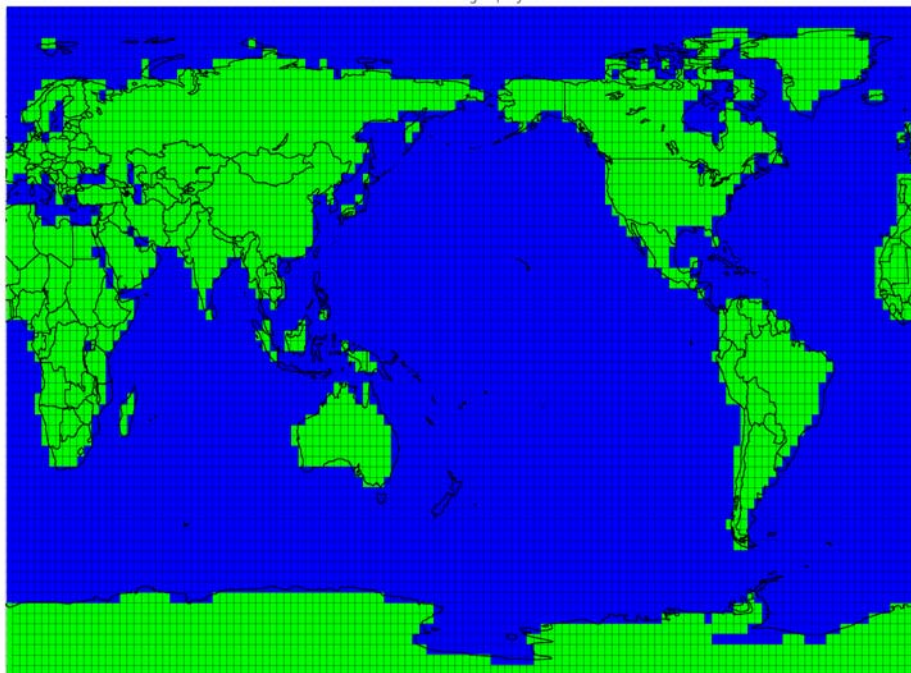


Figure 2.1. MATCH at T42 resolution with model land (green) and ocean/sea ice (blue) designations.

(left plot). The redistribution procedure transfers these emissions to adjacent land grid cells. The transfer is linearly weighted by the relative emissions of the adjacent land cells, e.g. the adjacent land cell with the highest emission receives the greatest amount of redistributed emission. In the case of Barrow, the grid emissions are shifted south, as can be seen from the right plot. The impact on simulated CH₄ mole fractions is shown in the bottom plots, which include the actual CH₄ observations. The non-redistributed case consistently overestimates summertime values because an emitting grid cell with strong summertime emissions (from wetlands) contains Barrow. The reaggregated case does not have these large values, because Barrow is no longer directly within an emitting grid cell. The elevated mole fractions are thus avoided, and the simulation more closely reproduces the observed seasonal trough (caused by high OH levels). Without reaggregation, it is still possible to avoid the strong seasonal overestimate by sampling a grid cell north of Barrow, which could be justified since Barrow samples mostly air of marine origin. However, redistribution allows us to sample the exact grid cell that contains Barrow.

Wherever possible, we have redistributed the MATCH methane emissions from oceanic to adjacent land designated grid cells (with the exception of a small international shipping source). For oceanic emissions that have no adjacent land grids at T42 resolution (e.g., New Zealand and Hawaii) the original

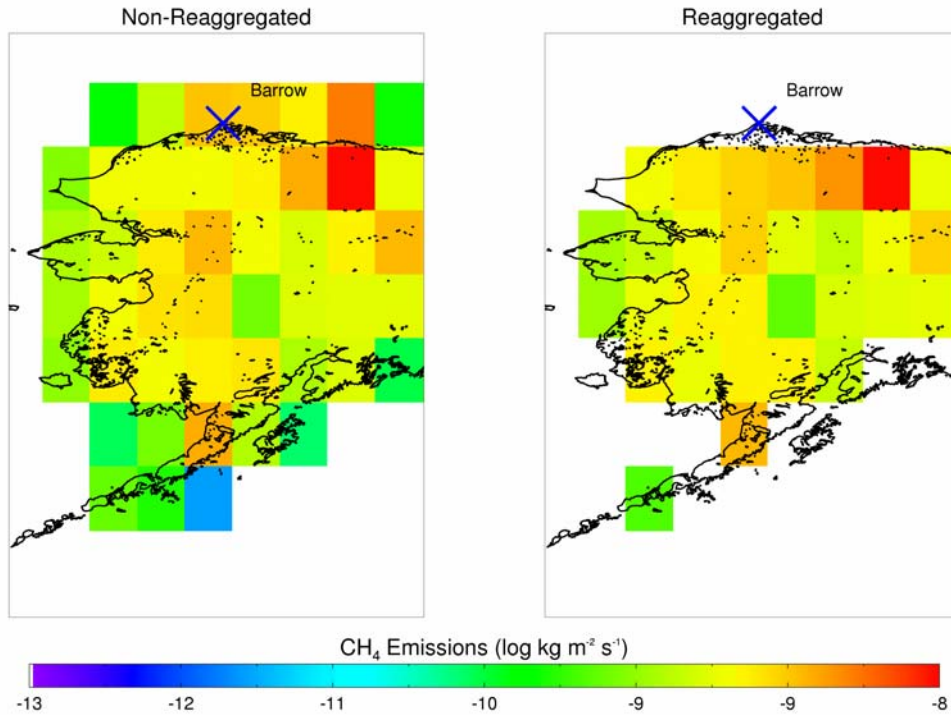


Figure 2.2 Match land/ocean redistribution near Barrow, Alaska. The left plot shows the non-redistributed model grid cell emissions. The right plot shows the redistributed case, where misallocated land emissions in ocean grid cells have been shifted to land grid cells (as defined by MATCH orography).

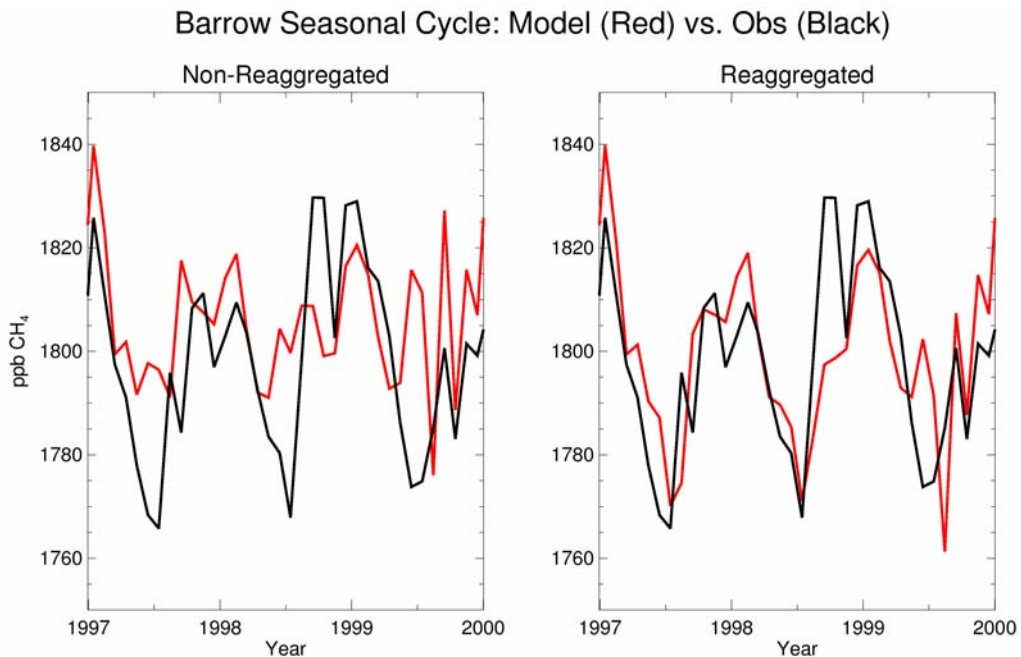


Figure 2.3 Barrow Detrended Monthly Mean values: Observed (Black) versus Modeled (Red) Seasonal Cycle. The left and right plots correspond to the non-redistributed and redistributed cases shown above, respectively. The observed mole fractions (black) are the same in each plot.

emission locations are retained, with the understanding that these oceanic grids actually contain land fluxes. For many coastal observing sites, redistribution improves the modeled comparison to the observed CH₄ seasonal cycle. It is particularly important for highly emitting coastal regions near Japan and the South China Sea. The land/ocean redistribution is significant only for coastal sites. The effect on simulated mole fractions is negligible for sites within continents, which are surrounded by land grids only.

2.3 Planetary boundary layer dynamics

This section describes the planetary boundary layer (PBL) scheme in MATCH, which is particularly important since most CH₄ and CO₂ observations are made at the earth's surface. An even more detailed account can be found in *Kiehl et al. (1996)* and *Holtslag et al. (1993)*. The planetary boundary layer height (PBLH) in MATCH is determined by the model height at which the bulk Richardson number exceeds the critical Richardson number.

$$Ri_{bulk} > Ri_{crit} \quad (2.1)$$

The bulk Richardson number is a ratio of thermal buoyancy to mechanical shear effects. In stable conditions this number is large and positive. The critical Richardson number is used to define this stable condition, which is set to 0.3 in MATCH. Starting from the surface layer, the bulk Richardson number is computed at each successive level until it exceeds the critical value. The occurrence of convective thermals within MATCH can further decrease the bulk Richardson number and increase the PBLH. All layers with the bulk Richardson number below the critical Richardson number are considered to be within the planetary boundary layer, and subject to more vigorous mixing than the stable layers above. The minimum PBLH is set equal to the lowest MATCH layer, between 75-100 meters.

The vertical transport within the boundary layer is given by

$$\overline{\omega' C'} = K_c \left(\frac{\partial C}{\partial z} - \gamma \right) \quad (2.2)$$

From Equation (2.2) it is evident that the factors controlling K_c will control the strength of mixing within the planetary boundary layer. The counter gradient term γ plays a role only under unstable conditions, and is ignored in the following discussion. Within the boundary layer, MATCH computes K_c as follows

$$K_c = k \omega_i z \left(1 - \frac{z}{h} \right)^2 \quad (2.3)$$

K_c = coefficient of eddy diffusion

k = von Karmon constant

ω_t = turbulent velocity scale

h = diagnosed PBLH

z = MATCH level

The value of ω_t , the turbulent velocity scale, depends on the stability condition at the surface. Within MATCH, this is determined by the sign of the virtual heat flux. For stable conditions, ω_t is mostly determined by mechanical turbulence derived from surface wind stresses. For unstable conditions, ω_t depends on both mechanical turbulence and thermal instability. Appendix A describes the equations for ω_t under these two conditions. The minimum value of K_c is equal to the diffusivity for the free troposphere above the planetary boundary layer.

Figure 2.4 displays monthly mean PBLHs from MATCH using 1990 NCEP meteorology for January and July. Over continental regions, the PBLH is high during the summer months and low during the winter months, due primarily to the effect of thermal buoyancy. The situation is generally reversed for oceanic regions. Since most of our observations occur in the surface layer, the PBLH can be an important component of transport, particularly for those locations directly above emitting grid cells. Very shallow PBLH values may lead to enhanced surface trapping of simulated tracers in these locations. Figure 2.4 indicates that the most shallow PBLH values can be found in the northern continental (i.e. boreal) and southern ocean regions during January, and in the northern oceans during July. The average PBLH in these areas is sometimes below 200 m. In these cases, MATCH may be underestimating the actual PBLH. Comparisons to observed PBLH values are, however, difficult due to the sparseness of observations. The surface mixing of tracers in MATCH can be influenced by changing the PBLH height (h) or eddy diffusivity (K_c) within the boundary layer. Changing the K_c value directly affects how fast tracers of surface origin are vented from the surface layer.

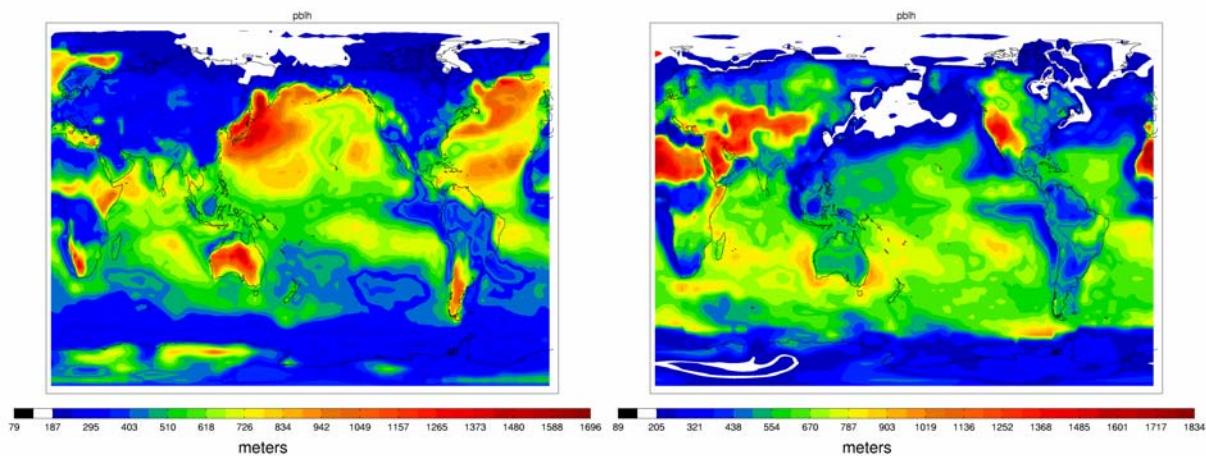


Figure 2.4. PBL Heights from MATCH for January (left) and July (right) in 1990. Note the large differences in continental PBL values between summer and winter. These PBLH are diagnosed in MATCH using NCEP meteorology.

To test the sensitivity of a simulated tracer to changes in the PBLH, we enforced minimum heights of 200 and 500 meters at every model time-step. These minimums can affect the PBLHs at those MATCH locations that have relatively shallow values as shown in Figure 2.4. An input field representing global CO₂ fossil fuel emissions from the Transcom 3 modeling intercomparison was used to test the effect on tracer mixing ratios (Chapter 6). The emission has been integrated forward in MATCH for 4 years; monthly mean results for the last year are analyzed. Figure 2.5 shows the vertical profile in a central European grid cell for the month of December. We specifically focus on a site within strongly emitting grid cells and a time of shallow PBLH. The original monthly mean PBLH at this site is 266 meters, although individual time-steps show values as low as 50 meters. The left and right-hand plots in Figure 2.5 show the effect of enforcing minimums of 200 and 500 meters respectively, with model level mid-points and CO₂ mole fractions shown by the asterisks. Enforcing a 200 meter minimum shows little change from the reference case. The 500 meter minimum shows much more significant mixing in the bottom 5 layers below 500 meters. The greatest difference (3 ppm) occurs in the surface layer. The increased vertical mixing does not propagate much higher than the PBLH maximum, with reference and modified values converging above 700 meters. This suggests that changing the PBLH has a relatively localized impact.

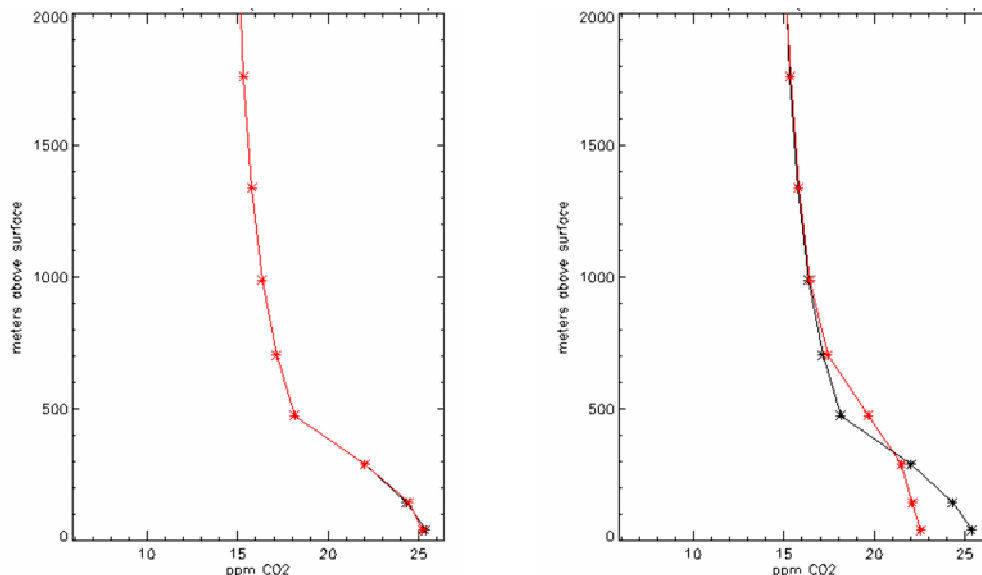


Figure 2.5. Effect of Changing PBLH on simulated CO₂ using a fossil-fuel source at a grid in central Europe during December. The original monthly mean PBLH is 266 meters, although individual time-steps show heights less than 100 meters. Black corresponds to the original model run, which is the same in both left and right cases. Red correspond to imposed PBLH minimums of 200 meters (left) and 500 meters (right) for all time-steps. Asterisks represent MATCH vertical level centers.

Accurate simulation of the surface layer is particularly important for sites within grids that have strong fluxes. Ideally we would compare the simulated profiles shown in Figure 2.5 to actual observations. However, fossil-fuel emissions are only one component of the real CO₂ fluxes; actual observations depend on the complex interplay of both anthropogenic and natural fluxes. A less complicated compound with well-known emissions would be preferable for a detailed study of PBL mixing. Unfortunately, very few vertical profiles of trace gases currently exist at the spatial and temporal

resolution required for a definitive study. In addition, simulation of strongly emitting regions also have greater model-measurement mismatch errors, which represent the difference between the model average value (over an entire grid box) and the observations (at a point in space). This potential error makes the testing of the transport within the PBL even more challenging. Continental sites are possibly the most sensitive to nearby emissions, but also the most difficult to model. As greater numbers of these sites become available, the necessity for PBL studies becomes more important.

The effect of adjusting the PBLH is small for sites not directly beneath strongly emitting grid cells. Changes in the PBLH generally affect simulated CO₂ observations more than CH₄ observations. Observing sites for both gases are mostly located on the coasts or in the oceans, but methane emissions are concentrated to continental regions. In contrast, CO₂ exchange occurs in both land and ocean regions, and therefore most observing sites lie within emitting grid cells. Thus, potential errors in PBL height and mixing would generally affect simulated carbon dioxide more than methane.

Chapter 3

Forward Modeling of Atmospheric Methane

This chapter describes forward modeling studies of methane, which involve the direct comparison between simulated and observed values. This tests the ability of the chemical transport model (MATCH) to simulate worldwide CH₄ observations, which have very different spatial and temporal signatures. These comparisons also provide insight into the observations, especially where the model-observation agreement is good. The initial efforts involved collection of available CH₄ observations and model inputs. For observations, all available reliable methane time-series data were collected, including both high (in-situ) and low frequency (flask) observations. The high-frequency observations (approximately once every 40-60 minutes) have largely been ignored in previous global modeling studies. We focus on these observations, which we will show to contain much more information than low frequency observations (approximately once per week). For model inputs, previous estimates of both sources and sinks were obtained and analyzed. The methane sources consist of various emission maps representing different methane processes. These were combined to form an initial (“reference”) methane field. For the sink, we used a seasonal OH distribution produced by a version of MATCH which contains photochemistry. The magnitude of this OH field was scaled to provide a best fit to methyl chloroform observations over the 1990s. Both the reference emissions and the OH field are seasonally-varying and representative of a single year. The reference emission field was run forward in MATCH using NCEP meteorology between 1993-2001. We then compared the forward run to observations, examining both general features and short term events.

Interannual changes in methane behavior at any particular site are governed by changes in transport, sources, and sinks. Since our reference run contains annually repeating sources and sinks, we were able to examine the importance of interannually varying transport at different sites. For example, do large scale atmospheric transport phenomena, such as El Niño, affect CH₄ observations in a predictable fashion? Most previous methane modeling studies have used only a single year of meteorology; this approximation may lead to errors when simulating CH₄ observations that are influenced by transport interannual variability (IAV). The comparison to high-frequency observations is generally straightforward because observations and model output frequency are similar. The model to flask comparison is more difficult due to the low sampling frequency of flasks; we test two methods of generating monthly means for flask comparison. Finally, we examine the sensitivity of the current methane observation networks to individual methane processes. These sensitivities are used in the Chapter 4 methane inversions to estimate the flux magnitudes of these processes.

3.1 Methane Observations

The locations of all methane time-series data used in this study are shown in Figure 3.1. Methane observations at other sites exist, but we include only those 87 sites that were active between our 1996 to

2001 period of study. A few sites were also omitted if their observations appeared suspect or contained local contamination. The 13 high-frequency stations (large, red) measure methane mole fractions in-situ between 24 and 36 times per day. The 74 low-frequency sites (41 blue and 33 green) represent locations of flask sampling, which occur approximately weekly. These two different sampling strategies broadly represent the two complementary approaches to global methane sampling: high sampling frequency versus high spatial coverage. The former requires a CH₄ measuring instrument on site, while the latter only requires discrete air sample collection for later analysis. As can be seen, most of the sites are located in the Northern Hemisphere. Tropical land regions in particular are relatively undersampled. We have further subdivided the flask measurements into sites which have observations for more (41 sites) and less (33 sites) than 70% of the 60 months used in this study (8/1996-7/2001). Table 3.1 lists the observational locations latitudinally, within each of three main groups shown in Figure 3.1. A few different laboratories employ one or more sites (i.e., networks) to measure methane. The Advanced Global Atmospheric Gases Experiment (AGAGE) operates the greatest number of high-frequency stations (5), while the Climate Monitoring and Diagnostics Laboratory (CMDL NOAA) operates the greatest number of flask sites, in conjunction with other laboratories.

The standards used for the absolute calibration of methane mole fractions differ between certain laboratories. Intercalibrations of these standards have been performed (e.g., *Cunnold et al.* (2002), *GlobalView-CH4* (2001)), allowing conversion of methane data to a common standard. Table 3.1 lists the calibration factor to convert other CH₄ measurements to the AGAGE standard, used throughout this study. The absolute calibration used by AGAGE is based on the Tohoku gravimetric technique, as described in *Cunnold et al.* (2002). This scale is also used for many of the Japanese NIES sites. *Dlugokencky et al.* (1994c) describe the absolute calibration used by CMDL, which is based on use of multiple high-stability tanks. This scale is used by the majority of flask sampling networks, as described in *GlobalView-CH4* (2001). Comparisons between the AGAGE/NIES and CMDL absolute CH₄ calibrations indicate that the CMDL calibration is about 1.1% lower (about 20 ppb). The exact calibration difference varies in the literature: multiplicative factors of 1.0119, 1.01069, and 1.0152 are reported by *Cunnold et al.* (2002), *Prinn et al.* (2000), and *GlobalView-CH4* (2001), respectively. We choose the 1.0119 value since that is the most recently reported inter-calibration factor that has been used to compare field data. All measurements based on the CMDL calibration are multiplied by this value in this work. *Cunnold et al.* (2002) noted that, after correction, some CMDL measurements are still about 1 ppb lower than the corresponding AGAGE measurements at the similar locations. This small offset can be either attributed to a small error in the inter-calibration factor, or to small differences in the exact sampling locations.

The reported precision due to random instrumental error of most methane measurements is between 0.07-0.2% (*Cunnold et al.* (2002), *CMDL* (2001)) which corresponds to a range of about 1-3 ppb. Typically, this precision is determined by repeated measurements of the same sample. The measurement precision is based on the spread in measured values due to instrumental imperfection. This error is generally small compared to the absolute calibration error. We consider overall measurement error in Chapter 4, and focus on direct model-observation comparisons in the following.

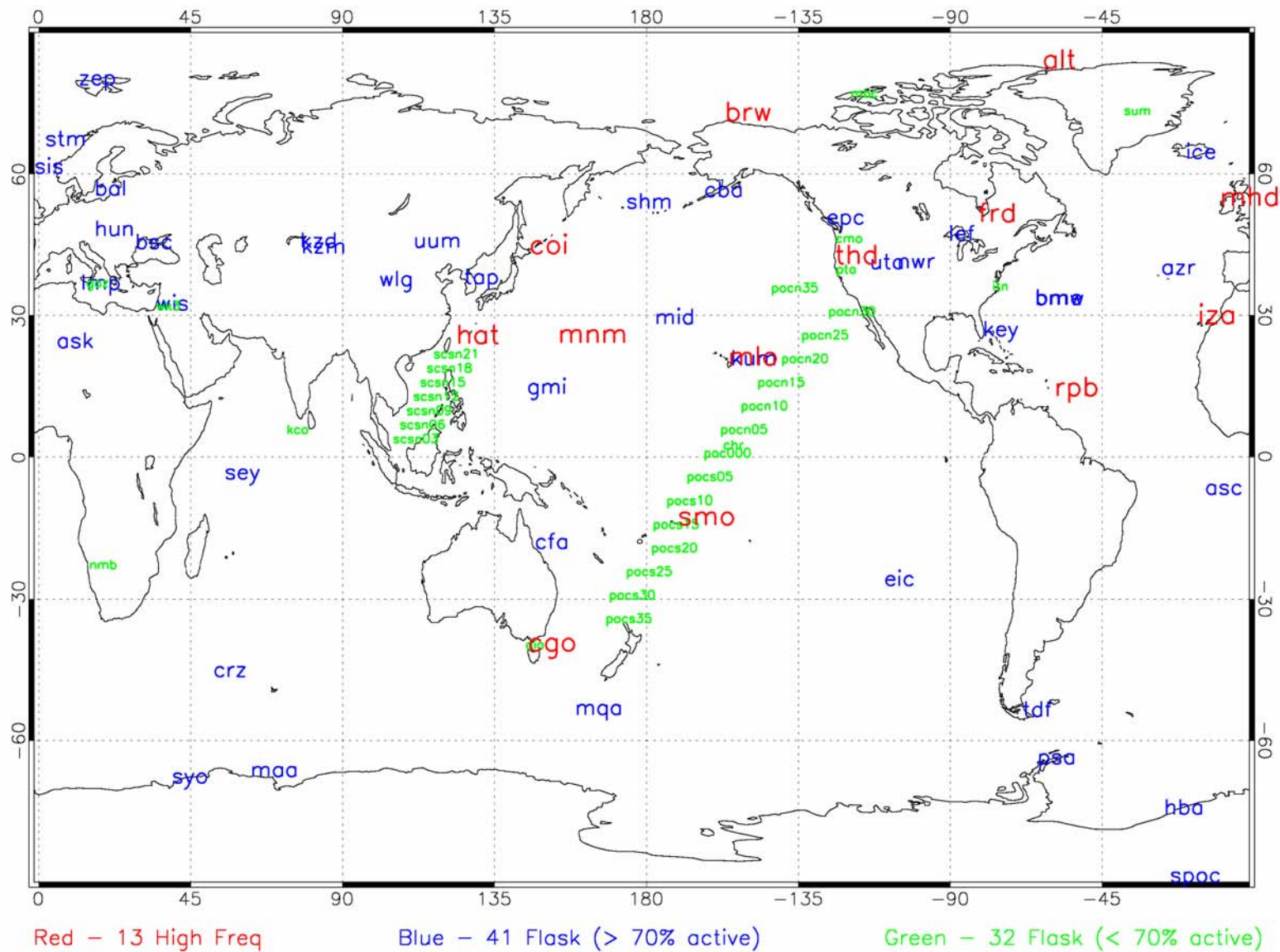


Figure 3.1: Location of methane time-series data used in this study. The large red sites denote high-frequency in-situ stations. Blue and green stations represent flask stations, with monthly data for greater and less than 70% of the 60 months between 8/1996-7/2001, respectively.

Table 3.1. List of Methane observing sites used in this study*

Number	ID	Station Location	Latitude	Longitude	Altitude	Laboratory	Calibration
High-Frequency Observations (13 Sites)							
1	alt	Alert, Greenland	82	-62	210	AES	1
2	brw	Barrow, Alaska	71	156	11	CMDL	1.0119
3	mhd	Mace Head, Ireland	53	-9	25	AGAGE	1
4	frd	Fraserdale, Canada	49	-81	250	AES	1
5	coi	Cape Ochi-Ishi, Japan	43	145	100	NIES	1
6	thd	Trinidad Head, CA	41	124	140	AGAGE	1
7	iza	Tenerife, Canary Islands	28	-16	2360	CMDL	1.0119
8	mnm	Minamitorishima, Japan	24	153	8	JMA	1
9	hat	Hateruma	24	123	47	NIES	1
10	mlo	Mauna Loa, Hawaii	19	155	3397	CMDL	1.0119
11	rpb	Barbados	13	-59	42	AGAGE	1
12	smo	Samoa	-14	170	42	AGAGE	1
13	cgo	Cape Grim, Australia	-41	145	94	AGAGE	1
Flask Sites > 70 % Active (41 Sites)							
14	zep	Zeppelin St., Norway	78	11	474	CMDL	1.0119
15	stm	Atlantic Ocean, Norway	66	2	7	CMDL	1.0119
16	ice	Storhofdi, Iceland	63	-20	100	CMDL	1.0119
17	sis	Shetland Is., Scotland	60	-1	30	CSIRO	1.0119
18	bal	Baltic Sea, Poland	55	16	7	CMDL	1.0119
19	cba	Cold Bay, Alaska	55	162	25	CMDL	1.0119
20	shm	Shemya Island, Alaska	52	174	40	CMDL	1.0119
21	epc	Estevan Pt, BC, Canada	49	126	39	CSIRO	1.0119
22	hun	Hegyhatsal, Hungary	46	16	344	CMDL	1.0119
23	lef	Park Falls, Wisconsin	45	-90	868	CMDL	1.0119
24	uum	Ulaan Uul, Mongolia	44	111	914	CMDL	1.0119
25	kzd	Sary Taukum, Kazakhstan	44	77	412	CMDL	1.0119
26	bsc	Black Sea, Romania	44	28	3	CMDL	1.0119
27	kzm	Plateau Assy, Kazakhstan	43	77	2519	CMDL	1.0119
28	nwr	Niwot Ridge, Colorado	40	105	3475	CMDL	1.0119
29	uta	Wendover, Utah	39	113	1320	CMDL	1.0119
30	azr	Azores	38	-27	40	CMDL	1.0119
31	tap	Tae-ahn Pen., Korea	36	126	20	CMDL	1.0119
32	wlg	Mt. Wanliguan, China	36	100	3810	CMDL	1.0119
33	lmp	Lampedusa, Italy	35	12	85	ENEA	1.0119
34	bme	Bermuda East	32	-64	30	CMDL	1.0119
35	bmw	Bermuda West	32	-64	30	CMDL	1.0119
36	wis	Sede Boker, Israel	31	34	400	CMDL	1.0119
37	mid	Midway	28	177	4	CMDL	1.0119
38	key	Key Biscayne, FL	25	-80	3	CMDL	1.0119
39	ask	Assekrem, Algeria	23	5	2728	CMDL	1.0119
40	kum	Kumukahi, Hawaii	19	154	3	CMDL	1.0119
41	gmi	Guam	13	144	2	CMDL	1.0119
42	sey	Mahe Island, Seychelles	-4	55	3	CMDL	1.0119

43	asc	Ascension Island	-7	-14	54	CMDL	1.0119
44	cfa	Cape Ferguson, Aust.	-19	147	2	CSIRO	1.0119
45	eic	Easter Island	-27	109	50	CMDL	1.0119
46	crz	Crozet, Indian Ocean	-46	51	120	CMDL	1.0119
47	mqa	Macquarie Island	-54	158	12	CSIRO	1.0119
48	tdf	Teirra Del Fuego	-54	-68	20	CMDL	1.0119
49	psa	Palmer Station, Antarct	-64	-64	10	CMDL	1.0119
50	maa	Mawson St., Antarctica	-67	62	32	CSIRO	1.0119
51	syo	Syowa Station, Antarct.	-69	39	11	CMDL	1.0119
52	hba	Halley Bay, Antarctica	-75	-26	10	CMDL	1.0119
53	spoc	South Pole	-89	-24	2810	CMDL	1.0119
54	spo	South Pole	-89	-24	2810	CMDL	1.0119

Flask Sites < 70 % Active (33 Sites)

55	mbc	Mould Bay, Canada	76	119	58	CMDL	1.0119
56	sum	Summit Greenland	72	-38	3238	CMDL	1.0119
57	cmo	Cape Meares, OR	45	123	30	CMDL	1.0119
58	pta	Point Arena, New Mexico	38	123	17	CMDL	1.0119
59	goz	Dwejra Pt., Malta	36	14	30	CMDL	1.0119
60	itn	Gritfton, North Carolina	35	-77	505	CMDL	1.0119
61	pocn35	Pacific Ocean	35	143	10	CMDL	1.0119
62	wk3	Sede Boker, Israel	31	34	400	CMDL	1.0119
63	pocn30	Pacific Ocean	30	126	10	CMDL	1.0119
64	pocn25	Pacific Ocean	25	134	10	CMDL	1.0119
65	scsn21	South China Sea	21	117	15	CMDL	1.0119
66	pocn20	Pacific Ocean	20	140	10	CMDL	1.0119
67	scsn18	South China Sea	18	115	15	CMDL	1.0119
68	pocn15	Pacific Ocean	15	147	10	CMDL	1.0119
69	scsn15	South China Sea	15	113	15	CMDL	1.0119
70	scsn12	South China Sea	12	111	15	CMDL	1.0119
71	pocn10	Pacific Ocean	10	152	10	CMDL	1.0119
72	scsn09	South China Sea	9	109	15	CMDL	1.0119
73	scsn06	South China Sea	6	107	15	CMDL	1.0119
74	pocn05	Pacific Ocean	5	158	10	CMDL	1.0119
75	kco	Kaashidohoo, Maldives	4	73	1	CMDL	1.0119
76	scsn03	South China Sea	3	105	15	CMDL	1.0119
77	chr	Christmas Island	1	157	3	CMDL	1.0119
78	poc000	Pacific Ocean	0	163	10	CMDL	1.0119
79	pocs05	Pacific Ocean	-5	168	10	CMDL	1.0119
80	pocs10	Pacific Ocean	-10	174	10	CMDL	1.0119
81	pocs15	Pacific Ocean	-15	178	10	CMDL	1.0119
82	pocs20	Pacific Ocean	-20	178	10	CMDL	1.0119
83	nmb	Bobabeb, Namibia	23	15	408	CMDL	1.0119
84	pocs25	Pacific Ocean	-25	174	10	CMDL	1.0119
85	pocs30	Pacific Ocean	-30	169	10	CMDL	1.0119
86	pocs35	Pacific Ocean	-35	168	10	CMDL	1.0119
87	aia	Bass Strait/Cape Grim	-40	144	500	CSIRO	1.0119

* Note that some flask measurements listed as CMDL may involve participation of other laboratories. See *GlobalView-CH4 (2001)*.

3.1.1 High-Frequency (In-situ) Observations

The five AGAGE stations (Table 3.1) provide the largest, most consistent set of high-frequency methane measurements on the global scale. The five locations are Mace Head (Ireland), Trinidad Head (California), Barbados, Samoa, and Cape Grim (Tasmania). As described in *Prinn et al. (2000)*, methane mole fractions are measured in-situ by Gas-Chromatography Flame Ionization Detection (GC-FID) approximately every 40 minutes (36 times per day). The inactive GAGE network (predecessor to AGAGE) measured methane approximately every 2 hours. However, GAGE methane measurements are generally considered to be less reliable than the AGAGE measurements (*Prinn et al. (2000)*). For the purposes of this study, we used CH₄ data from AGAGE only, with methane measurements starting between August 1993 (Cape Grim) and July 1996 (Samoa).

The AGAGE sites sample large volumes of air free of local contamination (and rejected if not) across the major latitudinal zones. The black curves in Figure 3.2 show methane data for the five different sites, with 100 ppb offsets for each station progressively from Cape Grim for clarity. Each measuring station has a distinctive seasonal cycle that depends on the seasonality of emissions, destruction by OH, and transport. The slow methane growth rate of approximately 0.5% annually is also observed at all sites, although it may be difficult to discern from the scale of this figure. For Cape Grim, which is relatively distant from strong seasonal emissions, the cycle is dominated mostly by the seasonal cycle of OH. The seasonal cycle for Samoa is similar in phase to Cape Grim, but smaller in amplitude. The springtime trough at Samoa is partially masked by the intrusion of Northern Hemispheric air which has higher methane concentrations. This intrusion is less during El Nino which is best seen by examining CH₃Cl₃ data (*Prinn et al. (1992)*, *Prinn et al. (2000)*). The three Northern Hemispheric sites are more complicated due to the influences of seasonal CH₄ emissions. The late summer troughs in their cycles, however, correlate with maximum OH concentrations during the summertime.

Very large methane peaks of short duration (i.e. less than a few days) usually represent air that has just passed over strongly emitting anthropogenic source regions. The peaks evident at Mace Head, Trinidad Head, and Cape Grim are caused by strong emissions from continental Europe, California/Oregon, and Southeastern Australia, respectively. In some cases, large methane variations do not represent emissions from a specific region but rather a different bulk airmass. For example, the large CH₄ fluctuations between January and April at Samoa represent shifts between Northern and Southern Hemispheric air, which contain relatively high and low methane values, respectively. This is a consequence of the ITCZ 's proximity to Samoa during those months, discussed in Section 3.4.1. The other high-frequency sites usually exhibit characteristics similar to at least one of the AGAGE sites. These other sites will be discussed in Section 3.4.1, which compares model and observed CH₄ values.

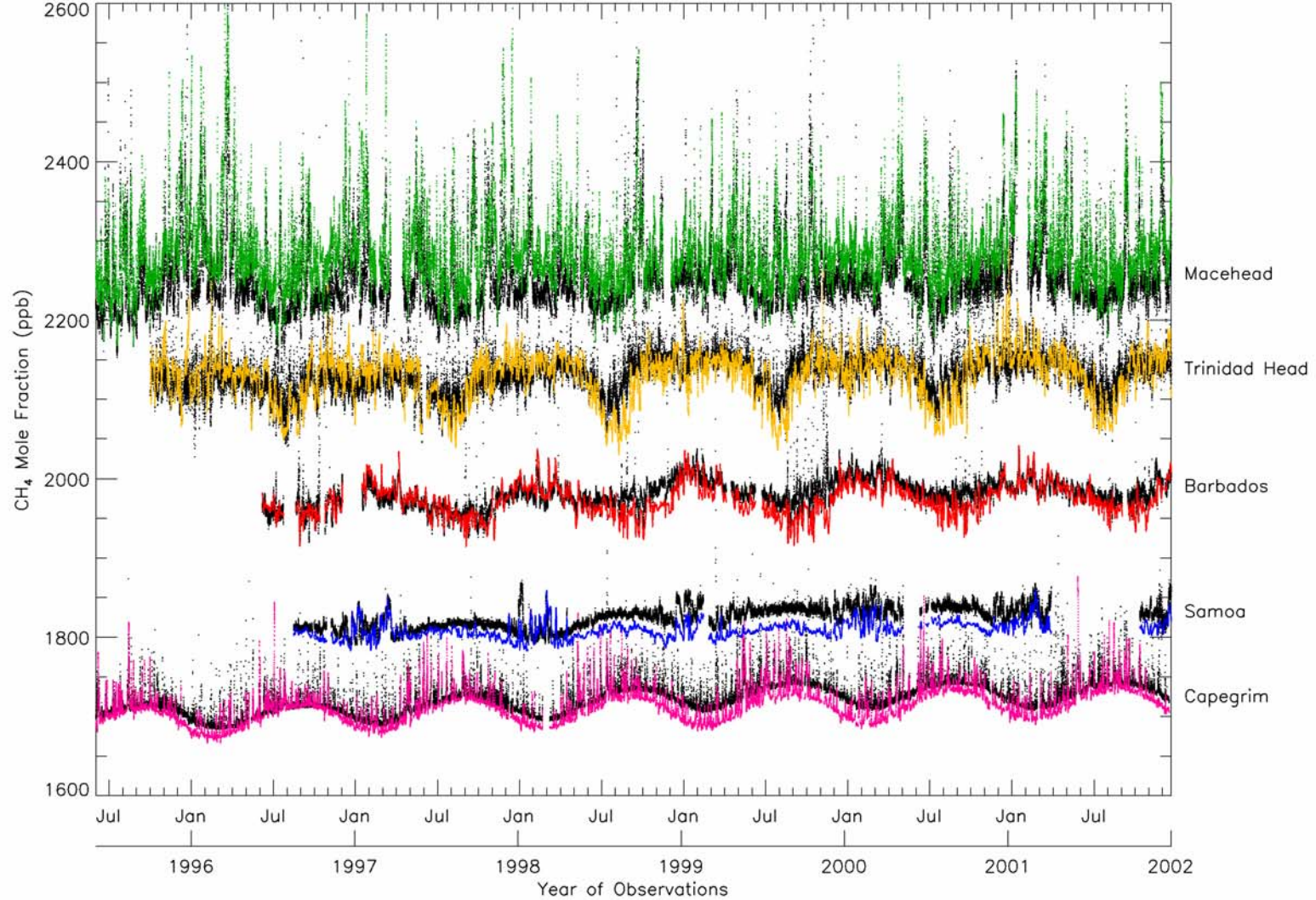


Figure 3.2: Time series of CH₄ mole fractions at 5 AGAGE stations, with station identification to the right of plot. Black values correspond to actual observations (36 / day), color corresponds to MACH output using the reference emissions as described in Table 3.2 and Figure 3.3. Each station has been offset progressively upwards from Cape Grim by 100 ppb for clarity. Each station has a different seasonal cycle and amplitude, as well as different peak levels, due to proximity to different sources and different OH levels. The MACH run uses annually repeating emissions and OH field; its interannual variations are therefore due only to interannual changes in transport. The actual observations include interannual changes in emissions, OH, and transport.

3.1.2 Low-Frequency (Flask) Observations

Given fixed resources, flask sampling allows greater spatial coverage than high-frequency sampling because samples need only be collected, rather than measured, at a site. The locations of 74 flask sites are shown in Figure 3.1 (blue and green sites). Most of these samples are taken by collecting air in stainless steel flasks, followed by delivery to a central laboratory for analysis. Our flask measurements have been obtained from the *GlobalView-CH4* (2001) database and the *WDCGG* (2003) data archive. CMDL maintains the greatest number of flask sites (70%), followed by CSIRO (21%). Most sites are fixed locations on continents and islands. Additional flasks are collected on ships transects across the South China Sea and the Pacific Ocean. Flasks are also collected from aircraft operating from a few locations, providing the few available time series of vertical CH₄ profiles. However, only the Cape Grim/Bass Strait aircraft measurements were readily available for this study.

The general method of flask sampling is as follows: at each site, two identical flasks are filled with air; these duplicates are then sent to a central measuring laboratory for analysis. The time between sample collection and CH₄ measurement is typically two weeks. CMDL uses GC-FID as the CH₄ measuring technique, with a comparable precision (0.1%, *Dlugokencky et al.* (1998)) to the similar AGAGE measurement technique (0.2%, *Cunnold et al.* (2002)). At most sites, collection occurs at times that maximize the chances of capturing air free of pollution (i.e. baseline air), which can otherwise lead to highly variable methane mole fractions. This is often attempted by sampling when the winds are coming from a specific direction (e.g., from the clean marine boundary layer) and at a specific time of day (e.g., during the day when the planetary boundary layer is higher and better mixed). The definition of baseline air varies from site to site, because many locations may have methane peaks that do not represent pollution. Non-baseline air is sometimes inadvertently sampled, as it is difficult to forecast the true origin of air masses.

In addition to the raw flask data, the GlobalView CH₄ data set (*GlobalView-CH4* (2001)) contains a data product based on flask observations collected between 1983 and the present. This product includes data from eight different measurement networks calibrated to the CMDL scale. Flask measurements above a certain threshold value (site-specific) have been removed according to a specific algorithm (*CMDL* (2001), *Masarie et al.* (1995)) in order to generate a smoother methane dataset. In addition to these filtered flask measurements, GlobalView CH₄ includes interpolated and extrapolated data to fill missing data at each site between 1984 and the present. The procedure for generating interpolated/extrapolated data at a particular site depends on real data from other active sites that are either nearby or in the same latitude zone. *Masarie et al.* (1995) describe this extension algorithm for CO₂. Interpolated/extrapolated data have been used in the CO₂ inversions described in Chapter 5. Its use can stabilize inversion results which may otherwise show large fluctuations due to the abrupt activation/deactivation of influential CH₄ sites. However, its use can also lead to inversion errors, because pseudo-data are being used. We use only real observations for the following study, and not these smoothed/interpolated data.

3.1.3 Other Observations

Several large scale field experiments over the past 15 years have also measured CH₄ in addition to other constituents. These measurements have been made from a variety of platforms, including ships, aircraft, and trains. Some of these measurements include high-frequency and high-density measurements over specific regions. We do not include them in this study, since our focus is on the seasonal and interannual variation of large-scale flux regions in which consistent time-series data is more useful. Field measurements over short-terms, however, offer additional data for future testing of our results.

There are approximately ten locations where methane flask samples have been measured for isotopic time-series analysis (¹³CH₄, CH₄D, ¹⁴CH₄). Several field measurement campaigns of short duration have also focused on measuring these isotopes. Isotopic measurements of methane generally require more sophisticated sampling and measurement techniques compared to the standard methane observations, since isotopic mole fractions are 1×10^{-3} to 1×10^{-9} less abundant than ¹²CH₄. In general, there has been less intercalibration between different laboratories measuring methane isotopes, than for methane mole fractions. We do not use methane isotopes in this study, but may use them in future forward and inverse modeling.

3.2 Sources

The individual methane emissions that were collected for input into MATCH are described in Table 3.2; together they constitute our methane “reference” emissions. These “bottom-up” emissions represent our best guess of the total methane flux before optimization of individual processes to get “top-down” emission estimates in Chapter 5. The choice of individual emission magnitudes and patterns in Table 3.2 was also influenced by preliminary MATCH simulations that tested different emission patterns and global total CH₄ inputs. Note that the individual reference magnitudes fall within the IPCC ranges. Figure 3.3 shows the annually averaged spatial distribution of these combined surface fluxes. The distribution also varies by month due to strong seasonal emissions. As can be seen, most of the emissions are concentrated in the Northern Hemisphere. This results in the large interhemispheric gradient of CH₄ observed between the Northern and Southern Hemispheres. The spatial distributions of several of the individual processes are found in Figure 3.4 and Figure 3.5. In the following we describe the sources of these emission fields.

The methane sources can be divided into different categories, for example seasonal vs. aseasonal, anthropogenic vs. natural, biogenic vs. geologic. The main division chosen here is between seasonal (wetlands, rice, and biomass burning) and aseasonal emissions (animals, waste, natural gas leakage, and coal). Seasonal sources are considered to show significant variation in magnitude between months and have a distinct seasonal cycle; aseasonal components are considered to vary much more slowly. The spatial distributions of seasonal processes also change by month. For example, biomass burning in the tropics shifts north and south depending on season. The spatial distributions of the aseasonal emissions are considered to be constant.

The “bottom-up” spatial estimates of most sources can be described by the following relationship:

$$\textit{Spatial Flux} = \textit{Base Quantity} \times \textit{Emission Factor} \times \textit{Spatial Distribution} \quad (3.1)$$

The base quantity typically refers to a measure of the process that emits methane. This may be total wetland area, animal population, and coal production, for example. For most processes, the base quantities are converted to methane flux values through an emission factor that relates the amount of methane produced to the process. Typically, these emission factors are estimated from laboratory experiments (e.g., the percentage methane released from the biomass burning) or field measurements (e.g., local flux measurements in wetlands). Large uncertainties may arise from the scaling of these few measured/estimated emission factors to an entire emitting process. For example, an estimate of the emission factor for rice may be applicable to a single rice field. Its application over an entire rice producing region, which contains thousands of rice fields, could lead to an error in the final magnitude of the estimate. The spatial distribution of these sources is also necessary for input into a global model. For many of the processes described in Table 3.2, there is a close coupling between the base quantity and its spatial distribution. The location and sizes of individual coal mines are well known, for example. For other processes, the spatial distribution may be mapped to a proxy (e.g., population density for landfills). Wetland emissions represent a process with a tight coupling between emission magnitude and spatial distribution. For this process, a wetland emissions model uses climatological parameters to diagnostically estimate methane efflux.

With the exception of biomass burning, the emissions in Table 3.2 are derived from the *EDGAR* (2002) and *Fung et al.* (1991) databases. These two data sets contain many of the same emission processes, although their distributions and magnitudes may differ. For most of the overlapping sources, we use the more current EDGAR 3.0 database. Unfortunately, the EDGAR fields do not include a seasonal information for its rice and biomass burning emissions. Note that some of the reference emission values in Table 3.2 may be slightly higher than the estimates associated with the original emission field. This reflects the global flux scaling used to create a 590 Tg yr⁻¹ total flux (as described in Section 3.4). The adjusted processes (10-15% are within the error range of their original emissions).

3.2.1 Seasonal Emissions

Wetlands

The wetland distributions used in this study are described in the *Fung et al.* (1991) methane simulations. Two distinct sets of wetland distributions are available. The first distribution (75 Tg yr⁻¹) includes modeled distributions for bogs, swamps, and tundra, based on temperature and precipitation distributions as described in *Matthews et al.* (1987). These wetland distributions have been estimated by combining three independent data bases on vegetation, soil properties, and inundation properties. In general, bogs and swamps dominate emissions in the northern and tropical/southern latitudes, respectively (Figure 3.4). Bog emissions tend to be temperature dependent and are located mostly in the Northern Hemisphere above 40° N. Swamp emissions are more dependent on precipitation and can be found in both temperate and tropical locations. The second wetland distribution (total 110 Tg yr⁻¹) was constructed by extrapolating flux measurements taken before 1987. Its global distribution is more strongly weighted towards the northern latitudes where most of the measurements were taken. We favor the first distribution because its spatial distribution depends on actual drivers of wetland flux and is also more consistent with recent field data. A larger wetland total of 151 Tg yr⁻¹ was also used which reflects more recent estimates (*Houweling et al.* (2000), *Lelieveld et al.* (1998))

Rice

The rice distributions used in this study are described in *Matthews et al.* (1991). They combined $1^\circ \times 1^\circ$ maps of agricultural land use with country statistics of rice harvest and maps of total harvest production. We use a reference rice emission of 92 Tg yr^{-1} . Greater than 80% of the flux originates from China, India, and South-East Asia (Figure 3.4). Monthly variations were incorporated by linking emissions to seasonal cropping activity. The timing of methane release is a source of some uncertainty. *Matthews et al.* (1991) assumed a constant flux of methane during a rice growing season. *Redeker et al.* (2000) measure large methane efflux from recently dried soil at the end of the growing season, suggesting that the temporal emissions behavior may be more complicated. Although the EDGAR dataset includes a rice emissions field, it lacks the seasonal information contained in *Matthews et al.* (1991).

Biomass Burning

We have used the $5^\circ \times 5^\circ$ spatio-temporal distributions of tropical biomass burning in Asia, South America, and Africa from *Hao et al.* (1993) interpolated to T42 resolution (Figure 3.4). To convert from biomass burning area to methane flux, we have used the *Hao et al.* (1994) biomass burning CH_4 estimates for each region, and have scaled according to the biomass burning distribution. The total CH_4 magnitude for these three regions is approximately 30 Tg yr^{-1} . There is a strong seasonal variation in the distribution of biomass burning due to changes in tropical precipitation, much of which is related to seasonal ITCZ shifts. Biomass burning in Southeast Asia, Northern Africa, and Northern South America dominates in the Northern Hemispheric spring. The burning shifts southward to Indonesia, Southern Africa, and Brazil in the Northern Hemispheric fall. This results in a bimodal seasonal behavior of tropical biomass burning emissions. Note that our biomass burning only includes tropical emissions; boreal biomass burning is not included due lack of spatial information. We discuss their possible influence on the inversion in Chapter 5.

Table 3.2. Methane sources ranked by emission contribution.

METHANE SOURCE	Type	Total Tg/yr	IPCC Range	% Total	Base Quantity	Emission Factor	Spatial Distribution	Emission Source
Wetlands	Seas	151	115-260	26%	Wetland Area	Model : f (T, P)	Wetland areas	<i>Fung et al. (1991), Matthews et al. (1987)</i>
Animals	Aseas	103	55-100	17%	Animal Populations	CH ₄ per animal from direct meas.	Animal Distributions	<i>Olivier et al. (1999), Lerner et al. (1988)</i>
Rice	Seas	92	30-120	16%	Rice production	Rice factor from field/lab	Rice Areas	<i>Matthews et al. (1991) Kreileman et al. (1994)</i>
Waste	Aseas	65	40-90	11%	Waste prod. per capita	Direct measure	Population density	<i>Olivier et al. (1999), Subak et al. (1992)</i>
Natural Gas	Aseas	51	30-75	9%	Gas Production	Leakage Estimation	Gas Production sites	<i>Olivier et al. (1999), Sagers et al. (1990)</i>
Coal	Aseas	39	30-75	7%	Coal Production	Leakage Estimation	Coal Mine locations	<i>Olivier et al. (1999), Smith et al. (1992)</i>
Other Anthropogenic	Aseas	36		6%				<i>Olivier et al. (1999)</i>
Biomass Burning	Seas	30	10-70	5%	Area Burned x Biomass	Factor from lab measurements	Remote Sensing	<i>Hao et al. (1993), Hao et al. (1994)</i>
Termites	Aseas	23	1-40	4%	Termite population	Laboratory and Field Estimate	Termite maps	<i>Fung et al. (1991)</i>
TOTAL (Tg/yr)		590		100%				

The magnitudes represent our reference emissions values. Note that some processes have seasonality while others do not (aseasonal). The combined spatial distribution of these emissions is shown in Figure 3.3; certain individual processes are represented in Figure 3.4 – Figure 3.5. Certain process may represent the combination of several data subsets. The IPCC ranges correspond to literature estimates, which may use different techniques, data sources, and represent different time periods. The Base Quantity, Emission Factor, and Spatial distribution correspond to the terms in Equation (3.1).

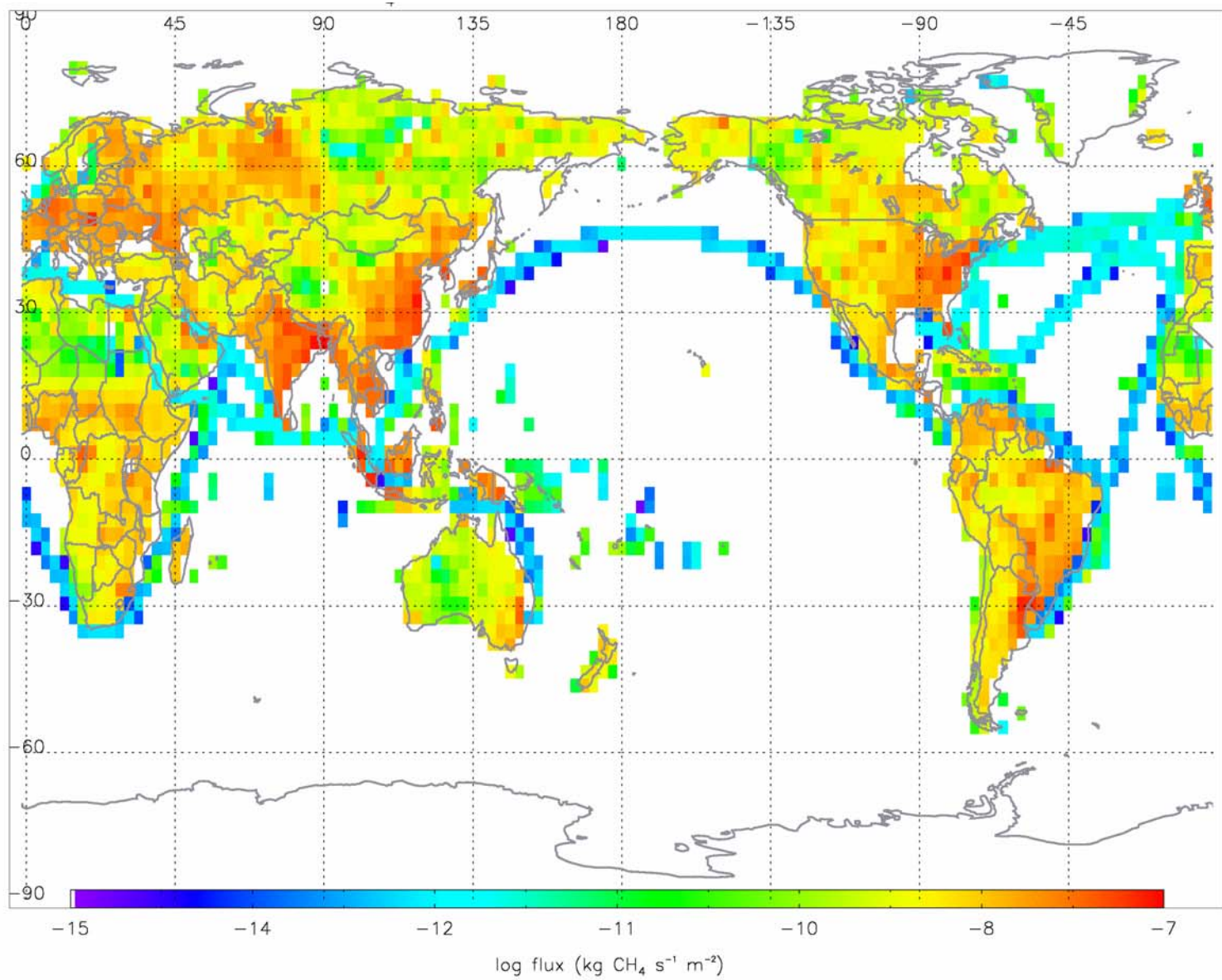


Figure 3.3: Annual Mean Distribution of Methane Emissions at 2.8° x 2.8° (T42) resolution. Note the Log scale. The emissions have significant month-to-month seasonality due to wetlands, rice cultivation, and biomass burning.

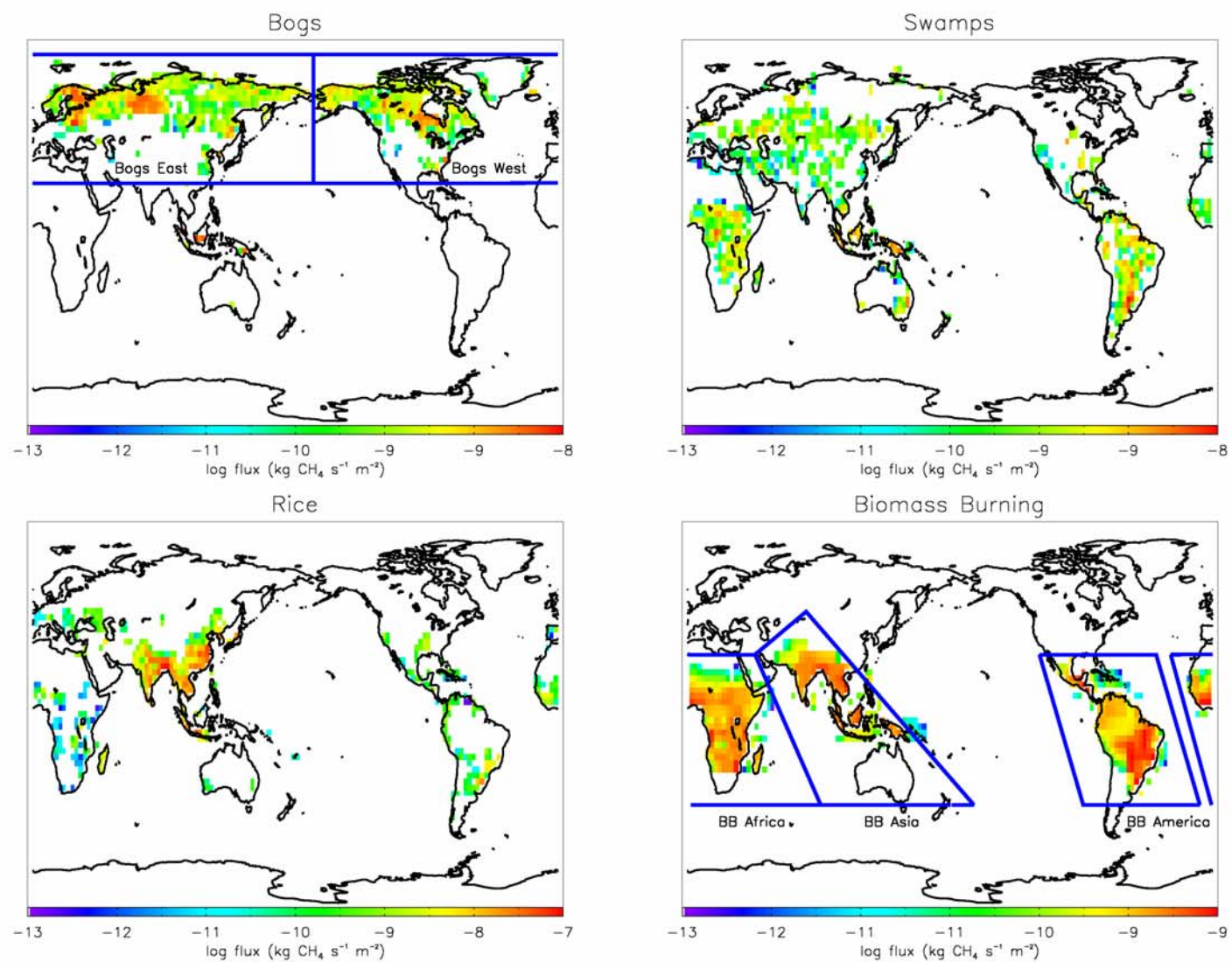


Figure 3.4. Annual Average Distributions of Seasonal Processes. Emission magnitudes and patterns will vary by month. Bogs (East and West) and Biomass Burning (Asia, America, and Africa) have been further subdivided for use in the inversion.

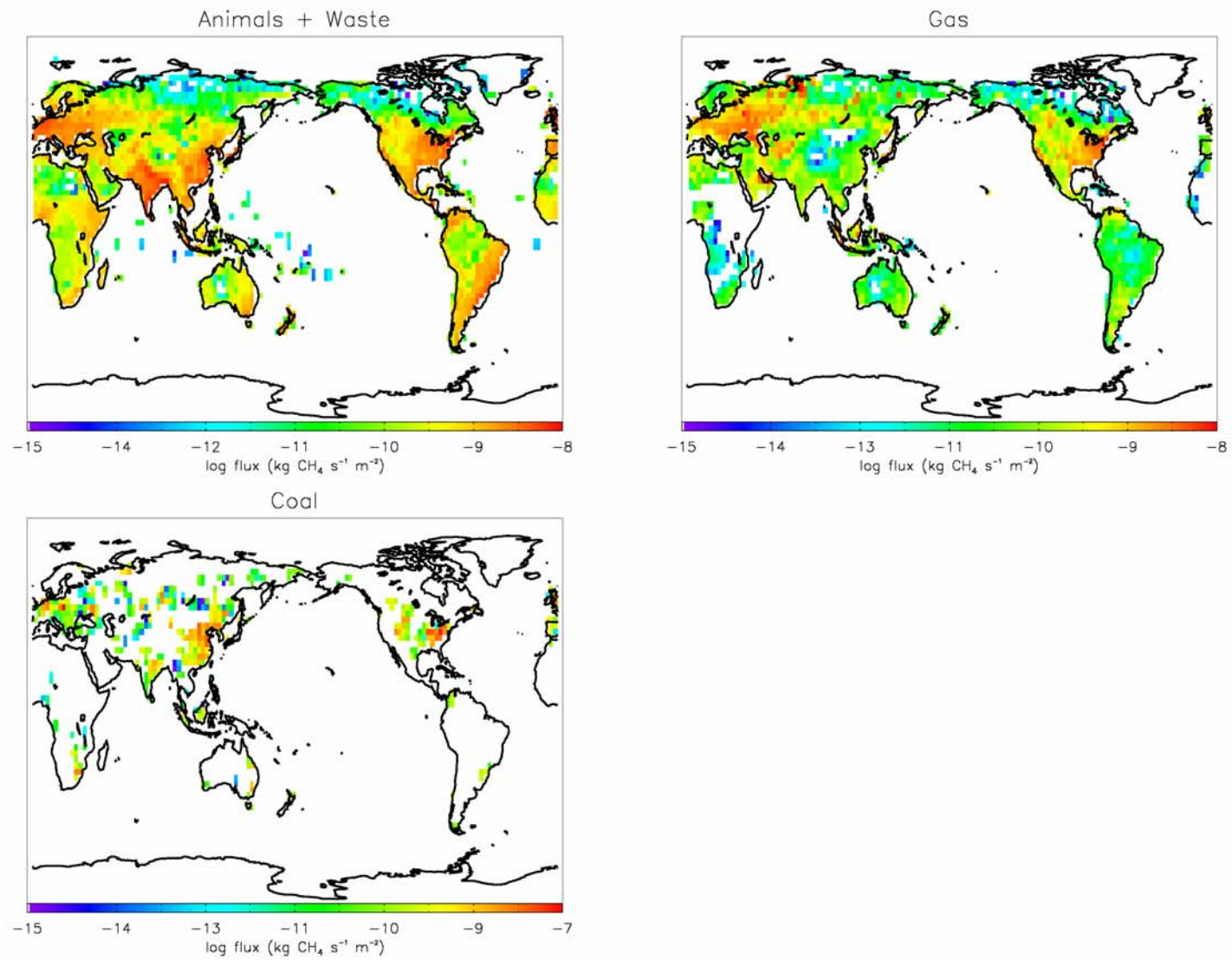


Figure 3.5. Aseasonal Emission. Emission magnitudes and patterns are constant month to month. Animals and Waste emission have been combined because their distributions are very similar.

3.2.2 Aseasonal Emissions

Animals

We assembled animal distributions from *EDGAR* (2002) and *Fung et al.* (1991), the latter based on *Lerner et al.* (1988). These two data sets are based on FAO animal population statistics by country for 1991 and 1984, respectively. These statistics were then combined with $1^\circ \times 1^\circ$ maps of agricultural land within individual countries or country subdivisions. The two distributions also used different CH_4 emission factors. The *EDGAR* (2002) study also includes animal waste emissions, which accounts for about 10% of the total animal emissions. The *EDGAR* (2002) total is 89 Tg, while the *Lerner et al.* (1988) total is 76 Tg. Both emission distributions are similar. The *EDGAR* (2002) distribution is shown in Figure 3.5 along with waste emissions; as can be seen, most continents contain significant animal emissions.

Waste

The *EDGAR* (2002) distribution for waste includes landfills, wastewater treatment, and waste incineration estimates. These distributions depend on urban population statistics and estimated emission factors (*Subak* (1999)). The *Fung et al.* (1991) data set combines population densities with a study of methane waste emissions from *Bingemer et al.* (1987). Both studies have total emissions of approximately 50 Tg annually. In the inversion, waste and animal emissions are solved as a combined emission, since they have similar spatial patterns.

Natural Gas Production/Transmission/Storage

Natural gas is comprised of approximately 90% methane. Significant emissions of natural gas occur due to leakage during production, transmission, and storage. The global locations of natural gas source, pipes, and storage sites are relatively well known (International Petroleum Exchange data, *Olivier et al.* (1999)). However, the total loss from these sources are much more difficult to quantify. For example, the estimates range from 1-2% for the OECD countries, to as high as 7% for Russia (*Dlugokencky et al.* (1994a)). Estimating the magnitude and spatial distribution of transmission loss is particularly difficult, because this leakage may occur along a pipeline that extends over thousands of miles, e.g. the West Siberian gas pipeline into Western Europe (*Reshetnikov et al.* (2000)). *Fung et al.* (1991) also followed a similar estimation procedure, although relying on the older sources then available. The *EDGAR* (2002) emissions are approximately 45 Tg yr^{-1} , while the *Fung et al.* (1991) emissions are about 20 Tg yr^{-1} .

Coal

The *EDGAR* (2002) coal distribution is derived from a 1994 IEA report based on 1990 data. A distinction is made between hard and brown coal, with a further subdivision into open pit and underground mines. A total of 2100 mines in 60 countries are represented as point sources. As shown in Figure 3.5, coal emissions are relatively localized. *Smith et al.* (1992) describe emission factors used to convert coal production to methane release. In comparison to *EDGAR* (2002), the coal distribution of *Fung et al.* (1991) is more homogenous, suggesting that individual mines were not resolved spatially. For example, coal emissions from China appear to be relatively uniform across the entire country rather than as discrete point sources. Both coal sources are around 30 Tg yr^{-1} .

In order to choose a single reference set of emissions, we constructed several plausible emission scenarios from the multiple emissions described above. These scenarios were then run forward in MATCH and compared to the observed methane interhemispheric gradient and seasonal cycles. The comparison focused on the use of different emission spatial distributions, while maintaining similar global emission magnitudes. For example, the *Fung et al.* (1991) and *EDGAR* (2002) fossil fuel (i.e., coal and gas) datasets have significantly different patterns. Even though a similar total emission was used, differences in their spatial characteristics lead to differences in simulated mole fractions at observing sites. We found this to be particularly evident for two wetland distributions of *Fung et al.* (1991), in which either tropical emissions or northern emissions dominate. Table 3.2 describes the emissions scenario that best fit the observations by this “trial and error” approach. Note that these emissions represent the most updated datasets available, suggesting that more recent (and presumably accurate) emission distributions give more realistic modeling results.

3.2.3 Other Sources

An additional 36 Tg yr⁻¹ source of methane from the *EDGAR* (2002) database is added to overall emissions (“Other Anthropogenic” in Table 3.2). This source represents the sum of smaller contributions from industrial and biofuel combustion sectors. Most of these sources are evenly spread over the populated regions, rather than emitting as concentrated sources. There is also a very small contribution from international shipping. We have also included a termite flux of 23 Tg yr⁻¹ based on the *Fung et al.* (1991) distribution. This magnitude is consistent with the *Sanderson* (1996) estimate based on ecological maps of termite populations and on the amount of CH₄ emitted per mass termite.

Geological sources may also contribute to atmospheric methane (*Etiopie et al.* (2002), *Milkov et al.* (2003)). These sources include both terrestrial and oceanic emissions from fossil CH₄ sources of geothermal and volcanic origin. Submarine sources account for most of the oceanic emissions of methane. Significant fractions of these emissions, however, become oxidized in the sediment layer and water column before reaching the atmosphere. *Milkov et al.* (2003) estimate a 15.9 Tg yr⁻¹ source from terrestrial mud volcanoes during quiescent periods, with approximately a factor of two increase during eruptions. This estimate is derived from the number estimates of onshore and offshore mud volcanoes coupled with direct flux measurements from a few locations. We do not explicitly consider this source, since the timing, spatial distribution, and overall magnitude of geologic emissions are highly uncertain.

We also ignore the potentially large reservoir of methane hydrates, which are estimated to contain as much as 10,000 Tg of methane (*Buffett* (2000), *Dickens et al.* (1997)). These reservoirs are located along seafloor sediments near the continents and in permafrost regions (such as in Siberia). Massive efflux of methane from these sources have been hypothesized to contribute to global warming between glacial to interglacial transitions (*Buffett* (2000)). However, there are no reported measurements of significant current methane releases from gas hydrates into the atmosphere in the literature.

3.3 Sinks

3.3.1 OH Fields

We use a seasonally varying OH field generated using a version of MATCH described in *Lawrence et al.* (1999), *Jockel* (2000), and *Kuhlmann et al.* (2003). This MATCH version included a full chemical package, including non-methane hydrocarbons, for studies of tropospheric photochemistry. We use monthly mean results from the meteorological year 1997 at T63 resolution reduced to T42. The original field has an average annual OH concentration of approximately 0.8×10^6 and 0.9×10^6 molecule cm^{-3} within the troposphere averaged by mass and volume, respectively. This is at the lower end of the range of the optimized OH fields of *Prinn et al.* (2001) and Jin Huang (personal communication) using methyl chloroform (MCF, CH_3CCl_3) observations. A diagnostic of the magnitude of an OH field is its ability to reproduce observed MCF observations, because the major sources of MCF are relatively well known, and its sink is dominated by reaction with OH. *Jockel* (2000) simulated the observed time-history of atmospheric MCF at the five ALE/GAGE stations using MATCH at T21 resolution and an OH distribution similar to ours. His results show overestimates of MCF at most of the sites, suggesting that the OH concentration is too low.

To estimate an OH global scaling factor to best fit MCF observations, we simulated high-frequency MCF observations between 1978-2001 at the 5 ALE/GAGE/AGAGE sites (*Prinn et al.* (2000)) using factors of 1.0, 1.1, 1.2, 1.3, 1.4, and 1.5 to multiply our MATCH OH field. Historical MCF emission strengths were taken from *EDGAR* (2002) which is based on the work of *McCulloch et al.* (2001), who estimated annual MCF emissions using industrial production data. The spatial distribution of MCF emissions were assumed to be constant over the entire period and are described in *Midgley et al.* (1995). Briefly, total emissions were first subdivided regionally, followed by a country-by-country subdivision based on GDP. Population density was then used as a spatial proxy for emissions within countries. We combine this spatial distribution with historical estimates of MCF emission magnitudes for MATCH input. *Huang* (2000) assumed an annual average emission uncertainty of less than 5%. The *JPL* (2003) OH + CH_3CCl_3 temperature dependent rate constant has been used. Finally, we have used an initial atmospheric MCF distribution for 1974 provided by Jin Huang (personal communication). With an approximate 4.8 year lifetime for MCF decay, we expect small inaccuracies in this initial condition to have been attenuated by the mid-1980s.

Figure 3.6 shows the modeled and observed MCF time history at the 5 stations. Consistent NCEP winds were used to drive the modeled mole fractions. The observations at Cape Meares (ALE/GAGE, 1980-1988) and Trinidad Head (AGAGE, 1995-present) are spatially separated by about 100 miles, but we have shown model results for Trinidad Head only, since they have similar modeled values. All simulated stations reproduce the increase in MCF until about 1992. A strong decrease is observed after this time, due to the ban on MCF emissions as part of the Montreal protocol. For the latter 1990's, a global scaling factor between 1.2 and 1.3 for MATCH OH best reproduces the observations. That all stations show a similar scaling factor suggests that the spatio-temporal characteristics of our OH field are broadly correct. The one station that shows inconsistency is the ALE/GAGE station at Cape Meares during the 1980's. It is possible that MATCH systematically overestimates these observations relative to the other stations.

Assuming correct emissions, interannual changes in OH are reflected in the shifts in observed MCF towards the 1.2 or 1.3 OH simulated curves. The fit is relatively constant over the late 1990's, suggesting that global OH varies by less than 5% over during this time. Consequently, we use an annually constant OH field for our methane simulations. In the above experiment, we have not included the oceanic sink of MCF, estimated to be about 5% of the total sink (*Butler et al. (1991)*). Addition of this sink would result in a lower OH scaling factor. Consequently, we choose an OH factor of 1.2 for our methane runs. This leads to a tropospheric annual average OH concentration of $\sim 1.1 \times 10^6$ molecules cm^{-3} weighted by mass, which is within 5% of the latest optimized OH values by Huang using MCF (personal communication) between 1996 - 2001.

Several $\text{CH}_4 + \text{OH}$ rate constants exist in the literature, e.g., *JPL (2003)* and *Gierczak et al. (1997)*. Figure 3.7 compares three rate constants over 200-300 K. As can be seen the 2 and 3 parameter JPL rate constants are nearly identical; these rate constant expressions contain kinetic data made by several laboratories. The *Gierczak et al. (1997)* expression, which includes kinetic measurements to temperatures less than 200 K, are about 0 to 8% higher than JPL values. The difference increases as the temperature decreases to levels found in the upper troposphere. We consider this difference to be relatively small since most of the methane destruction occurs at the higher temperatures and higher OH concentrations found in the tropical lower troposphere (*Lawrence et al. (2001)*). We use the 2-parameter JPL rate constant values for this thesis. Finally, a diurnal cycle scaled to the solar zenith angle is further applied to the daily average OH concentrations interpolated by MATCH from the monthly mean OH concentrations. This ensures zero nighttime values while maintaining the daily average OH concentration.

3.3.2 Other Sinks

The OH sink is estimated to account for approximately 90% of the total atmospheric methane loss (*IPCC (1995)*). The additional sinks include consumption of methane by soil bacteria and destruction by O(¹D) and Cl in the stratosphere. Using a process based model, *Ridgwell et al. (1999)* estimate an average uptake of 20 - 51 Tg yr^{-1} by soils. The uptake distribution shares some similarities with the wetland emission distributions, although there are significant uncertainties in its spatial distribution and magnitude. We have not included this sink in our forward runs, due to its lack of availability. Our implicit assumption is that areas of wetland efflux and uptake share a similar temporal and spatial distribution, in which the net wetland efflux is the difference between the two. Only large differences in their spatial distributions would significantly impact atmospheric mole fractions. However, when modeling methane isotopes, the soil sink must be explicitly modeled, since its isotopic fractionation is extremely high (*Snover et al. (2000)*).

In the stratosphere, the reactions with Cl and O(¹D) also remove CH_4 . Using a vertical profile of $^{13}\text{CH}_4$ in the stratosphere and a one-dimensional photochemical transport model, *Sugawara et al. (1997)* estimated relative contributions from OH, Cl, and O(¹D) of 80%, 15%, and 5%, respectively. We do not explicitly model stratospheric methane loss by Cl and O(¹D) since their mole fractions are poorly known, and their effect on CH_4 mole fractions lie within the uncertainty of MATCH's stratospheric OH field. Their impact on methane isotopes should, however, be taken into account for long-term simulations, since their isotopic effects are extremely strong (*Wang et al. (2002a)* and *McCarthy et al. (2001)*). In addition,

tropospheric destruction by Cl may also be important when modeling CH₄ isotopes, although its effect on non-isotopic mole fractions is negligible in the troposphere (*Allan et al. (2001)*).

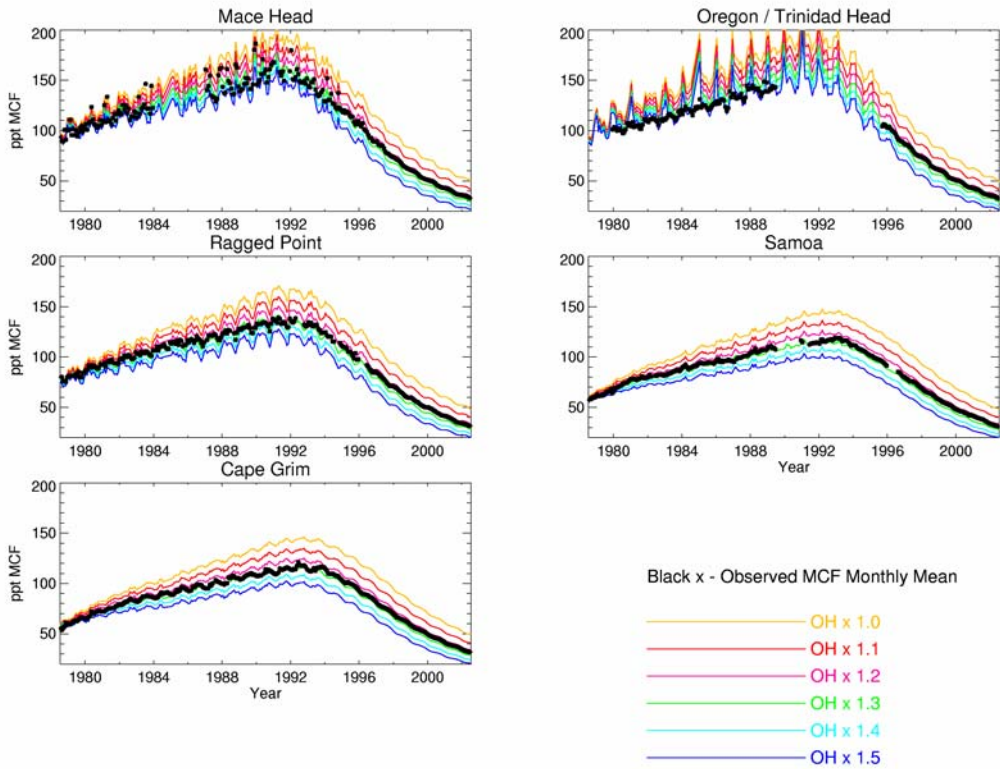


Figure 3.6: Methyl Chloroform evolution over the past 20 years using annually repeating (but monthly varying) OH fields with different constant scaling. For the late 1990's, the optimal scaling factor for the original MATCH OH field is about 1.2

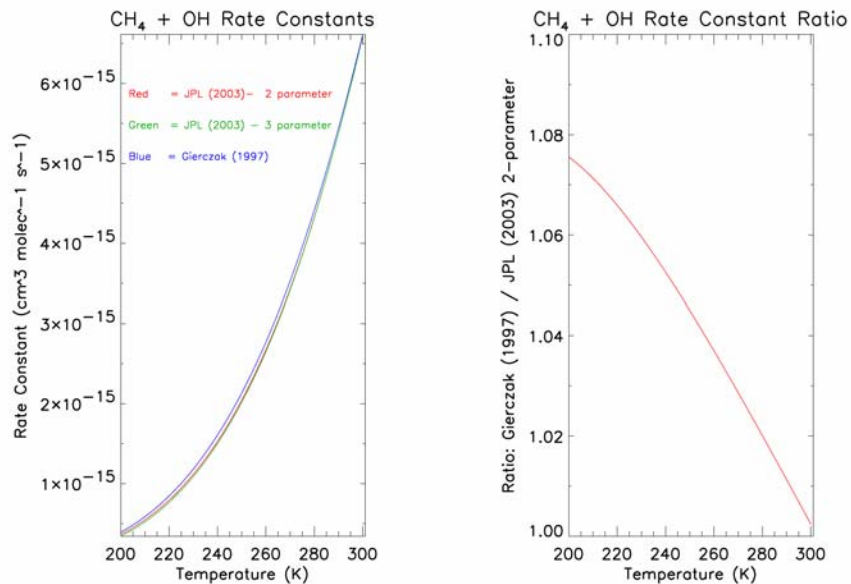


Figure 3.7: Left: comparison between *JPL (2003)* 2 parameter (red) and 3 parameter (green), and *Gierczak et al. (1997)* (blue) rate constants for $\text{CH}_4 + \text{OH}$ over a range of temperatures. The red and green JPL curves nearly overlap. Right: ratio between *Gierczak et al. (1997)* and JPL 2-parameter expression.

3.4 Modeled versus Observed Methane

A first step in this modeling study was to assess the ability of existing emissions fields to reproduce observations of atmospheric methane. Much information can be obtained from a direct comparison between the simulated and actual observations before optimizing the emissions for a better fit, as done in Chapter 4 and 5. For example, we can identify which sites show the greatest difference between model and observed values and will, subsequently, most strongly influence the inversion. We can also focus on methane variability due to changes in interannual transport, since these forward runs contain annually repeating sources and sink. The first step was to choose a reference set of emission patterns by testing several plausible emission fields as described earlier in Section 3.2. The total emissions were then scaled to approximate the observed methane growth rate over the late 1990's. The best fit was found to be approximately 590 Tg yr^{-1} . This total is largely controlled by the magnitude of the OH field, which, as noted above, had been scaled to fit MCF observations.

The reference run was created by integrating the reference emissions in MATCH between 1993 and 2002. We initialized the atmospheric distribution of CH_4 using the output from a previous multi-year run scaled to fit the observed mole fractions at Alert, Mauna Loa, and Cape Grim during January 1993. These stations were chosen because they well represent the global background interhemispheric gradient due to their distance from strongly emitting sources. Figure 3.8 shows the monthly mean modeled versus observed growth rate at these stations over the period of simulation. The observations and model share a similar growth rate. The model increase is due to the slow approach of methane mole fractions to a steady-state level that is determined by the reference emissions and OH sink. The main point is that a slow increase in methane mole fraction will occur even in the presence of constant emissions because CH_4 sources and sinks are not yet presently in steady-state (*Dlugokencky et al. (1998)*). However, more rapid changes, such as the strong increase in 1998, are likely due to year-to-year changes in emission and/or sinks. This is evident at Mauna Loa and Cape Grim, where the 1998 observed values become much higher than the modeled values.

Figure 3.9 shows the modeled and observed interhemispheric gradient (IHG) at 54 locations (13 High-Frequency and 41 Flask (>70 % Active), see Table 3.1). The annual average mole fractions were computed by averaging observed and modeled monthly means over the period 1996 - 2001. The reference run overestimates many of the sites in the NH and underestimates most of the sites in the SH. Tropical regions are also underestimated. It appears that the reference NH emissions are too strong compared to tropical and SH emissions. This suggests that any adjustment of CH_4 fluxes will lead to greater emissions from the SH and the tropics in order to better match averaged observations. This is formally calculated in the Chapter 4. First we examine the ability of MATCH to reproduce actual high-frequency and flask observations, focusing on its ability to capture short term synoptic events.

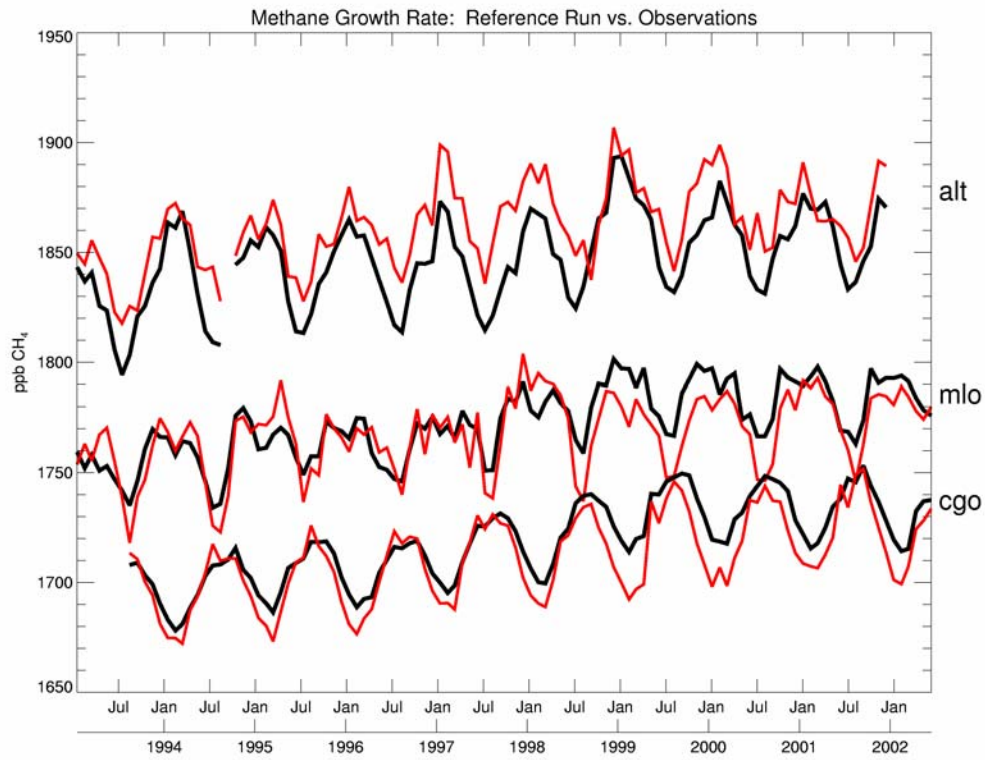


Figure 3.8. Reference model (red) versus observed (black) methane growth rate at three sites (monthly means). Note the positive growth rate even with annually repeating reference emissions.

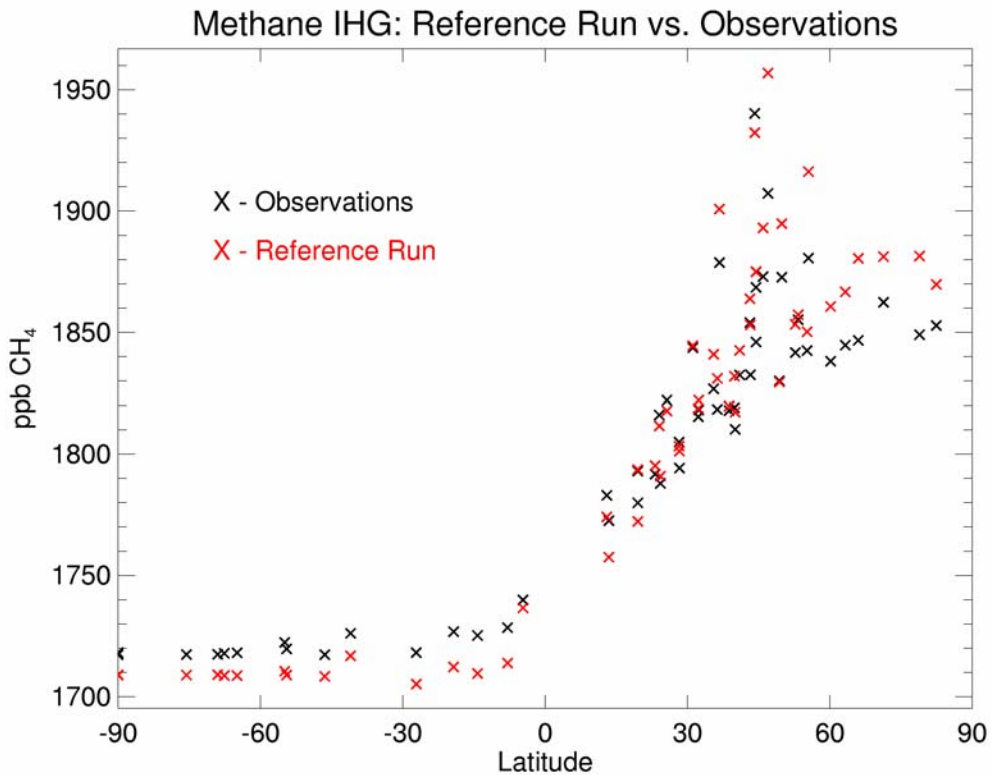


Figure 3.9: Reference model (red) versus Observed (black) Interhemispheric Gradient. Values are methane mean values between 1996-2001 at 54 sites (13 High-Frequency and 41 Flask (with >70% monthly values, see Table 3.1)). Note that the reference run overpredicts the observed IHG.

3.4.1 Comparison to High-Frequency (In-Situ) Observations

The reference run mole fractions (color) at the 5 AGAGE sites are compared to observations (black) in Figure 2. As can be seen, MATCH captures the distinct seasonal cycles at each site. The model-observed differences from IHG are also evident, with underestimations at Samoa and Cape Grim, and overestimations at Mace Head and Trinidad Head. Despite these inter-site differences, the seasonality and short-term fluctuations are mostly resolved at each site. The timing, if not the magnitude, of many methane peaks are successfully simulated (Figure 2). This indicates that much of this short-term behavior must then be due to transport interannual variability (IAV), since CH₄ emissions and OH concentrations are annually repeating.

Figure 3.13 compares the MATCH reference run to each high-frequency station, which are arranged latitudinally. The model values (red) are inverted compared to the observations (black) to facilitate comparison; a good fit is obtained when model values are the mirror image of the observations. These inverted plots allow the high-frequency variability and seasonal cycle to be more directly compared. It is important to note that some of these model-observational differences will be corrected by the inversion in Chapter 5 which optimize CH₄ emissions. The northern stations include sites that sample air from clean marine regions and air directly influenced by continental emissions. Alert (alt) and Trinidad Head (thd) sample mostly marine air and have very well-defined seasonal cycles that are captured by MATCH. Mace Head (mhd) and Barrow (brw) additionally sample significant quantities of terrestrial air, as shown by the strong CH₄ peaks. The variability of these peaks is reproduced by MATCH, as well as the timing of certain events. The MATCH reference run overestimates some peaks at Fraserdale (frd), which is in the middle of a wetland emitting region (*Worthy et al. (1998)*), especially in the winter. The model still captures the variability as well as the overall seasonal cycle (summertime trough). The Asian sites of Cape Ochi-Ishi (coi), Hateruma (hat), and Minamitorishima (mnm) and are located downwind of continental Asia and Japan. These sites show an OH induced seasonal trough during the summer, which can sometimes be obscured by strong rice/wetland emissions during this time. The observed seasonal phase is well reproduced by the reference run, although the amplitude is slightly overestimated, especially at Cape Ochi-Ishi (coi). The four tropical sites at Izana (iza), Mauna Loa (mlo), Barbados (rpb), and Samoa (smo) generally have well-defined seasonal cycles, since most are distant from emitting regions. In general, MATCH captures the variability and seasonality at these locations, in addition to specific peak events. The final station, Cape Grim (cgo), has excellent agreement between the observed and modeled seasonal cycle. The influence of strong CH₄ emissions from Southeastern Australia is also represented. We now focus on the ability of MATCH to capture short lived events at Samoa and Mace Head. These also serve as examples of how transport IAV can explain year-to-year changes in observations.

The large scale El Niño-Southern Oscillation (ENSO) phenomenon has a profound effect on the transport of the equatorial Pacific. The behavior of observed mole fractions in this region can be expected to differ between El Niño and La Niña years. The Samoan station, located near the ITCZ, is well situated to capture these differences. *Prinn et al. (1992)* have reported changes in methyl chloroform observations due to this phenomenon. Basically, cross-equatorial transport near Samoa is suppressed in

El Niño years; consequently, there is less influence from the higher mole fractions of the Northern Hemisphere.

Figure 3.11 compares Samoan CH₄ mole fractions between 1998 (strong El Niño) and 1999 (La Niña) for months between September – May. The 1998 observations contain fewer, but more intense, peaks compared to 1999. In addition, 1998 has a better resolved trough, which is less well defined in 1999. Excluding the very large peaks in 1998, the El Niño year observations show a lower variance compared to 1999, suggesting that SH air dominates, with infrequent but intense NH air intrusion. The greater variance of the 1999 observations suggest that both NH and SH air masses contribute over the observed period. As shown by the inverted plots, MATCH reproduces the general variability as well as many of the individual peaks in both periods. The average surface wind vectors during the trough period (January to April) for 1998 and 1999 are also plotted; they show striking differences in transport at Samoa. In 1998, southeasterly winds containing lower mole fractions dominate at Samoa; there are relatively few high mole fraction (northerly) peak events. In 1999, the average wind vector at Samoa is slightly northeasterly, suggesting that the air at Samoa is a mix of NH and SH air. This is consistent with methane mole fractions which oscillate frequently between high (northerly) and low (southerly) values. The Southern Oscillation Index (i.e. the normalized pressure difference between Tahiti and Darwin) shown at the bottom of Figure 3.11 shows the strong contrast between 1998 and 1999. Most years Samoa displays a behavior intermediate to 1998 and 1999, although closer to the latter.

As predicted by MATCH, other sites in the equatorial Pacific such as Christmas Island and the Pacific Cruise data also show a strong sensitivity to ENSO. Unfortunately, most of these flask sites were inactive during the early spring of 1998. In addition, a weekly sampling frequency is often insufficient to resolve the variability of mole fraction changes as shown in Figure 3.11, making these flask measurements more difficult to interpret. The Seychelles in the Indian Ocean is another station that is also predicted by MATCH to have anomalous tracer behavior due to El Niño transport. We examine this in the next section.

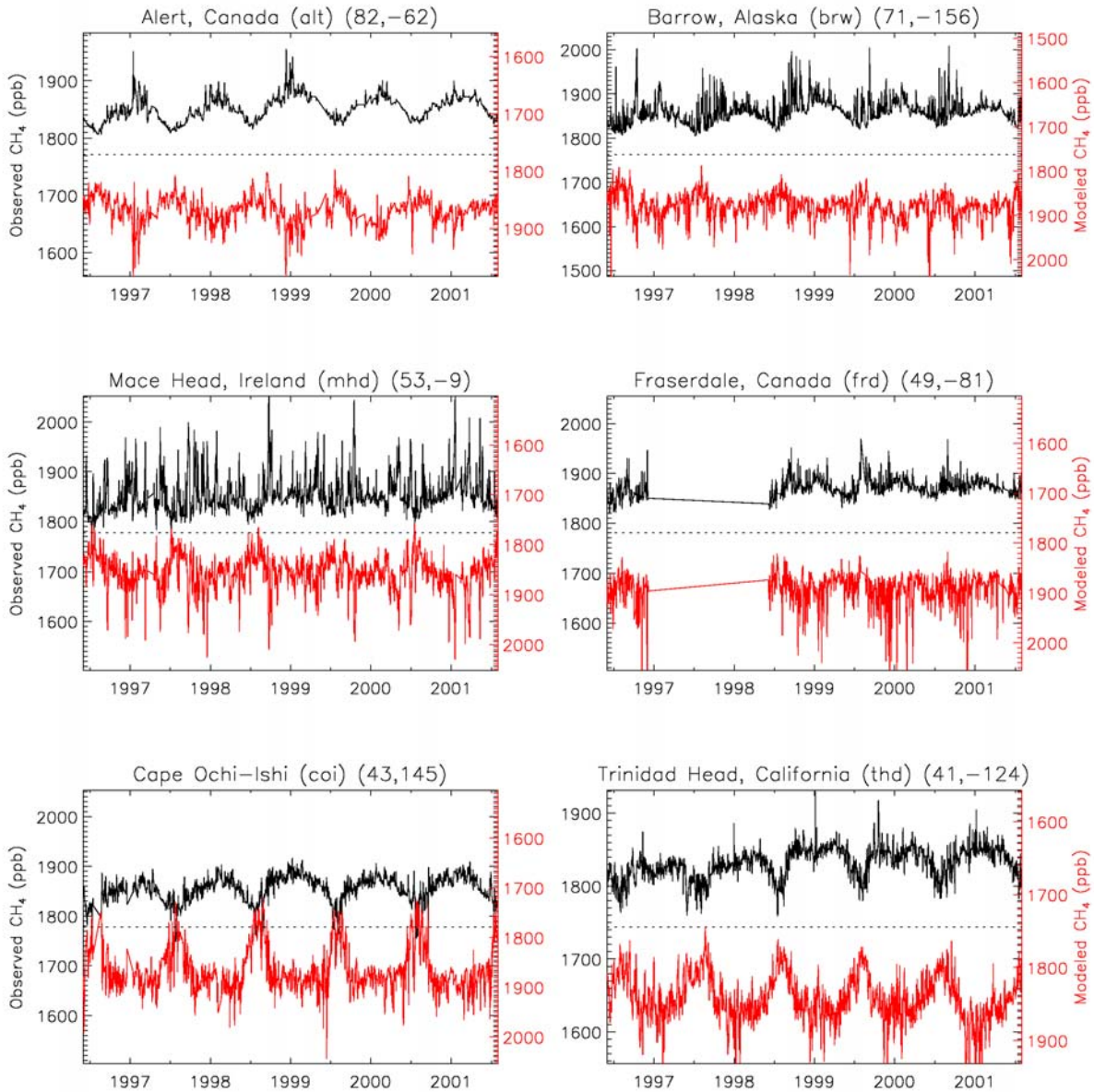
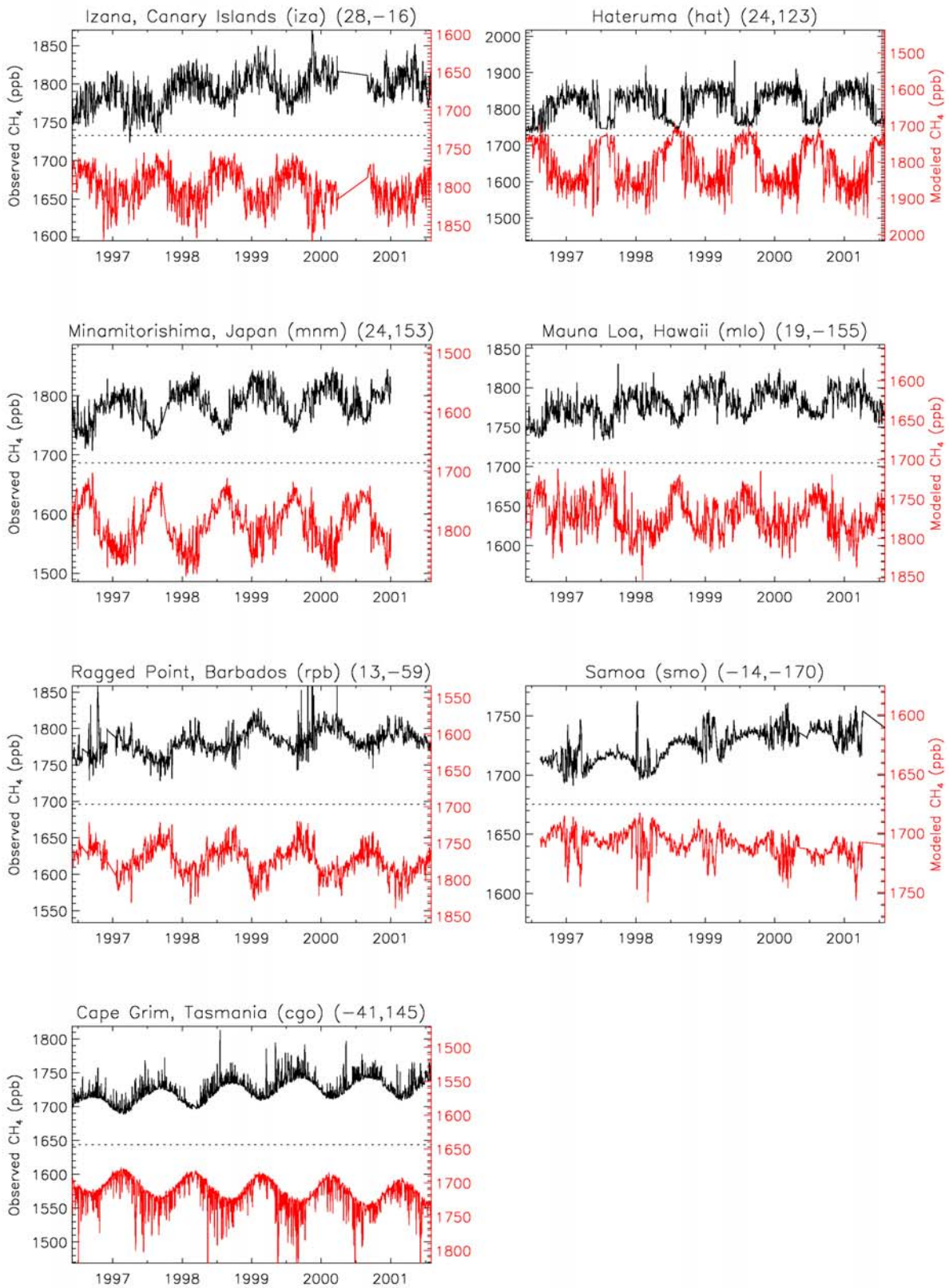


Figure 3.10. Observed (Black) and Modeled (Red) High-Frequency In-Situ values. The model values (right scale) are inverted compared to the observations to facilitate comparison; a good fit occurs when the model values are the mirror image of the observations. Latitude and longitude (degrees) for each station are indicated. The different sites use different y-axis scales. Also note that the optimized emissions in Chapter 5 will improve the seasonal fit for certain sites.



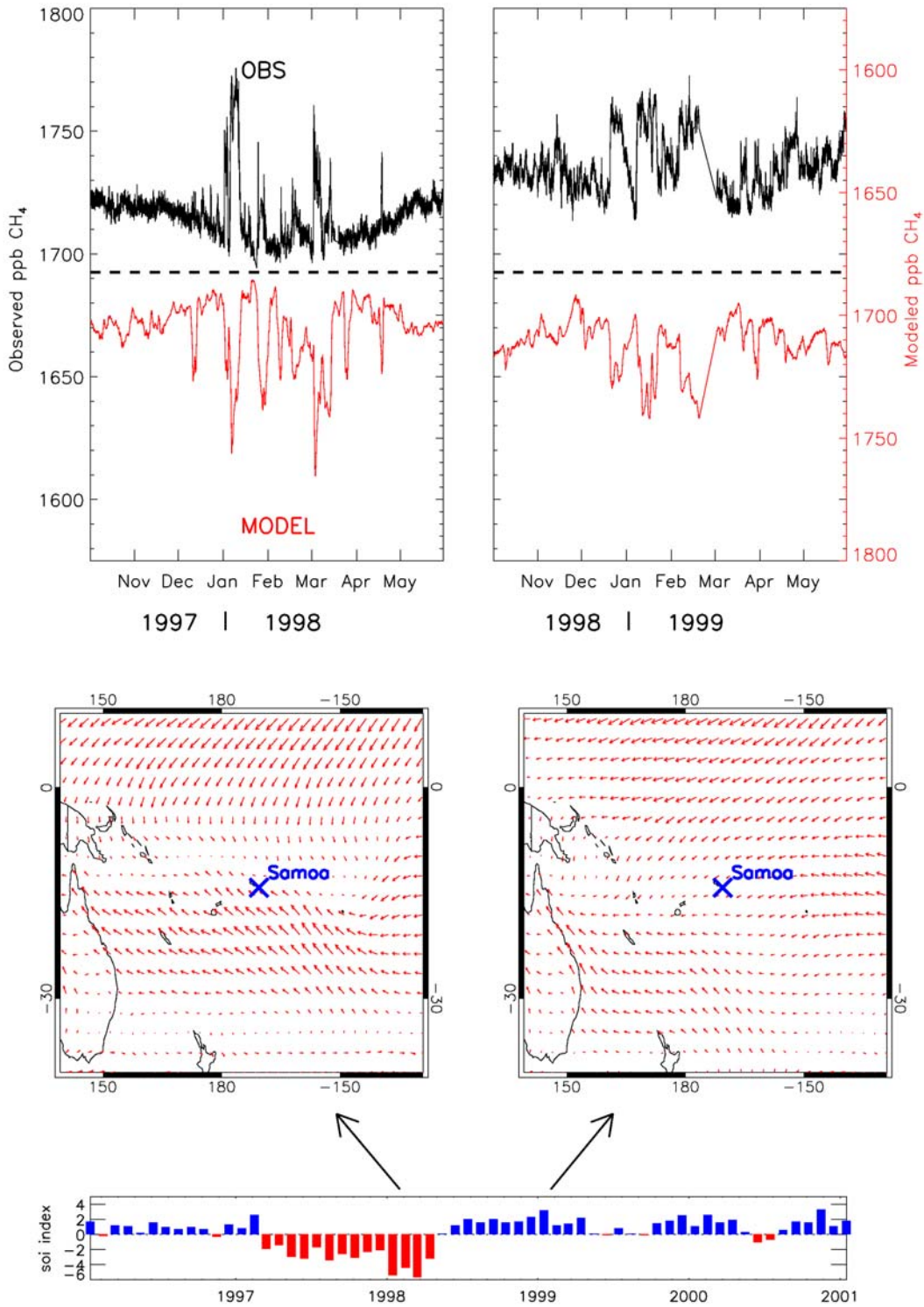


Figure 3.11: Effect of transport IAV at Samoa. Top: Observed and modeled (inverted) mole fractions. The comparison is for the same months during 1998 (El Niño) and 1999 (La Niña). MATCH correlates well with the observations, indicating that changes from transport (rather than OH or emissions) dominate. The straight line in Feb-Mar 1999 denotes lack of data. Middle: January to April average surface wind fields for the two years. The El Niño months show less influence from the NH, as can be seen by the strong average southeasterlies. The La Niña months show greater influence from the Northern Hemisphere (NH), which can be seen by higher mole fractions. The straight line in Feb-Mar 1999 denotes lack of data. Bottom: SOI index.

Mace Head also records significant interannual variations in CH₄, as shown in Figure 3.12. The low mole fractions can be attributed to relatively clean air coming off the North Atlantic. These baseline levels are interspersed by “pollution” events of varying magnitude. Most of the large peaks (i.e., 50-100 ppb above baseline) observed at Mace Head can be attributed to air which has recently been transported over European regions that have strong emissions. The frequency and duration of these events are highly variable. *O'Doherty et al.* (2001) examined Mace Head chloroform observations and removed peaks correlated with halocarbons, which are of purely anthropogenic origin. Even after this procedure, they observed the presence of peaks which correlated with low wind velocities during the nighttime, suggesting that changes in the PBL may enhance local mole fractions relative to the daytime. This phenomenon may also contribute to some of the observed methane peaks, although the majority of the peaks likely result from large scale transport off of continental Europe. Figure 3.12 compares the mole fractions between 1995 and 1996 for the months December to April. There is a striking difference between the relative number and intensity of pollution events between the two years. The 1995 observations show very few peak events while the 1996 observations show many. This strong difference is also captured by the MATCH simulation (inverted plots). As can be seen, MATCH captures the timing of most pollution events at Mace Head. There is no obvious seasonality to the high peak events, which occur throughout the year. Depleted values below 1800 ppb are also successfully modeled. The origin of these depleted values is as yet unclear, although they may be related to either midlatitude clean air masses that have undergone greater destruction by high summertime OH values or to air coming from more southerly latitudes.

Since the reference case contains no interannual changes in emissions or OH but still reproduces the observed peaks, transport IAV must be the dominant factor causing the high peak events. The December-April averaged surface wind vectors at Mace Head are shown for the two different years below the mole fraction plots. The 1995 average shows very strong south-westerlies containing relatively clean air off the North Atlantic. This is consistent with the observed clean baseline values off the Atlantic interspersed with few peak events from Europe. In contrast, the average winds during 1996 show a weak southeasterly component, indicating that continental sources will be a significant component of the observations. The result are many more and stronger peaks during this year.

The large difference between the two periods can be linked to the North Atlantic Oscillation (NAO), which dominates large scale transport variability in this region. The NAO index is shown below the surface wind plots. It is computed as the mean pressure difference between the Icelandic (polar) low and Spanish (subtropical) high pressure system between December and March. A positive index corresponds to a strong Icelandic low and subtropical high, which results in strong westerlies on a more northward track across the Atlantic. A negative index corresponds to a weaker Icelandic low and subtropical high, resulting in a weakened westerly flow on a more southward track. The NAO index between December-March 1994-1995 and 1995-1996 shows the greatest positive to negative shift over the past 30 years. This is reflected in the NCEP averaged wind fields, which show strong westerlies and weak easterlies hitting Mace Head during these periods, respectively.

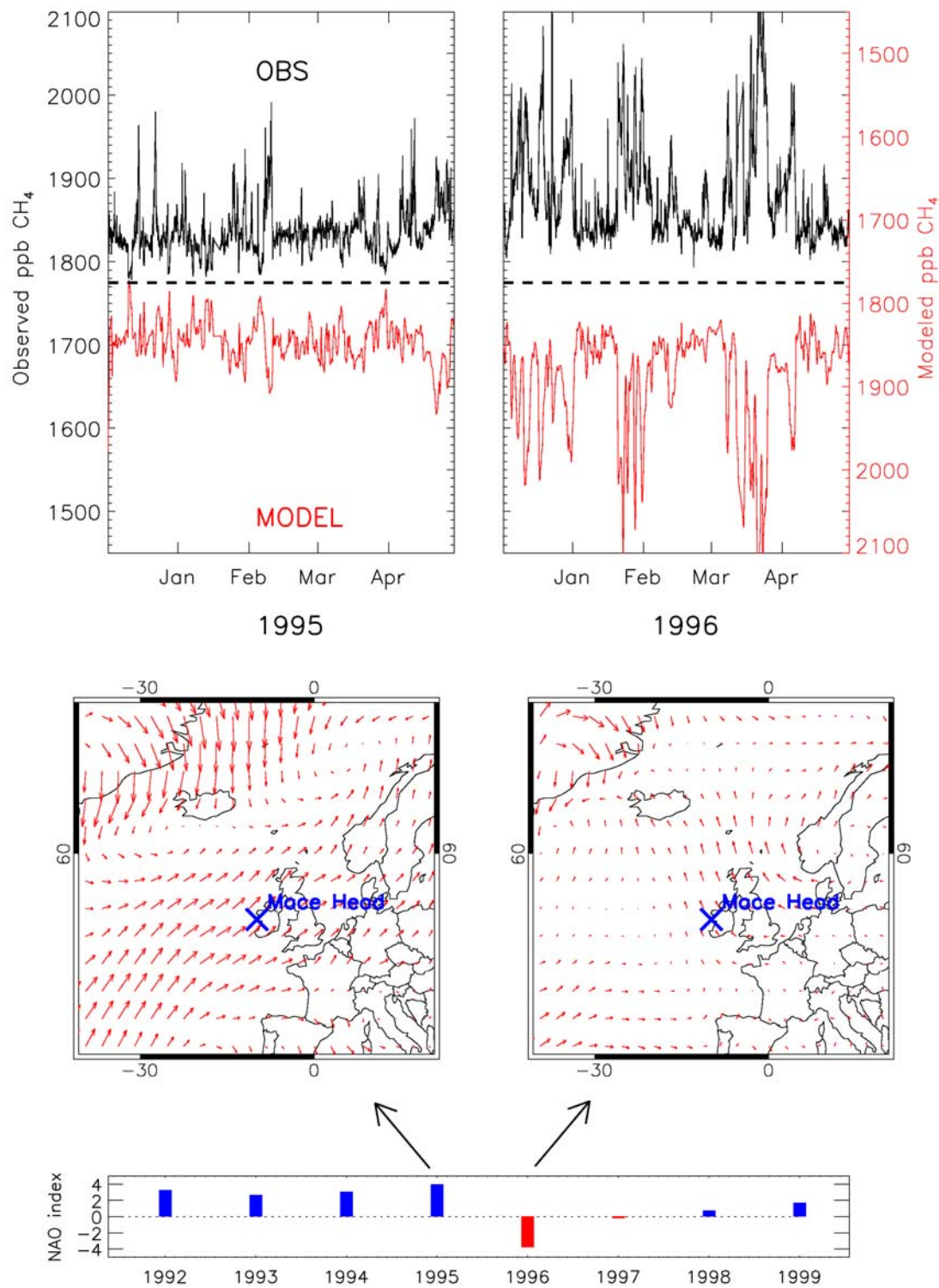


Figure 3.12: Effect of transport IAV at Mace Head. Top: Observations (black, left hand side) and MATCH (red, right hand inverted scale). The comparison is between 1995 and 1996 for Dec-May. Both observations and MATCH show that Mace Head experiences relatively clean background air in 1995, and much more polluted air from strongly emitting sources in continental Europe in 1996. Middle: December to May average NCEP surface wind vectors for the two periods. Clean North Atlantic air dominates in 1995, while 1996 experiences much more influence from Europe. This is reflected in the different observed mole fractions. Bottom: NAO Index.

3.4.2 Comparison to Low-Frequency (Flask) Observations

The number of flask sites makes a detailed comparison at each location impractical here. Instead, we compare modeled (color, inverted) and observed (black) CH₄ at six selected locations in Figure 3.13. These sites lie across a range of latitudes, and sample different regions than the high-frequency stations previously discussed. To compare to flask observations, the exact time of CH₄ sampling has been interpolated from the nearest two (bounding) MATCH CH₄ values (model output is every 2 hours). Cold Bay station (cba), is located at the tip of the Alaskan peninsula, and mostly samples marine air from the North Pacific. It has a large seasonal cycle, with a sharp summertime trough corresponding to maximum summertime OH values. MATCH captures the relatively well defined seasonal cycle, although it overestimates the summertime trough. The Baltic Sea (bal) and Niwot Ridge, Colorado (nwr) sites are two sites within strongly emitting regions. The Baltic Sea site in particular shows significant scatter due to nearby European sources, although the seasonal cycle is still discernable. MATCH can capture the phase of the bal and nwr seasonal cycles, but the magnitude of individual observations are much more difficult to reproduce. The difficulty lies in the possible influence of local emissions and the challenge of modeling a single weekly measurement.

The next sub-plot shows time-series at the Seychelles (sey) site, which is located in the Indian Ocean. It has an unusual seasonal cycle due to its proximity to the ITCZ. During the early part of the year (i.e., the austral fall), the ITCZ is shifted relatively southward; consequently, sey experiences strong northerlies from the Indian sub-continent. These northerlies carry enhanced methane mole fractions from multiple emission sources to sey which results in a very strong methane peak. During the spring the ITCZ shifts northward, resulting in net southerlies at sey. These bring relatively clean air from the Southern Hemisphere, resulting in a strong methane decline. For the rest of the year, the Seychelles mimic the seasonality of the southern hemispheric (SH) stations, which peak in August and September, the period of lowest OH in the SH. From the earlier high-frequency Samoan analysis, cross-ITCZ transport is suppressed during El Niño events, although this effect over the Indian ocean has not been quantified. Cross ITCZ suppression would result in a smaller peak at the Seychelles. Can we see an El Niño effect in the 1998 methane peak? Both model and observations suggest a reduced peak in 1998 compared to other years, suggesting that northerlies were weaker. The MATCH high-frequency output shows a pronounced minimum during this period. However, a definitive corroboration would require high-frequency observations at the Seychelles.

The mole fractions at Ascension Island (asc, off the coast of West Africa) are similar to SH sites, with low and high values during the SH summer (high OH) and SH winter (low OH), respectively. In addition, biomass burning in central Africa during the months of August – September may contribute to the peak amplitude of the observed cycle. Finally the South Pole has a very clean seasonal cycle that is well reproduced by MATCH. Most sites below 30° S have a similar cycle that is governed by OH.

Figure 3.13 shows that MATCH can capture the general seasonal behavior at flask sites, which have very different characteristics based on transport, emissions, and OH destruction. The model-observational comparison to sites remote from highly emitting region is generally good. The comparison worsens for flask measurements near or within strongly emitting regions. MATCH usually over predicts mole fractions at these sites (e.g., the Baltic Sea (bal), China (wlg), and Utah (uta)), but can also

underpredict them (e.g. Black Sea (bsc)). Mountain sites (such as wlg and hun) which experience well-mixed surface air in the daytime and free tropospheric air at nighttime are also difficult to model by MATCH due to the subgrid scale nature of this transport. In general, it is difficult to attribute specific CH₄ flask events due to transport IAV because of the low-frequency of flask sampling. For example, the correlation due to El Niño is more difficult to investigate at the Seychelles (low-frequency observations) than at Samoa (high-frequency observations). Despite their low sampling frequency, flask sites are nevertheless still useful because they provide most of our tropical observing locations. These stations provide information about those tropical emitting regions that are not sampled by the high-frequency measuring network.

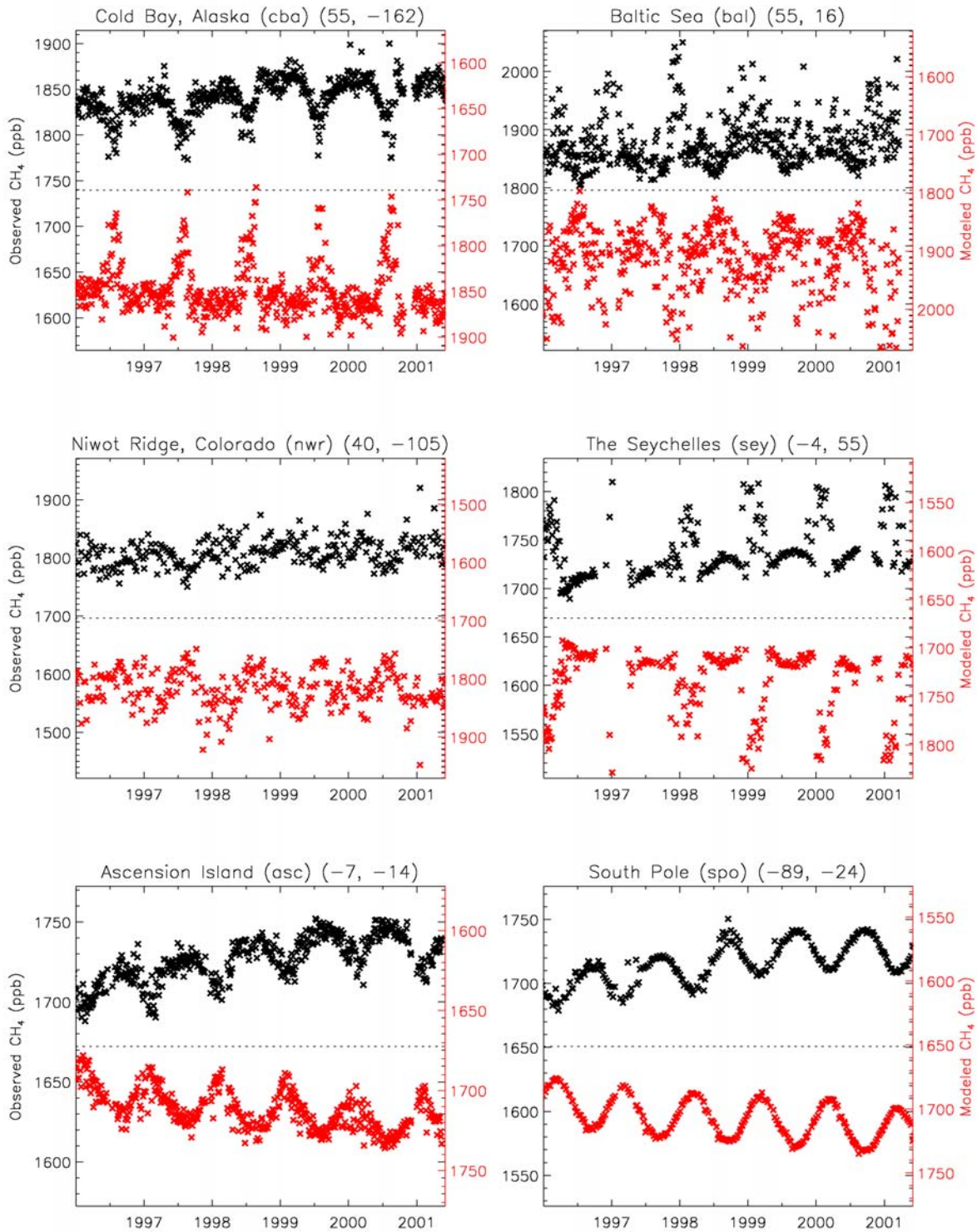


Figure 3.13. Observed (Black) and Modeled (Red) Flask values at representative locations. The model values (right scale) are inverted compared to the observations to facilitate comparison, and a good fit occurs when the modeled values are the mirror image of the observations. Latitude and longitude for each station are given. Note the difference in scales between different sites (e.g. Baltic Sea and the South Pole range between 1800-2100 ppb and 1675-1750 ppb, respectively).

3.4.3 Flask monthly averages from high and low-frequency MATCH sampling

In this section, we compare observed and modeled flask monthly means. In Chapter 4, the inversion will use monthly mean observations to solve for monthly mean fluxes. For high-frequency observations the monthly mean is well-defined, and can be compared directly to the corresponding modeled high-frequency average. The monthly mean of flask measurements is less well-defined due to the weekly sampling frequency. Nevertheless, this four value average can be taken to represent a monthly mean with an associated error to be quantified in Chapter 4. Here we compare two model sampling strategies for generating the model monthly mean. The first is to sample MATCH output at the exact time of flask measurement (i.e. selective sampling), followed by averaging. The second strategy is to use all MATCH high-frequency mole fractions to define the monthly mean. We denote these as low and high-frequency averages, respectively. Using CO₂ forward modeling, *Haas-Laursen et al. (1997)* cautioned against using the first method, concluding that it could exacerbate bias errors in the model representation of the observations. This analysis, however, was conducted using a single year of GCM winds, which in general cannot realistically capture the transport effect on individual flask measurements. Figure 3.13 indicates that MATCH can sometimes replicate individual flask measurements using realistic meteorology. Another strategy would be to sample MATCH during periods with the same wind direction as the flask sampling. Unfortunately, wind direction information at the flask sites is generally not available, preventing consistent model selection.

Figure 3.14 compares observed and modeled monthly means using the two sampling strategies at two sites. At Barrow, Alaska (brw, left plot) high-frequency averaging more closely represents the observed flask average. The low-frequency average overestimates the observed average during certain peak events. This suggests a difference between the flask sampling strategy and the MATCH simulation during periods of high CH₄ mole fractions. Because peak events can be of extremely short duration, (i.e. less than 1 day), a small temporal mismatch between the model simulation and actual event can lead to a large difference. At Barrow, the high-frequency monthly mean mitigates the influence of these peak errors.

At Mace Head (mhd, right plot) the low-frequency modeled mean does slightly better than the high-frequency mean, which more often overestimates the observations. The flask sampling at Mace-Head occurs during clean air conditions (i.e. when the wind is westerly). MATCH apparently simulates the CH₄ mole fractions quite well under these conditions. The high-frequency averages, which contain air from all wind sectors, lead to overestimates of the monthly mean at certain times. At most flask locations the comparison either favored high-frequency averaging or both methods equally. In Chapter 5, we investigate the use of both high and low-frequency model averaging for use in an inversion.

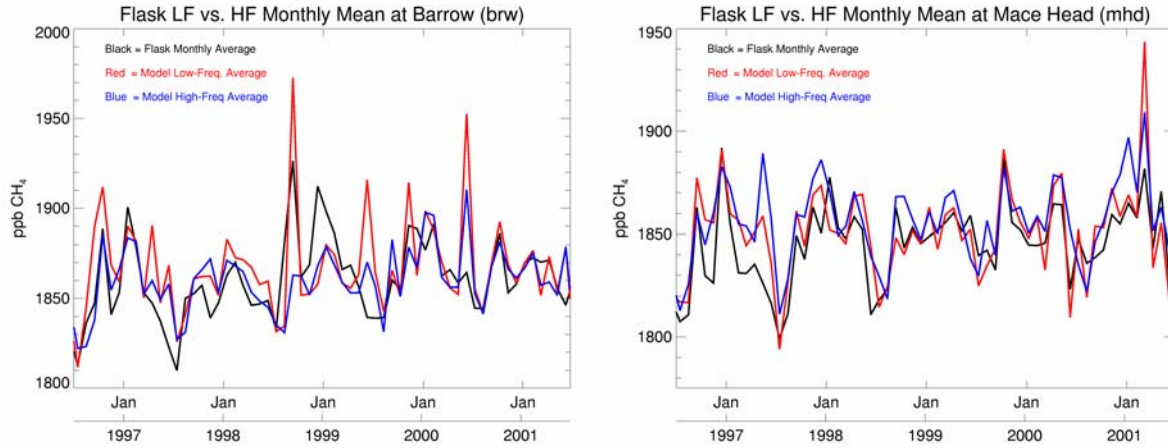


Figure 3.14. Monthly means at Barrow (left) and Mace Head (right) for observed (black), LF Flask (red), and HF Flask (blue). For Barrow, the Flask HF compares more favorably with the observed monthly mean (in this plot, 20 ppb have been subtracted from the modeled values to facilitate observational comparison). The LF Flask average contains elevated CH_4 peak mole fractions that overestimate the observations. For the monthly means at Mace Head, the LF and HF Flask averages reproduce the observations comparably well, although the low-frequency average captures more of the trough periods.

3.5 Impact of Transport IAV on Methane Seasonality

Mace Head and Samoa provide examples of sites which are strongly influenced by interannual changes in transport (Figure 3.11 and Figure 3.12). In the following, we analyze the importance of transport IAV at all surface locations. This can be accomplished globally by using monthly mean values from the MATCH reference run, in which transport is the only interannually varying component. We use RMS deviations of the interannual seasonal cycle from the mean seasonal cycle to quantify the impact of transport IAV at each surface grid cell, as defined by Equation (3.2).

$$RMS = \frac{1}{Amp} \sqrt{\frac{\sum_1^{N_{tim}} (x_t - \bar{x}_t)^2}{N_{tim}}} \quad (3.2)$$

x_t = detrended reference run

\bar{x}_t = seasonal average of x_t

N_{tim} = total number of months

Amp = Amplitude of seasonal cycle

Here, x_t represents the detrended interannual monthly mean at each surface grid point, in which linear and quadratic growth rates have been removed. $\overline{x_t}$ represents the seasonal average of x_t , taken by averaging x_t for each month of the time-series such that $\overline{x_t} = \overline{x_{t+12}} = \overline{x_{t+24}} = \text{etc...}$. The residual $(x_t - \overline{x_t})$ thus represents a deviation from the mean seasonal cycle at month t caused by transport IAV. Note that if only a single year of transport had been used in the reference run, $x_t = \overline{x_t}$, since sources and sinks are annually repeating, and RMS would be zero everywhere. N_{tim} represents the total number of months in the time series, approximately 60 months for 5 years. The RMS variability has been scaled by the seasonal amplitude for that grid point, Amp , since the relative impact on the seasonality is of interest.

Performing this RMS calculation for all model grid cells results in the surface latitude-longitude plot of Figure 3.15. Large RMS values, shown in red and yellow, indicate areas where transport IAV has a significant impact on the seasonal cycle. Low RMS values, shown in dark blue, indicate areas where transport IAV has minimal impact. Large values require the presence of both strong transport IAV and significant CH₄ gradients. The latter can be generated by either strong sources or transport barriers, such as the ITCZ. The impact of transport IAV is greatest across a tropical band that follows the ITCZ. The large gradient between the northern and southern hemispheric methane mole fractions is greatest at this transport barrier (Figure 3.9). Consequently, year-to-year shifts in the ITCZ will impact CH₄ values at sites that straddle it. This is especially pronounced between El Niño and La Niña years, as shown previously for Samoa. This high RMS band is concentrated in tropical ocean regions, with generally less extension over land regions (with the exception of South America). The CH₄ mole fraction seasonality over these tropical land regions appear to be less sensitive to year-to-year changes in cross-equatorial transport compared to the ocean ITCZ regions. This is partially due to the large emissions over land, which lead to larger, and hence less sensitive, seasonal cycles. In addition, the larger land emissions possibly lead to ITCZ methane gradients that are less sharp over land compared to ocean regions.

Certain regions of the Northern Hemisphere also show RMS variability due to transport IAV. Many NH sites are near strongly emitting source such as wetlands and energy related emissions. In many of these locations large scale wind changes (e.g., NAO) play a role in controlling observed mole fractions, as shown earlier for the effect of NAO at Mace Head (Figure 3.12). In addition, local meteorological conditions such as changes in convection and planetary boundary layer height may affect the year-to-year mole fractions. A particularly low winter surface temperature, for example, could lead to increased stability and near surface trapping of methane. The modeled methane mole fraction would then show an enhancement relative to other years. Changes in PBL heights are less pronounced in tropical regions, which experience less temperature change and more mixing throughout the year. The areas least sensitive to transport IAV are in the Southern Hemisphere far from strong sources, due to the relative homogeneity of the CH₄ mole fractions in this region. Although transport IAV itself may be large, weak methane gradients prevent any strong changes in the mean seasonality. Cape Grim also shows low sensitivity to IAV despite the frequent occurrence of pollution events from Southeastern Australia (Figure 3.2). This suggests that the number of these pollution events remains relatively constant each month for different years.

In Figure 3.16, we have plotted the variability by station, showing the same information as in Figure 3.15 but focusing on actual stations. The larger the circle, the greater the year-to-year variability due to transport. For the AGAGE sites, transport IAV affects Mace Head and Samoa most strongly. The relative impact is smaller at Trinidad Head, Barbados, and Cape Grim, which are less sensitive to large scale transport effect from NAO and ENSO. Those stations that have low RMS values are less

susceptible to transport IAV. The low sensitivity of South Pole and Cape Grim to IAV suggests that they could be adequately modeled using a single year of winds. For stations such as Samoa and Mace Head, however, transport IAV should be used in order to correctly simulate interannual monthly means. Those locations more sensitive to transport IAV changes should be also sampled at a high enough frequency to capture the effects of transport IAV.

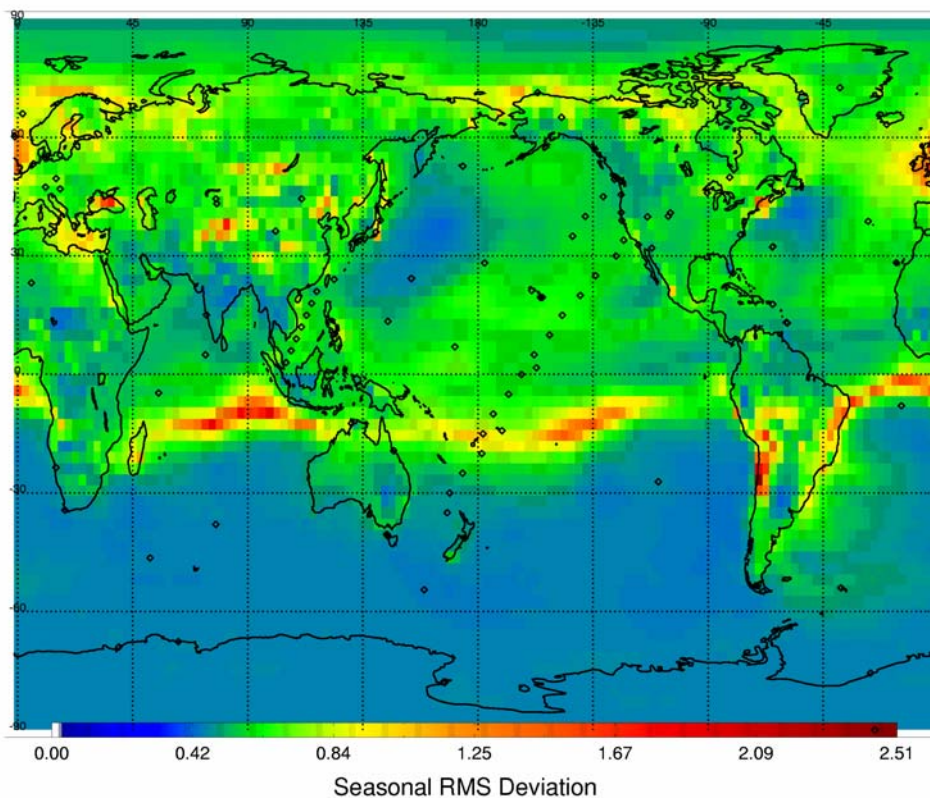


Figure 3.15: The effect of model transport IAV on methane surface seasonality. Colors indicate RMS residuals between the interannual and average seasonal monthly values at each grid point (see Eq. (3.2)). Deviations arise from interannual transport only, because the methane emissions and OH are annually repeating. The large band in the tropics indicate ITCZ transport variations.

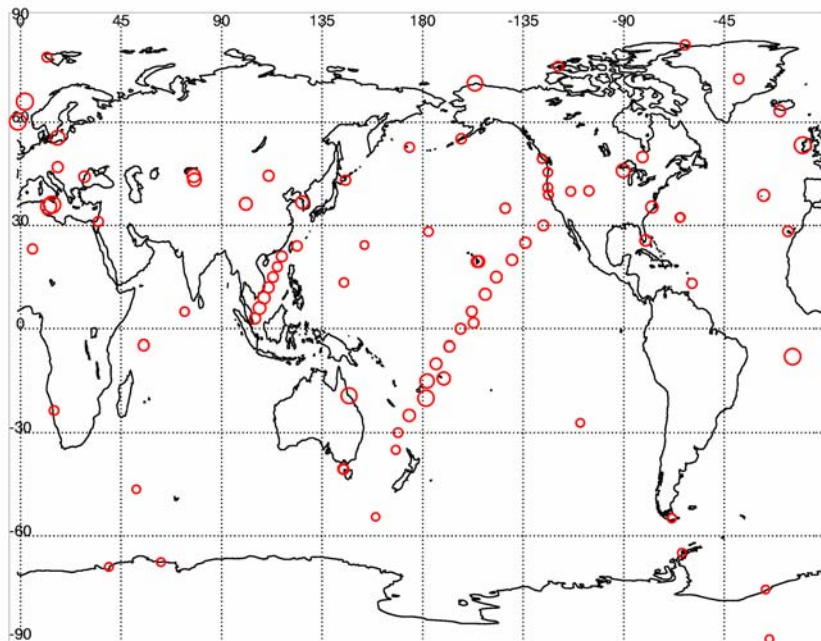


Figure 3.16. Same information as Figure 3.15 but at CH₄ observing stations. Circle radii are proportional to the impact of transport IAV on the average seasonal cycle.

3.6 Sensitivity to specific processes

This section examines the sensitivity of individual sites to the individual seasonal processes shown in Figure 3.4. These sensitivities contain the change in simulated methane mole fraction due to a change in emissions from a single processes. They are formally used in the inversion which optimizes flux magnitudes in Chapter 5. Certain process have also been divided geographically, for example bogs have been divided into Bogs East and Bogs West. The seasonal sensitivities are generated by emitting a month-long pulse from a particular process, followed by decay for a single year. This records the effect of a particular month of emissions, which are scaled to a flux of 1 Tg yr^{-1} . The sensitivity at a particular site corresponds to the resulting mole fraction; after a year of decay, nearly all sites have low sensitivity due to atmospheric mixing. In contrast to the seasonal sensitivities, the aseasonal sensitivities are generated as constant perturbations in MATCH. For example, coal emissions are increased by 20% over reference, and run within MATCH for the same duration as the reference run. The difference between the reference and perturbation runs then represents the sensitivity to coal. The difference between the procedures for generating aseasonal and seasonal sensitivities arises from the fact that we will later optimize for time-varying (monthly) seasonal process fluxes and constant aseasonal process fluxes. We focus on the seasonal sensitivities in the following.

In general the sensitivities can be written as

$$h_{ijk} = \frac{\Delta y_{ik}}{\Delta E_{jk'(<k)}} \quad (3.3)$$

where h_{ijk} represents the CH_4 mole fraction (y) response of a particular observational site (i) to a particular methane emitting region/process (E_j) for a particular month (k) in units of ppb $(\text{Tg CH}_4 \text{ yr}^{-1})^{-1}$. Note that the emissions are indexed at month k' , which represent individual months before the current month, k . This notation is used since we will be interested in all monthly fluxes for the seasonal processes; fluxes from months k' will have an impact on the CH_4 mole fractions at month k . In Chapter 4, the elements h_{ijk} are used quantitatively to relate unknown flux processes to observations. The following discussion focuses on the forward analysis of seasonal pulses.

Figure 3.17 shows the response of Alert Station (alt) and Cape Grim (cgo) to an August pulse from Bogs West (see Figure 3.4) using 1999 meteorology. After the month-long input, the mole fraction decays following atmospheric transport for 12 months. Since Alert is relatively close to the bog emissions, its sensitivity follows a sharp increase after several days of transport time between Bogs West and northern Greenland. This pulse lasts about the duration of the month-long emission, followed by a relatively smooth decrease due to atmospheric mixing. In contrast Cape Grim, on the opposite side of the world from Bogs West, will only detect the methane pulse months later. It shows a slow methane increase consistent with the spread of a methane pulse into the Southern Hemisphere. For an inert tracer, the mole fractions at Alert and Cape Grim would converge eventually to the same, constant value. Since methane is destroyed by OH, the mole fractions will always be decreasing. In addition, the two sites will maintain a small difference due to seasonal differences in OH destruction. For a transient emission pulse, the sensitivity during the first few months at a site dictates how sensitive a site can be to emissions from a

particular process-month. Thus Alert is very sensitive to Bogs West, while Cape Grim is not. Most stations fall between these two extremes in sensitivity.

The sensitivities at an individual site can also be influenced by transport IAV. Figure 3.18 shows the first six months of an August month-pulse from Bogs West at Alert, run with 1997 (blue) and 1998 (red) meteorology. The left plot shows the high-frequency values, while the right plot represents the corresponding monthly means. The differences between the plots are due to transport IAV only, as the magnitude of the pulse is identical for both cases. In 1997, mole fractions begin to rise within a week of the pulse initiation. Mole fractions reach a maximum at about 2 weeks, with values stabilizing after 3 weeks. After the pulse ends on August 31st, mole fractions decrease due to atmospheric mixing. The CH₄ peak magnitude and timing of the 1998 peak is strikingly different. The CH₄ peak occurs in the first week of September, more than 2 weeks after the 1997 peak, and after the emission pulse has terminated. This is due to a transport lag, which causes CH₄ fluxes to take longer to reach Alert in 1998 than in 1997. Mole fraction perturbations begin to relax only at week 6, in contrast to 1997 which relaxes at week 3. The inversions described in Chapter 4 use monthly means, which are shown in the right plot of Figure 3.18. The difference between the first two months, when sensitivities are at their maximum, is significant. The 1997 response has a larger sensitivity in August than September, with the reverse for 1998. Thus the sensitivity to the same emission pulse can be significantly affected by transport IAV. When combined with real observations in an inversion, sensitivities should therefore be generated using consistent meteorology.

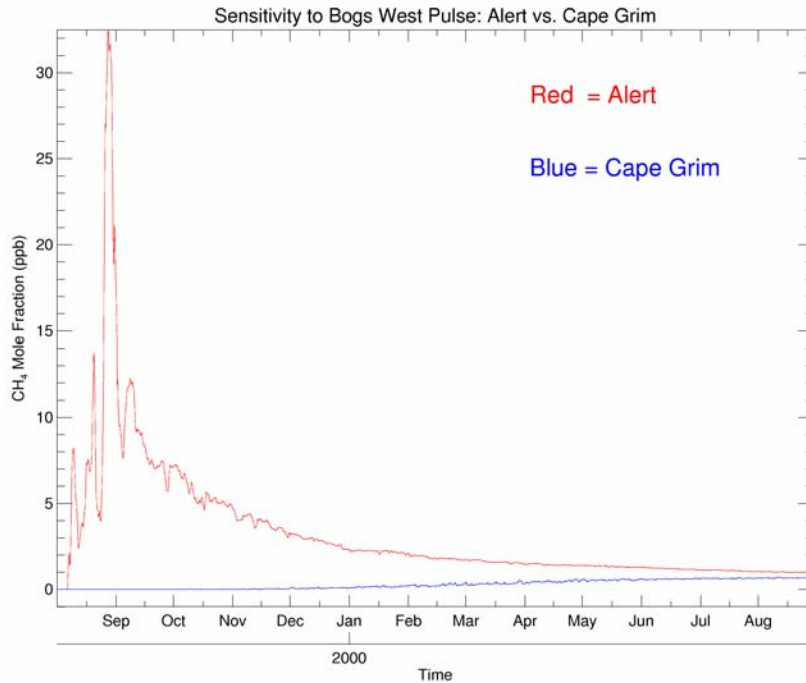


Figure 3.17. Sensitivity of Alert and Cape Grim to an August emission pulse from Western Hemispheric Bogs (as shown in Figure 3.4). Alert is much closer and more sensitive to the emission pulse than Cape Grim. Eventually the mole fractions reach values consistent with a small methane pulse in a well-mixed atmosphere, followed by a slow decrease due to OH destruction.

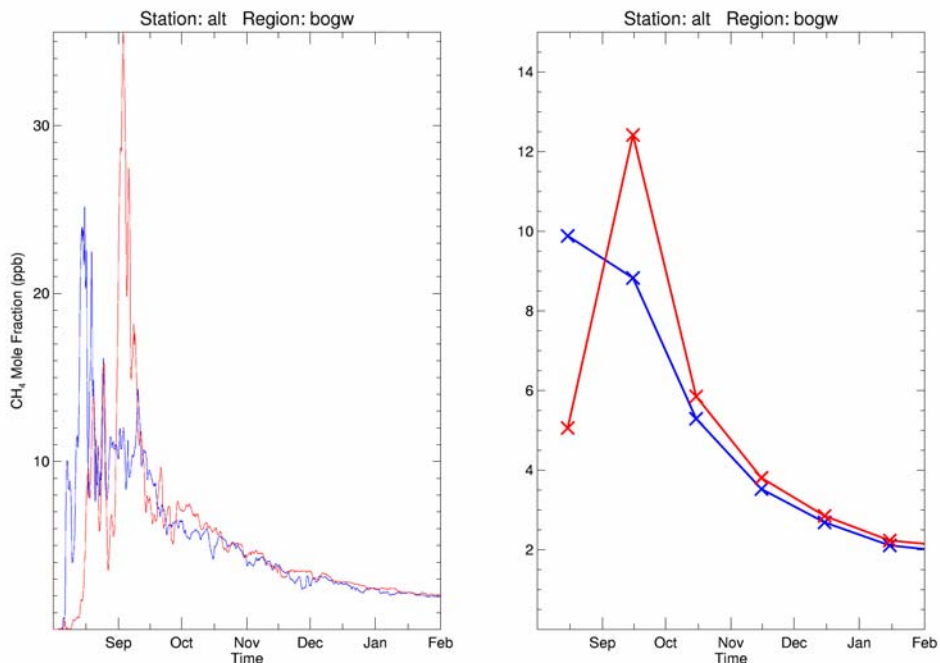


Figure 3.18: Sensitivity of Alert to an August month-pulse from Bogs West using 1997 (Blue) and 1998 (Red) meteorology. Left: High-frequency values. Right: Monthly Means. Because the input pulse magnitudes are identical, the mole fraction differences are due to transport differences only. Note that 1997 transport results in a pulse arrival that is more rapid, while 1998 transport results in a later and more intense peak.

We have modeled month-pulses, as described in Figure 3.17, for all seven seasonal responses between 1996-2001 for use in the inversion in Chapter 5. This amounts to 60 separate (12 months x 5 yrs) month pulses for each individual process. We now examine the most sensitive observing sites for each process. In order to rank the most sensitive sites, we have averaged the 60 month pulses for each site and process as follows:

- (1) Added the first two months (maximum sensitivity) of mole fraction perturbations at each site for all 60 individual month-pulses
- (2) Annually averaged these 60 values to create a single sensitivity for each site and process

Note that this averaging has removed the temporal information in the sensitivities, which are due to changes in both transport and the seasonal distribution patterns of individual emissions. For example, the sensitivity of Fraserdale (frd), Canada to Bogs West is a maximum in summer and minimum in winter, primarily due to a southward shift in Bogs West emissions away from Fraserdale in the winter. A related issue is that a single site can be sensitive to different processes at different times. For example, Mt. Waliguan (wlg), China is a flask site that is sensitive to both Rice and Biomass Burning Asia, but at different times of the year.

Table 3.3 lists the 5 most sensitive sites for each process from both high-frequency and flask sites, with flask sites further subdivided as in Table 3.1. We focus on high-frequency and on those flask sites with monthly values for at least 70% of the 1996-2001 time-period. These listed sensitivities are similar to a change in the mole fraction due to a year long input of 1 Tg yr^{-1} from an individual process (we have multiplied all values by 10 for clarity). As can be seen, the site sensitivity to Bogs East and Bogs West (in the Northern Hemisphere) is higher since there are multiple sites directly within these regions. The sensitivity of the other regions, located in tropical regions, are relatively small. The high-frequency and flask sites have similar sensitivities for the northern hemispheric processes. The high-frequency network is much less sensitive to tropical and southern processes due to lack of nearby stations. For these processes the flask measurements offer reasonable sensitivity, suggesting their usefulness as a complement to the high-frequency network.

Bogs East are constrained by downwind high-frequency sites including Barrow (brw), Alert (alt), and Cape Ochi-Ishi (coi). The Baltic Sea (bal) site is one of the few sites directly within the emitting region. Consistent time-series observations within areas of Siberia could help further constrain this large wetland emitting region. Bogs West is the most highly sampled region, with the two most sensitive sites, Fraserdale (frd) and the Wisconsin tower (lef), directly within the emitting region. In addition, this region is surrounded by sensitive sites. The relatively concentrated emissions of Bogs West also contribute to its high values. In contrast, Swamp emissions represent diffuse wetland emissions spread throughout tropical and temperate zones. Consequently, the sensitivities are relatively low and uniform. The top sensitivities are seen at Cape Grim (cgo), Cape Ochi-Ishi (coi), and the Black Sea (bsc) which are spatially very separated. For Rice, emissions are most sensitive to the Japanese sites of Hateruma (hat) and Cape Ochi-Ishi (coi), as well as Mt. Waliguan (wlg) in central China. The biomass burning emissions in Asia are also sensitive to Hateruma (hat) and Mt. Waliguan (wlg). Although Rice and Biomass Burning Asia have similar sensitivities on an annually average basis, they have different monthly sensitivities due to their different spatial emission characteristics. For example, Waliguan Mt.

(wlg) is sensitive to both rice and biomass burning emissions off continental South East Asia (including India), but at different times. During the dry season in this region (Dec – Feb), biomass burning dominates CH₄ emissions while rice emissions have shifted elsewhere. During the wet, rice-growing season (June-Aug), rice CH₄ emissions are strong in this region, while biomass burning shifts to Indonesia/Malaysia. The consequence is that Biomass Burning Asia and Rice peak sensitivities occur at Mt. Waliguan during February and September, respectively.

The sensitivity of the CH₄ observing network to Biomass Burning South America is weak, and depends on stations thousands of kilometers down wind, such as Samoa (smo) and Christmas Island (chr). BB Africa shows sensitivity at Ascension Island (asc), followed by the more distant Barbados (rpb). In general, the biomass burning regions also have lower sensitivity due to the greater convection found in the tropics which removes emissions from the boundary layer. More sites at the edge of these continents may be helpful in constraining their emissions.

Table 3.3. List of sensitivities to seasonal methane emissions for High-Frequency and Flask Sites. Units are in ppb (Tg yr⁻¹) multiplied by 0.1.

Process	HF		Flask (> 70 % Active Mon)		Flask (< 70 % Active Mon)	
	Site	Sensitivity	Site	Sensitivity	Site	Sensitivity
Bogs East	brw	14.59	bal	21.68	mbc	13.19
	alt	11.60	zep	18.78	wk3	8.42
	coi	10.95	stm	18.23	scsn03	8.37
	mhd	8.07	bsc	17.82	sum	8.14
	frd	6.83	uum	14.30	cmo	6.92
Bogs West	frd	77.23	lef	59.03	itn	28.7
	brw	39.11	ice	21.51	mbc	26.6
	alt	23.02	cba	16.79	sum	21.63
	mhd	17.97	sis	16.48	goz	9.47
	iza	6.68	stm	16.47	cmo	8.47
Swamps	cgo	1.15	bsc	2.46	scsn03	2.82
	coi	1.15	uum	1.86	scsn06	1.63
	rpb	0.86	bal	1.86	scsn12	1.58
	hat	0.82	key	1.69	scsn09	1.35
	frd	0.75	wlg	1.58	itn	1.24
Rice	hat	6.43	wlg	7.97	scsn12	10.95
	coi	3.98	uum	3.53	kco	9.8
	mnm	3.40	wis	3.51	scsn15	9.67
	mlo	3.26	sey	2.73	scsn18	8.75
	thd	2.01	gmi	2.68	scsn21	8.25
BB Asia	hat	8.01	wlg	5.16	scsn03	15.93
	mlo	4.10	sey	4.91	scsn15	14
	mnm	3.82	gmi	4.01	scsn12	13.92
	iza	1.84	kum	2.70	kco	13.51
	rpb	1.71	nwr	2.48	scsn06	12.5
BB America	smo	2.42	chr	5.01	chr	5.01
	mlo	1.75	asc	3.44	pocn05	4.76
	cgo	1.39	cfa	2.36	poc000	4.71
	rpb	1.19	sey	2.19	pocs05	4.12
	iza	0.75	key	1.54	nmb	3.42
BB Africa	rpb	5.86	asc	9.45	nmb	13.02
	iza	1.63	ask	3.86	kco	2.37
	mlo	1.28	sey	2.61	chr	2.37
	smo	1.24	chr	2.37	poc000	2.18
	cgo	0.83	key	1.73	pocn05	2.08

Refer to Figure 3.1 for station locations.

3.7 Conclusions

For the forward modeling of methane, we have collected available high and low-frequency CH₄ observations. A reference methane emissions field was constructed by combining pre-existing methane emissions fields, followed by preliminary model-observational comparisons using MATCH. An OH field from a previous run of MATCH was globally adjusted to match methyl chloroform observations. The reference run was integrated in MATCH between 1993 and 2001 and compared to both high-frequency and flask observations. Total methane emissions of ~600 Tg yr⁻¹ approximately match the observed CH₄ growth rate over this period. The slow global CH₄ growth rate between 1996-2001 can be nearly reproduced using constant emissions. This condition is consistent with an approach towards an approximate steady-state in which the global CH₄ emission rate and removal rate (by OH destruction) approximately balance.

Both in-situ and flask observations were compared to model simulations. High-frequency measurements allow a more direct comparison, particularly for sites which experience significant methane variability. MATCH can capture the general shape of the methane seasonal cycle at nearly all sites located in the remote marine boundary layer. Coastal sites, including those influenced by strongly emitting regions, can also be reproduced. Observations taken directly within strongly emitting regions are less well reproduced, although certain features can still be resolved. Flask measurements taken near or within highly emitting regions are difficult to model, due to the undersampling of the high variability of methane in these regions and the inability of MATCH to simulate strong local effects.

Using analyzed observed winds, MATCH can capture observed interannual CH₄ variation at most sites. In addition, using annually repeating sources and sinks allowed examination of the impact of modeled transport IAV on the CH₄ seasonality. Transport IAV can explain many observed year-to-year methane features, and is particularly important for locations near strongly emitting regions or large CH₄ gradients (such as the ITCZ). Global transport phenomena including ENSO and the NAO influence observed CH₄ at certain locations. For a particular location, proximity to strong methane gradients and strong transport IAV lead to large changes in the seasonal cycle between years.

Finally, the sensitivities at individual sites to specific methane processes were analyzed. The sensitivity to individual processes indicates high sensitivity for Northern Hemispheric sources, and low sensitivity for Tropical sources. The signal at an observing site from a monthly emission pulse can be strongly affected by transport. These sensitivities will be used to optimize methane emissions in the Chapter 4 and 5.

Chapter 4

Inverse Modeling of Atmospheric Methane: Methodology

In this chapter we describe the inversion methodology used to optimally estimate interannual methane emissions. These optimized emissions improve the fit to the CH₄ observations compared to the reference run, which include only annually repeating emissions as described in Chapter 3. The Kalman Filter (KF) is chosen as the inversion technique; it is a versatile tool that has been employed to study several atmospheric constituents at different scales. *Prinn et al.* (2001) and *Huang* (2000) have used it to deduce global magnitudes and trends of OH. *Mahowald et al.* (1997a) estimated global surface fluxes of CFC₁₁ (CFC-11) for several different regions using the KF. On the regional scale, it has been used to constrain emissions of chlorine compounds (*Kleiman et al.* (2000)) and methane (*Janssen et al.* (1999)). Here, we adapt the Kalman Filter to estimate methane fluxes at monthly time resolution on the global scale. Much of the methodology is derived from *Prinn* (2000) and *Enting* (2002).

The KF is a recursive technique that uses time-series data sequentially in contrast to a batch method which uses all the data in a single step. The KF has the advantage of providing a measure of the usefulness of new data in a time-series. When solving for a constant flux, it is possible to observe the degree of convergence towards a single value and the uncertainty reduction with each new piece of data. When solving for a transient flux, such as an emission from a particular month, the KF indicates how long subsequent observations will be useful as a constraint. For example, do observations 6 or 12 months after the emission of a transient flux still provide useful information? Another advantage of the KF is its computational convenience, which allows smaller matrices to be used in the inversion compared to certain batch methods. This avoids potentially large matrices which might exceed computer memory or lead to excessively long computation time.

Another important aspect of the inversion is the formulation of the observational errors. These errors determine the relative importance (i.e. weighting) of each observation in the Kalman Filter, and consequently, on the optimized emissions. Errors arise from imperfections in instrumental precision, spatial mismatches between model and observations, and the use of a finite number of measurements to define a monthly mean. Most methane inversions have focused on annually or seasonally averaged fluxes applicable over many years (*Houweling et al.* (1999), *Hein et al.* (1997)). These studies have utilized flask observations only, which have much lower time resolution than high-frequency in-situ CH₄ measurements. Our study optimizes interannual methane fluxes at monthly mean resolution. The higher time resolution of optimized fluxes requires that the monthly observational means be well defined. We have therefore incorporated as much high-frequency observational information as possible, in addition to the more numerous flask measurements. The high-frequency and flask observations have different errors based on their ability to define a monthly mean. In general high-frequency observations have more weight in the inversion. Finally, the chapter concludes with a check of the inversion by using optimized emissions to drive MATCH, followed by comparison to actual observations.

4.1 Kalman Filter Equations

4.1.1 Measurement Equation

The Kalman Filter includes the measurement and state-space equations, which can be described separately before they are combined. The measurement equation relates modeled and observed mole fractions through the following relationship:

$$y_k^o = \tilde{y}_k + H_k x_k + \mathcal{E}_k \quad (4.1)$$

y_k^o = monthly observations at all sites

\tilde{y}_k = monthly simulated observations from the reference run

H_k = partial derivative matrix (mole fraction sensitivity to emissions)

x_k = state vector containing monthly emissions for various regions

(deviations from the reference run emission)

\mathcal{E}_k = measurement/model error

k = month index (1 to 60)

The index k represents a specific month of observation and flux. The observation vector, y_k^o , contains the monthly mean observations at all sites for month k . \tilde{y}_k contains the corresponding values from the MATCH reference run which used an initial, “best guess” emissions field. Chapter 3 compared reference run and observed CH₄ mole fractions, specifically analyzing high-frequency events in terms of transport changes. The monthly means of these modeled and observed mole fractions are used here. Note that the preceding chapter showed the importance of using realistic interannual transport, which can affect monthly mean values independently of CH₄ emission or OH changes.

The primary objective is to obtain estimates of the state-vector, x_k , which contain the methane emitting processes to be optimized. The individual elements of x_k represent the flux adjustments that improve the reference emissions, in terms of providing a better modeled fit to the observed CH₄ monthly means, weighted by observational errors. The flux adjustments contained in x_k are related to the simulated CH₄ mole fractions through the time-dependent sensitivity matrix H_k . If $y_k^o = \tilde{y}_k$, i.e. the reference run perfectly matches the observations, then the flux adjustments will be zero from the inversion. x_k is synchronized with the monthly observational vector, y_k^o , but also includes seasonal elements which represent emissions previous to time k (i.e. $k-1$, $k-2$, etc.). This is because an observation depends not only on the emission at a particular month, but also on all previous emissions. Equation (4.2) shows the structure of the state-vector in compact form, with each X representing a sub-vector of process fluxes.

$$x_k = \begin{bmatrix} X_k^{asea} \\ X_k^{sea} \\ X_{k-1}^{sea} \\ \dots \\ \dots \\ X_{k-T}^{sea} \end{bmatrix} \quad (4.2)$$

Each X in Equation (4.2) represents a sub-vector of emissions with the following elements:

$$X_k^{sea} = \begin{bmatrix} x_k^{bogs\ east} \\ x_k^{bogs\ west} \\ x_k^{swamps} \\ x_k^{rice} \\ x_k^{bbasia} \\ x_k^{bbamerica} \\ x_k^{bbafrica} \end{bmatrix} \quad X_k^{asea} = \begin{bmatrix} x_k^{animals+waste} \\ x_k^{coal} \\ x_k^{gas} \end{bmatrix} \quad (4.3)$$

The state vector includes seasonal emissions previous to month k , but does not explicitly include previous aseasonal monthly fluxes. We are interested in the aseasonal fluxes (X_k^{asea}) as constant values over the entire data period, rather than for specific monthly values. For seasonal fluxes, in contrast, we are interested in individual monthly fluxes because these emissions have greater variability. We have determined from model sensitivity runs that an observation cannot meaningfully separate monthly emissions that are more than 1 year old (see Figure 3.17). For example, observations after July, 2000 contain little useful information about specific monthly fluxes previous to July, 1999 due to atmospheric mixing. Thus the state-vector only includes fluxes between times k to $k-T$, where T equals 12 months and represents an atmospheric mixing time. Note that the KF ultimately solves for seasonal emissions from $k=1$ to $k=N$, where N equals the total number of observational months. At any single month, k , however, the state-vector only includes fluxes between k and $k-12$. This decreases the size of the state-vector, which would otherwise contain all emissions from $k = 1$ onward and demand large amounts of computer memory. The effect of old fluxes between months 1 and $k - T$ no longer included in the state-vector are contained in an additional term, \tilde{y}_{k-T}^{adj} , to be added to Equation (4.1). This vector contains the influence of previously optimized emissions, whose contributions have already become well mixed in the atmosphere.

The sensitivity matrix, H , relates the CH_4 mole fraction at each site to the CH_4 emissions in the state-vector. Its elements are generated from multiple MATCH runs of the individual methane processes of interest (e.g. rice, wetlands, etc.) as described in Chapter 3. The elements of H can be written as:

$$h_{ijkk'} = \frac{y_{ik} - \tilde{y}_{ik}}{x_{jk'} - \tilde{x}_{jk'}} \equiv \frac{\partial y_{ik}}{\partial x_{jk'}} \quad (4.4)$$

i = site number

j = methane processes / region

k = current month

$k' \leq k$ (months previous to the current month)

for aseasonals k' represents cumulative emissions between $k=1$ to k

for seasonals k' represents specific monthly emissions prior to k ($k' \leq k$)

The procedure used to generate the aseasonal and seasonal sensitivities differ. For aseasonal fluxes (e.g. animal emissions) we perturb a single process above the reference level by 20% and run over the entire data period. The sensitivities are then determined by subtracting the perturbation and reference runs, and dividing by the total emission perturbation to produce a sensitivity in terms of ppb (Tg yr)⁻¹.

The aseasonal sensitivity elements thus contain the influence of previous months, while the seasonal sensitivities only contain information for a single month (k') before the month of interest (k). For the latter sensitivities (e.g. wetland flux from a specific month) the tracer must now be tracked individually for that month within the model. This is accomplished by emitting a pulse for that period, followed by some period of atmospheric decay (e.g. Figure 3.17). Compared to the aseasonal sensitivities, the number of model runs and computational expense now increases by the number of months of interest. For five years of interest (1996-2001) this corresponds to 5 yrs x 12 months = 60 model runs, which accounts for the large computational burden of solving for monthly CH₄ emissions. Each of the 60 month-pulses is a separate multi-tracer run (for 7 seasonal processes) in MATCH, all starting at different months.

In order to conserve computational resources, we have run each of the 60 modeled pulses for 6 months instead of over the full 1996-2001 time-period. Most of the sensitivity occurs during the first few months after pulse initiation. The effects of transport IAV on sensitivities are also attenuated after this time (see Figure 3.16). We have run the 1999 month-pulses for an additional 30 months, and used these results to extend the month-pulses of other years. For example, the August 1997 month-pulse for Bogs East has the same shape as the corresponding August 1999 month-pulse after the sixth month of model simulation. After several years, the methane pulse will become well-mixed in the atmosphere. The mixing time of an inert tracer, such as CO₂, is approximately 3 years in MATCH (as determined from the Transcom 3 experiment). A well-mixed pulse of methane will still undergo destruction by OH and thus retain spatial structure. A single representative decay run has been used to quantify the spatial pattern of CH₄ decay after 3 years of mixing.

The above inversion methodology requires a linear relationship between sources and mixing ratios, i.e. that transport and chemistry be linear in CH₄ mole fractions. The separate contributions from different processes to CH₄ mole fractions should be linearly additive. The linearity of a transport model depends on its specific transport algorithm. The use of a mass fixer is known to cause small non-linearities (*Enting* (2002)). To test the linearity of MATCH we have simulated pulses from Bogs East, Bogs West, and Bogs East + Bogs West combined. These three modeled pulses are shown in Figure 4.1, as blue, red, and yellow, respectively. We then compared the combined model run (yellow) with the summation of the two individual bogs responses (black-dashed). Exact transport and chemical linearity within MATCH would correspond to identical black and yellow lines. The good correspondence between the combined run and the post-run summation confirm the near-linearity of the pulsed emissions. The

slight differences (e.g. for the large peaks) become negligible for monthly mean values. Other non-linearities in the inversion are discussed in Section 4.3.

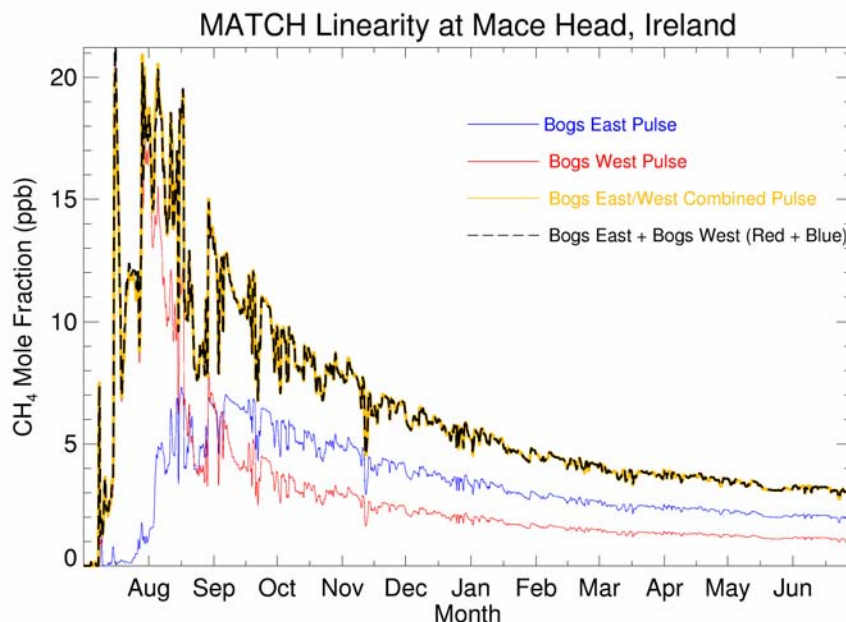


Figure 4.1. Test of the linearity of pulsed emissions. Three MATCH runs include Bogs East (blue), Bogs West (red), and Bogs East + West (yellow). The black-dashed curve represents is the sum of the separate Bogs East and Bogs West runs (i.e. red + blue). Note the overlap between the yellow and black-dashed, which indicates linearity.

The final term of Equation (4.1) is the observational error ε_k , which contains several different sources of error. These include instrumental and calibration error, as well as the uncertainty on how well the monthly mean is defined due to finite sampling frequency. Another error is the mismatch (or “representation”) error, which quantifies the difference between a model average quantity and a point observation. Although we cannot directly quantify ε_k , we have knowledge of its statistics. In the Kalman Filter, this information appears in the observational error covariance (noise) matrix $R_k = E(\varepsilon_k \varepsilon_k^T)$. We approximate R_k as a diagonal matrix whose non-zero elements are the variances of the observed mole fractions at each station. This assumes that the observational errors are uncorrelated. The errors that contribute to ε_k are described more quantitatively in Section 4.2. With the exception of the mismatch error, model errors (both parametric and structural) are not formally included in the inversion. Thus the errors in the physics and chemistry of the model must be separately determined and added to the Kalman Filter-derived errors. There are also uncertainties associated with model inputs, such as the OH sink and the regional distribution of emissions. One way to determine this error would be to test alternative source/sinks fields in MATCH, which would lead to alternative H_k matrices (*Prinn* (2000)). A full analysis of these errors is difficult given the computation burden of generating a single H_k . We discuss potential impacts of these model errors in Chapter 5.

With y_{k-T}^{adj} , which represents the cumulative effect on CH₄ mole fractions from optimized emissions previous to time $k-T$, Equation (4.1) becomes

$$y_k^o = \tilde{y}_k + y_{k-T}^{adj} + H_k x_k + \epsilon_k \quad (4.5)$$

Equation (4.6) shows the full matrices corresponding to Equation (4.5), including the complicated synchronization between H_k and x_k .

Kalman Matrices for N observations, A aseasional regions, S seasonal regions

k is the current month, $T =$ mixing time for a pulse of methane = 12 months

$$\begin{array}{c} \underbrace{y_k^o}_{\begin{pmatrix} y_1 \\ y_2 \\ \dots \\ \dots \\ \dots \\ \dots \\ \dots \\ y_N \end{pmatrix}} = \underbrace{\tilde{y}_k}_{\begin{pmatrix} y_1 \\ y_2 \\ \dots \\ \dots \\ \dots \\ \dots \\ \dots \\ y_N \end{pmatrix}} + \underbrace{y_k^{adj}}_{\begin{pmatrix} y_1 \\ y_2 \\ \dots \\ \dots \\ \dots \\ \dots \\ \dots \\ y_N \end{pmatrix}} + \underbrace{H_k}_{\begin{array}{c} \text{Aseasional Emissions} \quad \text{Seasonal Emissions} \\ \begin{pmatrix} \frac{\partial y_{1,k}}{\partial x_{1,k}} & \dots & \frac{\partial y_{1,k}}{\partial x_{A,k}} & \frac{\partial y_{1,k}}{\partial x_{1,k}} & \dots & \frac{\partial y_{1,k}}{\partial x_{S,k}} & \dots & \frac{\partial y_{1,k}}{\partial x_{1,k-T}} & \dots & \frac{\partial y_{1,k}}{\partial x_{S,k-T}} \\ \frac{\partial y_{2,k}}{\partial x_{1,k}} & \dots & \frac{\partial y_{2,k}}{\partial x_{A,k}} & \frac{\partial y_{2,k}}{\partial x_{1,k}} & \dots & \frac{\partial y_{2,k}}{\partial x_{S,k}} & \dots & \frac{\partial y_{2,k}}{\partial x_{1,k-T}} & \dots & \frac{\partial y_{2,k}}{\partial x_{S,k-T}} \\ \dots & \dots \\ \dots & \dots \\ \dots & \dots \\ \dots & \dots \\ \frac{\partial y_{N,k}}{\partial x_{1,k}} & \dots & \frac{\partial y_{N,k}}{\partial x_{A,k}} & \frac{\partial y_{N,k}}{\partial x_{1,k}} & \dots & \frac{\partial y_{N,k}}{\partial x_{S,k}} & \dots & \frac{\partial y_{N,k}}{\partial x_{1,k-T}} & \dots & \frac{\partial y_{N,k}}{\partial x_{S,k-T}} \\ \frac{\partial y_{1,k}}{\partial x_{1,k}} & \dots & \frac{\partial y_{1,k}}{\partial x_{A,k}} & \frac{\partial y_{1,k}}{\partial x_{1,k}} & \dots & \frac{\partial y_{1,k}}{\partial x_{S,k}} & \dots & \frac{\partial y_{1,k}}{\partial x_{1,k-T}} & \dots & \frac{\partial y_{1,k}}{\partial x_{S,k-T}} \end{pmatrix} \end{array}} \cdot \underbrace{x_k}_{\begin{array}{c} \begin{pmatrix} x_{1,k} \\ \dots \\ x_{A,k} \\ \dots \\ x_{1,k} \\ \dots \\ x_{S,k} \\ \dots \\ x_{1,k-T} \\ \dots \\ x_{S,k-T} \end{pmatrix} \\ \text{Aseas} \\ \text{Seas} \end{array}} \quad (4.6)
 \end{array}$$

The goal is to solve for the state vector (x_k) at each observational time k . The following section describes the how the state-vector evolves from one time step to another.

4.1.2 State-Space Equation

Equations (4.7) and (4.8) describe the how the state-vector (x_k) and its uncertainty (P_k) evolve from one time step to another before the use of observational information. This process allows emissions to be solved recursively as new observations are added; in other applications, Equation (4.7) is also known as the “forecast”. The subscript f denotes a quantity before observations are used to update the state. The state-space equation, Equation (4.7), uses the state-transition matrix, M_k to propagate the state-vector from one time-step to another. If our state-vector included the total seasonal emissions, rather than adjustments to the reference emissions, then M_k would describe the periodic evolution of seasonal emissions from one month to another. For our case, this seasonal variation is implicitly contained in the reference run, \tilde{y}_k . The random forcing term, η , may include multiple sources of error in M . For example, we do not expect

our periodic evolution (implicit in the reference run) to perfectly describe seasonal fluxes year after year. This error is contained in Q , the random forcing covariance matrix. The state-transition matrix also propagates the state-error covariance matrix, P_k , from one time-step to another, as shown in Equation (4.8).

$$x_k^f = M_{k-1} \cdot x_{k-1}^a + \eta_{k-1} \cong M_{k-1} \cdot x_{k-1}^a \quad (4.7)$$

$$P_k^f = M_{k-1} \cdot P_{k-1}^a M_{k-1}^T + Q_{k-1} \quad (4.8)$$

M_k = state transition matrix

η_k = random forcing

P_k^f = a priori state – error covariance matrix

Q_k = random forcing covariance matrix

f = state before use of observations (" forecast ")

a = state after use of observations (" analyzed ")

The state-transition matrix takes the following form:

$$M = \begin{bmatrix} I_{asea} & 0 & 0 & 0 & 0 \\ 0 & 0 & 0 & 0 & 0 \\ 0 & I_{sea} & 0 & 0 & 0 \\ 0 & 0 & I_{sea} & 0 & 0 \\ \dots & \dots & \dots & \dots & \dots \\ 0 & 0 & 0 & I_{sea} & 0 \end{bmatrix} \quad (4.9)$$

Note that the I_{asea} and I_{sea} represent square identity sub-matrices corresponding to the 3 aseasonal and 7 seasonal regions, respectively. The 0's also represent square matrices, with all zero elements. The state-transition matrix operates on the state-vector as follows (equivalent to Equation (4.7)).

$$\begin{bmatrix} I_{asea} & 0 & 0 & 0 & 0 \\ 0 & 0 & 0 & 0 & 0 \\ 0 & I_{sea} & 0 & 0 & 0 \\ 0 & 0 & I_{sea} & 0 & 0 \\ \dots & \dots & \dots & \dots & \dots \\ 0 & 0 & 0 & I_{sea} & 0 \end{bmatrix} \cdot \begin{bmatrix} X_{asea} \\ X_{k-1} \\ X_{k-2} \\ \dots \\ X_{k-T+1} \\ \boxed{X_{k-T}} \end{bmatrix} \begin{matrix} \rightarrow \\ \searrow \\ \searrow \\ \searrow \\ \searrow \\ \searrow \end{matrix} = \begin{bmatrix} X_{asea} \\ 0 \\ X_{k-1} \\ X_{k-2} \\ \dots \\ X_{k-T+1} \\ \boxed{X_{k-T}} \end{bmatrix} \quad (4.10)$$

= *optimized emission*

For the aseasonal components, the state-transition matrix retains the previous value, consistent with the estimation of a constant source over all time-steps. The seasonal components behave differently. The state-transition matrix shifts these elements of the state-vector down, with removal of the oldest subvector X_{k-T} representing fluxes from time $k-T$. (where $T = 11$ months). The X_{k-T} subvector represents the final, optimized solution for emissions at time $k-T$. Our choice of a zero row (below the aseasonal identity matrix) in M results in a new subvector on the right-hand side with zero contribution. This subvector represents the a priori values of the new seasonal fluxes to be optimized. We assume a zero adjustment flux before the use of observational information, because the adjustment flux could be positive or negative. A more sophisticated update might assume flux adjustment correlations from month to month. As a first guess, however, we assume no such correlations.

Equation (4.8) shows that the state-vector error covariance matrix, P_{k-1}^a , is also updated to contain a new flux error at each step. The effect of the first term on the right is to propagate the errors in a similar fashion that Equation (4.10) propagates fluxes down the state-vector. However, the new subvector to be solved for, shown as zero in Equation (4.10), also has an error associated with it. This error is determined by our choice of Q , as shown below.

$$Q_k = \begin{bmatrix} 0 & 0 & 0 & 0 & 0 \\ 0 & E(\eta\eta^T) & 0 & 0 & 0 \\ 0 & 0 & 0 & 0 & 0 \\ 0 & 0 & 0 & 0 & 0 \\ \dots & \dots & \dots & \dots & \dots \\ 0 & 0 & 0 & 0 & 0 \end{bmatrix} \quad (4.11)$$

Here, $E(\eta\eta^T)$ represents the error associated with new seasonal flux adjustment to be solved. It arises from the random error in the periodic emission forcing contained in the reference run. Note that it only contributes to the error for the new seasonal sub-vector to be optimized. For most seasonal fluxes the initial errors (used to define the a priori value of P_o^a) are taken to be the same magnitude as total emissions in the monthly reference run ($\pm 100\%$). We use smaller initial error of $\pm 30\%$ for the much

larger emissions of rice and swamps. The seasonal fluxes are thus given a large initial error, which the Kalman Filter reduces through use of 12 subsequent months of observation. The aseasonal errors are also initialized with an error equal to their reference magnitudes, but at $k=1$ only. Thus, for the first time step, Equation (4.11) also contains an error in the upper-left hand corner (not shown). The large aseasonal a priori error is reduced using observations over the entire time-series, since they represent constant fluxes.

4.1.3 Kalman Filter for Time-Dependent Inversions

The Kalman Filter produces an optimal estimate of the emissions contained in the state-vector. It combines the state-space equation and measurement equations previously described. The full equations are listed below.

$$\text{State - Space Equations} \tag{4.12}$$

$$x_k^f = M_{k-1} \cdot x_{k-1}^a$$

$$P_k^f = M_{k-1} \cdot P_{k-1}^a M_{k-1}^T + Q_k \tag{4.13}$$

$$\text{Measurement Equation (model components only)} \tag{4.14}$$

$$y_k = \tilde{y}_k + H_k x_k^f + y_{k-T}^{adj}$$

Gain Matrix

$$K_k = \frac{P_k^f H_k^T}{H_k P_k^f H_k^T + R_k} \tag{4.15}$$

State - Update

$$x_k^a = x_k^f + K_k \cdot (y_k^o - y_k) \tag{4.16}$$

Error covariance update

$$P_k^a = (I - K_k H_k) P_k^f \tag{4.17}$$

R_k = observational error covariance matrix

P_k^a = state error covariance matrix

K_k = kalman gain matrix

These equations are repeated over all times from $k = 1$ to $k = N$, at which point all available monthly observations have been exhausted. The first two steps are the state-space and measurement equations.

The measurement equation has been modified to include only modeled components, shown as y_k . The next step is the computation of K , the gain matrix. The gain matrix combines the prior state-error P_k^f , the observational error R_k , and the sensitivity matrix H_k to compute a weighting matrix that effectively determines the degree to which observations will modify the prior state. The state-update (Equation (4.16)) uses the prior state, gain matrix, modeled and actual observations to optimize the state. Note that if $y_k^o = y_k$, then no new update is necessary and the optimized state, x_k^a , is equal to the prior state, x_k^f . Since this is almost never true, the state will always undergo at least some change that is determined by the size of the gain matrix and $y_k^o - \tilde{y}_k$.

A large gain matrix K corresponds to a strong sensitivity to observations, while a small K corresponds to a very low sensitivity to observations. A few limiting cases help to illuminate the gain matrix. A very large observational error (i.e. large R_k) causes the denominator in Equation (4.15) to become very large and $K \rightarrow 0$. In the extreme case where $K = 0$ the optimized state equals the prior state, $x_k^a = x_k^f$, which should occur if the observations are useless. The opposite case of very small observational errors leads to the following (assuming a square and invertible H_k for simplicity)

$$K_k = \frac{P_k^f H_k^T}{H_k P_k^f H_k^T} = H_k^{-1}$$

Equation (4.16) then reduces to

$$\begin{aligned} x_k^a &= x_k^f + H_k^{-1} \cdot \left(y_k^o - \left(\tilde{y}_k + H_k x_k^f + y_k^{adj} \right) \right) \\ &= H_k^{-1} \cdot \left(y_k^o - \left(\tilde{y}_k + y_k^{adj} \right) \right) \end{aligned}$$

Thus the new state is not influenced by the prior state, but only by real and modeled observational values. Equation (4.17) updates the previous flux errors, P_k^f , to the new error, P_k^a . Note that the diagonal elements of P_k^a are always less than or equal to those contained in the prior error, P_k^f . The error reduction is an indicator of how effectively the observations constrain the fluxes.

In the following we show an example of the Kalman Filter in action, starting with the more complicated seasonal emissions. Since the state-vector contains emissions from many months, we focus on the evolution of a sub-vector representing a single month of flux. This allows us to observe how a single monthly estimate changes with the addition of subsequent data. Figure 4.2 shows the elements of a sub-vector of x , representing seasonal emissions during September, 1999, as it evolves with additional observations. Note that the plots do not show emissions for different months, but how a single monthly emission changes with each new month of data. The starting value for each of the seasonal processes is zero, corresponding to the zero subvector on the right-hand side of Equation (4.10). Recall that x contains deviations of the emissions from the reference run and not the total emissions. The large initial errors shown by the blue error bars centered around zero, correspond to the error described in Equation (4.11). With each new observation (x-axis) the value changes and the error decreases. Note that the adjustment and error reduction for a given process is greatest in the first 3-4 months. In the following months, emission values and uncertainties stabilize even with the addition of new data. This is because atmospheric mixing decreases the sensitivity of observations to a given monthly emission after the first few months. The optimized emission values for September, 1999 are taken as the final values in the plot.

After this step, no further optimization occurs, since we assume observations at month k cannot further constrain an emission which occurred at month $k - 12$. This final value represents an emission adjustment to the reference emissions that will provide a better fit the observations. At each month k , a new sub-vector of optimized emissions is thus produced. The optimized emissions that drop out of the state-vector are used to update y_k^{adj} , which represents the continued influence of these emissions on the background methane mole fraction. After all N observational months have been utilized, we have optimized emission adjustments over the entire period. The final, optimized set of seasonal emissions (after addition of reference values) are shown in Figure 4.4.

As can be seen in Figure 4.2, well observed processes such as Bogs East and Bogs West show significant uncertainty reduction. Their optimized fluxes also stabilize relatively quickly. The values of other, less well-constrained processes may take longer to stabilize, partially because they are not as sensitive to the observational network. For most processes, the final optimized value lies inside the range of the initial uncertainty. Poorly constrained regional fluxes, such as Biomass Burning America, may lie slightly outside the initial error bar. However, the initial and final uncertainties almost always overlap.

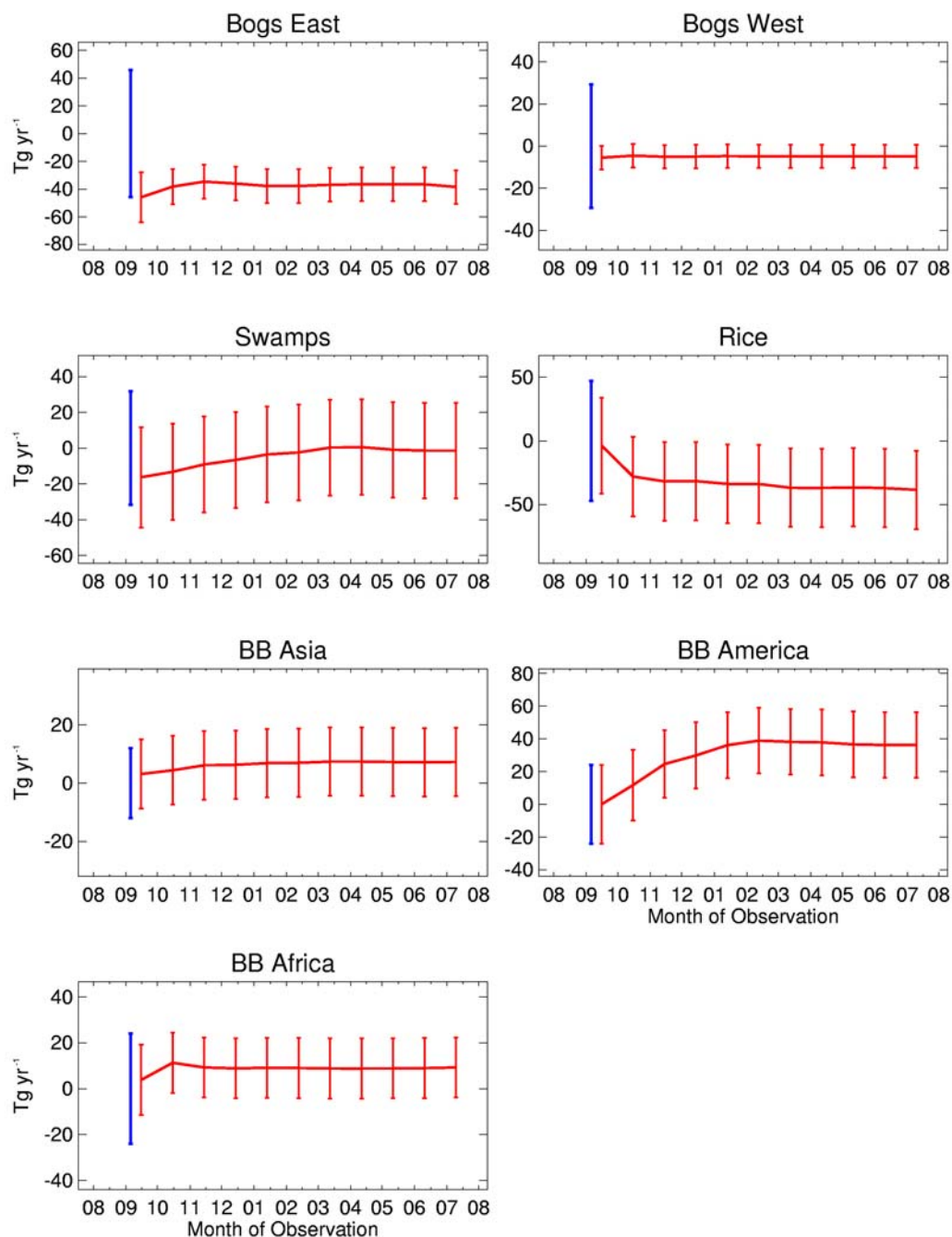


Figure 4.2 The evolution of a methane emissions for a single month (September, 1999) with the addition of new monthly data (horizontal). The vertical axis corresponds to emission adjustments from the reference value (Tg CH₄ / month). The blue line shows the prior error for the September, 1999 emission. Most of the adjustment and error reduction occurs with the use of the first few months of data, as the sensitivity to the emitting month by subsequent observations decreases with time. The final optimized emission is taken as the last step at which time the emission has stabilized.

The optimization of the aseasonal components are more straightforward. Since constant emissions are assumed, solution towards a single value occurs over all time steps, as shown in Figure 4.3. Note that the initial error (blue bar) is very high, and decreases relatively rapidly. The optimized value is the final value in each plot, corresponding to the final observation at July, 2001. Because the aseasonal emissions are only fully optimized at the final step of the time-series, earlier seasonal emissions (whose estimates also depend on the aseasonal values) at the beginning of the filter will not be fully optimized. In order to fully optimize all seasonal monthly values, we run the Kalman Filter a second time fixing the aseasonal values to their optimized values from the first run of the Kalman Filter.

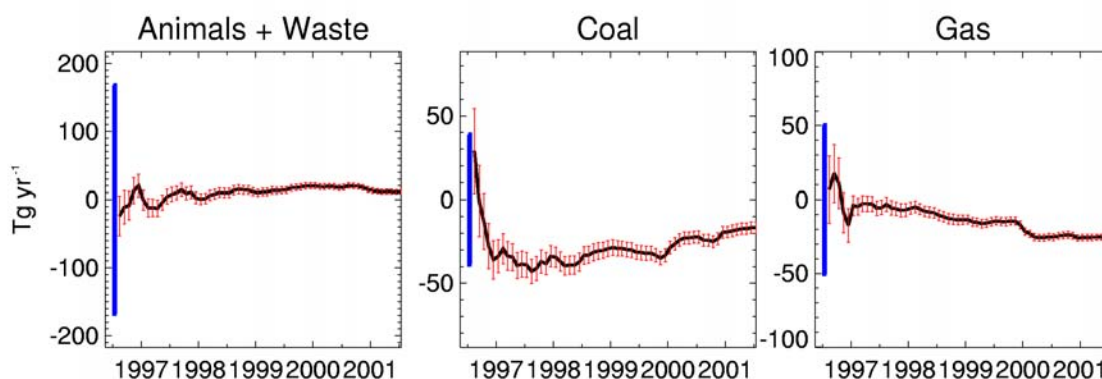


Figure 4.3. Kalman state-vector for 3 aseasonal sources. Unlike the seasonal inversion, which solved for monthly fluxes, a single optimized flux estimate is made for each aseasonal source over the entire 5-year time period. The optimized value is the last value, after all observations have been used. This flux represents an adjustment to the reference emission.

Note that in Figure 4.3 the final optimized values are within the initial uncertainty. This indicates that the initial uncertainty is large enough to accommodate filter adjustments. After all optimized seasonal and aseasonal emissions have been collected, a check of proper filter behavior involves generating the optimized mole fractions using Equation (4.14) over the entire time-series. These values should improve the reference fit to the observed CH_4 mole fractions. The ultimate check of the inversion is to run the optimized fluxes within MATCH, followed by comparison to actual observations (Section 4.3). First we examine a critical aspect of the inversion: the formulation of observational errors.

4.2 Observational Errors

The observational error (ε_k) on the monthly mean observations (y_k^o) in Equation (4.1) is not known; we only have some knowledge of its probability distribution function which for a normal distribution can be expressed by its standard deviation (denoted σ_k). The values of σ_k (in units of ppb) can be estimated as the sum of the errors associated with: (1) the instrumental and sampling errors (2) the frequency of sampling used to define the monthly mean, and (3) the mismatch error between observations and model. This assumes reasonably that these errors are uncorrelated.

$$\sigma_k = \sqrt{\sigma_{\text{measurement}}^2 + \sigma_{\text{mismatch}}^2 + \sigma_{\text{sampling frequency}}^2} \quad (4.18)$$

(1) $\sigma_{\text{measurement}}$ estimation

The measurement error includes those errors associated with instrumental, sampling, and inter-calibration imperfections.

$$\begin{aligned} \sigma_{\text{measurement}} &= \sqrt{\sigma_{\text{instrument precision}}^2 + \sigma_{\text{duplicate errors}}^2 + \sigma_{\text{intercalibration}}^2} \\ &= \sqrt{1 \leftrightarrow 4^2 + 0 \leftrightarrow 10^2 + 1} \\ &= \sqrt{2^2 \leftrightarrow 15^2} \end{aligned} \quad (4.19)$$

The precision of the methane measurements vary slightly between different laboratory groups, but for continuous measurements are reported as 0.1 to 0.2 % at the AGAGE sites (*Cunnold et al. (2002)*) and 0.07 % for the CMDL sites (*CMDL (2001)*). This corresponds to an uncertainty range between 1 - 4 ppb CH₄ at nearly all sites. We assume that the relative precision of the other high-frequency measuring laboratories is also close to these values. The instrumental precision used to measure flask measurements is similar to that of continuous measurements. We take a uniform instrumental precision error of 4 ppb at all sites.

Methane contamination at a measuring or collecting site can lead to sampling errors. These events are usually obvious at high-frequency locations, since anomalously large CH₄ signals can be immediately identified. These contaminated measurements are usually removed from the data (or flagged), and not used in the inversion. Contamination is more difficult to identify for flask measurements, since only duplicate or triplicate measurements are taken at the same time and location. A large difference between the flasks indicates contamination in one or more flasks; we have therefore discarded duplicate flask measurements which have differences greater than 10 ppb. For those duplicates with smaller differences, we have used an error equal to the standard deviation between the two or three values adjusted for small sample sizes using the Brewer's t factor (e.g. $\times 1.963$ for two values). This error usually varies between 0 to 10 ppb. If only a single sample has been taken, the sampling error is set to 5 ppb.

As discussed in Chapter 3, there exist differences between the absolute calibrations of different measuring networks. The calibration error, $\sigma_{\text{intercalibration}}$, should be zero after the appropriate calibration adjustments. *Cunnold et al. (2002)* report a 1 ppb difference at a number of co-located AGAGE and CMDL sites even after intercalibration. We take this value as $\sigma_{\text{intercalibration}}$ since we use measurements based on both calibration scales. A related error is possible calibration drift, in which a laboratory's CH₄ standard changes over time. This error is more difficult to quantify, and is assumed to be small over the 5 years of our inversion.

(2) $\sigma_{\text{sampling frequency}}$ estimation

The sampling frequency error accounts for how well the observational monthly mean is defined given a finite number of (m) measurements. Assuming temporally uncorrelated atmospheric CH₄ mixing ratios, the standard error determines the error on a mean quantity due to a limited sampling frequency, following Wunsch (1996), p. 189:

$$\sigma_{\text{sampling frequency}} = \sqrt{\frac{\sigma_{\text{mon}}^2}{m}} \quad (4.20)$$

σ_{mon}^2 = monthly mean variance (from MATCH reference run)

m = number of measurements during the month

Since we do not have continuous measurements everywhere, we approximate σ_{mon}^2 at all sites using the MATCH high-frequency output as an approximation. This assumes that the variability of the model is nearly equal to the variability of the actual observations, which is reasonable since the forward comparisons in Chapter 3 showed similar variability between MATCH modeled and observed high-frequency values. High-frequency observations have a very low monthly standard error given the high number of measurements ($m \sim 1000$). The standard error is much higher for flask measurements, which are typically taken weekly ($m \sim 4$). At the same site, the high-frequency standard error will be about 15 to 16 times smaller. This quantifies the greater usefulness of high-frequency measurements, especially at locations with a high monthly variance.

For flask measurements, the above error applies when using a mean that has used all modeled time-steps within a month, i.e. high-frequency average. As discussed in the Chapter 3, it is also possible to sample model output at the exact time that flask measurements were taken, i.e. low-frequency average. This results in a four value average for both model and observations. The sampling frequency error would no longer apply in this case, since we are no longer using a high-frequency modeled mean. However, it is particularly difficult to replicate a single point measurement of methane, as shown in the previous chapter. Small temporal mismatches between model and reality can lead to large differences for single measurements. In this case, the mismatch error (discussed next) would need to be increased significantly. Instead, we retain the sampling frequency error for the low-frequency model means. Forward modeling comparisons between the high and low-frequency sampling methods discussed in Chapter 3 did not suggest a clearly superior strategy. In the inversion, we test model monthly means using both sampling strategies.

(3) σ_{mismatch} estimation

Another error is known as the “mismatch” or “representation” error between an actual and simulated observation. A hypothetical model with perfect physics and chemistry still has a finite spatial resolution, and can at best determine the mean mole fractions over a specified grid volume. The degree to which a

point measurement fails to represent this volume dictates the size of the mismatch error. This error may also be considered a model error, since it is also the degree to which the model fails to represent a point measurement. We choose to put this error into the observation error, thus assuming a perfect transport model in the inversion. Most methane observing sites are located far from large local sources in order to sample large, well-mixed volumes of air, which can be more accurately modeled. The mismatch error increases significantly over continental sites near emitting regions, since MATCH does not have the resolution to cope with local influences. Note that this may include bias error, in which the model systematically over or underestimates the observed mole fractions.

The mismatch error is difficult to quantify, and previous studies have used the temporal variability (of flask measurements) at a particular site as a proxy for this error (e.g. *Gurney et al. (2002)* for CO₂). For CFC-11, *Mahowald et al. (1997a)* used the difference between observations and their reference (forward) run to estimate total model error, which includes the mismatch error. A more thorough approach to estimating mismatch errors would involve characterizing the spatial variability of CH₄ mole fractions within a single grid area using multiple ground, aircraft, or ship measurements. This, however, would be difficult to accomplish at even a single observing location. We have chosen to estimate the mismatch error at each site using the standard deviation of the CH₄ mole fraction at the four surrounding grid cells (i):

$$\begin{aligned}\sigma_{mismatch} &= \sqrt{\sigma_{surrounding\ 4\ grid\ cells}^2} \\ &= \sqrt{\frac{1}{4} \sum_{i=1}^4 (y_{ik} - \bar{y}_k)^2}\end{aligned}\tag{4.21}$$

We are thus assuming that the spatial variability within single grid cell is related to the variability of the neighboring grid cells. This qualitatively satisfying: the mismatch error will be much larger over strongly emitting continental sites compared to remote ocean locations. Note that the mismatch error at any particular site varies by month.

σ_{total} estimation

Table 4.1 compares the ranges of high-frequency and flask monthly 1-sigma error. The total range is the quadratic sum of the individual errors. The sampling frequency error accounts for most of the difference between the two types of measurements. Table 4.2 lists the contributions to the observational error at all sites averaged between 8/1996 – 7/2001. This table is also divided into high-frequency and flask sites, which are listed latitudinally. Most of the total high-frequency error is due to the measurement and mismatch errors, with very small sampling frequency errors. The sampling frequency errors can dominate the total flask error, especially for sites in highly variable emitting regions. Flask samples in the far Southern Hemisphere have very small errors which are comparable to the high-frequency sites. This is due to the relatively smooth CH₄ variations in this region. The errors on individual monthly mole fractions used in the inversion are shown in Chapter 5. Here, we list error ranges and average errors.

Table 4.1. Monthly Observational Error Ranges: High-Frequency versus Flask (ppb)

Error ppb	Measurement	Sampling Freq.	Mismatch	Total
High-Frequency	1↔ 4	.1↔ 3	1↔ 20	1.7↔ 20.5
Flask	1↔ 10	3↔ 100	1↔ 20	3.4↔ 102

Table 4.2. Monthly mean observational errors (as standard deviations in ppb) averaged over 1996-2001. The total error represents the quadratic sum of the 4 separate errors.

#	Name	Lat	Lon	Instrument/ Calibration	Flask Duplicate	Sampling Frequency	Mismatch	Total Error
High Frequency In-Situ Stations (13 Stations)								
1	alt	82	-62	5.00	0.00	0.83	2.83	5.81
2	brw	71	-156	5.00	0.00	1.52	11.52	12.65
3	mhd	53	-9	5.00	0.00	0.87	7.67	9.19
4	frd	49	-81	5.00	0.00	1.50	9.42	10.77
5	coi	43	145	5.00	0.00	2.31	6.53	8.55
6	thd	41	-124	5.00	0.00	0.63	3.71	6.26
7	iza	28	-16	5.00	0.00	1.74	1.85	5.61
8	mnm	24	153	5.00	0.00	2.97	2.31	6.26
9	hat	24	123	5.00	0.00	3.80	7.84	10.04
10	mlo	19	-155	5.00	0.00	0.53	1.60	5.28
11	rpb	13	-59	5.00	0.00	0.38	1.07	5.13
12	smo	-14	-170	5.00	0.00	0.23	0.78	5.07
13	cgo	-41	145	5.00	0.00	0.43	2.66	5.68
Flask Sites > 70 % Active (41 Sites)								
14	zep	78	11	5.00	2.60	11.30	2.71	12.91
15	stm	66	2	5.00	1.35	10.78	3.73	12.53
16	ice	63	-20	5.00	1.64	11.87	2.09	13.15
17	sis	60	-1	5.00	5.03	21.01	4.76	22.68
18	bal	55	16	5.00	1.60	20.74	15.36	26.34
19	cba	55	-162	5.00	1.34	5.59	1.86	7.84
20	shm	52	174	5.00	1.42	8.39	1.58	10.00
21	epc	49	-126	5.00	1.57	17.58	6.04	19.31
22	hun	46	16	5.00	1.66	46.66	49.90	68.52
23	lef	45	-90	5.00	1.81	20.38	7.39	22.32
24	uum	44	111	5.00	1.53	14.13	5.37	15.99
25	kzd	44	77	5.00	3.40	12.43	4.32	14.48
26	bsc	44	28	5.00	1.72	34.60	17.02	38.92
27	kzm	43	77	5.00	1.30	10.49	5.00	12.72
28	nwr	40	-105	5.00	1.34	10.87	5.37	13.18
29	uta	39	-113	5.00	1.63	10.44	15.14	19.13
30	azr	38	-27	5.00	1.57	9.83	1.45	11.23
31	tap	36	126	5.00	1.48	35.56	21.60	41.93
32	wlg	36	100	5.00	1.39	20.19	10.41	23.30
33	lmp	35	12	5.00	5.00	9.32	4.16	12.42
34	bme	32	-64	5.00	1.74	14.45	3.99	15.89
35	bmw	32	-64	5.00	1.59	13.77	4.71	15.47
36	wis	31	34	5.00	1.21	10.59	3.77	12.36

37	mid	28	-177	5.00	1.37	8.66	1.95	10.28
38	key	25	-80	5.00	1.72	20.77	12.09	24.60
39	ask	23	5	5.00	1.75	6.96	1.42	8.86
40	kum	19	-154	5.00	2.56	6.69	1.61	8.89
41	gmi	13	144	5.00	1.47	5.11	1.80	7.52
42	sey	-4	55	5.00	1.45	8.27	4.72	10.85
43	asc	-7	-14	5.00	1.61	1.75	0.53	5.56
44	cfa	-19	147	5.00	3.40	6.53	1.72	9.06
45	eic	-27	-109	5.00	1.56	1.46	0.20	5.44
46	crz	-46	51	5.00	1.62	2.20	0.20	5.70
47	mqa	-54	158	5.00	3.28	2.97	0.52	6.70
48	tdf	-54	-68	5.00	1.51	6.22	1.77	8.31
49	psa	-64	-64	5.00	1.32	1.80	0.86	5.55
50	maa	-67	62	5.00	2.37	1.76	0.20	5.81
51	syo	-69	39	5.00	1.86	1.52	0.14	5.55
52	hba	-75	-26	5.00	1.15	1.39	0.33	5.32
53	spoc	-89	-24	5.00	2.83	1.49	0.27	5.94
54	spo	-89	-24	5.00	2.49	1.05	0.27	5.69

Flask Sites < 70 % Active (33 Sites)

55	mbc	76	-119	5.00	2.29	6.06	1.59	8.34
56	sum	72	-38	5.00	1.05	8.45	1.48	9.98
57	cmo	45	-123	5.00	1.80	14.20	6.66	16.56
58	pta	38	-123	5.00	1.17	21.88	15.01	27.02
59	goz	36	14	5.00	2.96	16.09	4.07	17.59
60	itn	35	-77	5.00	2.04	27.23	16.24	32.16
61	pocn35	35	-143	5.00	0.98	14.38	1.05	15.30
62	wk3	31	34	5.00	7.34	8.85	2.64	12.81
63	pocn30	30	-126	5.00	1.67	11.38	2.01	12.70
64	pocn25	25	-134	5.00	1.77	10.75	0.91	12.02
65	scsn21	21	117	5.00	1.87	22.97	16.62	28.85
66	pocn20	20	-140	5.00	2.32	11.06	1.24	12.42
67	scsn18	18	115	5.00	2.12	26.98	9.73	29.19
68	pocn15	15	-147	5.00	2.22	11.89	1.75	13.20
69	scsn15	15	113	5.00	6.47	20.64	6.49	23.13
70	scsn12	12	111	5.00	1.47	21.28	4.95	22.46
71	pocn10	10	-152	5.00	2.43	11.21	2.01	12.68
72	scsn09	9	109	5.00	1.86	19.29	8.50	21.74
73	scsn06	6	107	5.00	1.78	15.49	5.03	17.13
74	pocn05	5	-158	5.00	1.82	6.39	2.56	8.70
75	kco	4	73	5.00	1.10	17.97	7.36	20.09
76	scsn03	3	105	5.00	1.86	17.22	11.14	21.19
77	chr	1	-157	5.00	1.48	3.78	1.88	6.71
78	poc000	0	-163	5.00	1.67	5.39	0.63	7.57
79	pocs05	-5	-168	5.00	1.79	4.42	0.68	6.94
80	pocs10	-10	-174	5.00	2.49	4.54	1.00	7.27
81	pocs15	-15	-178	5.00	2.20	5.25	0.84	7.62
82	pocs20	-20	-178	5.00	1.77	4.31	0.66	6.87
83	nmb	-23	15	5.00	1.54	6.00	2.15	8.25
84	pocs25	-25	174	5.00	1.71	4.46	0.61	6.94
85	pocs30	-30	169	5.00	1.86	3.37	0.67	6.35
86	pocs35	-35	168	5.00	2.12	3.10	0.62	6.28
87	aia	-40	144	5.00	8.49*	9.88	2.03	14.10

* The relatively high flask error for aia also arises from the sampling of different vertical levels.

4.3 Inversion Check

The detailed results of the inversions are given in Chapter 5. In this section, a representative set of the optimized emissions are tested using MATCH to help provide confidence in the overall results. The inversion covered the 5 year period between August 1996 to July 2001. Our choice of time period was determined by the number of available high-frequency sites necessary for a global inversion. Although observations have been available as early as the 1980's, only by the mid-1990's were sufficient stations operational to conduct an inversion using only high-frequency data. We used a starting point of August 1996 when the AGAGE network became fully operational for CH₄ measurements. The 13 high-frequency and 46 flask sites used in this inversion are listed Table 4.2. Those stations that had data less than 70% of the 72 months between 1996-2001 were excluded in the standard inversion. In addition, a few stations that were considered to be overly influenced by local sources were also ignored.

Figure 4.4 shows both optimized (red) and reference (blue) monthly seasonal results between 1996 – 2001. The reference values are annually repeating (i.e. no interannual variability). As can be seen, there are significant changes from the reference seasonal cycle for nearly all processes. There are also sub-optimized emissions at the beginning and end of the inversion periods. The emissions after August 2000 are not fully optimized, since they do not have a full 12 months of subsequent observations. The January 2001, for example, will be optimized using only 7 monthly observations which end in July 2001. Figure 4.4 shows the “most” optimized solution in this case, i.e. the emission estimate which has incorporated the most number of observations (up to the 12 maximum). The inversion also produces another set of sub-optimized solutions for the 11 months preceding the first observation of August 1996 (not shown). This is because the state-vector always includes emissions from k to $k-11$, even at $k = 1$. These initial emissions are sub-optimized because they lack the full 12 months of observations to constrain them, especially the first (and often most important) month of observation. The July 1997 emissions, for example, cannot be optimized fully using observations starting at August 1997, since the July 1997 observation may be the most critical.

The inversion results contain much information on the average, seasonal, and interannual behavior of methane emissions. We analyze these results in Chapter 5. In addition, the inversion can be performed using different observational sites, averaging strategies, and errors. The impact of these sensitivities are also explored in the next chapter. Here we focus on the ability of the results to better fit the observations compared to the reference run. The optimized seasonal emissions in Figure 4.4 and aseasonal emissions in Figure 4.3 were used to create a single optimized emission map for MATCH input. This was integrated in MATCH over the entire inversion time-period.

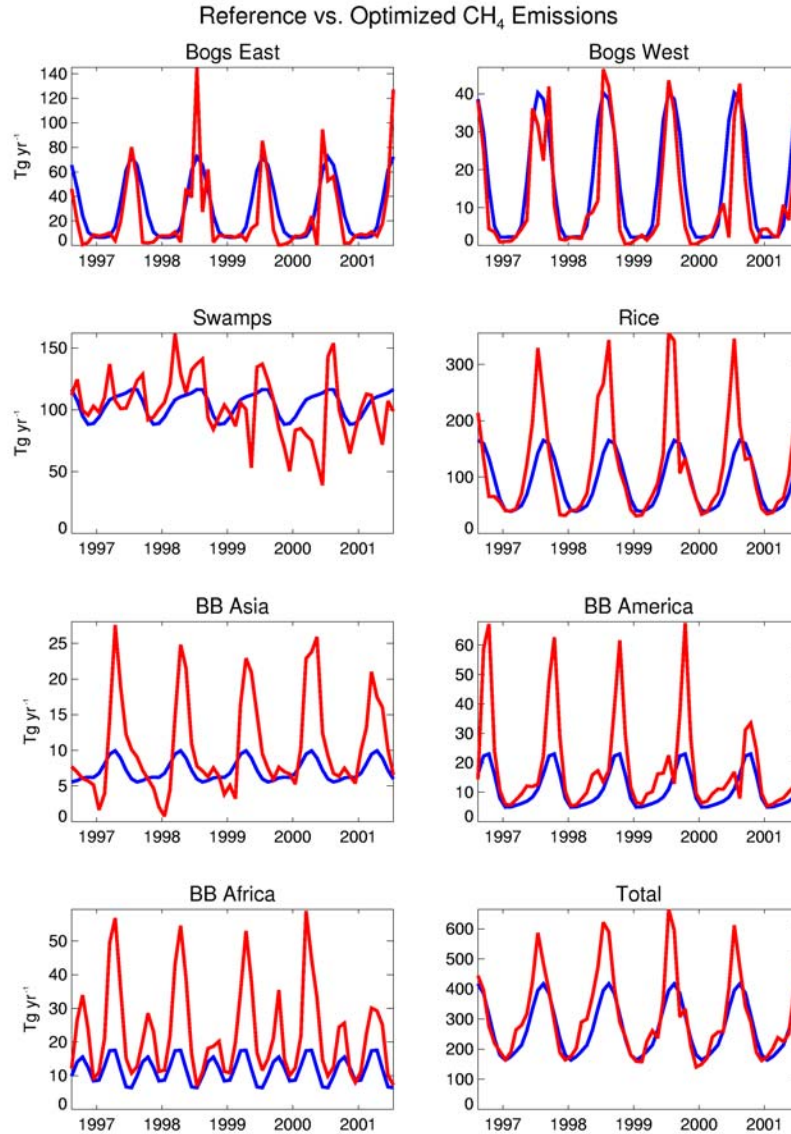


Figure 4.4. Inversion results for the seasonal processes. Blue line shows reference emissions, which are annually repeating. Red line shows optimized emissions, which contain interannual variability.

Figure 4.5 shows the improvement at the AGAGE sites between the reference (top) and optimized (bottom) MATCH model runs. Both plots show modeled values (color) compared to the set of observations (black). The most obvious improvements are at Samoa and Cape Grim in the Southern Hemisphere. The reference run underestimates these observations, while the mole fractions in the optimized run are increased for a better fit. The optimized seasonal cycle at Barbados also shows a better seasonal match to the observations, with a less pronounced seasonal cycle. The improvements at the Northern Hemispheric stations are obscured in these plots by the variability of the high-frequency data. These improvements are more obvious using monthly mean comparison, which will be shown for all sites in Chapter 5. Figure 4.6 shows the improvement at 4 different globally distributed flask sites. The South

Pole and Seychelles stations most clearly show the improvement in comparison to the observations from the reference (blue) to optimized (red) cases. The reference case overall underestimates the global growth rate, while the optimized version captures the observed growth. The improvement at Cold Bay, Alaska (cba) and Guam Island (gmi) are more subtle. However, the overestimates of the seasonal cycles have been reduced, particularly for the early years at Cold Bay (cba). The overestimate of the seasonal troughs have also been improved. The optimized monthly means as predicted by the inversions are shown as the yellow lines in Figure 4.6. These are produced by inputting the optimized emissions in Equation (4.14) after the inversion. The correspondence between the optimized MATCH run and the mole fractions predicted by the inversion are generally good.

Figure 4.7 shows the comparison between the optimized monthly means as predicted by the inversion using Equation (4.14) (orange) and generated by MATCH (red) at Alert (alt) and Barrow (brw). The reference (blue) and observed (black) monthly means are also shown. Alert and Barrow are sites that are sensitive to highly variable bog emissions. Both sets of optimized values (red/orange) show a significant improvement in fitting the observations (black) compared to the reference (blue) case. Absolute linearity and zero computational error would result in a perfect correspondence between the inversion-predicted and MATCH generated monthly means, i.e. identical orange and red curves. Although the linearity of two month-pulses was shown in Figure 4.1, our method of generating sensitivities may contribute small errors. This arises from a subtle point about how emissions are input into MATCH. We set the monthly mean emission value at the mid-point of the month (e.g. day 15.5). At each time-step, MATCH computes an emission flux by interpolating between the two surrounding mid-month values. The time-variation of emissions over an entire month will thus depend on the values of the preceding and following month. The month-long sensitivity pulses follow the timing of the reference emissions. For example, the 1 Tg mon^{-1} pulse from Bogs West during May increases nearly linearly over the entire month because April and June emissions are lower and higher, respectively, than May. The optimized emissions, however, define a new set of mid-month emission values that differ from the reference. This may result in a different timing of emissions over a month, leading to small differences between the inversion-predicted and MATCH generated monthly means. Note that these differences are small compared to the overall improvement from the reference case. These particular computational errors does not affect the aseasonal sensitivities or solutions since those emissions are constant for each month.

Another source of error in the inversion arises from the use of a prescribed OH field which are assumed to be perfect, thereby ignoring the $\text{CH}_4 - \text{OH}$ feedback (see *Enting (2002)*). That is to say, the true change in global methane follows

$$\frac{d[\text{CH}_4]}{dt} = P_{\text{CH}_4} - k[\text{OH}][\text{CH}_4] \quad (4.22)$$

where $[\text{OH}]$ is a weak function of $[\text{CH}_4]$. A pulse of methane will decrease the OH burden, and thus increase the overall methane lifetime. Ideally, our OH field would be recomputed using our optimized methane fluxes, to account for small effect of CH_4 on OH. Full inclusion of the $\text{CH}_4 - \text{OH}$ feedback would require a full chemical version of MATCH, which would be too computationally demanding to perform the sensitivity runs described here. However, we discount the error in neglecting this feedback, since our methane adjustments do not show strong global trends between 1996-2001. The total optimized CH_4 emission fluctuations are also less than 5% annually (i.e. 30 Tg yr^{-1}) for our time period. Another

approach to including all OH fluctuations is to use an independent tracer to estimate interannual OH changes. An improvement to our annually repeating OH field would be an interannually varying OH field based on the methyl chloroform (MCF) observations. MCF is at too small a concentration to affect OH concentrations, and in principle record OH changes due to changes in methane, as well as other forcings (e.g. CO, sunlight, etc.). Investigations into the changes in OH global magnitudes using MCF suggest trends, as well as year-to-year fluctuations, over the past two decades *Prinn et al. (2001)*. Future work will aim to incorporate these interannual OH variations.

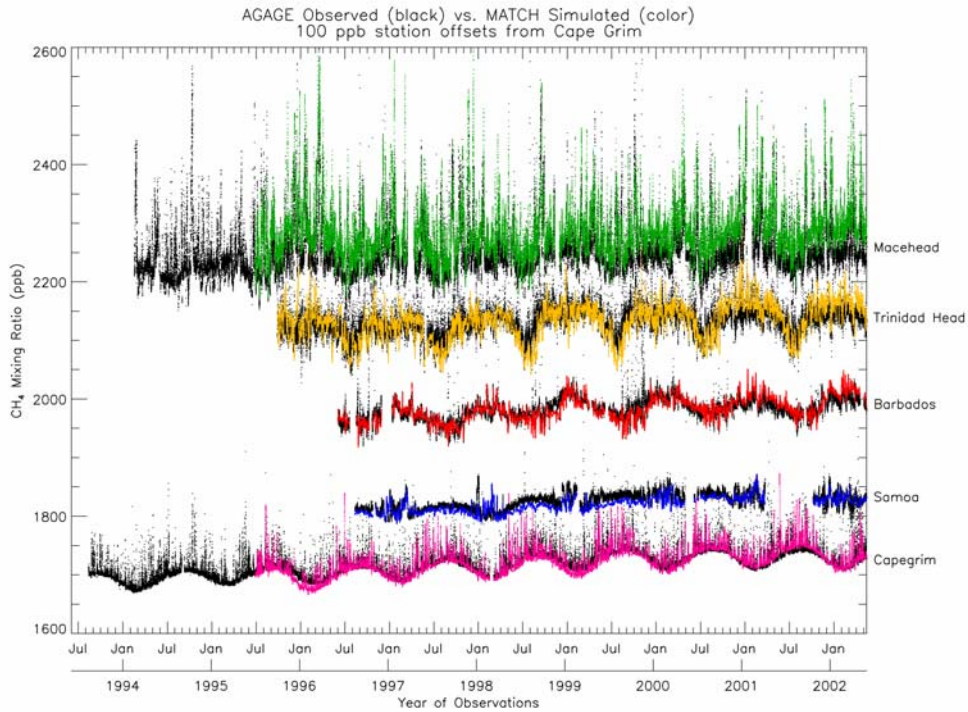
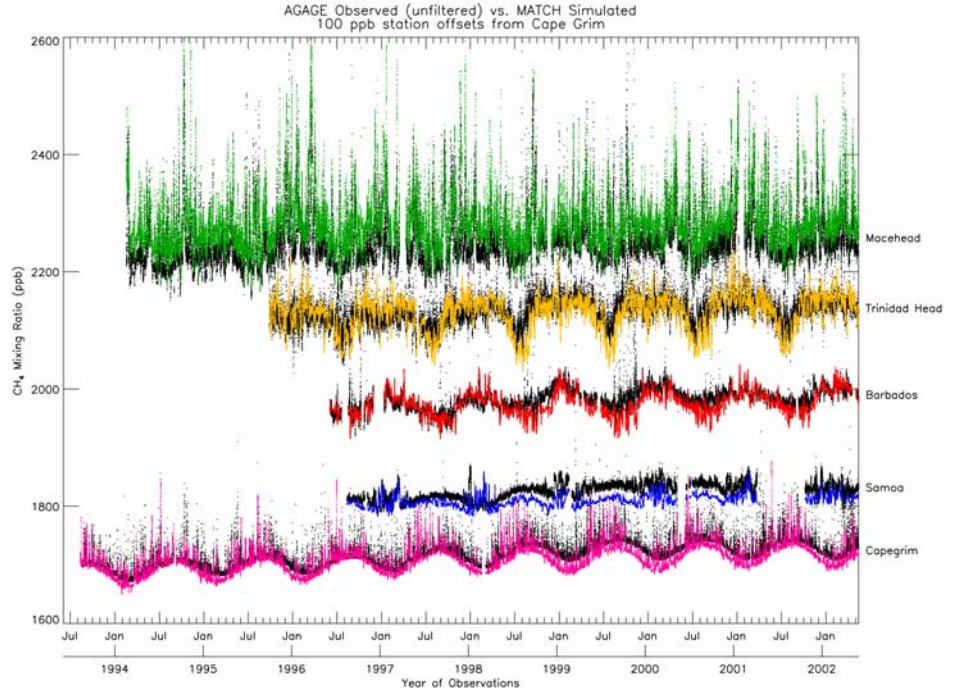


Figure 4.5. Comparisons between reference (top) and inversion optimized (bottom) MATCH runs with observations at the AGAGE sites. Black = Observations (same in both plots), Color = Model Runs. The improvement is most obvious at the Southern Hemispheric sites of Samoa and Cape Grim, where simulated methane mole fractions have increased to better fit the observations. The seasonal cycle at Barbados also more closely matches the actual observations. The improvement at the Northern sites is real but more difficult to discern in these plots because of the high-frequency of data.

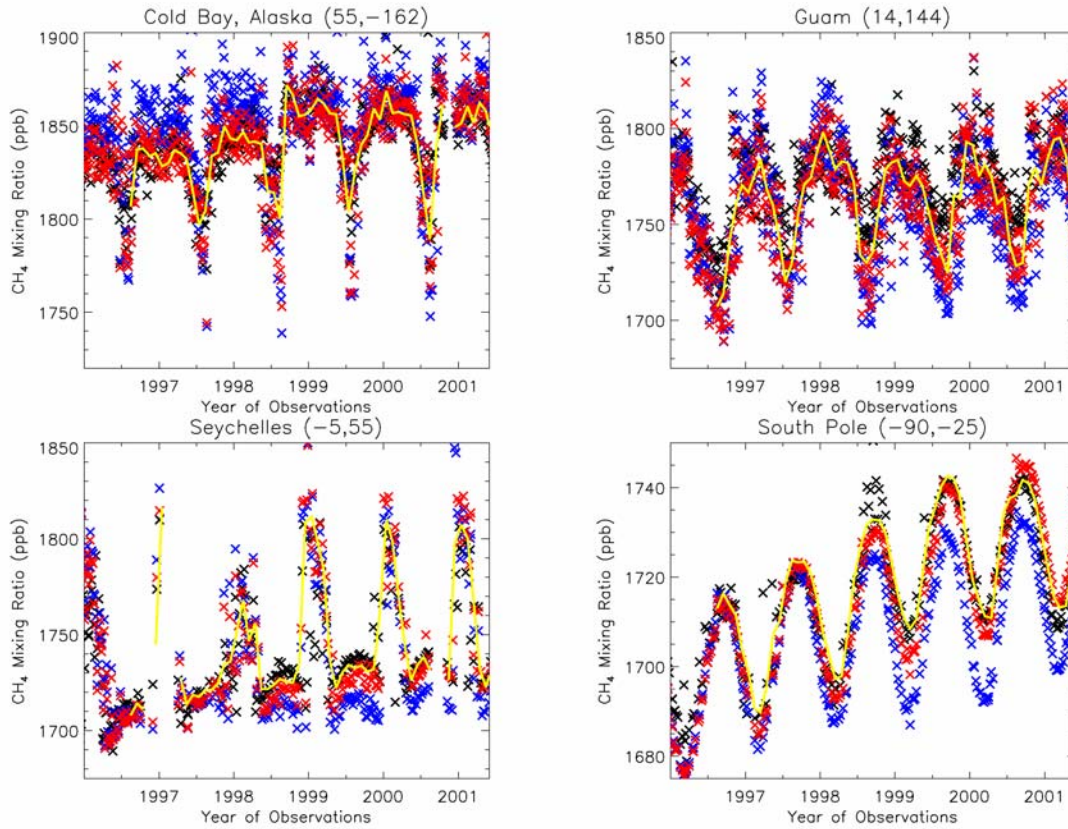


Figure 4.6. Modeled mixing ratios from reference (blue) and inversion optimized (red) MATCH runs, as compared to flask observations (black). The improvement is more obvious in the Southern Hemispheric sites, where the flask measurement scatter is less. The yellow lines represented the optimized monthly means as predicted by the inversion using Equation (4.14).

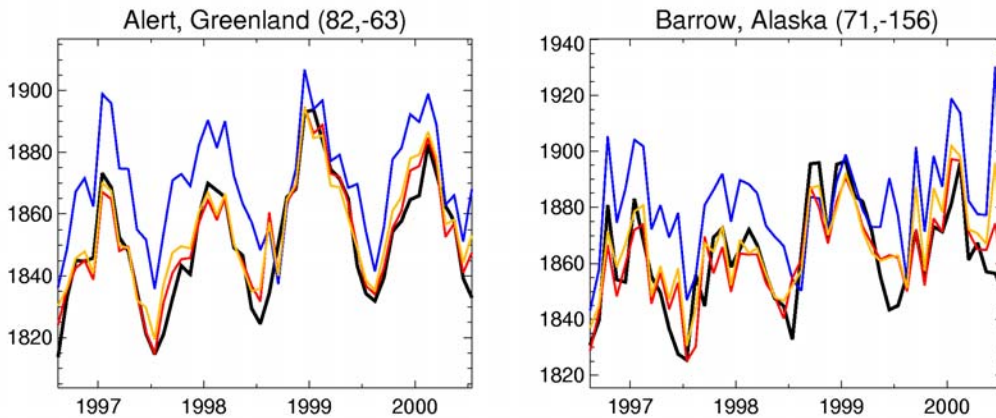


Figure 4.7. Comparison between MATCH and inversion-predicted monthly means at Alert and Barrow. Four curves are shown in each plot: Optimized MATCH run = Red, Optimized Inversion using Equation (4.14) = Orange, MATCH reference run = Blue, Observed Monthly Mean = Black. The inversion produces a better fit to the observations. There is a good correspondence between the monthly means using Equation (4.14) and the MATCH run, as expected.

4.4 Summary

In this chapter we have adapted the Kalman Filter for the simultaneous solution of 3 aseasonal and 7 seasonal methane processes. The aseasonal processes are solved as constant fluxes over the entire time period between 1996-2001. The seasonal processes are solved as monthly means, and contain the interannual variability in emissions. Each seasonal monthly flux uses observations of 12 subsequent months for optimization. The observational errors incorporate instrumental imperfections, mismatch (representation) errors, and sampling frequency errors. High-frequency observations have a small sampling frequency error, since the monthly mean is very well-defined using hourly data. For flask measurements, this error can be very large, depending on the CH₄ variability at the collection site. In the inversion certain flask stations are thus significantly deweighted. The final optimized emissions have been integrated forward in MATCH. Simulated observations show an improved fit to actual observations, as expected, compared to the reference run. As a test of linearity, the inversion predicted monthly mean mole fractions were compared to the MATCH optimized monthly means. The overall correspondence is good, although small differences occur for specific months. The following chapter focuses on the detailed results of the inversion methodology developed here.

Chapter 5

Inverse Modeling of Atmospheric Methane: Results

In this chapter we optimally estimate methane emissions between 1996-2001 using the inverse methodology described in Chapter 4. The optimized emissions include annual, seasonal, and interannual flux values for specific methane emitting processes and regions. The inversion also reduces, to varying degrees, the large uncertainties in the initial estimates. We divide the inversion results into three parts. The first part focuses on the optimized seasonal cycle and uncertainties. The second part focuses on the annually averaged fluxes over the entire inversion period, and includes the aseasonal processes. Here, we compare the results of several different inversion cases. The third part analyzes interannual methane fluxes for the 7 seasonal processes at monthly time resolution. In particular, we examine the sources of the strong increase in atmospheric methane during 1998. This year experienced a strong El Niño with associated positive global temperature and precipitation anomalies. These factors likely contributed to the global increase in observed atmospheric methane. Can the inverse model identify increases in specific methane production processes which are sensitive to El Niño? The inversion results are also compared to bottom-up studies when available. We also discuss the potential impact of model errors, which have different effects on the three inversion time-solutions. For example, certain model biases may influence the annually averaged results more than the interannual anomalies.

This work has emphasized high-frequency in-situ CH₄ observations, which are more straightforward to model with a high-resolution 3-D model than the low-frequency flask measurements. We compare the inversions using in-situ data with and without additional flask data. We also examine the impact of using different sets of flask measurements, including the use of intermittent flask observations that do not cover the entire inversion period. As described in Chapter 3, model output can be sampled at either high or low-frequency (synchronously) when determining a flask monthly mean for comparison with observations. We also test the sensitivity of the inversion results to these two different model sampling strategies. These different inversion cases provide a further measure of uncertainty in the results.

5.1 Inversion Description

In this section we show the raw inversion results and describe the different sensitivity experiments. We also show the modeled improvements at every site in the CH₄ observational network using a representative set of optimized emissions. These will later be used to interpret the inversion results. Figure 5.1 contains the inversion methane flux and flux uncertainties for the seasonal processes. The left side of the figure is the same as Figure 4.4, in which the optimized monthly values (red) are compared to the annually repeating reference values (blue). These optimized values contain the full interannual variability in the emissions, as well as new, optimized average seasonal cycles. There are significant deviations from the reference case for some emission processes. The inversion also simultaneously solves for the aseasonal Animals/Waste, Gas, and Coal emissions as constants. Their solutions were

shown in Figure 4.2, as deviations from the reference; the optimized total aseasonal emissions are the sum of the deviations and the reference values. The right side of Figure 5.1 superimposes the optimized (red) uncertainties on top of the reference (blue) uncertainties. Note that the inversion always acts to reduce the initial uncertainty by amounts depending on the value of the observations in constraining each emission process. The error reduction can be large (e.g. Bogs West) or small (Biomass Burning regions).

The biomass burning regions have the smallest uncertainty reduction of all processes yet the greatest relative change from reference. We also tested the effect of increasing the initial uncertainties on these three regions from 100% to 200% of the reference emission. The final optimized errors are larger in the 200% error case, indicating that the choice of initial error can limit the final, optimized error for these regions. In terms of optimized flux values, doubling the uncertainty range also increases the optimized flux for certain months. However, the annual average flux of the two cases fall overlap within their optimized uncertainties. In addition, we consider a 100% monthly flux uncertainty on the reference emissions to encompass the uncertainty of the bottom-up estimates. Although this may have some impact on the optimized values for certain months, we find it reasonable to constrain these poorly observed regions based on prior knowledge of their emissions.

Much information is contained in Figure 5.1; the following sections divide these results into more interpretable time domains. First we discuss the different inversions that were performed, of which Figure 5.1 is just one example. Table 5.1 describes the different inversion cases, which involve the use of different sets of flask data. The first case uses the 13 high-frequency sites only (In-situ only). This is followed by adding on flask sites from the South Pole (In-situ SPO) and the clean marine boundary layer (Flask MBL). These include 21 sites mostly located in the Southern Hemisphere (labeled in the footnote of Table 5.1). The next inversions incorporate the 41 flask sites active for at least 70% of the 60 months between 8/1996 and 7/2001 (Table 4.2). The flasks are further subdivided into cases involving MATCH high and low-frequency flask monthly means (Flask LF and HF). As described in Chapter 3 and 4, the model monthly means can be computed using all model time-steps (HF) or at the 4-5 flask sampling times (LF). The flask samples in the remote MBL are insensitive to this distinction and thus only low-frequency results are used for the Flask MBL case. The Flask LF All and Flask HF All cases include the additional 33 sites which have data for less than 70% of the inversion months. The locations of all stations were shown in Figure 3.1. The distinction between sites with greater and less than 70% of the data is made because sites with significant amounts of missing data may affect the inversion results independently of their observational values. Most previous atmospheric inversions use a constant observational network, avoiding possible effects from the abrupt activity/inactivity of intermittent sites. These impacts are sometimes difficult to separate from emission changes due to the interannual variability of actual observations. The 70% cutoff is taken as an approximate value above which these impacts are minimized. The Transcom 3 CO₂ inversion also used a 70% active observational criteria, but further used GlobalView interpolated/extrapolated CO₂ to fill any missing data. Here we only use actual monthly mean values, and do not fill missing data.

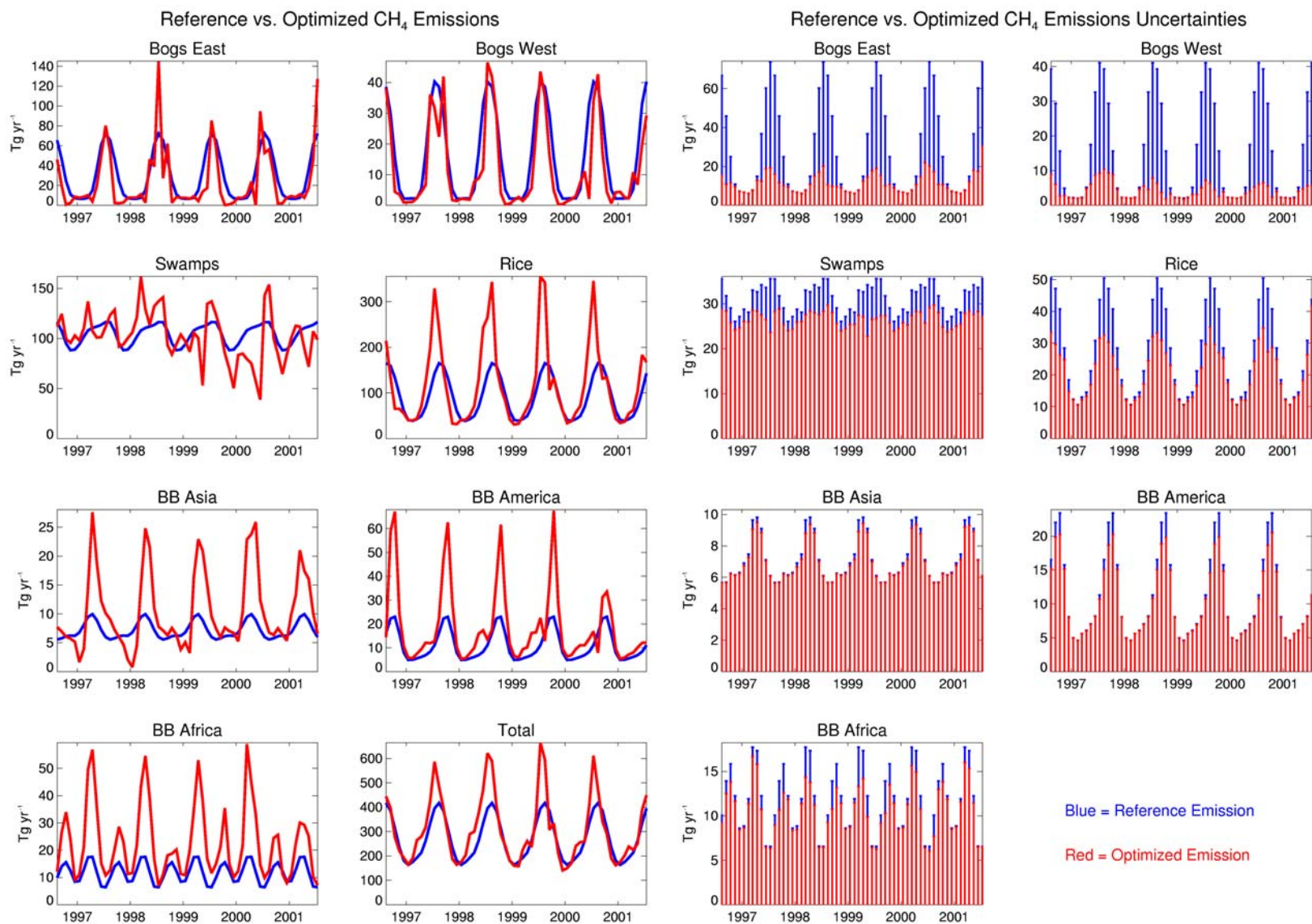


Figure 5.1. Seasonal Inversion Results for the Flask LF case (see Table 5.1). The reference (blue) and optimized (red) monthly methane fluxes are shown in the left plots. Note that the reference fluxes are annually repeating, while the optimized values contain significant interannual variability. The corresponding seven uncertainties are shown on the right seven plots, with the optimized error bars (red) superimposed upon the reference (blue) errors. Note that each process plot uses a different flux scale.

Table 5.1. Inversion Case Descriptions

Case	# Sites	In-situ	Flask	Flask Averaging
<i>In-situ only</i>	13	all	none	none
<i>In-situ + SPO</i>	14	all	South Pole Only (spo)	Low-Frequency (LF)
<i>In-situ + Flask MBL</i>	35	all	Flasks in MBL ¹	Low-Frequency (LF)
<i>Flask LF</i>	54	all	active > 70% time	Low-Frequency (LF)
<i>Flask HF</i>	54	all	active > 70% time	High-Frequency (HF)
<i>Flask LF All</i>	87	all	all flasks	Low-Frequency (LF)
<i>Flask HF All</i>	87	all	all flasks	High-Frequency (HF)

¹21 flask sites (active > 70 % inversion time) that sample marine boundary layer (MBL) air are: asc,azr,bme,bmw,cba,chr,crz,eic,hba,ice,kum,mid,psa,shm,spo,syo,tdf,cfa,cgr,maa,mqa.

Figure 5.2 - Figure 5.4 show the observed (black), reference (blue), and optimized Flask LF (red) CH₄ monthly mean mole fractions at each observing site. The optimized values are generated by running MATCH using the optimized fluxes shown in Figure 5.1. The figures have been divided into the 13 in-situ, 41 flask (active > 70 % months), and 33 extended flask (active < 70 % months) subsets. Within each subset, the sites are listed latitudinally and correspond to the order shown Table 4.2. The optimized values have been generated using the Flask LF optimized emissions in MATCH. The different inversions in Table 5.1 produce qualitatively similar optimized CH₄ mole fractions in MATCH, although the optimized fluxes differ. The observational improvements represented by the cases in Table 5.1 are useful for interpretation of the inversion results in the following sections. The observed values also contain error bars which represent the monthly mean errors as computed in Chapter 4. Note that there can be significant interannual variability in the error bars, particularly for the flask measurements. Very large error bars usually correspond to a monthly mean observation defined by only 1 or 2 flask measurements.

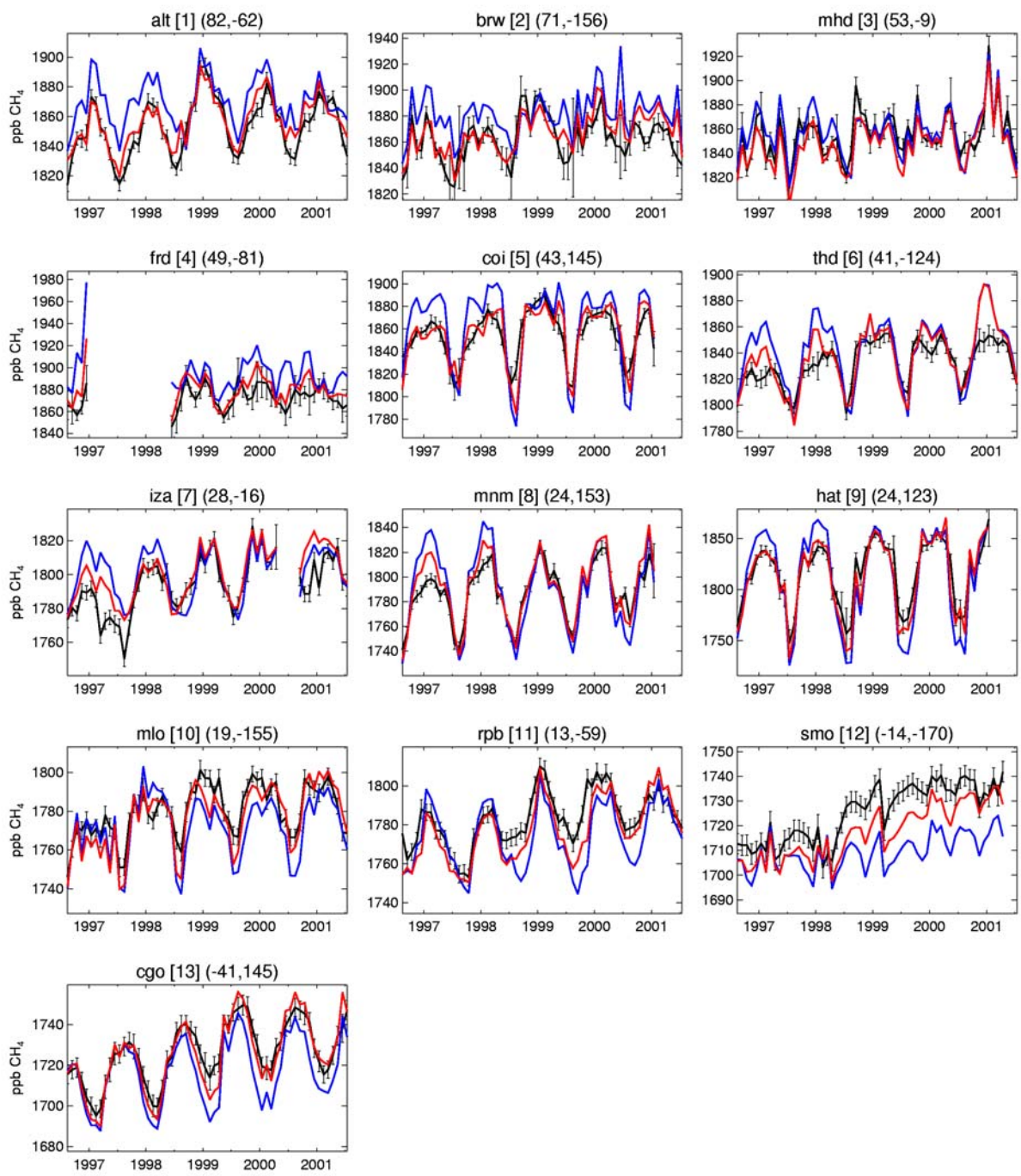


Figure 5.2. Monthly mean observations at high-frequency inversion sites, arranged by latitude and numbered according to Table 4.2. The three letter identifiers are followed by [station numbers] and (latitude, longitudes). The observations (black) are shown with corresponding error bars. The reference (blue) and optimized (red) values represent MATCH monthly means. The optimized values correspond to a MATCH run using the results of the Flask LF inversion.

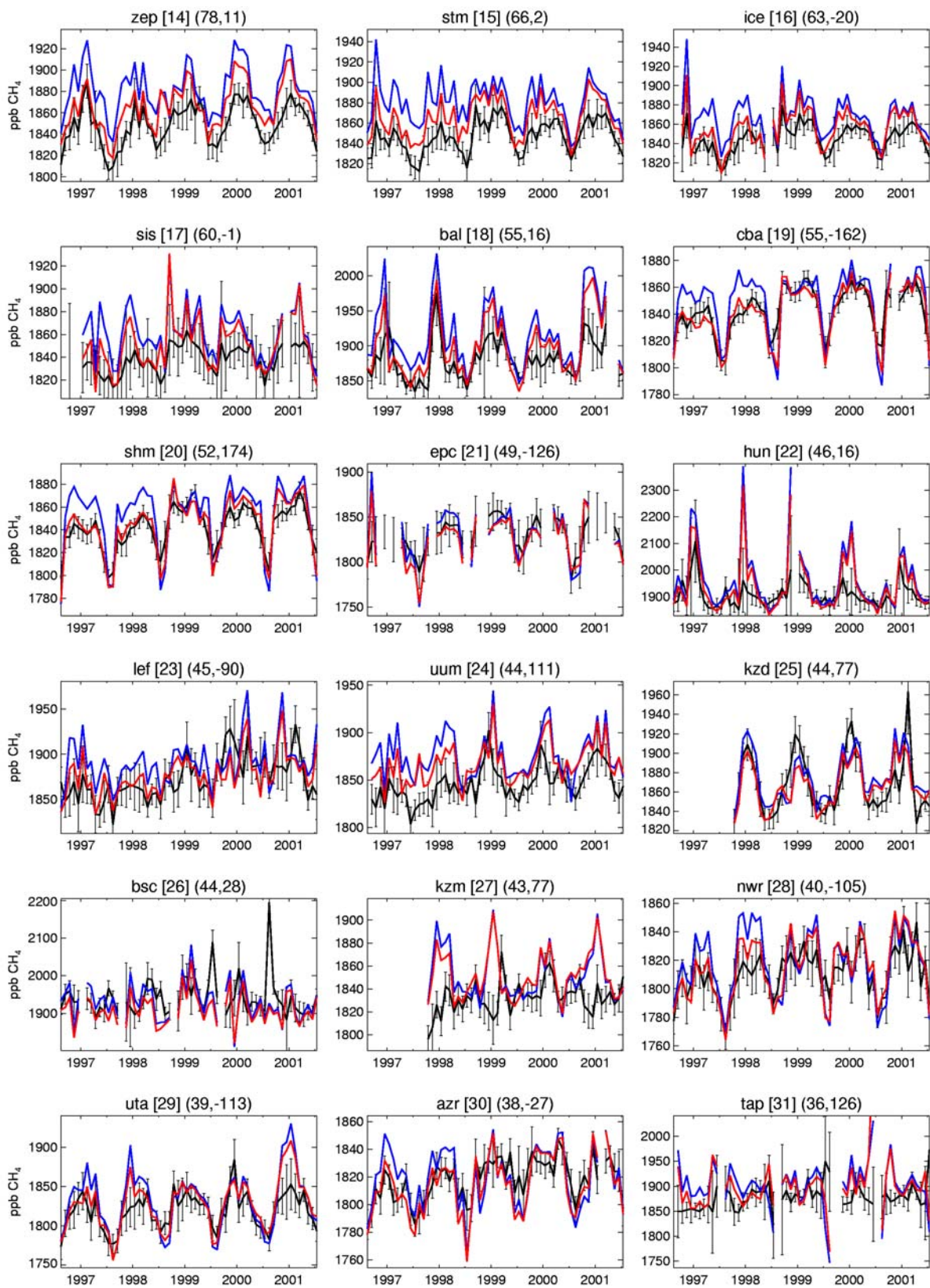


Figure 5.3. Same case as described in Figure 5.2, but showing flask sites which have monthly means for at least 70% of the inversion months (see Table 4.2). The modeled monthly values have been computed by sampling MATCH at the exact time of measurement.

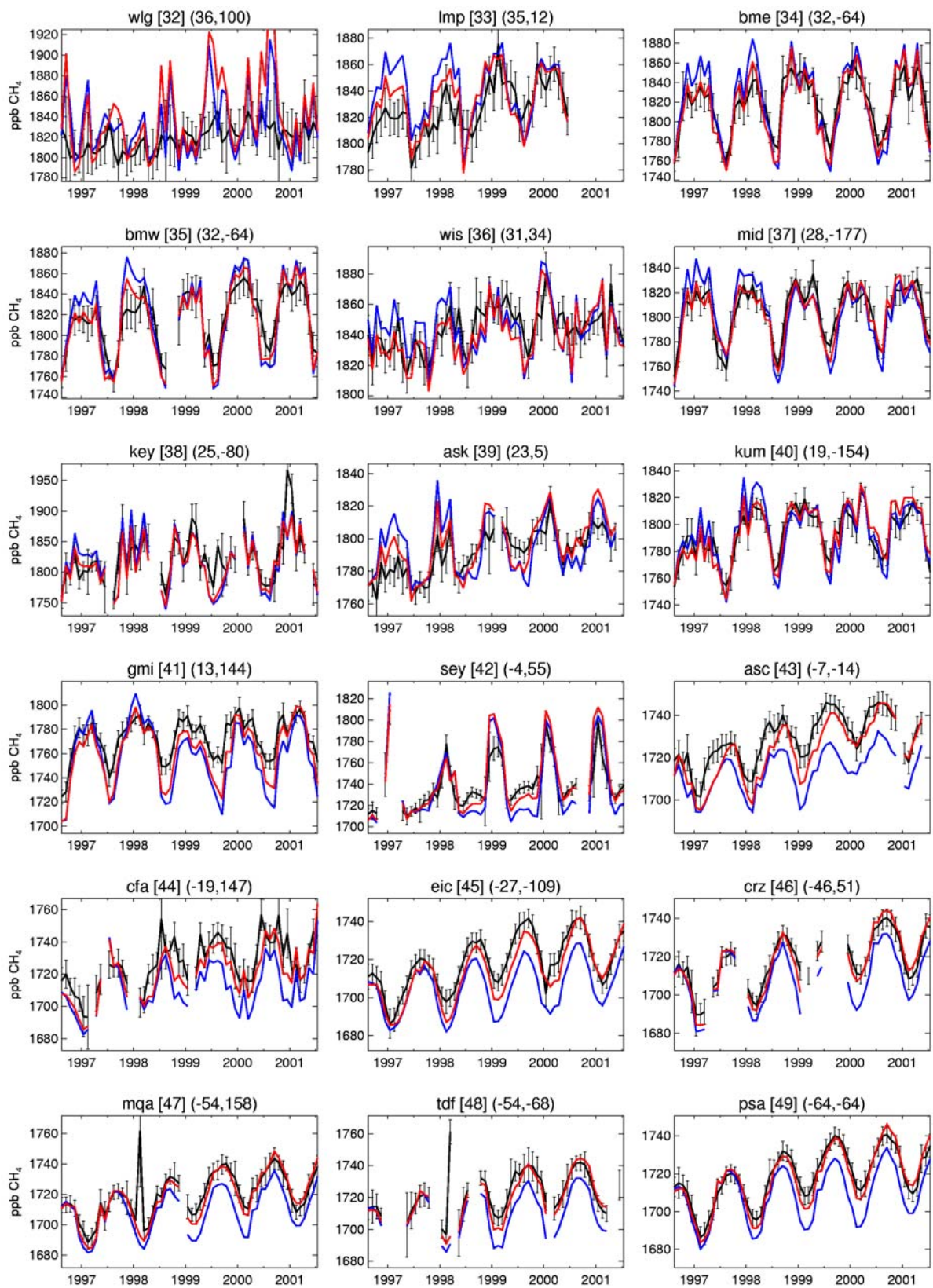


Figure 5.3 continued

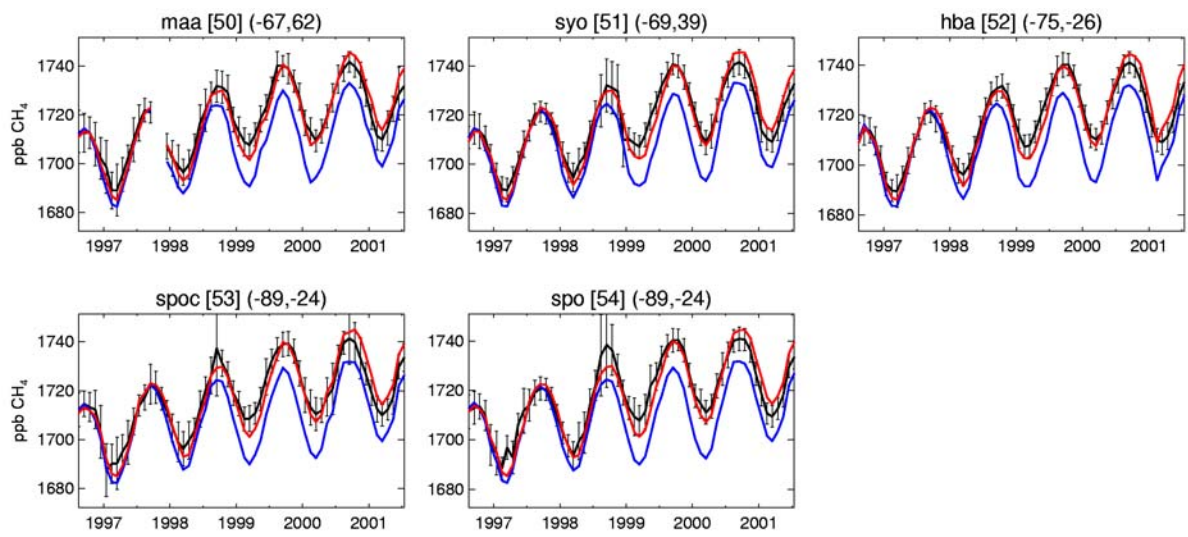


Figure 5.3 continued

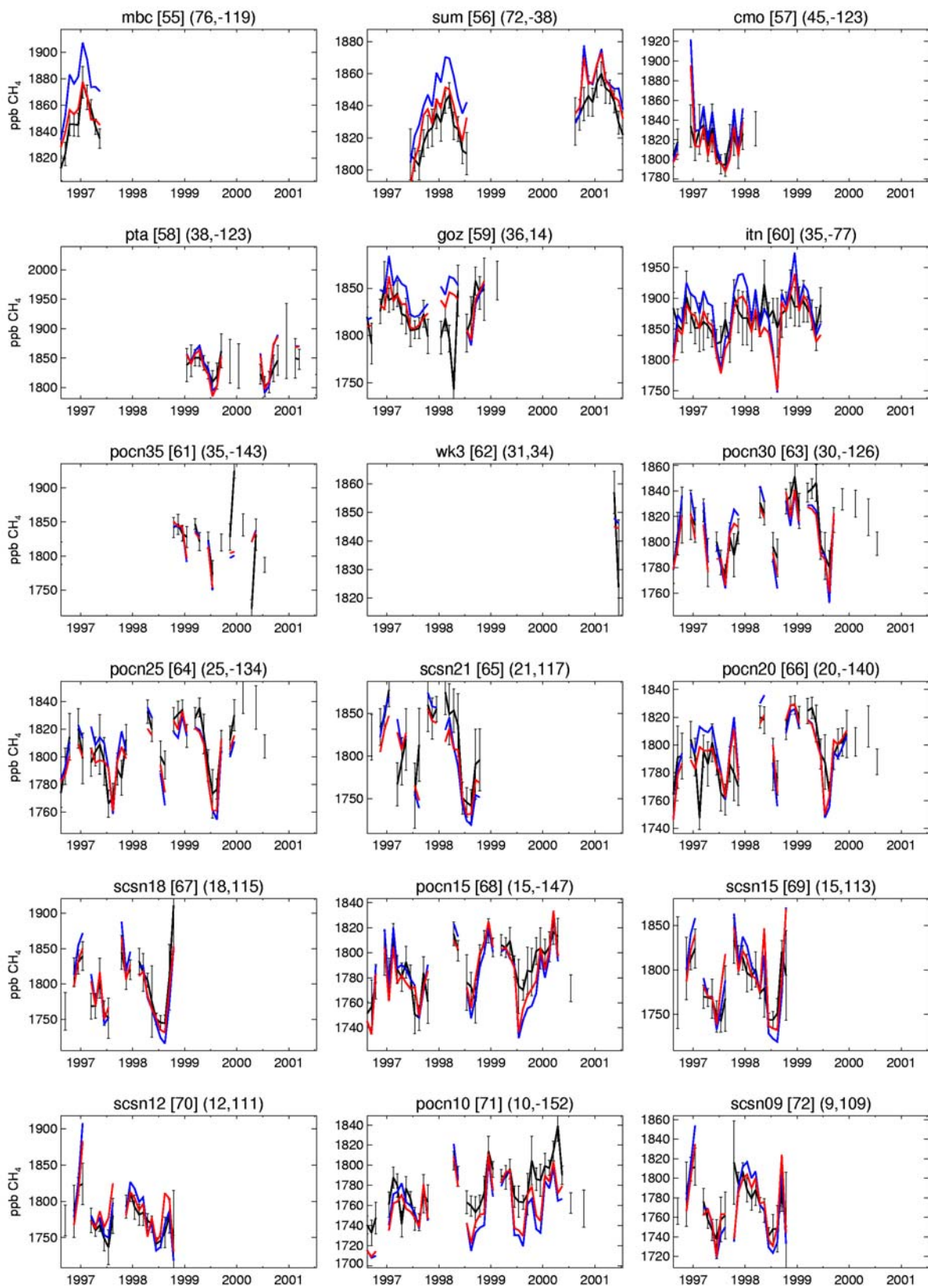


Figure 5.4. Same case as described in Figure 5.2, but showing flask sites which have monthly means for less than 70% of the inversion months (see Table 4.2). The modeled monthly values have been computed by sampling MATCH at the exact time of measurement.

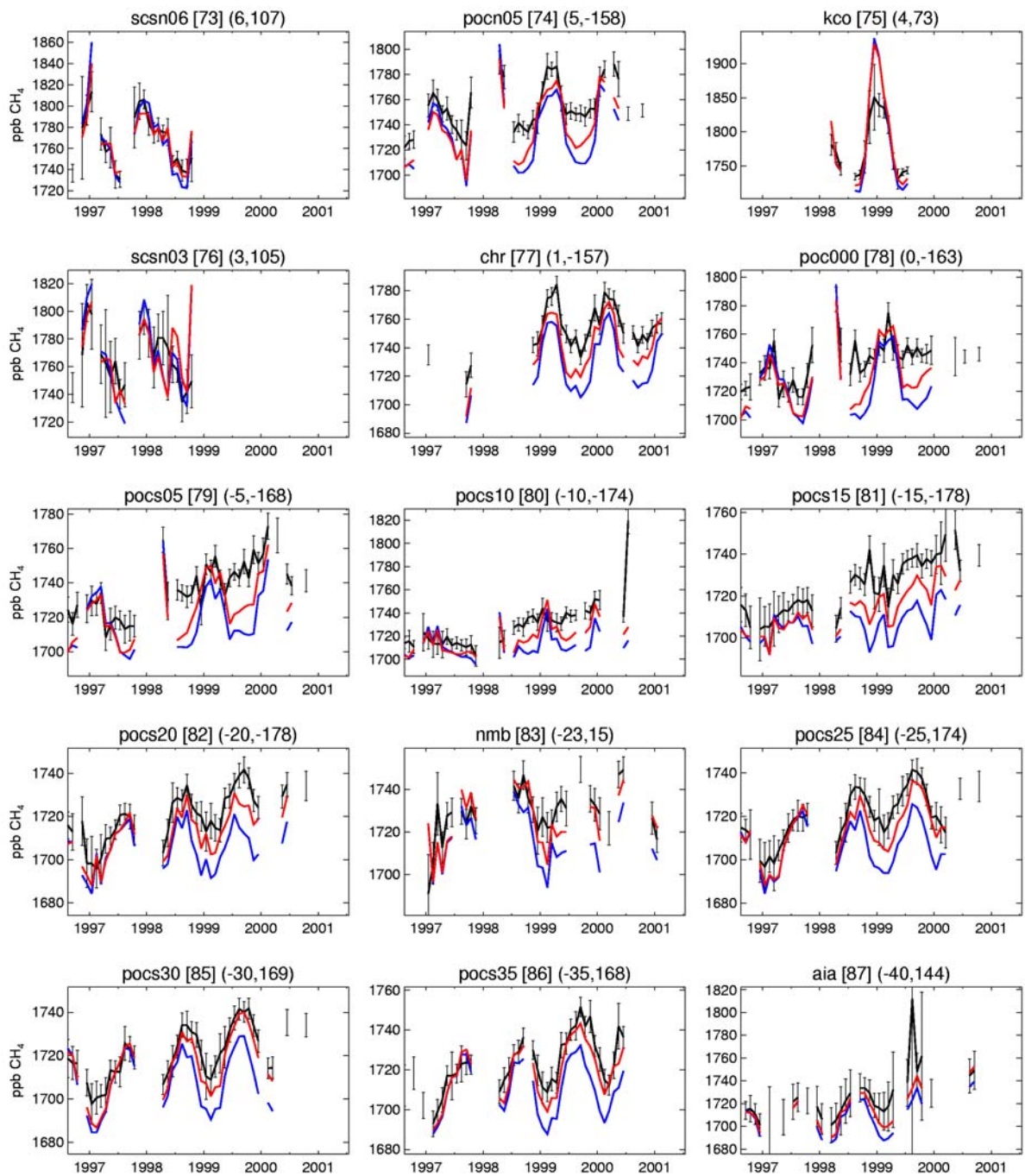


Figure 5.4 continued.

5.2 Average Seasonal Results

We begin by averaging the interannually varying inversion results shown in Figure 5.1 into a single representative seasonal cycle. This makes the general inversion results more clear before proceeding to the comparison of all sensitivity cases in Section 5.3. Figure 5.5 (left) shows the results taken by averaging monthly values between 8/1996 – 7/2001. Two inversion cases are shown for each process: Flask LF (red), and In-situ only (green). The original reference case is shown in blue. The inversion also produces uncertainties for each month between 8/1996 – 7/2001. These errors have also been averaged, and are shown on the right side of Figure 5.5. The average uncertainties are computed as errors on a mean quantity, following Wunsch (1996), p. 189.

$$\bar{\sigma}_{mon} = \sqrt{\frac{\sum^N \sigma_t^2}{N}} \quad (5.1)$$

where t represents a particular month (e.g. January) and $N = 5$, for the five years of the inversion.

We first compare the Flask LF inversion to the reference emissions. Both Bogs East and Bogs West show decreases, particularly during the fall, winter, and spring. The overall decrease in the northern wetland regions is consistent with the reference run overestimate of the northern hemispheric mole fractions (Figure 3.9). These effects are particularly evident at the nearby stations of alt[1], brw[2], and frd[4] (Figure 5.2) where the reference overestimate has been corrected by the inversion. Swamp emissions show a dip during the spring months centered around May, compared to the relatively smooth reference emissions. This late spring decrease is compensated by increases during the late summer and early spring, maintaining the annual total Swamp magnitude. Note that the Swamp emissions are still globally significant throughout the year. The inversion produces significant Rice emission increases above the reference, with a shift from an August to July maximum. The optimized emissions are also decreased after September. At least part of the large increase can be attributed to downwind sites off of Asia, in which the reference run exaggerates the mole fraction seasonal trough during June and July. This is most clearly seen at coi[5] and hat[9], the two high-frequency stations most sensitive to Rice (Table 3.3). The inversion compensates by shifting the Rice emissions to an earlier and more intense July maximum, followed by a sharper decline. Note that an overestimate of tropical summertime OH in MATCH values could also lead to an overestimate of the reference mole fraction seasonal trough. This possibility is, however, discounted by the good representation of the seasonal cycle at Samoa, which is located in the remote tropics far from emissions. The Biomass Burning (BB) regions have stronger emissions with greatly enhanced peak values. This result is consistent with the overall need for greater tropical emissions than in the reference to explain the observations. The total emission for all seasonal processes (Figure 5.5) shows a significant increase above reference. This increase is mostly compensated by decreases in the aseasonal emissions as discussed in Section 5.3. The shift to a July peak is a mostly due to Rice, with smaller contributions from Swamps and Bogs East.

Compared to the Flask LF inversion, the In-situ only case includes nearly offsetting increases and decreases in Bogs East and West, respectively. Part of the difference lies in the removal of flask sites

sensitive to Eurasian wetland emitting regions. Flask sites sensitive to Bogs East (e.g. zep[14], stm[15], and bal[18]) show reference mole fraction overestimates; their inclusion leads to a stronger emission reduction. The Swamp emission trough is also present in the In-situ only case, but emissions are nearly uniformly greater than the Flask LF case. The greater swamp emissions are nearly offset by the lower Rice and Biomass Burning emissions. The optimized seasonalities are similar to the Flask LF results, but the magnitudes differ. The optimized seasonal totals are nearly identical for the two cases.

The right side of Figure 5.5 shows the average monthly error reduction from the inversion. Bogs East and Bogs West have the greatest error reduction; these processes have several observational sites within and downwind of these regions. Moderate error reduction is seen for Rice, largely due to downwind Asian sites. The least well constrained sources are Swamps and Biomass Burning (BB), which are mostly located in the tropics. The additional error reduction due to the flask network can be seen by the differences between the green and red lines. The high-frequency sites account for most of the error reduction for Bogs East, Bogs West, and Rice, since there are sufficient high-frequency sites to constrain these processes. The flask measurements provide additional error reduction for Swamps, BB Africa, and BB America. BB Asia is the least well constrained even with flask measurements.

5.3 Average Annual Results

Table 5.3 and Figure 5.6 contain the methane fluxes averaged over the entire period between September 1996 – August 2001. We have further aggregated individual processes into Energy, Wetland, and Biomass Burning emissions; their individual fluxes are listed in Table 5.3. Reducing the optimized emissions to a single average fluxes facilitates comparison between the different sensitivity cases. The averages for the seasonal processes are derived by averaging the results shown in Figure 5.5 (left seven plots). The inversion directly solves for the aseasonal process emissions as annually averaged differences from the reference. The final values shown in Figure 4.3 are added to the reference values to obtain the optimized aseasonal emissions. Table 5.3 also includes the optimized errors, which are always less than the reference error due to the Kalman Filter. For the seasonal processes, Equation (5.1) has been extended to all months to determine the annual average error. The aseasonal uncertainties are taken from the last step of the Kalman Filter as shown in Figure 4.3. Note that the errors from the aseasonal components are much smaller than the seasonal components. This arises for two reasons. The first is that the aseasonal processes have very broad geographical distributions and strong sensitivities at many observing sites. This is in contrast to the seasonal processes, which are more localized regionally and/or have relatively low sensitivities to the observing network (e.g. biomass burning). The second reason is that the inversion solves the aseasonal process as constants over the entire time period, allowing error reduction at each time-step. The seasonal processes, in contrast, are solved as monthly fluxes which adds greater uncertainty to their five-year averages.

For the aseasonal processes, the inversion increases Animals/Waste slightly, and decreases Gas and Coal significantly compared to the reference (Table 5.3). As discussed previously for the seasonal processes, the optimized emissions act to decrease the reference overestimate of the methane interhemispheric gradient. The effect of an Animals/Waste increase (globally distributed) and Gas/Coal decrease (northern hemispheric distribution) is a net increase in tropical and southern hemispheric emissions. Wetlands show some reduction, mostly from decreases in northern bog emissions. Rice emissions, which are dominated by sources between 0 – 30° N, increase by up to 40%. Individual tropical biomass burning sources are also increased between 30 - 100%. We have aggregated the processes into 5 main groups listed in Table 5.2. Note that the emission total is similar for all optimized cases; differences between cases correspond to shifting emissions between groups. The addition of flask data generally decreases emissions from Animals/Waste and Wetlands, and increases Energy, Biomass Burning, and Rice. Addition of flask data also lead to greater uncertainty reduction for each group.

Figure 5.6 shows the optimized values for the Flask LF case (red) compared to the reference (blue). The reference error bars refer to the a priori uncertainties of each aggregated set of processes. The optimized case contains two sets of error bars. The left error bar corresponds to the spread in inversion values for all the inversion cases in Table 5.2. The right error bar represents the uncertainty from the Flask LF inversion. For the aseasonal processes, the inversion spread is larger than the inversion uncertainty. As described before, the aseasonal processes have small inversion uncertainties due to their large sensitivities to observations and solution as constant fluxes. The seasonal processes display opposite behavior, with the inversion uncertainty dominating the spread in inversion cases. These processes are less well constrained due to their lower sensitivity to observations and solution as monthly fluxes. They are also somewhat less sensitive than the aseasonal processes to the addition of flask data.

The leftmost (yellow hanging) error bars in Figure 5.6 correspond to the range of estimates found in the literature for each process. Note that the optimized values fall within this spread, although certain processes lie at the far end of the range. Our total emissions are at the high end of the IPCC range of 500-600 Tg yr⁻¹. This total is dictated by the total OH sink, as discussed in Chapter 4. The higher total value contributes to the higher emission estimates for most processes compared to the literature range.

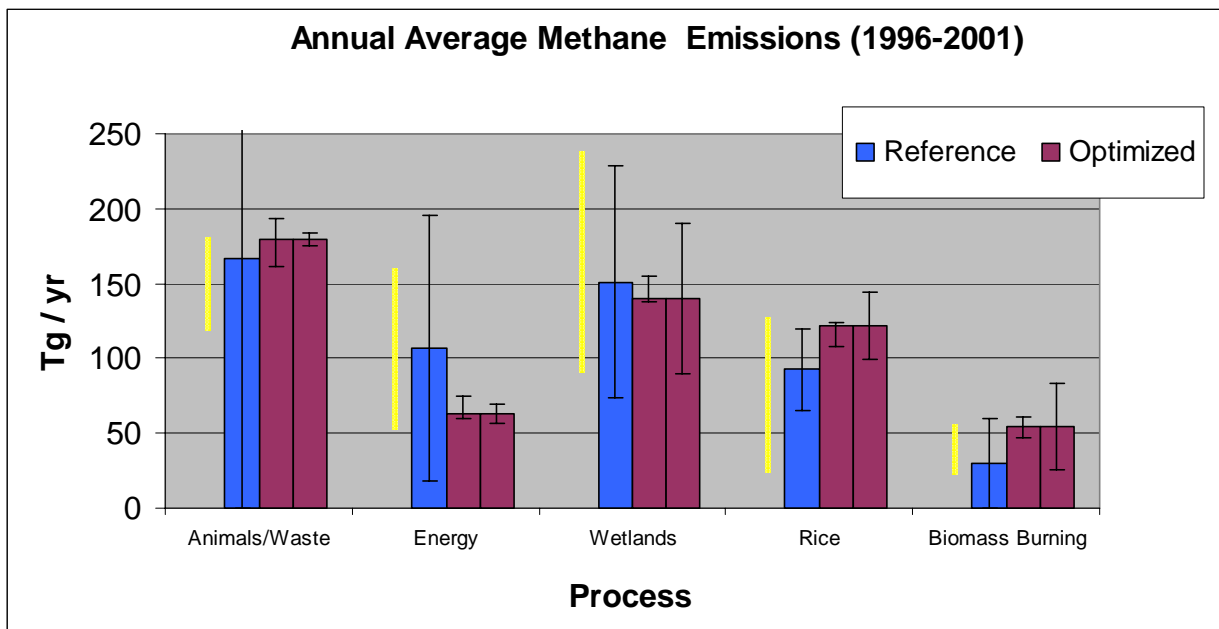


Figure 5.6 Annual Average Methane Emissions. Shown are reference (blue) and optimized (red) using the Flask LF inversion. The error on the reference is the assumed a priori inversion uncertainty. The optimized values include two error bars: left bars corresponds to the spread of inversion results in Table 5.2, right bars to the inversion uncertainty for the Flask LF case. The leftmost errors (yellow) represent the range of emission values found in the literature. See Table 5.2.

Table 5.2. Five-year averaged inversion emission values and errors for aggregated regions (units of Tg yr⁻¹)

Case	Animals /Waste	Energy ¹	Wet- lands ²	Rice ³	Bio Burn	Total ⁴
<i>Literature Range</i> ⁵	120-180	53-159 ⁶	92-260 ⁷	25-100	23-55	500-600
<i>reference</i>	167 ±167	107 ±89	151 ±78	93 ±28	30 ±30	588.7
<i>In-situ only</i>	193 ±4	60 ±7	154 ±50	108 ±23	47 ±29	604.3
<i>In-situ + SPO</i>	184 ±4	64 ±7	153 ±50	113 ±23	48 ±29	602.4
<i>Flask MBL</i>	173 ±4	66 ±6	146 ±47	120 ±22	53 ±28	600.8
<i>Flask HF</i>	182 ±4	63 ±7	142 ±50	120 ±23	53 ±29	600.8
<i>Flask LF</i>	180 ±3	63 ±5	140 ±42	122 ±21	54 ±28	601.7
<i>Flask HF All</i>	163 ±3	73 ±5	138 ±41	124 ±20	60 ±27	600.3
<i>Flask LF All</i>	161 ±4	75 ±5	140 ±43	124 ±21	60 ±28	601.0

1. Energy = Gas + Coal + 18 Tg yr⁻¹ from other processes not solved by the inversion

2. Wetlands = Bogs East + Bogs West + Swamps

3. Biomass Burning = BB Asia + BB America + BB Africa

4. Includes contribution from other sources (e.g. termites, local burning) totaling 18.5 Tg yr⁻¹

5. Literature Range from IPCC (2001) unless otherwise noted.

6. Range from Quay *et al.* (2000).

7. Upper estimate from Walter *et al.* (2001a).

Table 5.3. Five-year averaged individual inversion values and errors for Energy, Wetland, and Biomass Burning in Table 5.2. All values in Tg yr⁻¹

Case	Energy		Wetlands			Biomass Burning		
	Gas	Coal	Bogs East	Bogs West	Swamps	BB Asia	BB America	BB Africa
<i>reference</i>	50 ±50	39 ±39	30 ±30	16 ±16	104 ±31	7 ±7	11 ±11	12 ±12
<i>In-situ only</i>	22 ±3	21 ±4	33 ±16	9 ±5	112 ±28	9 ±7	18 ±11	20 ±11
<i>In-situ + SPO</i>	25 ±3	21 ±4	34 ±16	9 ±6	110 ±28	9 ±7	18 ±11	21 ±11
<i>Flask MBL</i>	35 ±2	14 ±4	32 ±15	10 ±5	104 ±27	10 ±7	20 ±10	23 ±11
<i>Flask HF</i>	30 ±3	15 ±4	23 ±16	12 ±5	106 ±28	10 ±7	21 ±11	23 ±11
<i>Flask LF</i>	34 ±2	11 ±3	24 ±12	12 ±5	104 ±27	10 ±7	20 ±12	24 ±11
<i>Flask HF All</i>	35 ±2	20 ±3	23 ±12	12 ±5	103 ±26	10 ±7	25 ±11	25 ±10
<i>Flask LF All</i>	31 ±2	26 ±3	22 ±12	13 ±5	106 ±26	10 ±7	26 ±11	24 ±11

5.3.1 Comparison to Bottom-up Estimates

Wetlands

Cao et al. (1996b) used a process model that incorporated substrate availability and climatic variables to estimate global wetland emissions of 92 Tg yr⁻¹. Their total is broken down into northern, temperate, and tropical contributions of 23.3, 17.2, and 51.4 Tg yr⁻¹, respectively. Using another wetland process model, *Walter et al.* (2001b) estimated total wetland emissions of 260 Tg yr⁻¹, with a 25% contribution from wetlands north of 30° N. The tropics dominate wetland emissions in both studies. The discrepancy between these two estimates likely resides in the parameters linking temperature and methane production. Our annual average result of 140-150 Tg yr⁻¹ lies between these two estimates but is closer to the *Cao et al.* (1996b) estimate. The optimized wetland emissions in our study also show a dominance of tropical/southern (~70%) over northern emissions (~30%), which is consistent with both of the process model studies. The wetland peak during July in our inversion is also found by *Cao et al.* (1996b).

Rice

Over the past two decades, bottom-up rice emission estimates have been decreasing as more knowledge is gained (*Mosier et al.* (1998)). This is largely due to the greater number of individual flux measurements used for extrapolation. *Sass* (1994) estimated global rice emissions between 25 – 54 Tg yr⁻¹ by combining rice cultivation area and flux estimates. Much of the uncertainty involves extrapolating single flux measurements, which may not be representative in space or time, to the global scale. Using a process based model of CH₄ emissions from rice, *Cao et al.* (1996a) estimated a global flux of 53 Tg yr⁻¹. Our rice emissions of 110-120 Tg yr⁻¹ are about twice current bottom-up estimates, but are closer to other top-down studies (*Lelieveld et al.* (1998), *Hein et al.* (1997)). Some of the difference may be attributable to spatial overlap between wetland and rice emitting regions in Asia, particularly in China and India. The inversion approach in general cannot separate these emissions because they emit at similar latitudes and times of the year. Consequently, the inversion may be attributing some wetland emissions to rice in this region. Bottom-up estimates focus on rice cultivation areas and may ignore other nearby inundated regions formed by either natural or anthropogenic processes. In addition, emissions during the non-growing season are also excluded (e.g. *Yan et al.* (2003)). Incorporation of these other emissions would lead to larger bottom-up estimates from areas that include rice cultivation.

For our inversion, most of the overall rice emission is caused by enhanced emissions during July and August (Figure 5.5). The global seasonality of rice paddy emissions bottom-up are difficult to estimate because different regions have different rice planting seasons. For flooded rice fields, peak methane emissions usually occurs several weeks after the initial flooding. The timing and magnitude of flux depend strongly on soil characteristics, plant type, and fertilizer composition, in addition to climatological factors. *Cao et al.* (1996a) used their process model to estimate that over half of rice emissions occur between July and October globally, with peak emissions occurring in August. In a study of methane emissions from China, *Yao et al.* (1996) estimated peak methane emissions in June using regional classification and emission rates from six sites.

The measurements at the high-frequency stations of hat[9] and coi[5] are most sensitive to rice emissions, and are reproduced well by the optimized MATCH run. The measurements at the most

sensitive flask site, wlg[32] in north-central China, are sometimes overestimated by the optimized MATCH run during July and August. Note that the nearby South China Sea observations in Figure 5.4 are not overestimated by MATCH. This discrepancy suggests that additional land based measurements in this region should be made. The large observational error bars of wlg[32] (± 23 ppb, Table 4.2) due to the sampling frequency error additionally call for high-frequency measurements in this region. We also performed an inversion which excluded the aseasional processes (i.e. they were kept at reference values). There was almost no net increase in total rice emissions, although a strong seasonal shift to one month earlier than the reference still occurs. This suggests that decreases in the aseasional processes are compensating for rice increases in the full inversion. Coal emissions share a similar spatial pattern to rice, and decrease by nearly the same amount as the rice emissions increase in the inversions.

Biomass Burning

The optimization increases biomass burning for all regions, but the estimated emissions are still within the current literature range. Biomass burning emissions are poorly constrained in the inversion due to observational undersampling in the tropics. Bottom-up studies also have large uncertainties, due to the difficulty in estimating total amounts of biomass burning and appropriate CH₄ emission factors. The emission factor depends strongly on the fire type (*Hao et al.* (1993)). The only bottom-up value for global CH₄ emissions corresponds to our reference case from *Hao et al.* (1993). The inversion further enhances the bimodal behavior of Biomass Burning Africa (Figure 5.5). This bimodal behavior is largely caused by shifts in the ITCZ, resulting in different dry and wet periods within a single region (*Duncan et al.* (2003)). Table 5.3 shows that BB Africa and BB America have similar annual emissions, with BB Asia only half as large. This result is qualitatively consistent with the *Hao et al.* (1993) estimate applicable for the 1980's. In contrast, *Duncan et al.* (2003) find greater CO emissions from Asia compared to the Americas during the 1990's, but whether or not this result applies also to CH₄ is not clear. More exact determination of the tropical biomass burning will require more sensitive observations.

Aseasonal Processes

The IPCC (2001) lists a range of 120 to 180 Tg yr⁻¹ for Animals/Waste emissions. Our inversely estimated total of 160 - 180 Tg yr⁻¹ is at the higher end of most estimates. Much of the bottom-up uncertainty lies in estimates of fluxes from landfills and other waste management sites. Our larger estimate for Animals/Waste is offset by our deduced strong decreases in Coal and Gas sources. The IPCC lists a total energy emissions range between 75-100 Tg yr⁻¹, mostly based on bottom up studies using economic data. The literature range for energy emissions in Table 5.2 is based on *Quay et al.* (1999), who used global measurements of ¹⁴CH₄ to estimate a percentage of fossil (energy) methane emissions between 9-27% of the total. We have applied this percentage range to our reference emission total of 590 Tg yr⁻¹ to derive an absolute range. Our combined energy total of 60 – 70 Tg yr⁻¹ is toward the lower end of this range, with Gas and Coal each contributing approximately 25 Tg yr⁻¹. The Energy source also includes ~18 Tg yr⁻¹ of other energy sources taken as given (Section 3.2.3) and not included in the inversions. Most of the literature estimates of energy emissions correspond to time periods before our inversions. The EDGAR (2002) data set show decreases in the gas and coal CH₄ emissions between 1990 and 1995. At least part of the decrease was associated with the collapse of the centrally planned economies of Eastern Europe and the former Soviet Union (FSU). Total coal production, and to a lesser extent gas, from these countries are reported to have decreased starting in the early 1990's (*EIA* (2003)).

In addition, *Dlugokencky et al.* (1994b) suggest a decrease in FSU gas leakage around this time. Coal production also decreased in China in the late 1990's due to the centrally planned closure of many small scale mines (*EIA* (2003)). Coal emissions in the United States are also considered to have decreased by over 30% between 1990 and 2000 partially due to increased methane recovery efforts (*DOE/EIA* (2002)). These reported energy trends may explain some of the difference between the older bottom-up literature values and our more current inversion results.

5.3.2 Errors

Although the observational mismatch error (see Section 4.2) accounts for some of the model transport error, the inversion otherwise assumes a perfect atmospheric model. Thus, systematic errors in transport, OH sink, and emission geographic patterns can contribute to biased inversion estimates. For example, deficiencies in the modeled interhemispheric transport and hence mole fraction gradient (IHG) can influence the annual average values. However, as mentioned in Chapter 2, the MATCH's IHG for anthropogenic compounds such as SF₆ and CFC-11 shows no systematic difference from the observed IHGs. In addition, the ability of MATCH to reproduce measurements at many high-frequency CH₄ sites (see Chapter 3) adds confidence in its synoptic scale transport. Errors in the OH spatial and temporal pattern might also contribute to a bias error, but large errors are not detected from the methyl chloroform simulations over our time period (see Figure 3.6). The seasonal cycle at Samoa, which is dominated by tropical OH values and interhemispheric transport, and not by far-away emission sources, is also well reproduced (Figure 5.12).

Another possible source of error lies in the emission spatial patterns used to solve for emissions. This error is potentially greater for the large aseasonal processes that contain many sensitive observing sites. A different assumed pattern might change the computed sensitivity at these sites and, consequently, the inverted emissions. The sensitivity to the emission pattern is smaller for localized regions that do not contain observing sites such as the tropical biomass burning regions. For these regions, a different emission pattern would likely still result in a similar signal at a downwind site. The proper test of this error would be to use alternative emission patterns, especially for the aseasonal components. We have not included such tests because of the scarcity of alternative estimates of spatial distributions, as well as the large computational burden already associated with using just a single set of flux spatial patterns.

5.4 Interannual Results

We now examine the interannual methane results, which are computed as the monthly anomalies (deviations) from the optimized average seasonal cycles in Figure 5.5. Figure 5.7 shows the Flask LF (red) and In-situ (green) cases for each emission process. These values represent the monthly anomalies over the inversion time period; for each process, the summation of these anomalies over all months is zero. Figure 5.8 contains the same results, but plots each process on identical vertical scales to emphasize relative contributions to the total variability. Bogs East, Swamps, and Rice dominate the interannual variability. These are also the largest seasonal processes, although Bogs East emissions are only about 20-30% as large as the other two (Table 5.3). Bogs West contributes modestly to the total anomaly, while the contributions from the three Biomass Burning (BB) processes are small. However, the BB variations

expressed as a percentage of their total emissions are comparable to the other processes. For a given process, the magnitude of the inverted interannual variability will depend on its sensitivity to the global network. For example, air from Biomass Burning Asia is poorly sampled by the network; this likely contributes to its relatively low variability compared to Bogs West despite having similar total flux magnitudes (Table 5.3).

Figure 5.7 shows comparable anomalies for both Flask LF and In-Situ only. The Flask LF case has slightly more month-to-month variability than the smoother In-situ only case (e.g. Bogs East in 1998). The global total variabilities are similar. The Flask LF and In-situ cases track one another closely for the relatively well observationally constrained Wetland and Rice processes. Differences between these latter two inversion cases are more apparent for the Biomass Burning regions. The flask measurements provide additional constraints in the tropical regions, leading to different inversion results. For BB Africa, for example, the presence of the downwind Ascension Island flask site (asc[43]) likely leads to the inversion differences.

The interannual differences between the Flask LF and Flask HF cases are shown in Figure 5.9. The month-to-month differences between the two cases are small, although larger than the negligible differences in their annual average values (Table 5.3). Both cases show annually optimized emissions of 23-24 and 12 Tg yr⁻¹ for Bogs East and West, respectively. Figure 5.11 compares the interannual variability of these two processes in expanded form. Note that the LF and HF case anomalies are relatively similar for most months. However, the Flask LF anomaly is greater than Flask HF by nearly 40 Tg yr⁻¹ for Bogs East in mid-1998. Conversely, the Flask HF anomaly is greater than Flask LF by about 10 Tg yr⁻¹ for Bogs West during this time. Using different model sampling strategies to compute flask monthly means can thus lead to significant monthly flux differences. The processes with strong sensitivities to the flask measurement sites, such as Bogs East and West, are most susceptible to producing these inversion differences. In contrast, the Flask LF and HF inversions produce similar results for processes that produce only weak signals at flask sites, such as Biomass Burning.

Figure 5.10 compares the Flask LF case and the Flask LF All case, showing the effect when the additional 33 flask stations are utilized. The shipboard measurements across the Pacific and the South China sea account for most of the additional observations (see Figure 5.4). BB America and BB Asia emission estimates are sensitive to these respective shipboard observations. The new flask site in Namibia (nmb[83]) further constrains BB Africa. The addition of the new flask measurements increases the deduced interannual variability (IAV) for biomass burning emissions. Most of the changes are in the form of increased peak heights in the Flask LF All case compared to the Flask LF case (especially for BB Africa). The additional stations thus enhance the estimated month-to-month structure, more than changing the timing of peak events. This suggests that although the smaller network can capture the general characteristics of the IAV, sites more sensitive to emissions from certain regions are needed to capture the full magnitude of actual changes in these emissions. This argues for more long-term measuring sites directly downwind of these tropical regions. Note that the additional measurements do not significantly change the Wetland and Rice processes, since these processes are relatively well constrained by the 54 sites in the Flask LF case. The total emissions are nearly the same between the LF and LF All cases. We have also compared the Flask LF All and Flask HF All cases, which again compares the effects of the different MATCH flask sampling strategies. The differences between the two cases are similar in magnitude to those in Figure 5.9.

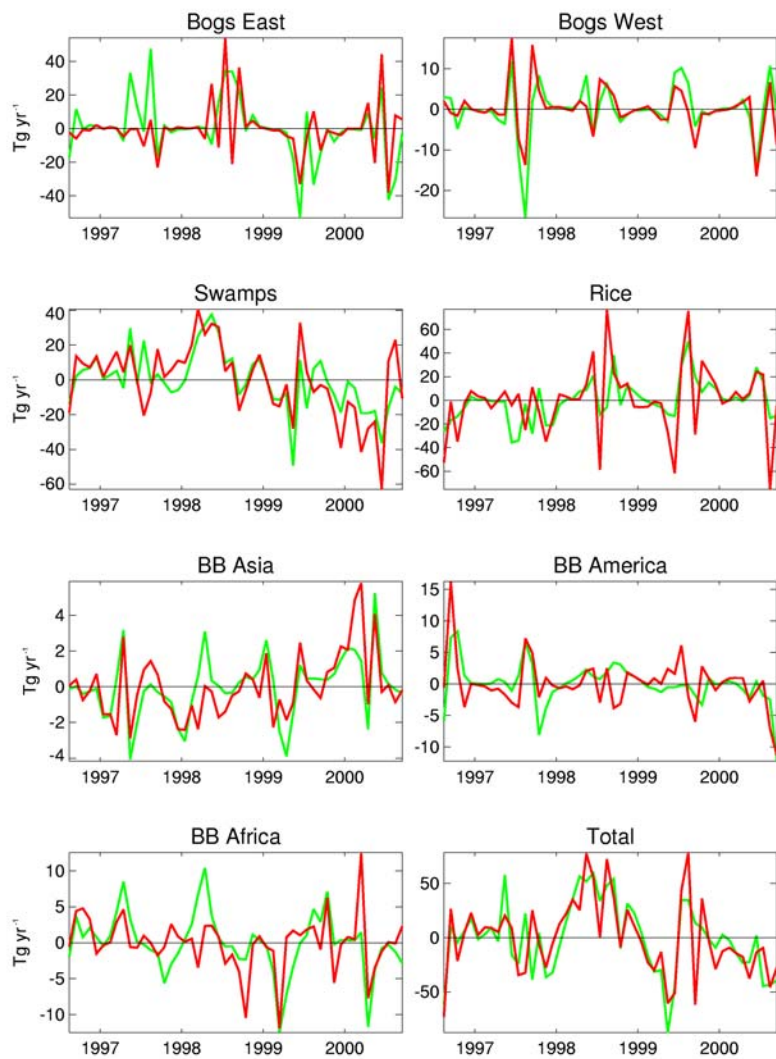


Figure 5.7 Monthly Mean Anomalies (from the 5 year mean value) for Flask LF (Red) and In-situ only (Green). Note the different scales for different processes.

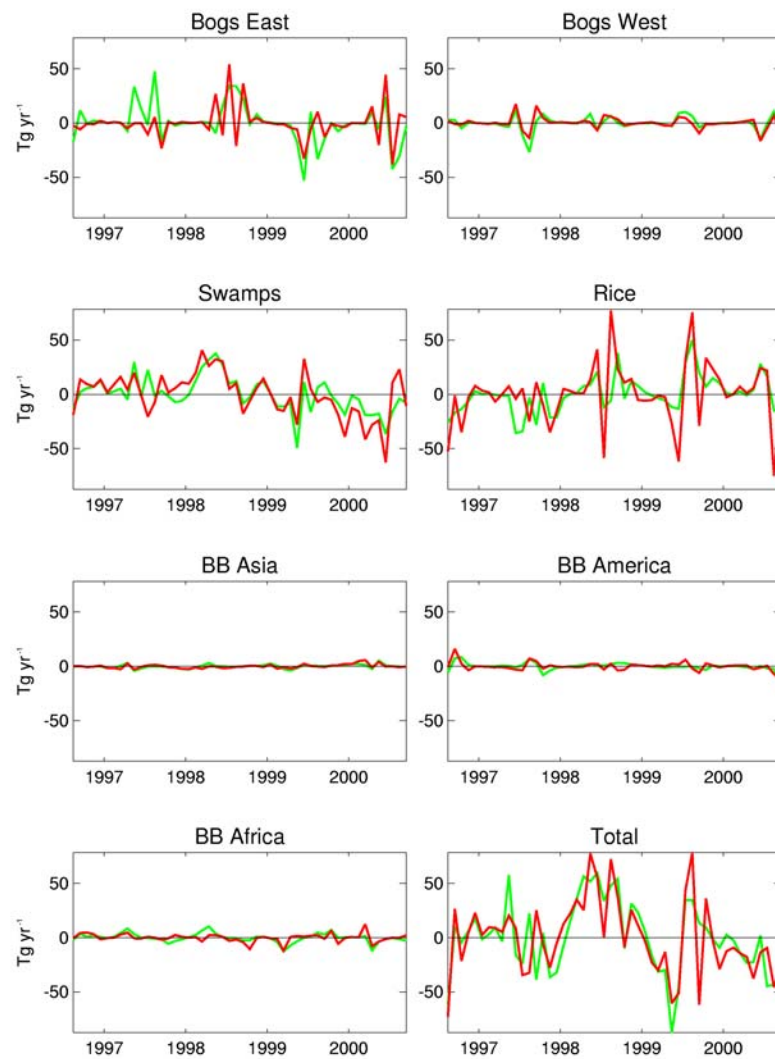


Figure 5.8. Same as Figure 5.7, but with the same vertical range for all processes to emphasize contributions to the total change.

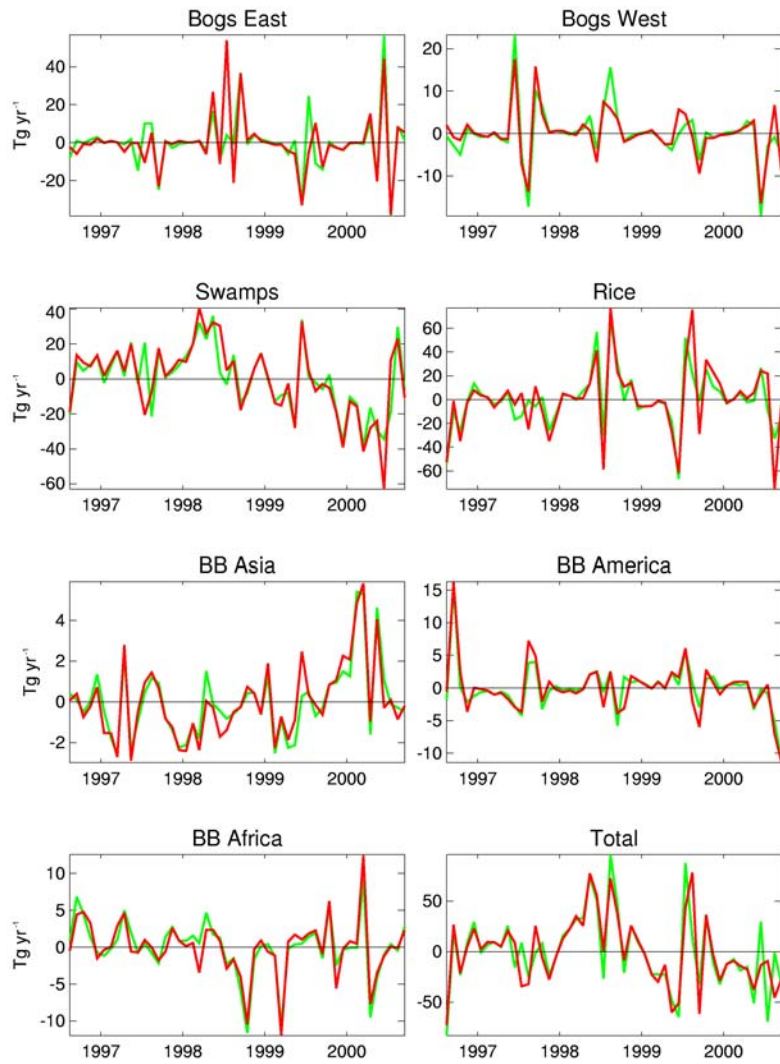


Figure 5.9 Flask LF vs. Flask HF interannual results. This plot shows the effect of using different flask sampling strategies in the model. The differences for Bogs East and Bogs West are shown in expanded form in Figure 5.11.

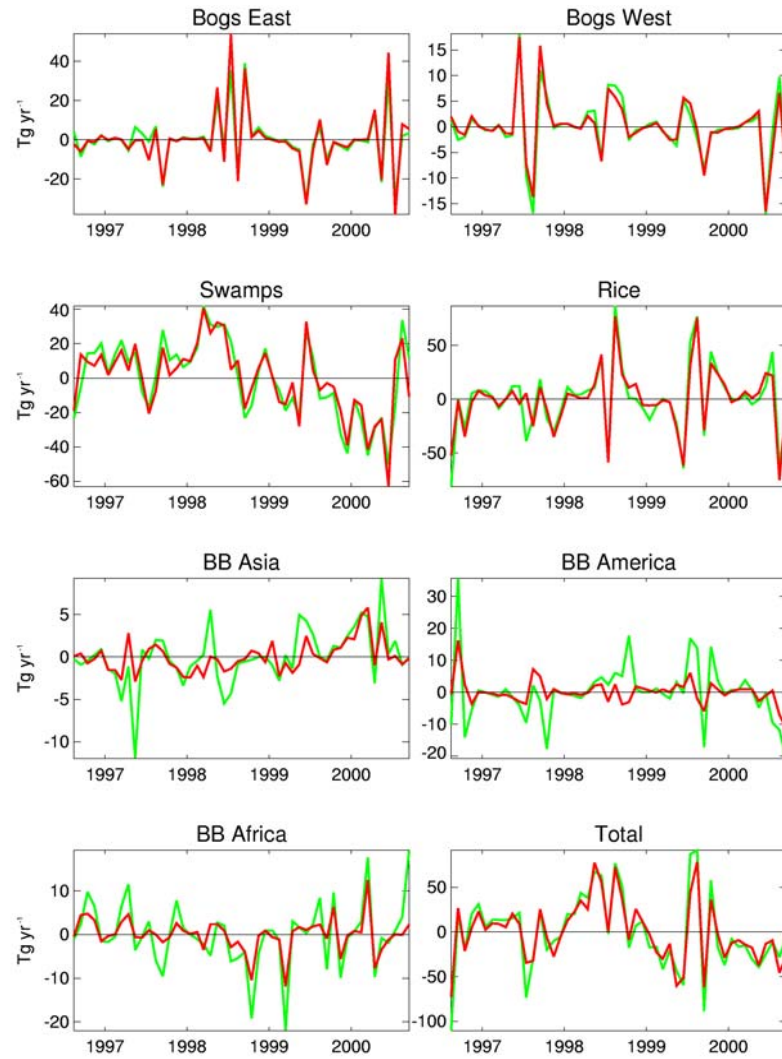


Figure 5.10. Flask LF vs. Flask LF All. This plot shows the effect of using the extended flask stations.

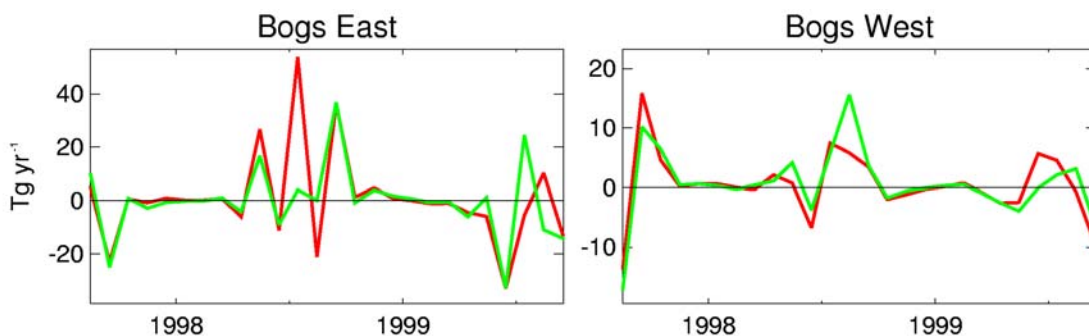


Figure 5.11. Flask LF (red) vs. Flask HF (green) interannual variability inversions for Bogs East and West (expanded from Figure 5.10). Note the differences in mid-1998 between the different inversions.

Table 5.4 to Table 5.6 contain the flux anomalies averaged for each year for the In-situ only, Flask LF, and Flask LF All inversion cases. The flux results from 2001 are not shown as the inversion does not fully optimize these months (see Section 4.3). Total emission changes fluctuate between ± 30 Tg yr⁻¹. This compares well with estimates by *Cunnold et al. (2002)*, who used a semi-inverse method to compute global annual changes of up to ± 37 Tg yr⁻¹. Our combined wetland values fluctuate up to ± 20 Tg yr⁻¹. *Walter et al. (2001b)* used a wetland process model based on changes in precipitation and temperature to also estimate annual changes of approximately ± 20 Tg yr⁻¹. Using the difference between Alert and Fraserdale mole fractions between 1990-1998, *Worthy et al. (2000)* estimated a variability in the Hudson Bay Lowland (HBL) wetland emissions of 0.23 to 0.5 Tg yr⁻¹. Assuming the HBL represents about 10 % of northern hemispheric wetlands (*Worthy et al. (2000)*), this corresponds to a range of 2.3 to 5.0 Tg yr⁻¹ for Northern wetlands, which is somewhat smaller than our ± 7 Tg yr⁻¹ range for Bogs East + Bogs West. There have been fewer studies on the interannual variability in rice emissions. However, rice emissions can be expected to vary similarly to wetlands emissions, as both are influenced by climatic conditions (although the rice flooding stage is managed). *Sass et al. (2002)* measured emissions at a single site in the U.S over nine years and observed a year-to-year flux variability of approximately $\pm 50\%$ of the annual mean over the entire period. Biomass burning is also known to fluctuate significantly from year to year (*Duncan et al. (2003)*). Some of the fluctuation may be underestimated due to the lack of proximate observing sites. Note that Figure 5.7 does not suggest a trend in the total seasonal methane emissions. There may, however, be weak trends for individual regions such as Swamps and BB Asia, although the flux time-series is short for definitive analysis.

Table 5.4 In-situ only annual anomalies (Tg yr⁻¹)

Region	1996	1997	1998	1999	2000
Bogs East	-0.22	5.67	8.87	-10.18	-4.14
Bogs West	0.11	-1.72	0.73	1.2	-0.31
Swamps	1.15	3.39	13.87	-7.9	-10.5
Rice	-4.98	-11.24	6.04	8.22	1.95
BB Asia	-0.07	-0.83	0.14	0.02	0.75
BB America	0.94	-0.15	1.41	-0.65	-1.54
BB Africa	0.44	0.34	1.71	-0.95	-1.53
Wetland Total	1.04	7.34	23.47	-16.89	-14.96
BB Total	1.31	-0.65	3.25	-1.58	-2.33
Total	-2.63	-4.55	32.76	-10.25	-15.34

Table 5.5. Flask LF annual anomalies (Tg yr⁻¹)

Region	1996	1997	1998	1999	2000
Bogs East	-0.67	-2.67	7.23	-5.11	1.22
Bogs West	0.14	1.18	0.8	-0.62	-1.5
Swamps	2.08	4.95	14.27	-7.83	-13.47
Rice	-6.96	-5.54	10.51	3.75	-1.77
BB Asia	0.02	-0.64	-0.78	0.19	1.22
BB America	1.2	0.01	-0.17	0.51	-1.56
BB Africa	0.87	0.66	-1.3	-0.54	0.3
Wetland Total	1.54	3.47	22.3	-13.56	-13.76
BB Total	2.09	0.03	-2.24	0.16	-0.04
Total	-3.33	-2.03	30.57	-9.65	-15.5

Table 5.6. Flask LF ALL annual anomalies (Tg yr⁻¹)

Region	1996	1997	1998	1999	2000
Bogs East	-0.44	-1.1	6.66	-4.78	-0.33
Bogs West	-0.12	0.37	1.55	-0.87	-0.93
Swamps	1.7	8.07	13.8	-10.63	-12.94
Rice	-7.86	-6.06	10.72	5.11	-1.91
BB Asia	-0.04	-1.85	-0.79	0.95	1.74
BB America	0.53	-2.83	3.06	2.68	-3.43
BB Africa	1.32	0.69	-3.46	-1.3	2.75
Wetland Total	1.14	7.33	22.01	-16.28	-14.2
BB Total	1.81	-3.99	-1.2	2.32	1.05
Total	-4.91	-2.72	31.52	-8.84	-15.06

5.4.1 Global Methane Increase in 1998

The strong ENSO event during 1998 influenced climate on a global scale. It was at least partly responsible for the observed strong global anomalies in temperature, precipitation, and biomass burning. These changes likely contributed to the dramatic increase of global CH₄ mole fractions during this time (*Dlugokencky et al. (2001)*). Figure 5.12 shows the observed (black) mole fractions compared to MATCH runs using reference (blue) and optimized (red) emissions at Samoa. The large increase during 1998 is evident in the observations, especially compared to the reference which uses constant annual-average emissions. Figure 5.8 shows the monthly interannual methane flux anomalies as contributions to the total flux. Note the gradual total increase in 1998 followed by a steep decline during early 1999. Table 5.5 lists the optimized CH₄ anomalies between 1996 and 2000 for Flask LF, and indicates a total anomaly of 30 Tg yr⁻¹ during 1998. This total falls in the middle of the reported anomalies of 24 Tg yr⁻¹ and 37 Tg yr⁻¹ estimated by *Dlugokencky et al. (2001)* and *Cunnold et al. (2002)*, respectively. Their estimates are based on hemispherically averaged mole fractions. Our inversion further indicates that the dominant increases are from Wetlands (22-23 Tg yr⁻¹ total) and Rice (6-11 Tg yr⁻¹). The Wetland emissions can be further subdivided into emissions of 7.2, 0.8, 14.3 Tg yr⁻¹ from Bogs East, Bogs West, and Swamps, respectively.

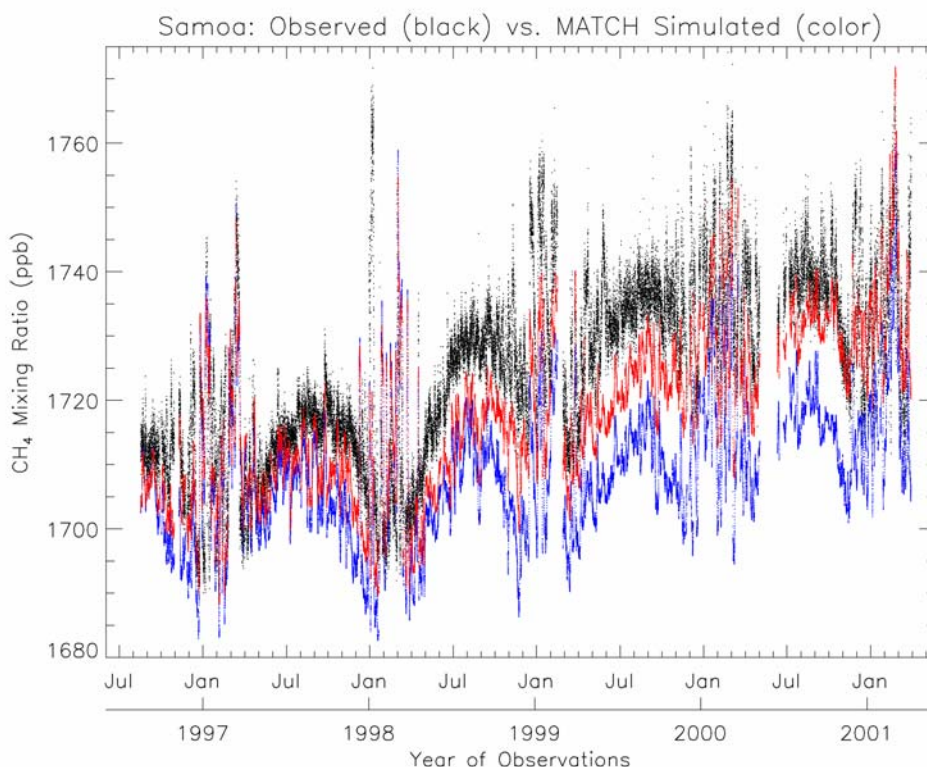


Figure 5.12. Observed high-frequency mole fractions (Black), and MATCH runs with reference (Blue) and optimized (Red) emissions at Samoa. Note the anomalously large observed increase in 1998. The optimized emission curve captures most, but not all, of the 1998 increase.

Global annual mean temperatures are considered to be highest for 1998 since the advent of reliable, direct measurements (NOAA (1999)). Average surface temperature anomalies of approximately +1° C occurred over the northern and tropical land masses. In general, increased soil temperatures will enhance methanogenic activity, leading to increased CH₄ production and emission. Anoxic environments are also necessary for methanogens to survive; increased precipitation generally increase anoxia in soils. Our inversely estimated emission anomalies are also consistent with increased methane flux from wetlands. Rice emissions also show an increase in 1998 in our inversions; this result is not surprising because both natural and rice processes will have similar sensitivities to temperature and precipitation.

How do our results compare to previous bottom-up estimates? *Dlugokencky et al.* (2001) used the wetland CH₄ emission model of *Walter et al.* (2001a) to estimate 1998 flux anomalies. The model was driven by NCEP soil-temperature and precipitation data from 1980 to 1999. The spatial distribution of the wetland model was further subdivided into northern and tropical wetlands based on the *Matthews et al.* (1987) distribution, and is therefore spatially similar to our Bogs East + Bogs West and Swamps distributions. In terms of sensitivity to climate, modeled methane fluxes increased by approximately 20% for a 1° C temperature increase, and 8% for a 20% precipitation increase. The modeled 1998 emission anomalies for northern and tropical wetlands were +12 and +13 Tg yr⁻¹, respectively, compared to the 1980-1999 average. These values correlate well with our values of +9 and +14 Tg yr⁻¹, although our results indicate that Bogs East emissions dominate over Bogs West for the northern component. We could not find any literature estimates for global rice emission anomalies, preventing corroboration of our inverted value.

Biomass burning is also known to have increased in certain areas during 1998. Based on AVHRR data, *Kasischke et al.* (2002) estimated 2.9 – 4.7 Tg methane release from boreal fires in a small area of Eastern Siberia between July and September 1998, due to unusually warm and dry conditions. Since we do not explicitly solve for boreal fires, the inversion would likely attribute this increase to enhanced emissions of Bogs East. This possibly contributes to the dominance of Bogs East over Bogs West anomalies for 1998. Southeast Asia also experienced ENSO related biomass burning between August 1997 and April 1998. *Levine* (1999) estimated anomalous Indonesian biomass burning emissions of 1.9 Tg yr⁻¹ during the late fall of 1997. The 1998 average value in Table 5.5 does not indicate greater emission from BB Asia, possibly because the increase is only for specific months. Figure 5.10 indicates enhanced BB Asia emissions during late 1997 and early 1998 using Flask LF All, while the smaller Flask LF network shows an increase only in late 1997. Using remote sensing, *Duncan et al.* (2003) also show weak and strong emissions during the spring of 1997 and 1999, respectively, near India. The Flask LF All results are consistent with this finding, with strong negative and positive peaks during these time periods. The above results suggest that the extra 33 sites in Flask LF All are needed to capture changes in biomass burning emissions. Unfortunately, many of these stations, such as the ship-tracks in the South China Sea and in the Pacific are no longer active. The closest high-frequency site, Hateruma, does not indicate an obvious methane enhancement during the Southeast Asian/Indonesian fires of August - December 1997, perhaps due to the large downwind distance. Central America also experienced large amounts of burning between April and June 1998 due to an ENSO related drought (*Duncan et al.* (2003)). The exact timing of this event is not captured by the inversion, again possibly due to the distance from observing sites. The Flask LF All inversion does show an overall increase in BB America during 1998 (and 1999) compared to 1997, consistent with *Duncan et al.* (2003). No positive anomalies are recorded

from either bottom-up or our top-down inversions for BB Africa, which was less affected by the 1998 ENSO compared to Asia and America.

Figure 5.12 shows the MATCH mole fractions at Samoa using reference and optimized emissions. The optimized run only compensates for about half the difference between the reference run and observations. Given the remote location of Samoa to strongly emitting regions, it is unlikely that any of the emissions (including aseasonal processes) can compensate for this difference without first adversely influencing more sensitive stations. The Samoan mismatch suggests that decreased OH concentrations may also have contributed to the increased 1998 methane growth rate. *Prinn et al.* (2001) deduced anomalously low OH levels in 1997 and 1998 from inversion of CH_3CCl_3 measurements. The driver for reduced OH concentration may be increased cloudiness (consistent with increased precipitation) which would reduce the amount of sunlight necessary for OH production. This effect would be pronounced for tropical regions where OH concentrations dominate CH_4 loss, such as Samoa. *Novelli et al.* (2003) linked the strong 1997-1998 increases in wildfires and globally observed CO mole fractions; they further calculated significant decreases in global OH due to the large CO increase. Finally, the small feedback between CH_4 and OH may also have led to small decreases in OH, due to increases in CH_4 itself. The full estimation of the CO- CH_4 -OH feedback and climatologically induced OH changes would require a full chemical mechanism within MATCH. This is beyond the scope of this study.

5.4.2 Model Errors

The interannual results are generally susceptible to different model errors than those that affect the annual average results. Errors in the interhemispheric exchange rate and the OH magnitude will bias the average modeled atmospheric CH_4 distribution, and consequently, the deduced annually averaged emissions. The interannual emissions results, in contrast, depend less on average CH_4 distributions and more on observed and simulated monthly mole fraction anomalies. The deduced interannual emission values would thus be less affected by these potential model biases. Interannual flux values are, however, more susceptible to errors from unmodeled short term changes in the spatial flux patterns. For example, the inversion could not identify the boreal fires in Siberia during July – September 1998 because this pattern was not explicitly modeled. Instead, the inversion likely attributed this increase to Bogs East emissions. The individual seasonal patterns are also assumed to hold for approximately a month's duration over large regions. This assumption of spatial correlation becomes less true for very short time-periods, i.e. it is unlikely that the entire Bogs East pattern varies uniformly over the course of a day. This assumption of spatial correlation likely sets at least one of the limits for solving for progressively shorter time-periods. A solution is to use even smaller process-regions, but the number of available measurements and the computational burden make such an approach currently impractical at the global scale. A possible solution is to use a mesoscale model for regions sampled by nearby high-frequency observations.

The constancy of aseasonal emissions is another inversion simplification. Although bottom-up studies indicate that the climate-driven seasonal processes considered here dominate the interannual variability, Animals/Waste and Energy emissions can also change year to year. Large fluctuations in these processes have not been reported over our 1996-2001 time period. Possible changes should, however, be modeled for inversions of longer time-periods. It has been hypothesized that reductions in gas and coal

emissions led to the global decline of the CH₄ growth rate in the early 1990's *Dlugokencky et al. (1994b)*, *Law et al. (1996a)*). For this time period, an assumed trend should perhaps be used in the reference run. We added aseasonal trends of +1 Tg yr⁻¹ to each of our aseasonal processes over the inversion period as a sensitivity test, but found little impact from these small changes. We also modified the inversion to solve for linear aseasonal emission trends in addition to their constant values. It was found that the inversion could not adequately constrain small trends, because the trend sensitivities to the global measuring network were small and not sufficiently distinct.

The final potential model error involves possible interannual changes in OH, as discussed for the 1998 observed CH₄ mole fraction increase. Using methyl chloroform data, *Prinn et al. (2001)* determined an increase followed by a decrease in the global average OH field between the 1980's to 1990's. Estimates from Jin Huang (per. comm.) indicate interannual changes in global OH as large as 10%. These changes will likely have impacts on the inversion. A possible strategy to incorporate these changes involves first optimizing global OH interannual variability using methyl chloroform, which unlike CH₄ has well known emissions and is too scarce to affect OH concentrations. An optimized interannual OH field should then be used to drive the MATCH reference run and calculations of sensitivities.

5.5 Summary and Conclusions

We solved for annual, seasonal, and interannual methane fluxes using the Kalman Filter as described in Chapter 4. In addition, several sensitivity tests were conducted which tested the effect of using different observational networks and modeled flask data. The main conclusions are as follows:

Inversion Results

- The annual average values show a reduction in northern hemispheric emissions and increase in tropical and southern hemispheric emissions compared to the reference.
- The inversion leads to significant uncertainty reduction for northern wetlands, moderate reduction for rice, and small reduction for the tropical biomass burning and swamp processes.
- The deduced seasonal maximum in emissions is shifted to June from the July reference, and is more intense. This result is dominated by deduced phase changes and increases from rice emitting regions relative to the reference.
- Global wetlands dominate the 1998 CH₄ increase, consistent with a bottom-up study using a wetland processes model (*Dlugokencky et al. (2001)*).
- The inverted methane flux increases for 1998 cannot fully reproduce the CH₄ growth rate at Samoa, suggesting that a decreased OH sink may also have contributed to the observed increase.

Sensitivity Results

- High-frequency observations lead to most of the emission uncertainty reduction for the Wetland and Rice processes. Flask observations offer additional constraints for tropical emissions.
- Low and high-frequency MATCH model sampling strategies to compute flask monthly means lead to similar annual average inversion results; however, significant differences for interannual (monthly) fluxes are observed for processes for which flask data provide significant constraints.

Most of the inverted emission values fall within the range of previous bottom-up estimates. The inverted emissions for wetlands compare well with other recent estimates. Inverted energy emission are on the low side of prior estimates, but are consistent with expected recent decreases in methane emissions. The inversion yields rice emissions nearly twice the current bottom-up estimates. Part of the difference may be that the inversion solves for emissions from the entire rice emitting region, and includes those wetland emissions not formally associated with rice cultivation but still produced by similar biogenic processes. More comprehensive measurements of these overlapping emissions, in addition to those strictly associated with growing rice, would help to constrain total fluxes from these regions.

The most difficult processes to constrain are the tropical biomass burning regions, although using the extended flask network produces results consistent with interannual bottom-up studies. More sites would be needed to better constrain these BB emissions. This leads to the following question: Where should new sites be located? The inversion methodology in Chapter 4 can also be adapted for the determination of the optimal placement of future observing sites, also known as network design. Such studies have been conducted for CO₂ (*Patra et al. (2002)*, *Gloor et al. (2000)*). The determination of new, optimal observing sites depends heavily on not only the species of interest, but also the model to be used for the inversion. In general, the higher the resolution and the greater the accuracy of transport in the model, the better the chance of successfully reproducing mole fraction observations at sites situated directly within emitting regions. The most sensitive sites are often the most difficult to model, due to the influence of sub-grid scale effects. The network design algorithm should strike a balance between process/region sensitivity and model error when selecting an optimal site. An inversion algorithm similar to that used here could be used in principle to determine uncertainty reductions, and hence usefulness, associated with new observing sites.

Chapter 6

Annual Mean Carbon Dioxide Inversions

This chapter describes annual mean carbon dioxide inversions which were conducted as part of the Transcom 3 Level 1 modeling intercomparison (*Gurney et al. (2002)*, *Gurney et al. (2003)*). A total of 15 atmospheric transport models were used in this experiment. We contributed model simulations using MATCH driven by 1990 NCEP meteorology. A consistent set of CO₂ surface flux fields were provided to all modeling groups. The intercomparison used a standard batch inverse technique to combine model simulations and observations to optimize CO₂ fluxes from 22 global regions. The Level 1 experiment focused on inter-model inversion differences rather than on performing a comprehensive CO₂ inversion. Consequently, we emphasize here the comparison between MATCH results and the other inversion models, rather than perform a detailed comparison of MATCH fluxes to bottom-up estimates. The first section describes the inversion methodology. The second section describes the inversion differences between MATCH and the model mean, and attributes the main differences to certain model and transport characteristics. We also compare our MATCH transport to a similar version of MATCH driven by climate model meteorology (as opposed to NCEP meteorology). The final section includes inversion sensitivity results using our MATCH simulations.

6.1 Control Inversion

Gurney et al. (2002) describe the main scientific results of the Transcom 3 experiment. A more detailed account of the intercomparison, including a description of all participating models can be found in *Gurney et al. (2003)*. In the 2003 paper, our model is described as MATCH.NCEP; we refer to MATCH.NCEP as MATCH, unless making a comparison to another version of MATCH. In the following we review the inversion inputs and methodology, emphasizing those aspects important for later interpretation of the differences between MATCH and the other models. The sensitivity tests in Section 6.3 will also refer to the control inversion parameters.

6.1.1 Observations

The locations of the 76 observational sites used in the Transcom 3 experiment are shown in Figure 6.1 and listed in Appendix B. These observations are taken from the *GlobalView-CO2 (2000)* dataset, which are based on weekly flask measurements. At each site, 5 years of data between 1992 and 1996 were averaged into a single value. Although CO₂ was collected at more than 76 sites between 1992 and 1996, only those sites that sampled for at least 70% of the weeks between 1992-1996 were used. The *GlobalView-CO2 (2000)* dataset contains interpolated and extrapolated values based on the values of nearby active sites. These values were used to “fill” any missing data in order to provide a complete 5

year average. Most observing sites are at fixed locations on islands and continents. A few flasks are also taken on moving platforms such as ships (green) and aircraft (blue), with the latter platform used for vertical profiles.

The different box sizes in Figure 6.1 correspond to the inverse of the standard deviation of the annually averaged observations, which are listed in Appendix B. These standard deviations are related to the monthly CO₂ standard deviations at each site, as described in *GlobalView-CO2* (2000). Those sites in the remote marine atmosphere which have low CO₂ variability have smaller errors. The larger errors (i.e. smaller boxes) occur in the middle of continental regions where the CO₂ observations are highly variable. The larger the box, the greater the weighting in the inversion (although the inversion formally uses variances, i.e. σ^2).

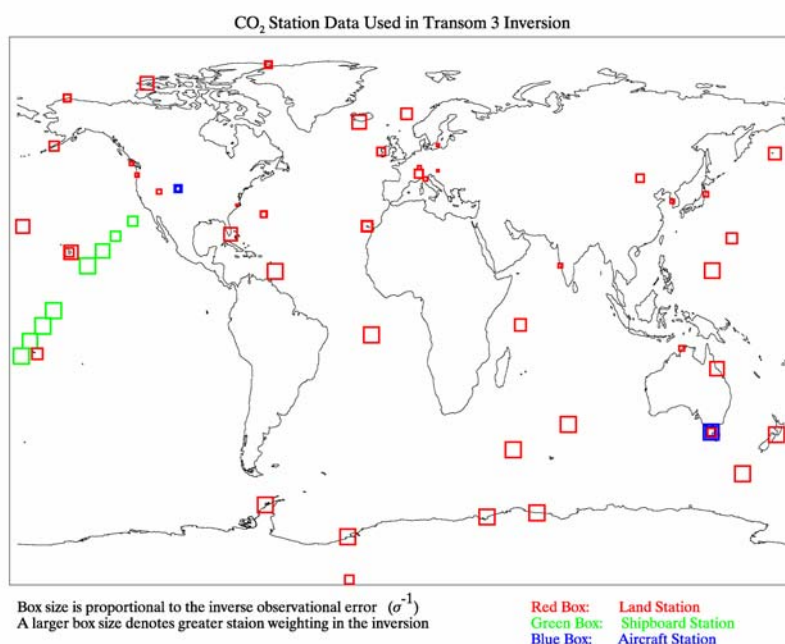


Figure 6.1. CO₂ flask observing sites used for the Transcom 3 experiment. The box sizes are proportional to the inverse of the observational standard deviation used in the inversion.

6.1.2 Transcom 3 Protocol and Surface Flux Description

In the following we describe the Transcom 3 Protocol (Level 1), which required the forward simulations of many tracers. Surface flux maps at 0.5° x 0.5° resolution representing different components of the carbon cycle were provided to all modeling groups. These fluxes were then interpolated by each group onto their respective model grids, followed by land/ocean redistribution as described in Chapter 2. The provided surface fields fall into two broad categories. The first category includes four CO₂ surface flux fields based on bottom-up studies: 1990 and 1995 fossil fuel emissions (FF95 and FF90), neutral exchange with the terrestrial biosphere (BIO), and oceanic uptake (OCN). The fossil fuel distributions are similar, and we denote them as FF hereafter. These “background”, which are not optimized in the inversion, are shown at T42 resolution in Figure 6.2. The second group of fluxes,

shown in Figure 6.4, represent 22 unknown (“basis”) regions that are optimized in the inversion. The Transcom 3 Protocol required forward simulations of all surface fluxes (26 tracers total) for four years. The average CO₂ mole fractions for the fourth year of simulation at the 76 observing sites are used in the inversion.

Although the background fluxes are not optimized, they have a large influence on the inversion results. The flux for FF is concentrated around the industrial and urban areas of the developed world in the northern hemisphere (Figure 6.2). Much of this data comes from economic data and is relatively well constrained in both magnitude (~6 Gt C yr⁻¹) and spatial distribution (*van Aardenne et al. (2001)*). A time-invariant geographical flux pattern is assumed for the FF emission. In the inversion, the FF90 and FF95 fossil fuel simulations are combined as a linearly weighted mean for comparison to observations averaged between 1992-1996. The BIO flux represents terrestrial CO₂ exchange due to photosynthesis and respiration (*Randerson et al. (1997)*), and is shown for the months of January and July in Figure 6.2. The BIO flux differs from FF flux in two important respects: (1) the BIO flux distribution varies by month, while FF is constant, and (2) the total annual flux of BIO is zero, whereas FF is 6 Gt C yr⁻¹. Although the total annual flux of BIO is zero and does not change the total atmospheric burden of CO₂, it nevertheless creates atmospheric CO₂ gradients. This is due to a covariance between the timing of emissions and transport, described in *Denning et al. (1995)* as the “rectifier effect”. During the boreal summer, the flux of CO₂ is negative due to net photosynthesis of plants (Figure 6.2 bottom-right), while in the winter the flux is positive due to net respiration of plants (Figure 6.2 bottom-left). The atmospheric boundary layer during the summer and winter will be deep and shallow, respectively, due to thermally driven turbulence. Over an annual cycle, this leads to positive perturbations to CO₂ surface mixing ratios over the large boreal regions in the Northern Hemisphere. The third background flux (OCN) represents estimates of oceanic CO₂ uptake based on pCO₂ measurements in air and water, air-sea CO₂ flux wind-dependent parameterizations, and analyzed observed wind speeds (*Takahashi et al. (2002)*). The ocean gyres and the Southern Ocean dominate the ocean uptake. The equatorial regions have a net efflux of CO₂ to the atmosphere. The OCN regions also vary by month, although the seasonal variation is much less than BIO. The OCN net total uptake is -2.2 Gt C yr⁻¹.

The surface interhemispheric gradient (IHG) for FF and BIO are shown in Figure 6.3 for all 15 models in the Transcom 3 intercomparison. These results were obtained by running the emissions fields for 4 years from a uniform initialization of 350 ppm CO₂. The values represent the latitudinal averages for the fourth year of simulation. Note that a 4-year spin up time is sufficient to create a pseudo-steady state where mole fraction gradients, such as the IHG, remain constant with a slowly increasing global (background) average. Both FF and BIO have greater tracer concentrations in the northern hemisphere, due to their terrestrial source locations. The MATCH version used in this study labeled (MATCH.NCEP) are shown by the black dotted lines. Note that the individual forward runs cannot be directly compared to CO₂ observations, which represent contributions from all components of the carbon cycle. Here, we can only use these forward results to diagnose differences in model behavior.

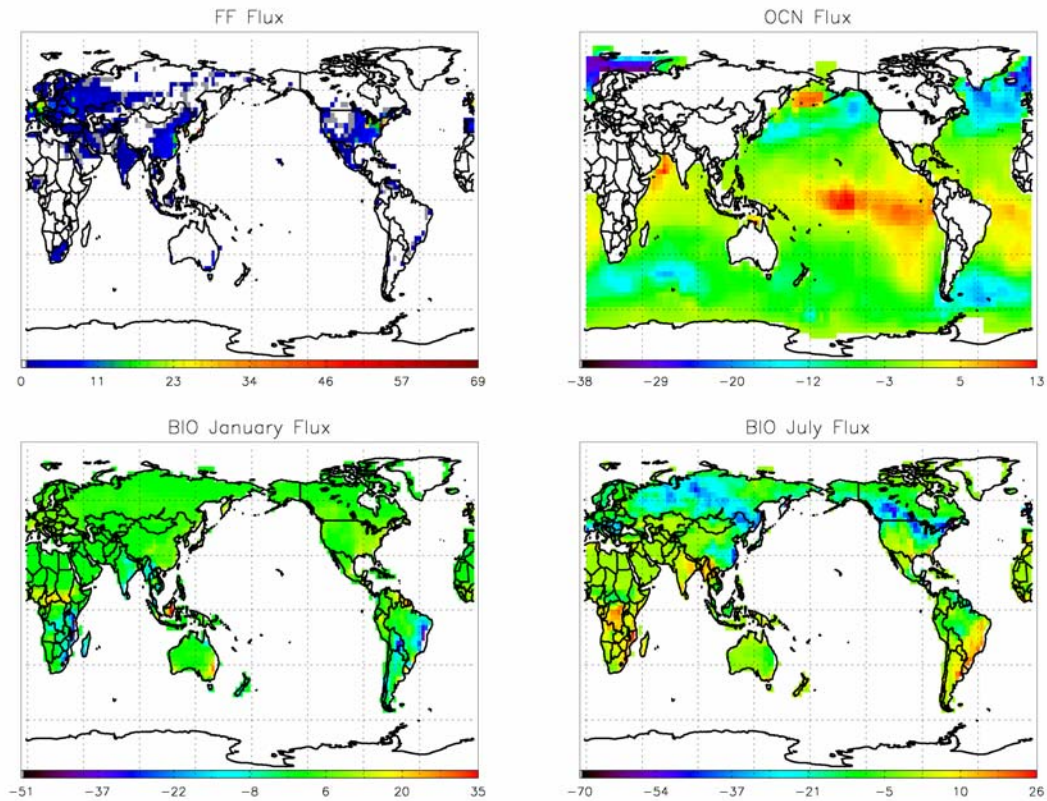


Figure 6.2. Background (prior) fluxes from the Transcom 3 Intercomparison. Upper left: Fossil-fuel (only FF95 shown, which is very similar to FF90) emissions. Upper right: Annually averaged ocean exchange (OCN). Bottom left and right: Neutral biospheric exchange for January and July, respectively. All fluxes in $10^{-9} \text{ kg C m}^{-2} \text{ s}^{-1}$.

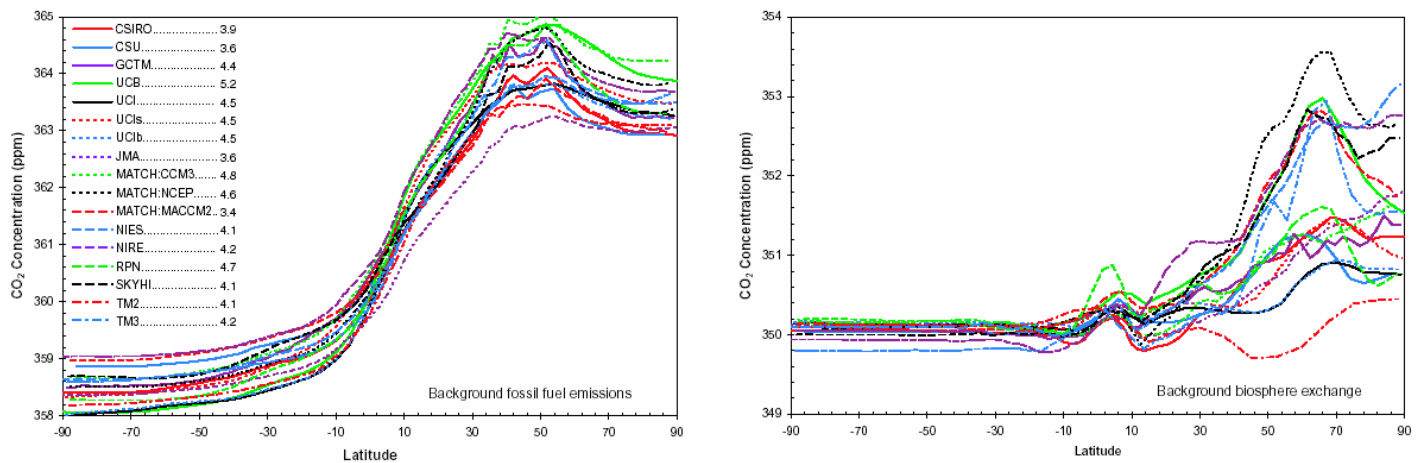


Figure 6.3. Fossil Fuel (left) and Neutral Biosphere (right) tracer responses for all models. MATCH-NCEP is shown by the black-dashed line. Taken from Gurney *et al.* (2003).

The FF interhemispheric gradient shows that most models follow a similar behavior, with a gradient of 4 - 5 ppm between the northern and southern hemispheres. In contrast, the BIO IHG shows much greater variability, with some models showing weak gradients (e.g. MATCH.CCM3) and some showing strong gradients (e.g. MATCH.NCEP). Why does the IHG vary so much for BIO but not for FF? The BIO flux distribution covers a much greater area than the more localized sources of FF (Figure 6.2). This makes the latitudinal surface average much more sensitive to differences in vertical resolution and boundary layer transport. The BIO IHG depends strongly on changes in the boundary layer mixing throughout the year due to its covariance with fluxes. Those models which have strong seasonal changes in PBL transport, i.e. weak mixing in boreal winter and strong mixing in boreal summer, will produce a strong BIO IHG. Note that, for each model, the inversion itself depends on the model CO₂ at those specific grid points that coincide with observing sites. These IHG give a sense of the bulk transport differences, but do not automatically translate into inversion differences. For example, there are significant differences between the MATCH.NCEP and 15-model mean FF values at specific observational sites which do not contribute to the IHG differences in Figure 6.3.

The greater interhemispheric gradient of MATCH.NCEP for BIO can be partially attributed to its greater vertical resolution at the surface (i.e., lower surface layer height) compared to the other models. MATCH has a relatively shallow surface layer of 50-75 meters. Only 2 out of 15 model have more vertical levels than MATCH. Given the same positive surface flux, surface mole fractions in MATCH will tend to be higher compared to models with a higher surface layer, due to a smaller mixing volume. Note that MATCH.NCEP (black dotted line) also has a much stronger BIO IHG than MATCH.CCM3 (green dotted line), which is a similar version of MATCH using CCM3 meteorology (contributed by a different group). This climatological meteorology has the same horizontal resolution (T42, 2.8° x 2.8°) but a coarser vertical resolution (18 levels) than the NCEP meteorology. In Section 6.2.1 we separate the effects of vertical resolution and driving meteorology for the MATCH.NCEP and MATCH.CCM3 simulations. The MATCH.MACCM2 represents a third realization of MATCH (submitted by yet another group). This particular version of MATCH uses different schemes for advection and physics, and is therefore not as easily compared to MATCH.NCEP and MATCH.CCM3.

The 22 regions that are optimized by the inversion are shown in Figure 6.4. The terrestrial regions have additional geographic patterns of exchange (not shown) based on estimated net NPP distributions. Unproductive mountainous, desert, and polar grid regions do not exchange CO₂ with the atmosphere. The oceanic regions are "flat", i.e. there is no spatial structure within the ocean regions. This is in contrast to the OCN background flux, which does have structured oceanic CO₂ flux regions (e.g. upwelling and downwelling regions). In Section 6.3 we test the inversion using an alternate set of 11 oceanic regions with oceanic CO₂ flux structure. Each one of these basis regions is used to create a modeled sensitivity, with units of ppm (Gt C yr⁻¹)⁻¹, at the 76 observational sites. This is accomplished by emitting a constant flux of 1 Gt C yr⁻¹ from each region individually for four years and averaging the CO₂ mole fraction for the fourth year at each site. These sensitivities are used quantitatively by the inversion. Note that the regions do not have same shape as the background flux emissions. The results of the fourth year of simulation are averaged at each site to generate a 22 (region) x 76 (site) sensitivity matrix.

Transcom 3 Basis Regions

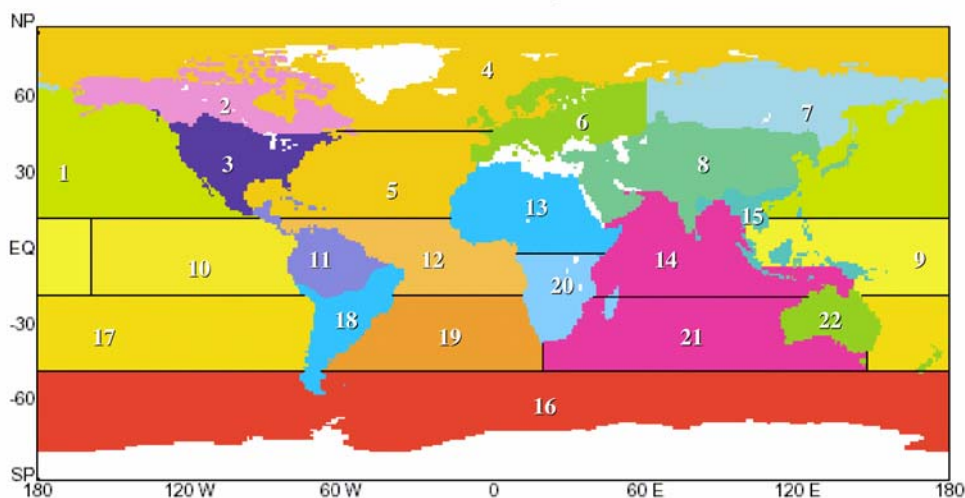


Figure 6.4. 11 Land and 11 Ocean regions optimized in the Transcom 3 intercomparison. The land regions have additional structure (not shown) representing the regions of strong carbon exchange based on NPP estimates. The ocean regions do not have much structure (flat pattern), other than ignoring areas of sea-ice.

6.1.3 Inversion Methodology

The following describes the methodology used in the inversion of the Transcom 3 Level 1 experiment. This inversion solves for annually averaged emissions between 1992-1996 and does not include a time-varying component. A batch method is used which combines all measurements and unknowns simultaneously to produce an optimized solution. This is in contrast to the Kalman Filter, which uses time-series data in a stepwise (recursive) fashion as described in Chapter 4. We start with the measurement equation, which relates real observations to modeled quantities.

$$y^o = \tilde{y} + H \cdot x + \varepsilon \quad (6.1)$$

y^o = vector of observed CO_2 mole fractions

\tilde{y} = vector of simulated CO_2 mole fractions using the background fluxes

H = sensitivity matrix

x = vector of unknown source/sink deviations from the background fluxes

ε = observational error

The measurement equation includes both actual and simulated observations, the latter derived from the background fluxes. The observation vector, y^o , includes the 76 annually averaged observations; the vector \tilde{y} represents the corresponding simulated observations using the background fluxes. The 22 unknown fluxes to be optimized are contained in the vector x . These can be considered as adjustments to

the background fluxes in order to obtain a better fit to the observations. If the background simulations matched the observations perfectly, then no adjustments would be needed, i.e. $x = 0$. The unknown flux strengths (x) are related to changes in simulated observations (y) through the 22×76 sensitivity matrix H . The elements in H are computed from forward runs using the 22 regions described in Section 6.1.2. The elements of the model measurement equation, Equation (6.2), which contain only simulated mole fractions are shown below in expanded form:

$$Hx + \tilde{y} = y^s \quad (6.2)$$

$$\begin{array}{c}
 \text{Modeled Sensitivities}(H) \\
 \left(\begin{array}{cccc}
 \frac{\partial y_1}{\partial x_1} & \dots & \frac{\partial y_1}{\partial x_{22}} & 1 \\
 \frac{\partial y_2}{\partial x_1} & \dots & \frac{\partial y_2}{\partial x_{22}} & 1 \\
 \dots & \dots & \dots & \dots \\
 \dots & \dots & \dots & \dots \\
 \frac{\partial y_{76}}{\partial x_1} & \dots & \frac{\partial y_{76}}{\partial x_{22}} & 1 \\
 1 & \dots & 1 & 0
 \end{array} \right) \cdot \begin{array}{c}
 \text{Unknowns}(x) \\
 \left(\begin{array}{c}
 x_1 \\
 \cdot \\
 \cdot \\
 \cdot \\
 x_{22} \\
 [CO_2]_{glob}
 \end{array} \right)
 \end{array} + \begin{array}{c}
 \text{Simulated observations from} \\
 \text{Background Fluxes}(\tilde{y}) \\
 \left(\begin{array}{c}
 \tilde{y}_1 \\
 \tilde{y}_2 \\
 \dots \\
 \dots \\
 \dots \\
 \tilde{y}_{76} \\
 0
 \end{array} \right) = \begin{array}{c}
 \text{Simulated} \\
 \text{Observations}(y^s) \\
 \left(\begin{array}{c}
 y_1^s \\
 y_2^s \\
 \dots \\
 \dots \\
 \dots \\
 y_{76}^s \\
 X_{tot}
 \end{array} \right)
 \end{array} \quad (6.3)
 \end{array}$$

where

$$X_{tot} = \sum_{j=1}^{N_{unknowns}} x_j \quad (6.4)$$

The extra element X_{tot} represents an additional constraint that is equal to the global total for all unknown fluxes. For the inversion, this corresponds to $-0.646 \text{ Gt C yr}^{-1}$, which represents the net surface uptake required to balance fossil fuel emissions ($6.12 \text{ Gt C yr}^{-1}$), atmospheric growth ($3.274 \text{ Gt C yr}^{-1}$), and the background ocean uptake ($-2.2 \text{ Gt C yr}^{-1}$). The inversion formally includes values for FF, BIO, and OCN in the H matrix; however, these emissions are not optimized and we have combined them into \tilde{y} for clarity. The last element of the x vector contains a global average mixing ratio $[CO_2]_{glob}$ which represents the global average concentration in the absence of sources and sinks. The inversion also solves for this value. The extra row of 1's in H forces the sum of all fluxes contained in the state vector x to equal the specified global total, X_{tot} . The extra column of 1's in H adds the mixing ratio offset, $[CO_2]_{glob}$, to the modeled CO_2 mixing ratios.

Generally we seek to minimize the difference between y^o and y^s , with additional prior knowledge of the unknown fluxes x , using a scalar cost function J . This is a Bayesian approach, meaning that prior information is used in the form of a prior guess of x , which includes a prior uncertainty range. The Bayesian Least-Squares cost function includes: (1) the difference between modeled and observed CO_2 , and (2) the difference between the initial and final values of x :

$$J = \frac{1}{2} \left[(y^o - y^s)^T R^{-1} (y^o - y^s) + (x - x^f)^T (P^f)^{-1} (x - x^f) \right] \quad (6.5)$$

where

x = fluxes to optimized

x^f = initial ("prior") flux values

R = observational error covariance matrix

P^f = initial ("prior") flux error covariance matrix

Minimization of J (i.e. taking the derivative of J with respect to x and setting the result to zero) yields the following equation for x :

$$x = x^f + \left(\frac{H^T R^{-1}}{H^T R^{-1} H + P^{f-1}} \right) (y^o - y^s) \quad (6.6)$$

In addition to the optimized values of x the final error is also computed. This takes the form:

$$P^a = \left(P^{f-1} + H^T R^{-1} H \right)^{-1} \quad (6.7)$$

Note that the final error is always smaller or equal to the initial error, P^f , as additional information from the observations reduce the initial error by amounts varying inversely with observational errors (variances) contained in R .

Figure 6.5 shows the modeled CO₂ mole fractions before and after the inversion using MATCH. The background fluxes (blue +'s) strongly overestimate the observations (black diamonds) in the Northern Hemisphere, although a net uptake of -0.646 Gt C yr⁻¹ is required to balance the budget. There also is some underestimation in the Southern Hemisphere. The inversion adjusts the 22 unknown flux regions by creating NH sinks and, to a lesser extent, SH sources. The partitioning between regions of similar latitude are more complicated and cannot easily be determined from Figure 6.5. The optimization yields flux adjustments which give a much better fit to the observations (red) than the initial background (blue).

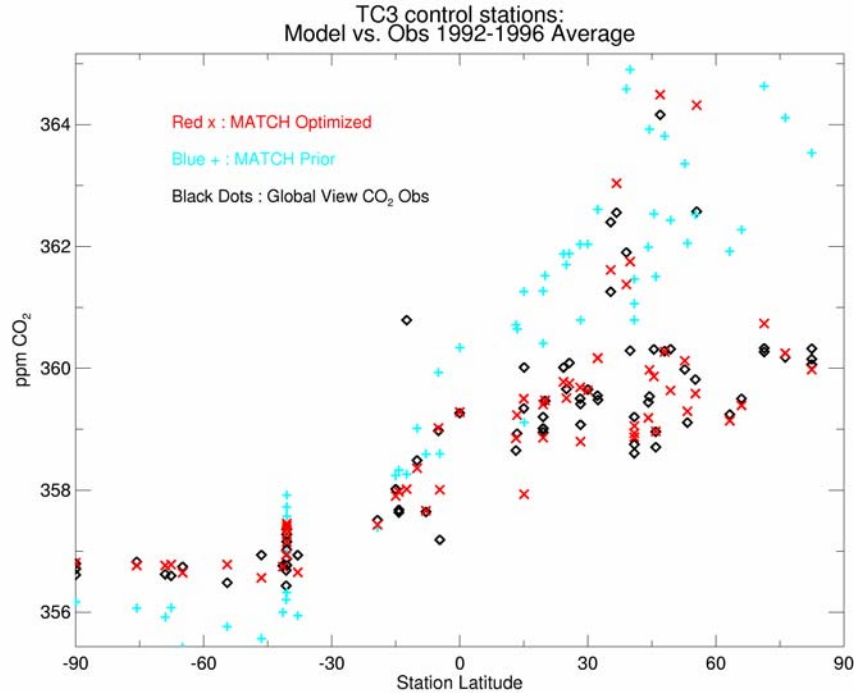


Figure 6.5. Observed (black diamonds), background or “prior” (blue +’s), and optimized (red x’s) CO₂ mole fractions from MATCH.

6.2 MATCH versus other model results

In this section we compare the MATCH.NCEP inversion results to the 15-model mean. The OCN background value totaling $-2.2 \text{ Gt C yr}^{-1}$ has been added to the appropriate oceanic sub-regions. With this additional sink, the sum of the 22 inverted regions equals a global uptake of $-2.78 \text{ Gt C yr}^{-1}$, or about 50% of the total annual fossil fuel input. Figure 6.6 shows the Transcom Level 1 inversion results for the 22 regions. These values are also listed in Appendix C. MATCH.NCEP results (red) are plotted alongside the model mean (black). The three main plots correspond to northern, tropical, and southern regions with land and ocean regions in green and blue, respectively. The vertical lines denote the final inversion error for MATCH.NCEP and the model average. The model average includes an additional error, shown as small squares, which represent the standard deviation across the 15 models. The large rectangles which surround the error bars correspond to the initial error for each region, i.e. the square root of the diagonal terms found in P^f . The horizontal bars in the middle of the rectangles are the prior values, x^f , which are mostly zero. Regions with smaller prior errors, such as the northern ocean regions, are considered to be relatively well-constrained by existing bottom-up estimates. Poorly constrained regions such as the tropical land regions are given large initial errors.

The final errors are always smaller than the initial errors. The amount of individual error reduction tells us how well the observations constrain the flux. Most land regions begin with an initial uncertainty larger than 1 Gt C yr^{-1} . The final uncertainty is reduced to less than 1 Gt C yr^{-1} uncertainty for most regions. In general, the northern land regions experience greater uncertainty reduction compared to the

southern and tropical land regions, due to the greater number of northern observations. The ocean regions, which start with much lower initial uncertainties, have less absolute uncertainty reduction. Note that the standard deviation of all 15 models (small squares about the model means) are generally lower than the model mean inversion uncertainty. A major conclusion from Transcom 3 is that the inversion uncertainty (primarily due to observational undersampling) is larger than the spread in the models.

For each individual region, the MATCH.NCEP inversion values lie within the model mean inversion uncertainty range. The sink for Temperate North America (which includes the United States) is $-0.77 \text{ Gt C yr}^{-1}$ for example, which is nearly indistinguishable from the model mean of $-0.83 \text{ Gt C yr}^{-1}$. The MATCH sink is about -0.2 to $-0.47 \text{ Gt C yr}^{-1}$ greater than the -0.3 to $-0.58 \text{ Gt C yr}^{-1}$ estimated by *Pacala et al.* (2001) for the U.S. using bottom-up techniques. Note that the Temperate North American region contains more area than the U.S, so the top-down and bottom-up estimates cannot be compared exactly. Relative to the model mean, the MATCH.NCEP result shows stronger uptake in Boreal Eurasia, as well as in South America and Southern Africa. Since the global total uptake is fixed, these larger land sinks are offset by larger ocean sources. In the northern hemisphere, this trade-off is evident in the stronger uptake in Boreal Eurasia and weaker sinks in the North Atlantic and Northern Oceans, as well as a positive efflux in the North Pacific. In the southern hemisphere, the very strong uptake in South America and Southern Africa are partially offset by more positive fluxes in the South Indian, South Pacific, and Southern Oceans. Globally, this leads to a stronger land and weaker ocean uptake by MATCH.NCEP compared to the 15-model mean.

The strong efflux by Tropical America and Tropical Africa, and strong influx by South America and Southern Africa suggest that these adjacent, poorly observed regions are not well resolved from each other. Figure 6.1 indicates that no observational sites are in these particular land regions. Consequently, the inversion has difficulty resolving their fluxes, leading to large positive and negative values for adjacent regions (also known as “dipoles”). The anti-correlation between these regions can be seen in their negative off-diagonal terms in the error covariance matrix P^a . A negative off-diagonal for two regions results in a total uncertainty for their sum that is less than the individual sum of their variances. For example, the error on Tropical America/Tropical Africa is 1.40 Gt yr^{-1} assuming independent errors, but 1.18 Gt yr^{-1} with inclusion of their negative covariance. This result suggests that the inversion may be solving for more regions than it can successfully resolve.

Figure 6.11 shows aggregated results between MATCH.NCEP (red) and the model mean (black). These include the north, tropics, and south, which correspond to the aggregate of the three plots shown in Figure 6.6. Also plotted in Figure 6.11 is the land and ocean partition. For the north, tropical, and southern regions, MATCH.NCEP is within the inversion error of the 15-model mean. Both MATCH.NCEP and the 15-model mean indicate that the north is a strong sink of CO_2 , and the south a weaker sink. The tropics are a net CO_2 source in both cases. Compared to the 15-model mean, MATCH.NCEP shows a stronger source in the tropics, with a corresponding stronger sink in the south. There is a greater difference between MATCH.NCEP and the 15-model mean for the land/ocean partition, although the error bars still overlap. The MATCH.NCEP inversion indicates that the land sink accounts for the entire global carbon sink, with the oceans acting as a small net source, but the errors still allow ocean uptake of 0.5 Gt C yr^{-1} . The 15-model mean result indicate that the carbon sink is nearly equally partitioned between the land and the oceans. Overall, MATCH shows larger adjustments from the background case compared to the 15-model mean.

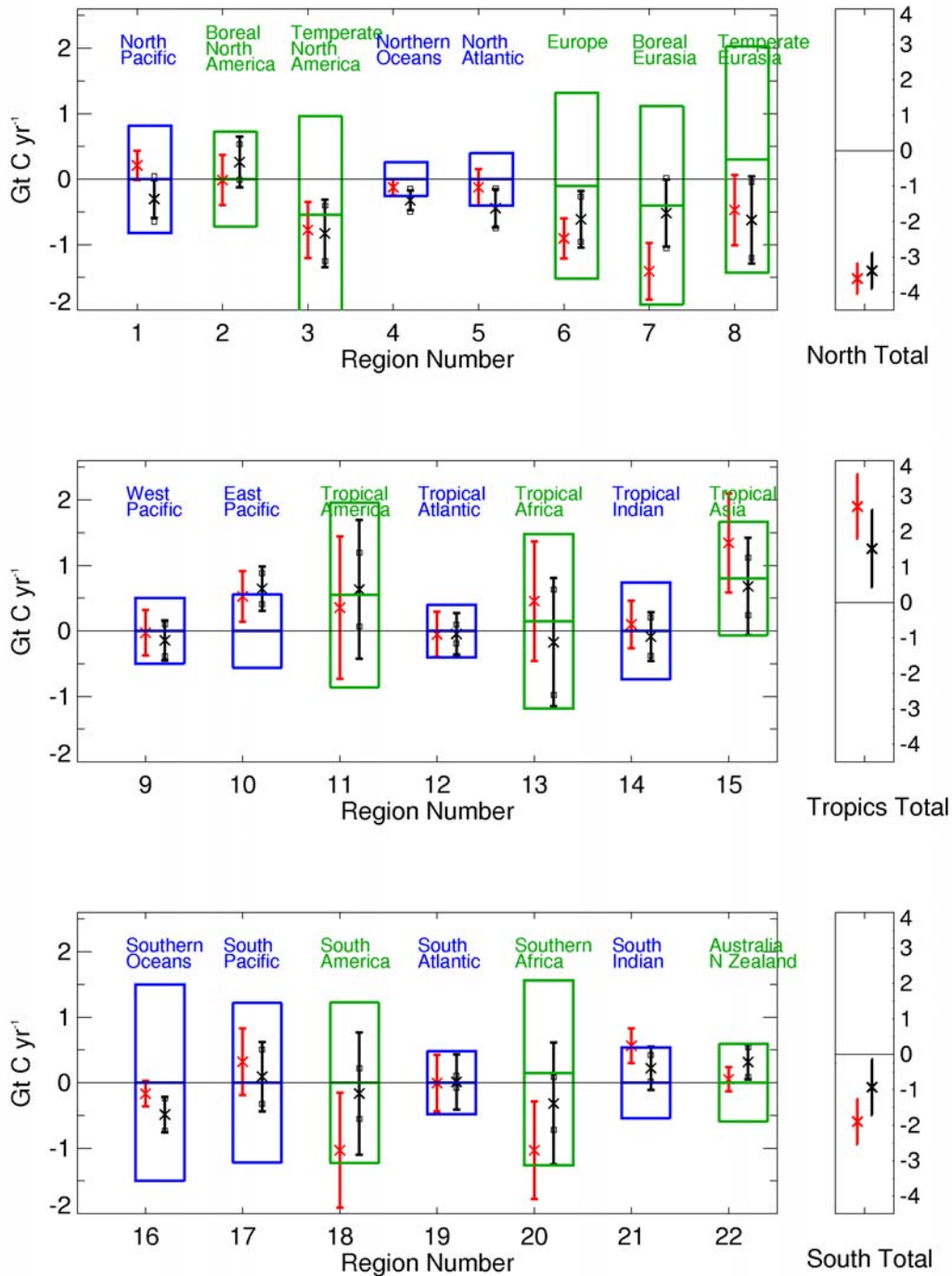


Figure 6.6. Transcom 3 Inversion results for the 11 land (green) and 11 ocean (blue) regions shown in Figure 6.4. Each region contains the MATCH result (red) and 15-model average result (black) with uncertainty bars. The initial (prior) uncertainty is shown by the larger boxes, with a central value corresponding to the prior value (usually zero). The boxes to the right show the aggregated values for the north, tropics, and south, respectively.

Transcom 3 Annual Mean Inversion:
MATCH vs. Model Mean for Major Groupings

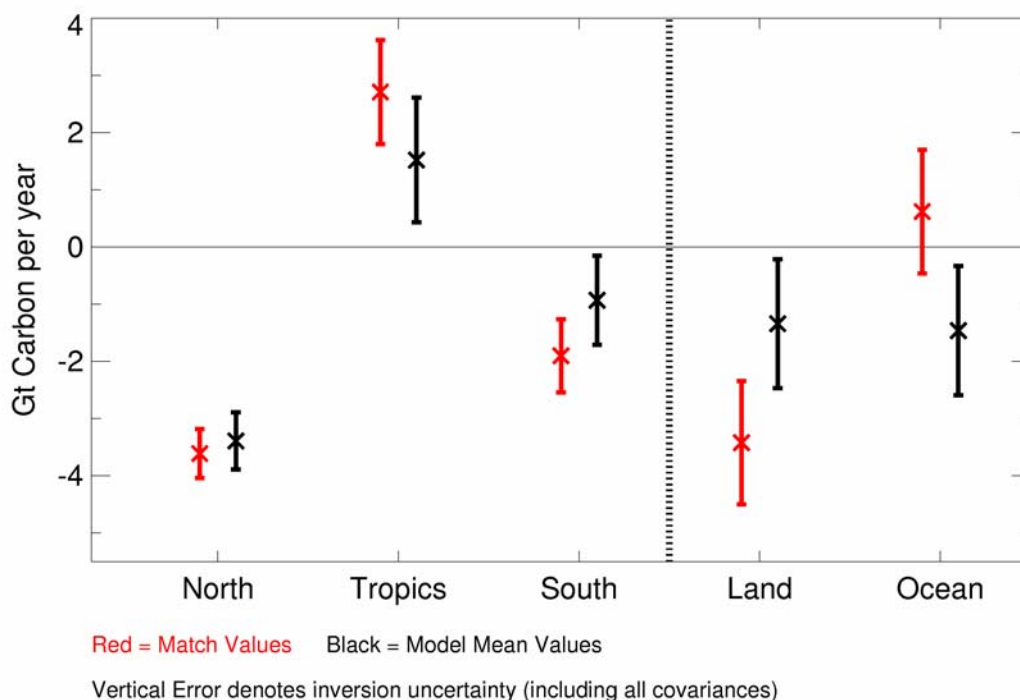


Figure 6.7. MATCH versus model mean for aggregated regions. The total global uptake is 2.78 Gt C yr⁻¹.

What is causing the differences between the MATCH and model mean inverted values, particularly for the land/ocean partition? We return to the difference in background simulation which is generated by the combination of FF, BIO, and OCN fluxes (\tilde{y}). Figure 6.8 shows the differences between the MATCH and 15-model mean mole fraction using the background fluxes (black), i.e. $\tilde{y}_{match} - \tilde{y}_{model\ mean}$, at all 76 observing sites. A zero difference would indicate that the two sets have identical background flux responses, and consequently, similar inversion values. As can be seen, the MATCH background mole fractions are greater than the model mean for northern hemispheric sites. This is largely because MATCH has higher mole fractions due to FF and BIO emissions at these locations compared to the 15-model mean. In the inversion, this results in a more negative y residual (where $y = y^o - \tilde{y}$) for MATCH compared to the model mean; consequently, the inversion produces stronger northern land sinks for MATCH (see Equation (6.6)). This result is seen for Boreal Eurasia, Boreal North America, and Europe. In contrast, the MATCH background fluxes are lower than the model mean for the southernmost sites. This relative depletion is at least partially caused by the greater mole fraction surface depletion in MATCH due to the OCN background flux, which is a strong sink in the southern hemisphere. The observational sites in this region are most sensitive to ocean regions. Consequently, the MATCH southern ocean regions need to be increased more than the 15-model mean. The inversion thus produces higher values for the Southern Oceans, South Pacific, and South Indian. Overall, MATCH is more sensitive to the background fluxes than the 15-model mean, which leads to most of the inversion

differences. We have also tested an inversion which does not include any of the prior fluxes. The inversion difference then depends only on modeled differences in the sensitivity matrix, H . The MATCH and model mean values were found to be much closer in this case.

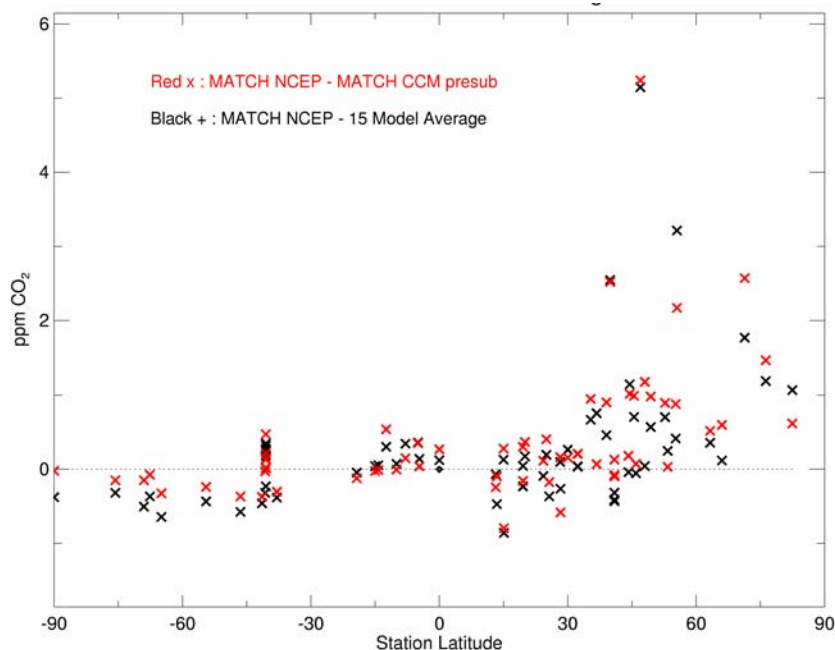


Figure 6.8. Differences in the simulated CO₂ mole fractions at the 76 control sites from the FF, BIO, and OCN background fluxes: $\tilde{y}_{match} - \tilde{y}_{model\ mean}$ (black) and $\tilde{y}_{match} - \tilde{y}_{match\ CCM}$ (red). In both cases MATCH calculates higher mole fractions in the Northern Hemisphere and lower mole fractions in the Southern Hemisphere.

6.2.1 Difference between MATCH.NCEP and MATCH.CCM3

As mentioned earlier, the larger surface CO₂ mole fractions computed from background fluxes, from both sources and sinks, are at least partially attributable to MATCH.NCEP's greater vertical resolution. However, differences in model physics and input meteorology also play a role. The MATCH.CCM3 results allowed a comparison to a similar model which used different meteorology. Recall that MATCH.NCEP and MATCH.CCM3 have relatively large and small IHG's, respectively, due to the BIO flux (Figure 6.3, right). The difference between MATCH.NCEP and MATCH.CCM3 (submitted by a different group) background simulations at each site are shown in Figure 6.8 (red). Note that MATCH.CCM3 shows nearly the same difference from MATCH.NCEP as the 15-model mean. MATCH.CCM3 consequently has inversion results closer to the 15-model mean. The CCM3 meteorology has 18 vertical levels, as opposed to the 28 NCEP levels, which may explain part of the tracer difference.

In order to separate the effects of vertical resolution and driving meteorology, we reduced the NCEP fields to 18 vertical levels (NCEP18 hereafter) using the average pressure levels of the CCM3 input meteorology. We then used the FF and BIO surface fluxes to simulate 1-year runs using the three MATCH meteorological inputs: NCEP (28 levels, same as MATCH.NCEP), NCEP18, and CCM3. Note

that we redid the MATCH runs driven by CCM3 meteorology with our own background surface fluxes in order to maintain consistency. Although shorter than the 4-year run used in the inversion, these 1-year simulations are long enough to diagnose differences in transport behavior. We have focused on the December values since the major transport differences at the surface were found to occur during the winter.

Figure 6.10 compares surface mole fraction differences between the three MATCH simulations. The left and right column shows results using the FF and BIO background fields, respectively. The plots correspond to the following MATCH surface mole fraction differences: NCEP – CCM (top), NCEP – NCEP18 (middle), and NCEP18 – CCM3 (bottom). As expected, the greatest difference is between the NCEP – CCM3 case, in which vertical resolution and meteorology both contribute. Note that the sum of the middle and bottom plots nearly equal this difference. The NCEP – NCEP18 difference is significant for both FF and BIO. Thus, just decreasing the vertical resolution from 28 to 18 levels can lead to differences in tracer behavior, especially for regions with strong surface fluxes. The NCEP18 - CCM compares the difference caused by the driving meteorological fields only, since the resolutions are the same. The differences here are also significant, accounting for much of the structure found in NCEP - CCM. Distinctive tracer behavior is observed for areas not directly above regions with strong fluxes, such as the northern oceans. Thus both vertical resolution and meteorological differences are found to play a role.

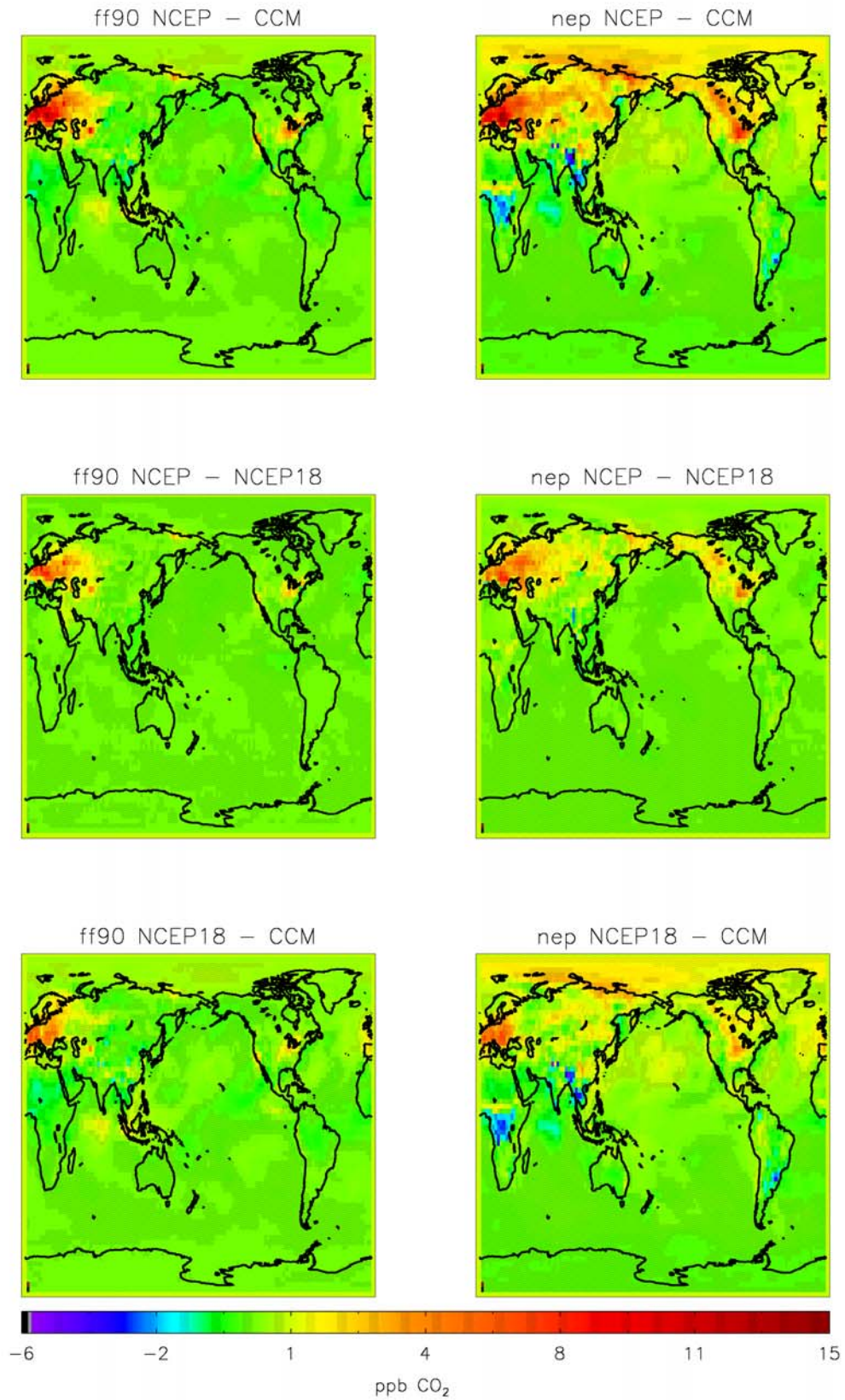


Figure 6.9. December surface mole fraction differences between different MATCH runs for FF (left plots) and BIO (right plots). Top: NCEP - CCM, middle: NCEP - NCEP18, bottom: NCEP18 - CCM. Note that the top difference roughly corresponds to the sum of the middle and bottom differences.

How do the NCEP18 and CCM surface transport diagnostics compare? Figure 6.10 shows the *PBLH* and K_c differences for CCM – NCEP18. Only locations where CCM values are greater than NCEP18 are shown (otherwise values are white). Both plots indicate that for most of the Northern Hemisphere, there is greater vertical mixing for the CCM case. This is consistent with generally lower surface CO₂ mole fractions for CCM. As discussed in Chapter 2, the K_c depends on the turbulent velocity scale, which in turn depends on the turbulence caused by thermal (i.e. surface heat fluxes (SHFLX)) and mechanical forcing (i.e. surface stresses (TAUX, TAUY)). Examination of these fields did not indicate a large difference in any single field. The observed difference in *PBLH* and K_c probably arises from a combination of effects which leads to greater surface layer venting of tracers for CCM surface emissions. The input fields (SHFLX, TAUX, TAUY) thus play an important role in the simulation of surface tracers, with subsequent impacts on the inversion.

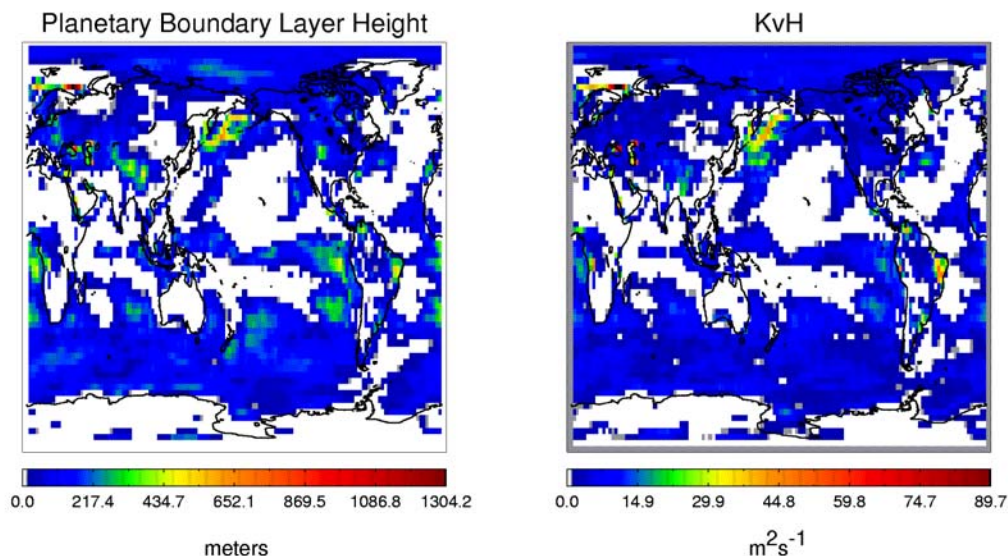


Figure 6.10. December difference (CCM – NCEP18) between the Planetary Boundary Layer Height and the bottom level K_c . Only values where CCM is greater than NCEP18 are shown, otherwise values are white. Greater values generally lead to greater tracer mixing in the boundary layer.

6.3 Inversion Sensitivity Experiments

In this section, we conduct a series of inversion sensitivity tests using the MATCH simulations. The MATCH results described in Figure 6.6 are referred to as the “control” inversion in the following. Some of these MATCH sensitivity studies are also included in *Law et al. (2003)* as contributions to the 15-model mean results. The full results of the sensitivity experiments for all regions are listed in Appendix C, in the sequence described below. Most of the differences are in the inversion flux values, rather than their uncertainties, which show much less variability.

Removal of background fluxes

Figure 6.11 shows the effect on the aggregated regions of removing BIO (green), OCN (blue), and both BIO and OCN (yellow) background fluxes from the MATCH inversion. These selective removals change the observational residuals ($y = y^o - \tilde{y}$) in the inversion. Recall that the annual global mean of BIO is zero. The largest differences from the control are seen for the No BIO and No OCN cases, with the No BIO/OCN providing intermediate values. The differences between No BIO and No OCN are significant.

In general, the No BIO case leads to weaker northern and southern extra-tropical uptake, compensated by weaker tropical efflux. Removal of the BIO flux causes a nearly 1 Gt C yr⁻¹ shift in Boreal Eurasia, from a strong sink of -1.41 Gt C yr⁻¹ to a weak carbon source of +0.36 Gt C yr⁻¹ (Appendix C). This is qualitatively consistent with removal of the large positive effect of BIO on the northern extratropical CO₂ mole fractions (especially over Eurasia) as shown earlier in Figure 6.3. The control inversion compensates for this large CO₂ signal by increasing the northern sinks, which are largely dominated by Boreal Eurasia. With BIO removal, less uptake by northern hemispheric regions is necessary. Conversely, the positive flux from the tropics is reduced. For example, Tropical Africa shifts from a weak source of +0.46 Gt C yr⁻¹ to a strong sink of -1.07 Gt C yr⁻¹. This region experiences a strong negative effect from BIO in the control inversion. The strong tropical land efflux needed to offset this negative effect is no longer necessary when BIO is removed. Overall, No BIO leads to little change for the oceans; most of the flux redistribution occurs on land. These examples show that the strength of the “rectifier” effect plays an important role in CO₂ inversion results, especially on the regional scale. Different biospheric exchange maps could significantly affect the inversion results. Ideally, a suite of feasible BIO exchange maps would be tested to assess the uncertainty in inversions.

In contrast to No BIO, removal of the OCN prior leads to stronger northern and southern uptake, compensated by strong tropical efflux. The OCN background flux generally increases CO₂ values in the tropics and depletes CO₂ in the extra-tropics. The control inversion compensates with tropical uptake and extra-tropical efflux. With this OCN removed, the inversion simultaneously increases the extra-tropical uptake and the tropical efflux. In addition, the ocean total shifts from a source of +0.62 Gt C yr⁻¹ to a sink of -0.45 Gt C yr⁻¹. With the ocean prior removed, the land becomes a weaker sink and the ocean a stronger sink of carbon by nearly a gigaton. This global change occurs from summing relatively small changes for most ocean regions. The Southern Indian Ocean shows the largest change from +0.57 to -0.13 Gt C yr⁻¹. Offsetting land increases occur mostly in the poorly constrained tropics, with Tropical America jumping from +0.36 to +1.42 Gt C yr⁻¹. The No BIO/No OCN case shows values intermediate to the separate No BIO and No OCN case for the north, tropics, and south (Figure 6.11). However, the land/ocean partition is closer to the No OCN case.

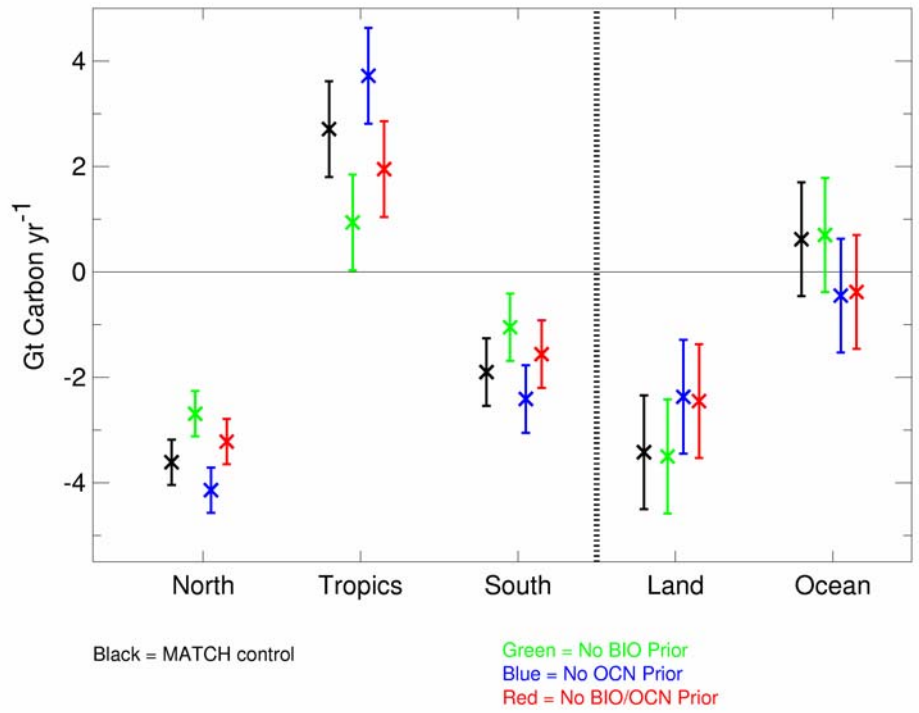


Figure 6.11. Aggregated CO₂ flux estimates for MATCH control (red) and 15-Model Mean (black). The additional cases (green, blue, and red) test the effect of removal of BIO and OCN background fluxes.

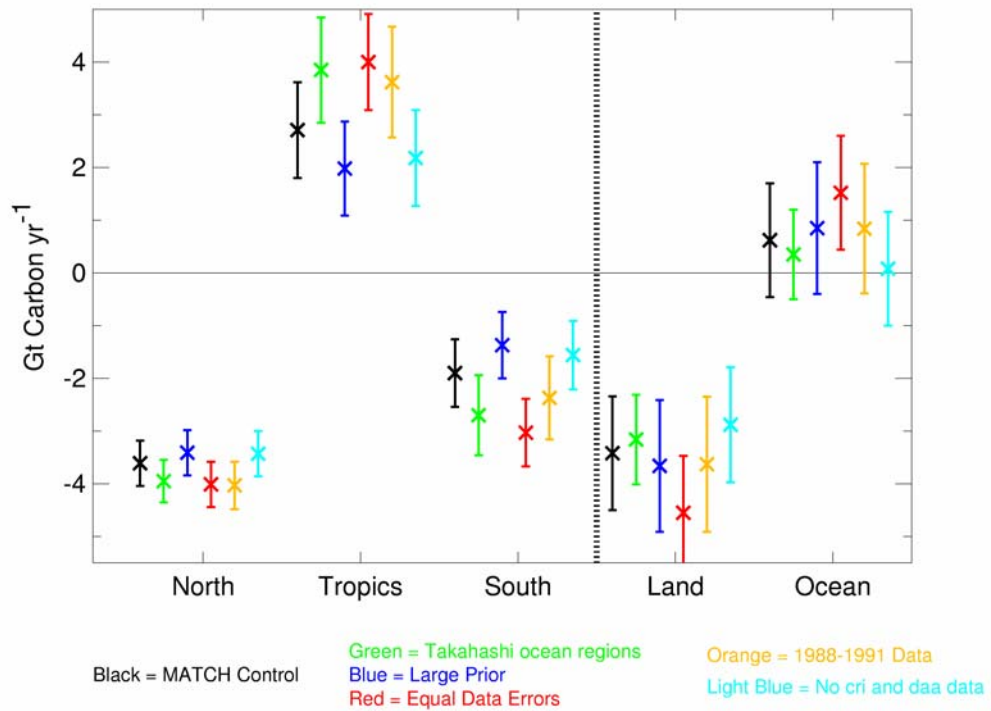


Figure 6.12. Aggregated flux estimates for MATCH reference (black) different sensitivity cases as described in the text.

Ocean Basis Regions with Structure

The OCN background field has spatial structure that represent CO_2 exchange based on *Takahashi et al.* (2002), Figure 6.13 (left). In contrast, flux exchange from 11 ocean basis regions in the control case are assumed to be spatially homogenous, Figure 6.13 (right). In this figure, we have scaled the flux magnitudes of the 11 ocean regions to match the OCN regional fluxes (global total $-2.2 \text{ Gt C yr}^{-1}$). These differences in structure may have an effect on the optimized fluxes, since the inversion assumes one flux pattern (OCN) but uses another set of flux patterns (i.e. the 11 ocean regions) for optimization. In order to create a more consistent set of ocean basis regions, we generated 11 new ocean flux patterns that are consistent with the regional spatial structure as OCN. These patterns were run forward in MATCH to generate new ocean sensitivities (in Equation (6.3)). These sensitivities were used in place of the 11 original, “flat” ocean sensitivities. The aggregated results in Figure 6.12 generally show some differences from the MATCH control, although the error bars still overlap. The tropical efflux increases by 1.2 Gt C , which is mostly offset by increased southern uptake. The relatively well constrained northern ocean regions (i.e. Northern Oceans, North Pacific, and North Atlantic) also show increased CO_2 influx .

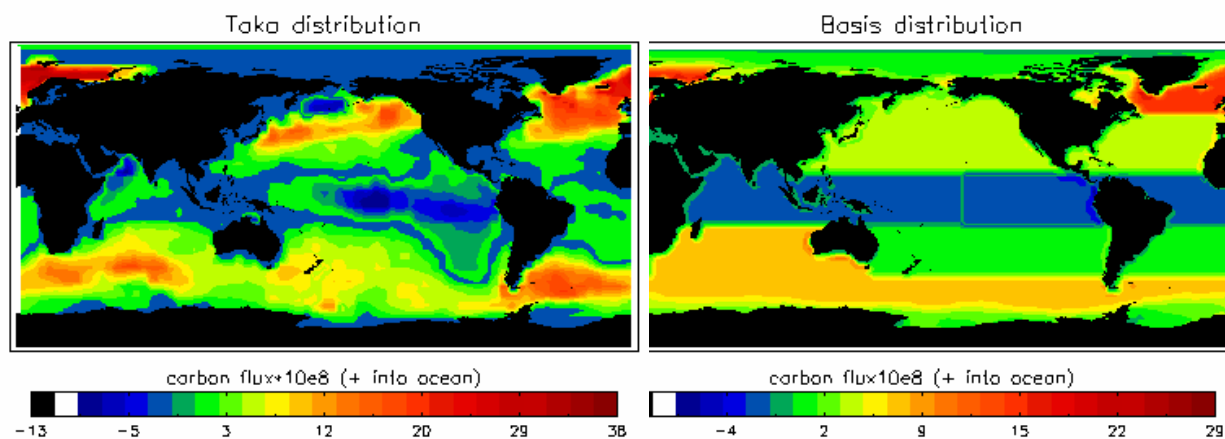


Figure 6.13. Comparison between OCN background distribution (based on *Takahashi et al.* (2002)) and the 11 homogenous ocean region that are optimized in the control inversion. The CO_2 flux magnitudes for each of the 11 regions roughly correspond to the intra-regional flux exchange found in OCN, but spread over a larger, homogenous area. Both maps sum to $-2.17 \text{ Gt C yr}^{-1}$ uptake. Note that the OCN distribution has significant structure in its carbon exchange, while the basis regions used by the inversion do not. Red and blue denote ocean uptake and efflux, respectively.

Larger Prior Errors

In order to test the impact of larger prior errors, we apply a uniform prior uncertainty of 2 Gt C yr^{-1} to each region. In the inversion, this corresponds to an increase in the diagonal terms found in P^f . We find that there are no significant differences in the estimated mean fluxes from the control case for any of the individual or grouped regions (Appendix C). This suggests that the initial prior does not overly constrain the final mean values. The final errors using larger initial errors are slightly larger than the control, although the amount of error reduction is similar. The amount of uncertainty reduction still decreases from the north, to south, to tropics.

Equal Data Errors

Next we apply uniform measurement errors (0.5 ppm) at all sites. Most of the measurement errors (55 sites) lie below 0.5 ppm, as shown in Appendix C of Appendix 2. A few stations experience significant measurement error reduction in this case, including sites in continental Europe and the US. Figure 6.12 indicates that no aggregated regions are significantly affected. Examination of individual regions shows that the greatest change occurs for the Tropical Indian Ocean, which increases from +0.1 to +1.4 Tg yr⁻¹. This flux change can be attributed to the simultaneously increased and decreased weighting of Darwin, Australia (daa) and the Seychelles (sey), respectively. Darwin has relatively high CO₂ mole fractions which require efflux from the Tropical Indian Ocean. In the control inversion, this large efflux is suppressed by the relatively mole fraction values at the Seychelles. Increasing the relative weighting at daa and decreasing sey causes the flux from the Tropical Indian to increase. In terms of final uncertainties, both temperate North American and European errors are reduced relative to the control due to the increased weighting of their continental sites with uniform 5 ppm errors (Appendix C).

Data time period

We have tested time-periods other than the 5-year (1992-1996) control period. *Law et al.* (2003) describe these experiments for the model mean values. It was found that using different time-periods of data does not lead to large overall changes in the inversion results. Figure 6.13 shows the results for the MATCH control case using data from the 3 year period between 1989-1991. As can be seen, there are slight shifts in the inversion values, although aggregated errors in emissions do not exceed the control error bars. A slight increase in the North America sink from -0.77 to -1.04 Gt C yr⁻¹ occurs, consistent with possible larger carbon uptake during this time relative to 1992-1996 as suggested by *Fan et al.* (1998).

Sensitivity to station removal

We also analyzed the effect of removing measurements from certain sites which are not well simulated even after optimization. The two sites with the greatest post-inversion difference are Darwin, Australia (daa) and Cape Rama, India (cri). These locations take flask measurement which may be hard for a global model to reproduce. The major effect of their removal is to decrease the control ocean efflux from +0.62 to +0.8 Gt C yr⁻¹. Most of this difference occurs through greater estimated uptake in the Tropical Indian Ocean.

Selective Time Sampling within MATCH

In this section we sample the modeled high-frequency output at each site to better simulate the actual flask measurements contained in the GlobalView dataset. Flask sampling usually seeks to sample air masses originating from clean air sectors. Most sampling also occurs during the daytime when the boundary layer is relatively well-mixed. Consequently, the flask annual average is lower than an average which includes all CO₂ values during the year. The modeled monthly averages used in the inversion are generated using all modeled CO₂ values, which are at 4 hour resolution. An alternative averaging strategy

would be to sample the model at the exact time of flask sampling, followed by averaging. Because we have used 1990 winds repeatedly, it is not possible to synchronize model output and flask samples taken between 1992-1996. An alternative would be to select for wind directions consistent with flask sampling. Unfortunately, this wind data is not provided with the GlobalView Data set. Instead, we create annual averages for the 1992-1996 data period by sampling MATCH high-frequency output for the following: (1) noon-time values, (2) minimum daily values, and (3) minimum weekly values. Both the control background fluxes and sensitivity runs have been selectively sampled in this way. This selective sampling generally decreases the values of the MATCH background tracers, leading to smaller deviations from the observations (i.e. $y = y^{\circ} - \tilde{y}$ is lower). Consequently, the inverted adjustment fluxes are less than found in the control inversion.

Figure 6.14 shows that selective sampling decreases the amount of estimate flux adjustment (from the zero line) for the depicted aggregated regions. This is particularly true for the case using minimum weekly mole fractions, where the total oceans become a sink (consistent with the background OCN value). The individual regions in Appendix C also show less of a deviation. The exception is Boreal Eurasia, which shows an increasing sink with selective sampling. The uncertainties on the optimized values also increase as the sensitivity decreases, due to the time-sampling.

Averaging above the surface layer

The final sensitivity test involves taking MATCH averages over several layers, rather than just the surface value for surface sites. Here, we average over the lowest 3 and the lowest 4 layers, roughly corresponding to heights of approximately 350 and 500 meters, respectively. This may compensate for the lack of selective sampling in the control case. It should also mitigate any overestimation of near surface trapping of fluxes from MATCH, especially in areas of large CO₂ surface exchange.

Figure 6.14 shows that averaging over the lowest 3-4 MATCH layers shows similar differences from the control case. Both cases show less deviation from the background values, especially for the land/ocean partition. Here, the ocean becomes a net sink of CO₂. Individual regions (Appendix C) generally show less deviation than the control case, particularly for land sinks. For example, Europe has dropped from -0.9 to -0.56 Gt C yr⁻¹ for the 4 layer average.

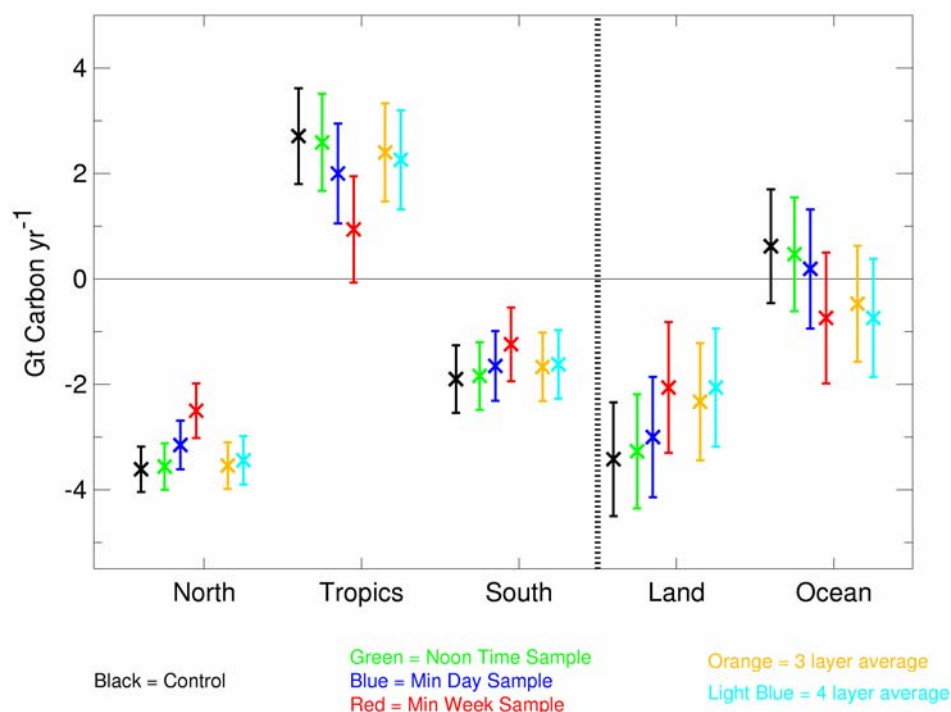


Figure 6.14. Aggregated flux estimates for MATCH control (black) and for five additional sensitivity tests. These tests involve selective time and space sampling within MATCH.

6.4 Summary

In this chapter, annual mean carbon dioxide inversions were conducted as part of the Transcom 3 modeling intercomparison. As noted earlier, the purpose of this intercomparison was to elucidate model differences and not to obtain the best possible estimates of CO₂ fluxes. In general, MATCH using NCEP meteorology tends to give stronger surface trapping of tracers in the boundary layer compared to other models, partially due to its greater vertical resolution. Surface trapping in MATCH.NCEP is also greater than MATCH.CCM3 meteorology at the same resolution, which is due to meteorological differences. The modeled responses to the background fluxes explain much of the inversion differences. In general, MATCH.NCEP has stronger optimized flux adjustments to the prior background fluxes compared to most models. Ultimately, model resolution, driving meteorology, and model structure all contribute to the differences in the inverted surface CO₂ flux values.

We also tested the sensitivity of the MATCH inversion to different input parameters. Overall, the individual regions show greater differences than the aggregated regions. The choice of prior background fluxes (i.e. FF BIO, OCN) can have a large effect on the optimized fluxes. More tests using alternative background fields should be conducted, particularly for the highly uncertain BIO flux. Finally, a more realistic model sampling strategy can be used when comparing to flask observations, which requires the use of consistent meteorology, such as NCEP. For certain regions in MATCH, this would likely result in

weaker optimally estimated flux adjustments to the prior background fluxes due to lower background and sensitivity values.

Chapter 7

Conclusions

The goal of this work was to estimate global methane emissions using a “top-down” or “inverse” approach with the incorporation of three new, previously unused elements: (1) high-frequency CH₄ observations, (2) interannually varying driving meteorology obtained from reanalysis of observations, and (3) optimization of interannual monthly methane emissions using the Kalman Filter. This new approach was augmented by the exploration of other aspects of atmospheric methane, including a detailed examination of CH₄ observations using forward modeling. We also participated in a carbon dioxide modeling intercomparison, which focused on the effect of model transport differences on inverted CO₂ fluxes. In this final chapter, we first briefly summarize the main results from the preceding chapters. Some general conclusions are then drawn from these results. The second part of this chapter describes possible future studies, including the use of new observations and alternative top-down approaches to constraining methane emissions.

7.1 Summary

Methane Forward Modeling

We first assembled all reliable methane time-series data, specifically focusing on high-frequency data. In addition, all available prior estimates of CH₄ emissions were collected and merged for input into MATCH. An OH field calculated from a previous MATCH run with full chemistry was scaled to reproduce ALE/GAGE/AGAGE methyl chloroform observations over the past 25 years. Using this corrected OH field, a reference CH₄ emissions source of approximately 600 Tg yr⁻¹ best reproduced the observed the methane growth rate between 1993-2001. This annually repeating emissions surface field was integrated forward in MATCH using interannually varying NCEP meteorology. Model and observed CH₄ mole fractions between 1996-2001 were compared, leading to the following conclusions:

- Using NCEP analyzed observed winds, MATCH can reproduce much of the interannual variation in observed CH₄ due to transport at most high-frequency observing sites.
- Interannual variability (IAV) in global transport, including effects from ENSO and NAO, can and does significantly impact the observed methane seasonality at certain locations.

This latter conclusion applies to sites near large CH₄ gradients, and includes sites far from emitting regions, such as Samoa. High-frequency measurements are more useful for these model-observational comparisons, since weekly flask measurements cannot capture many of the observed synoptic events. In general, observations in the marine boundary layer and in the coastal regions are well reproduced. Mid-

continental sites directly above strongly emitting regions are more difficult to simulate, due in part to the larger mismatch error associated with comparing point measurements with grid-volume averages in MATCH. We also examined the sensitivity of the current methane observing network to 7 seasonal processes/regions using forward modeling. The current methane observing network, being biased to the northern hemisphere extratropics, is sensitive to emissions from northern latitudes (e.g. northern wetlands), but much less sensitive to emissions from tropical latitudes (e.g. biomass burning).

Methane Inverse Modeling

Methane has multiple spatially and temporally varying sources. We developed an inversion methodology based on the Kalman Filter in order to estimate both time-varying and approximately time-invariant sources of methane. The time-varying emissions were solved at monthly time-resolution, which is the highest time-resolution performed to date in a global methane inversion. The expected near linearity of MATCH methane mole fractions to different spatial inputs of methane was confirmed. We estimated the errors associated with monthly mean observations which include instrumental, mismatch, and sampling frequency errors. The sampling frequency error dominates the total error difference between high-frequency and flask monthly means, since only ~4 flask measurements are taken each month compared to ~1000 high-frequency measurements. After their estimation, the optimized emissions were run forward in MATCH to confirm the improved to actual observations compared to the MATCH reference mole fractions calculated from prior emission estimates.

The Kalman Filter was used to solve for 7 seasonal (time-varying) and 3 aseasonal (constant) methane emissions between 1996-2001. We examined the optimized fluxes in terms of the total average, seasonal, and monthly interannual variability.

- Compared to the reference emissions, the optimized 5-year average emissions show reductions in energy-related emissions and increases in rice and tropical biomass burning emissions.
- The inversion increases the seasonal emission maxima relative to the reference and shifts the peak from August to July. This result is dominated by deduced phase changes and increased emissions from rice producing regions.
- Global wetland emissions increases dominate the anomalous observed 1998 global atmospheric methane increase, consistent with a bottom-up study using a wetland processes model (*Dlugokencky et al. (2001)*).
- However, the optimized methane flux increases for 1998 can only reproduce about half of the observed CH₄ mole fraction growth rate at Samoa, suggesting that a decreased OH sink may also have contributed to the observed increase. There is independent evidence of anomalously low OH in 1998 from methyl chloroform observations (*Prinn et al. (2001)*).

The optimized fluxes generally fall within the (albeit wide) range of previous estimates, although some processes lie at one end or the other of the current range. The larger inverted rice emissions compared to bottom-up estimates deserves further study. Part of the difference may be that bottom-up estimates are

usually restricted to emissions arising from rice cultivation only, while the top-down approach solves for both rice and wetland emissions from these regions. The impact of interannually varying OH on the observed CH₄ mole fractions needs to be further examined. For example, an interannually varying OH field optimized to CH₃CCl₃ could be used in place of our annually-repeating field.

We also tested the sensitivity of the inversion to the use of different sets of observations. We used two model sampling strategies to compute monthly mean mole fractions for comparison to flask monthly means. The first strategy sampled MATCH output at the exact time of flask measurement (low-frequency) while the second strategy used all model time steps (high-frequency). We further tested the sensitivity of the inversions to inclusion of an additional set of flask measurements which covered only a fraction of the 1996-2001 inversion period. The main results from these sensitivity studies are given below:

- For the current CH₄ observing network, high-frequency observations lead to most of the emission uncertainty reduction relative to the reference for the Wetland and Rice processes. Flask observations, however, offer additional constraints for tropical Biomass Burning emissions since tropical high-frequency sites are absent.
- Low and high-frequency model sampling strategies for comparing with flask monthly means lead to similar annual average CH₄ flux values; however, significant differences for interannual monthly fluxes can result for processes that are sensitive to flasks.

This latter result again shows the limitations of flask measurements. The low-frequency of observations makes the modeled and observed monthly mean mole fractions difficult to compare, resulting in greater inversion uncertainties.

Carbon Dioxide Inverse Modeling

We participated in the Transcom 3 CO₂ modeling intercomparison using our version of MATCH, following a protocol used for 15 participating models. In terms of forward modeling, MATCH driven by 1990 NCEP meteorology gives stronger surface trapping of emissions compared to most other models. At least part of this difference can be attributed to MATCH's higher vertical resolution at the surface and to the use of NCEP (as opposed to purely predicted) meteorology, in addition to possible effects from MATCH subgrid-scale transport parameterizations. Consequently, inverted fluxes using MATCH show relatively greater deviation from the prior (background) fluxes compared to the 15-model mean. The differences between models for individual regions, however, are still within the model optimized flux uncertainties. The MATCH inversion produces reasonable flux values for relatively well-constrained regions in the northern hemisphere compared to other studies. Certain adjacent regions in the tropics show unrealistic positive and negative optimal flux adjustments (dipoles), suggesting that the inversion cannot successfully resolve these regions. This suggests that the number of unknown regions used in Transcom 3 should be reduced, or that additional observational constraints should be utilized. Finally, a more realistic inversion would use meteorology and model sampling that is more consistent with flask sampling.

7.2 Further conclusions

The forward CH₄ simulations suggest that interannual inversions at monthly time resolution should employ consistent meteorology, rather than purely theoretical, climatological or annually repeating wind fields. We showed the influence of interannually varying transport on methane observations at locations near strongly emitting regions (Mace Head) as well as regions remote from emission sources (Samoa). Interannual transport can significantly impact the modeled CH₄ monthly means used in the inversion. This work compares, for the first time, top-down interannual inversions at monthly time-resolution with bottom-up estimates of methane fluxes. The significant error reduction by the inversion for the northern wetland regions suggests that additional observations can in principle constrain the currently poorly resolved tropical regions. High-frequency observations are necessary to capture the variability of methane observations, and thus to define accurate month means for inversions, especially at sites near regions of large emissions or strong transport induced CH₄ gradients, such as the ITCZ. The utility of flask measurements relative to high-frequency measurements decreases in these regions, due to the large flask sampling error. The inversion sensitivity experiments showed that using two reasonable but different ways of generating the modeled flask monthly means can result in different optimized monthly values. Although the use of flask measurements can be useful for annual and seasonally averaged inversions, their use in interannual inversions at monthly time-resolution can result in ambiguous flux estimates for the reasons cited above.

Bottom-up studies that produce more realistic spatial distributions of CH₄ emissions are essential to improving methane simulations. In Chapter 3 we compared CH₄ forward runs using older and more recent spatial distributions of anthropogenic methane emissions. The simulated CH₄ using the more recent distributions reproduced the synoptic variability and seasonality of actual observations much more successfully. The fluxes neglected in this study, such as boreal biomass burning and soil uptake generally do not have well-defined spatial emissions readily available for input into a global transport model. The distribution (and magnitude) of geologic sources is also very poorly known at this time. As bottom-up studies continue to better define the spatial distributions of these fluxes, their inclusion into the top-down approach will result in more accurate flux estimates. In addition, continued improvements in bottom-up flux magnitude estimates will be useful for further comparison to top-down flux values.

Many of our general conclusions for CH₄ also apply to CO₂ inversions. Both are relatively long-lived tracers and are sampled at nearly the same observing sites. The same limitations of flask measurements that were found for CH₄ must apply to CO₂, which also has strong anthropogenic and natural sources. High-frequency CO₂ measurements are currently measured at approximately 10 sites worldwide; these should be incorporated into future inversions, especially those focusing on interannual variability. The importance of using consistent observationally-derived meteorology as shown for CH₄ applies equally to CO₂. Carbon dioxide inversions are potentially more difficult than methane because they include strong two-way fluxes. In addition, both land and ocean play a role for CO₂, leading to adjacent flux regions that may be difficult to discriminate using the current observational network. Evidence of this difficulty was shown in the Transcom results for MATCH which showed strong positive/negative adjustments to the reference fluxes (dipoles) for adjacent regions in the tropics. The solution to this uniqueness problem is to solve for fewer regions, or use additional observational information. For example, tracers such as O₂ and ¹³CO₂ could be used to further constrain the land/ocean partitioning.

Model improvements and other approaches

One step in our future methane studies should be to progress from T42 ($\sim 2.8^\circ \times 2.8^\circ$) to the full NCEP resolution of T62 ($\sim 1.8^\circ \times 1.8^\circ$) to drive MATCH. In general, the mismatch error should decrease with this increased resolution. Global meteorological datasets at resolutions greater than T62 exist (e.g. ECMWF), although their availability for multi-year simulations is limited. Although increased resolution should increase our ability to more accurately simulate CH_4 , the degree of accuracy still depends on the model physics (and chemistry). The observing locations most sensitive to specific emission processes will likely be collocated with emissions. In Chapter 2 we showed the importance of the boundary layer transport formulation at these latter locations. The parameterization of this aspect of model transport is thus worth examining in more detail as more mid-continental observing stations become operational. Vertical profiles within the boundary layer from tall towers or aircraft could be particularly useful in this regard. It would be extremely useful to compare these profiles with MATCH simulations, which has levels at approximately 35, 120, 260, and 400 meters. To test the accuracy of MATCH's planetary boundary layer transport, these studies should perhaps employ gases whose emissions are better constrained than CH_4 . For example vertical profiles of anthropogenic compounds such as sulfur hexafluoride or CFC's may be useful.

With this thesis, the use of a global, top-down approach to solve for specific interannual CH_4 flux regions/processes has reached the stage of approximately monthly time-resolution. As discussed in Chapter 5, further increasing the time-resolution of the optimization may require the optimization of spatially smaller emission regions. The smallest possible spatial scale is ultimately the model grid resolution. The appropriate tool in this case would be an adjoint of the MATCH, which could in principle efficiently optimize the flux from each model grid cell. This technique has been applied to both CO_2 and CH_4 (*Houweling et al. (1999)*) at coarse resolution. However, even this technique requires use of prior information in order to successfully constrain specific processes; otherwise the number of unknown regions becomes too large and the inversion becomes ill-posed. Regional scale modeling offers a complement to the global approach. *Janssen et al. (1999)* and *Wang et al. (2002b)* have estimated regional methane emissions using meso-scale models and high-frequency observations. These studies are useful in constraining regional emission changes and have the advantage of high resolution, with potentially lower mismatch error. However, global CH_4 anomalies, such as occurred in 1998, may be misinterpreted by a regional model which only focuses on a select region. Even when using a regional model and observations, the global methane behavior must still be taken into account as a boundary condition.

New observational locations and other observations

The low uncertainty reductions for the tropical emission regions found in our inversion raises the obvious question as to where new observations should be located. Forward runs of individual methane emitting regions can determine the sites of maximum sensitivity to these regions, as described in Chapter 4. However, sites with maximum sensitivity to emitting regions are also typically subject to greater mismatch error compared to less sensitive sites due to their greater trace gas variability. The mismatch error is one of the most difficult to quantify; other, more sophisticated methods could be used in place of

our ad-hoc approach. Multiple measurements of the surrounding observational area may be necessary to establish the spatial “footprint” of an observational site. The observational goal should be to sample air that represents not a single point but the volume of a model grid cell. As we proceed to higher resolution in MATCH, the overall mismatch error should however decline. The most complete ground based observing scenario would likely have observing sites upwind, downwind, and inside an emitting region. Logistical or budget constraints, however, prevent the deployment of the spatially optimal configuration. An inversion technique such as the Kalman Filter can in principle be adapted to determine an optimal network given limitations in the number of sites and in geographical deployment.

Methane isotopes ($^{13}\text{CH}_4$, $^{14}\text{CH}_4$, CH_3D) could be extremely useful as separate constraints on the methane cycle. Isotopes can help to resolve isotopically distinct processes that have otherwise similar spatial and temporal patterns. The $^{13}\text{CH}_4$ isotope is the most well observed isotope, with measurements at approximately 12 flask sites (*Miller et al. (2002)*, *Lowe et al. (1994)*, *Tyler et al. (1999)*). This isotope can be useful in resolving the difference between biomass burning emissions, industrial emissions, and biogenic emissions (animals, wetlands, rice) which emit methane with different isotopic signatures. However, the modeling of $^{13}\text{CH}_4$ includes several additional complications to those normally encountered for modeling CH_4 mole fractions. The isotopic fractionation factors of different processes have large uncertainties. In addition, the influence of small and poorly constrained sinks, such as soil uptake and stratospheric destruction by Cl and (O^1D) must be accounted for due to their large isotopic fractionation factors. Finally, $^{13}\text{CH}_4$ measurement frequency is low and intercalibration between laboratories is less well established than for methane mole fractions. Measurements of CH_3D can also act as an additional constraint on different processes, similar to $^{13}\text{CH}_4$ (*Bergamaschi et al. (2000)*); however, its emission and sink fractionation factors are even less well known. The atmospheric burden of $^{14}\text{CH}_4$ does provide information on the total amount of fossil methane in the atmosphere (*Quay et al. (1999)*). This can help constrain fossil, and perhaps, geologic (clathrate) methane emissions. Unfortunately, the release of $^{14}\text{CH}_4$ from certain types of nuclear reactors complicates the use of this tracer. Estimating of the amount released from this source is difficult due to the secrecy surrounding this source of energy.

Isotopic measurements of methane require larger volumes of sample air than for mole fraction ($^{12}\text{CH}_4$) measurements. Consequently, isotopic measurements are currently constrained to flask sampling, usually at weekly or longer time-resolution. At this frequency, use of isotopes can currently aid in the estimation of overall methane magnitudes or trends (*Lassey et al. (2000)*). However, as was shown for methane, high-frequency observations are often necessary for accurate estimation of changes in methane emission processes at monthly time-resolution. This is especially true for sites adjacent to or within highly variable emitting regions. The interpretation of weekly (or even less frequent) isotopic measurements will have the same challenges as for total CH_4 mole fractions at these sites. High-frequency isotopic measurements, with simultaneous total mole fraction measurements, could be invaluable in the determination of specific methane process changes. However, analytical and instrumental challenges currently preclude high-frequency isotopic measurements.

The use of multiple tracers could aid in the attribution of methane sources. For example, *Bartlett et al. (2003)* have examined methane mole fractions off the Asian continent with other anthropogenic gases such as ethane (C_2H_6), ethyne (C_2H_2), propane (C_3H_8), and perchloroethene (C_2Cl_4). These latter gases are associated with industrial processes. The presence of elevated levels of CO with methane can also signify a biomass burning source. The use of multiple tracers generally requires the same source characteristics as methane; different spatial and temporal characteristics can significantly complicate their

use. Thus far, most analyses using multiple tracers have been qualitative in their application. For example, the absence of particular constituents can be used to discount particular sources of methane. Future inversions might seek to quantitatively incorporate multi-tracer species, including CH₄, to solve for emissions from several specific processes.

Finally, satellite data from sources such as MOPPITT and TES can provide global coverage of methane mole fractions, although information is often coarse in the vertical, and is less precise than ground based measurements. However, the global coverage can compensate for the lower precision of such measurements, as discussed for CO₂ in *Rayner et al.* (2002). Satellite measurements may thus be a useful complement to ground based observations for further unraveling the methane emissions puzzle.

Appendices

Appendix A MATCH PBL Vertical Transport

In the following we examine the turbulent velocity scale, ω_t , which determines the eddy diffusivity at any height within the PBL. It therefore plays a critical role in the total amount of mixing within the boundary layer. The eddy diffusivity (Equation (2.3)) is repeated below.

$$K_c = k\omega_t z \left(1 - \frac{z}{h}\right)^2$$

Within MATCH, the equation for the turbulent velocity scale depends on a stable versus unstable criterion within the boundary layer. This in turn is determined by the sign of the diagnosed virtual heat flux at the surface $(\overline{\omega' \theta'_v})_0$:

$$(\overline{\omega' \theta'_v})_0 = \left(\frac{1}{c_{p,air} \times \rho_{air,0}} \times (\overline{\omega' \theta'})_0 \right) + 0.61 \times \theta \times \left(\frac{1}{\rho_{wv,0}} \times (\overline{\omega' q'})_0 \right)$$

which depend on the following meteorological inputs from NCEP (or other source).

$$(\overline{\omega' \theta'})_0 = \text{surface sensible heat flux (SHFLX)}$$

$$(\overline{\omega' q'})_0 = \text{surface water vapor flux (WVFLX)}$$

Stable Conditions: $\left((\overline{\omega' \theta'_v})_0 \leq 0 \right)$

Under stable conditions, the turbulent velocity scale is determined by surface stress inputs from MATCH.

$$\omega_t = \frac{\mu_*}{\phi_H}$$

where

$$\mu_* = \left(\overline{u' \omega'^2} + \overline{v' \omega'^2} \right)^{\frac{1}{4}} = \left(\left(\frac{\tau_{xz}}{\rho_a} \right)^2 + \left(\frac{\tau_{yz}}{\rho_a} \right)^2 \right)^{\frac{1}{4}} = \text{friction velocity}$$

where $\tau_{xz} = \text{TAUX}$, $\tau_{yz} = \text{TAUY}$

$$\phi_H = \begin{cases} 1 + 5 \frac{z}{L} & \text{for } 0 \leq \frac{z}{L} \leq 1 \\ 5 + \frac{z}{L} & \text{for } 1 < \frac{z}{L} \end{cases}$$

= dimensionless vertical temperature gradient

$$L = \frac{-\mu_*^3}{k \frac{g}{\theta_{v0}} (\overline{\omega' \theta'_v})} = \text{Obukhov length}$$

θ_{v0} = virtual potential T at the surface

Unstable Conditions: $(\overline{\omega' \theta'_v})_0 > 0$

Under unstable conditions, the turbulent velocity scale is related to both the friction velocity (mechanical turbulence) and the convective velocity scale (thermal instability).

For the outer layer of the PBLH $\left(0.1 < \frac{z}{h} < 1\right)$

$$\omega_t = \frac{\omega_m}{\text{Pr}}$$

$$\omega_m = \mu_*^3 + c \omega_*^3 = \text{turbulent momentum velocity scale}$$

$$\omega_* = \left(\left(\frac{g}{\theta_{v0}} \right) (\overline{\omega' \theta'_v})_0 h \right)^{1/3} = \text{convective velocity scale}$$

$$\text{Pr} = \frac{\phi_h}{\phi_m} \left(\frac{z}{L} \right) + ak \frac{z}{h} \frac{\omega_*}{\omega_m} = \text{turbulent Prandtl Number}$$

$$\phi_m = \left(1 - 15 \frac{z}{L} \right)^{-1/3} = \text{dimensionless wind gradient}$$

where c, a, k are constants

Note also that only the unstable, outer layer case has a counter gradient term: $\gamma = 7.2 \frac{\omega_*}{\omega_m^2 h}$

For the model levels that are less than 10% of the PBLH $\left(\frac{z}{h} \leq 0.1\right)$

$$\omega_t = \frac{u_*}{\phi_H}$$

$$\phi_H = \left(1 - 15 \frac{z}{L} \right)^{-1/2}$$

Appendix B CO₂ stations and errors

CO₂ Flask data used for the Transcom 3 Level 1 Intercomparison. The values represent annual averages between 1992-1996. The computation of the standard deviations are described in *Gurney et al. (2003)*.

Station	Latitude	Longitude	ppm CO ₂	Std. Dev.
aia005_02D2	-40.53	144.3	356.77	0.5
aia015_02D2	-40.53	144.3	356.879	0.433
aia025_02D2	-40.53	144.3	357.026	0.433
aia035_02D2	-40.53	144.3	357.156	0.433
aia045_02D2	-40.53	144.3	357.279	0.354
aia065_02D2	-40.53	144.3	357.363	0.25
alt_00D0	82.45	-62.52	360.065	0.512
alt_02D0	82.45	-62.52	360.325	0.5
alt_06C0	82.45	-62.52	360.058	0.522
alt_06D0	82.45	-62.52	360.152	0.625
ams_11C0	-37.95	77.53	356.937	0.25
asc_00D0	-7.92	-14.42	357.646	0.25
bal_00D0	55.5	16.67	362.572	1.411
bhd_15C0	-41.41	174.87	356.762	0.25
bme_00D0	32.37	-64.65	359.483	0.584
bmw_00D0	32.27	-64.88	359.554	0.626
brw_00C0	71.32	-156.6	360.271	0.535
brw_00D0	71.32	-156.6	360.33	0.484
car030_00D2	40.9	-104.8	359.204	0.671
car040_00D2	40.9	-104.8	358.752	0.741
car050_00D2	40.9	-104.8	358.607	0.495
cba_00D0	55.2	-162.72	359.818	0.381
cfa_02D0	-19.28	147.06	357.511	0.266
cgo_00D0	-40.68	144.68	356.435	0.433
cgo_02D0	-40.68	144.68	356.686	0.433
cmn_17C0	44.18	10.7	359.443	0.908
cmo_00D0	45.48	-123.97	360.313	0.978
cri_02D0	15.08	73.83	360.016	0.84
crz_00D0	-46.45	51.85	356.938	0.25
daa_02D0	-12.42	130.57	360.792	0.697
esp_06D0	49.38	-126.55	360.316	0.902
gmi_00D0	13.43	144.78	358.932	0.25
hba_00D0	-75.67	-25.5	356.828	0.25
hun_00D0	46.95	16.65	364.161	1.856
ice_00D0	63.25	-20.15	359.245	0.261
itn496_00C3	35.35	-77.38	361.257	1.846
itn_00D0	35.35	-77.38	362.399	2.232
izo_00D0	28.3	-16.48	359.416	0.354
izo_27C0	28.3	-16.48	359.076	0.37

key_00D0		25.67	-80.2	360.09	0.282
kum_00D0		19.52	-154.82	359.204	0.263
maa_02D0		-67.62	62.87	356.598	0.25
mbc_00D0		76.25	-119.35	360.18	0.28
mhd_00D0	1	53.33	-9.9	359.112	0.439
mid_00D0		28.22	-177.37	359.504	0.274
mlo_00C0		19.53	-155.58	358.953	0.433
mlo_00D0		19.53	-155.58	359.016	0.433
mlo_02D0		19.53	-155.58	359.01	0.433
mm_19C0		24.3	153.97	360.016	0.347
mqa_02D0		-54.48	158.97	356.484	0.25
poc000_00D1	2	0	-163	359.266	0.25
pocn15_00D1	2	15	-147	359.345	0.25
pocn20_00D1	2	20	-140	359.469	0.264
pocn25_00D1	2	25	-134	359.662	0.376
pocn30_00D1	2	30	-126	359.653	0.384
pocs05_00D1	2	-5	-168	358.978	0.25
pocs10_00D1	2	-10	-174	358.491	0.25
pocs15_00D1	2	-15	-178	358.018	0.25
prs_21C0		45.93	7.7	358.708	0.432
prs_21D0		45.93	7.7	358.962	0.449
psa_00D0		-64.92	-64	356.745	0.25
rpb_00D0		13.17	-59.43	358.654	0.25
ryo_19C0		39.03	141.83	361.902	0.732
sch_23C0		48	8	360.285	1.057
sey_00D0		-4.67	55.17	357.188	0.321
shm_00D0		52.72	174.1	359.984	0.3
smo_00C0		-14.25	-170.57	357.638	0.354
smo_00D0		-14.25	-170.57	357.68	0.354
spo_00C0		-89.98	-24.8	356.795	0.433
spo_00D0		-89.98	-24.8	356.613	0.433
spo_02D0		-89.98	-24.8	356.71	0.433
stm_00D0		66	2	359.504	0.336
syo_00D0		-69	39.58	356.624	0.25
tap_00D0		36.73	126.13	362.555	0.921
uta_00D0		39.9	-113.72	360.292	0.769
uum_00D0		44.45	111.1	359.54	0.472

References

- Allan, W., D.C. Lowe, and J.M. Cainey, Active chlorine in the remote marine boundary layer: Modeling anomalous measurements of delta C-13 in methane, *Geophysical Research Letters*, 28 (17), 3239-3242, 2001.
- Bartlett, K.B., G.W. Sachse, T. Slate, C. Harward, and D.R. Blake, Large-scale distribution of CH₄ in the western North Pacific: Sources and transport from the Asian continent, *Journal of Geophysical Research-Atmospheres*, 108 (D20), 2003, doi:10.1029/2002JD003076.
- Bergamaschi, P., M. Braunlich, T. Marik, and C.A.M. Brenninkmeijer, Measurements of the carbon and hydrogen isotopes of atmospheric methane at Izana, Tenerife: Seasonal cycles and synoptic-scale variations, *Journal of Geophysical Research-Atmospheres*, 105 (D11), 14531-14546, 2000.
- Bingemer, H.G., and P.J. Crutzen, The Production of Methane from Solid-Wastes, *Journal of Geophysical Research-Atmospheres*, 92 (D2), 2181-2187, 1987.
- Bousquet, P., P. Peylin, P. Ciais, C. Le Quere, P. Friedlingstein, and P.P. Tans, Regional changes in carbon dioxide fluxes of land and oceans since 1980, *Science*, 290 (5495), 1342-1346, 2000.
- Buffett, B.A., Clathrate Hydrates, *Annual Reviews of Earth and Planetary Science*, 28, 477-507, 2000.
- Butler, J.H., J.W. Elkins, T.M. Thompson, B.D. Hall, T.H. Swanson, and V. Koropalov, Oceanic Consumption of CH₃CCl₃ - Implications for Tropospheric OH, *Journal of Geophysical Research-Atmospheres*, 96 (D12), 22347-22355, 1991.
- Cao, M.K., K. Gregson, S. Marshall, J.B. Dent, and O.W. Heal, Global methane emissions from rice paddies, *Chemosphere*, 33 (5), 879-897, 1996a.
- Cao, M.K., S. Marshall, and K. Gregson, Global carbon exchange and methane emissions from natural wetlands: Application of a process-based model, *Journal of Geophysical Research-Atmospheres*, 101 (D9), 14399-14414, 1996b.
- CMDL, CMDL Summary Report #26 Methane Section, 26, CMDL, Boulder, CO, 2001, <http://www.cmdl.noaa.gov/publications/index.html>.
- Cunnold, D.M., L.P. Steele, P.J. Fraser, P.G. Simmonds, R.G. Prinn, R.F. Weiss, L.W. Porter, S. O'Doherty, R.L. Langenfelds, P.B. Krummel, H.J. Wang, L. Emmons, X.X. Tie, and E.J. Dlugokencky, In situ measurements of atmospheric methane at GAGE/AGAGE sites during 1985-2000 and resulting source inferences, *Journal of Geophysical Research-Atmospheres*, 107 (D14), art. no.-4225, 2002, doi:10.1029/2001JD001226.
- Denning, A.S., I.Y. Fung, and D. Randall, Latitudinal gradient of atmospheric CO₂ due to seasonal exchange with land biota, *Nature*, 376, 240-243, 1995.
- Denning, A.S., M. Holzer, K.R. Gurney, M. Heimann, R.M. Law, P.J. Rayner, I.Y. Fung, S.M. Fan, S. Taguchi, P. Friedlingstein, Y. Balkanski, J. Taylor, M. Maiss, and I. Levin, Three-dimensional transport and concentration of SF₆ - A model intercomparison study (TransCom 2), *Tellus Series B-Chemical and Physical Meteorology*, 51 (2), 266-297, 1999.
- Dentener, F., M. van Weele, M. Krol, S. Houweling, and P. van Velthoven, Trends and inter-annual variability of methane emissions derived from 1979-1993 global CTM simulations, *Atmospheric Chemistry and Physics*, 3, 73-88, 2003.

- Dickens, G.R., C.K. Paull, and P. Wallace, Direct measurement of in situ methane quantities in a large gas-hydrate reservoir, *Nature*, 385 (6615), 426-428, 1997.
- Dlugokencky, E.J., K.A. Masarie, P.M. Lang, P.P. Tans, L.P. Steele, and E.G. Nisbet, A Dramatic Decrease in the Growth-Rate of Atmospheric Methane in the Northern-Hemisphere During 1992, *Geophysical Research Letters*, 21 (1), 45-48, 1994a.
- Dlugokencky, E.J., K.A. Masarie, P.M. Lang, and P.P. Tans, Continuing decline in the growth rate of the atmospheric methane burden, *Nature*, 393, 447-450, 1998.
- Dlugokencky, E.J., K.A. Masarie, P.M. Lang, P.P. Tans, L.P. Steele, and E.G. Nisbet, A Dramatic Decrease in the Growth-Rate of Atmospheric Methane in the Northern-Hemisphere During 1992 - Reply, *Geophysical Research Letters*, 21 (22), 2447-2448, 1994b.
- Dlugokencky, E.J., L.P. Steele, P.M. Lang, and K.A. Masarie, The Growth-Rate and Distribution of Atmospheric Methane, *Journal of Geophysical Research-Atmospheres*, 99 (D8), 17021-17043, 1994c.
- Dlugokencky, E.J., L.P. Steele, P.M. Lang, and K.A. Masarie, Atmospheric Methane at Mauna-Loa and Barrow Observatories - Presentation and Analysis of in-Situ Measurements, *Journal of Geophysical Research-Atmospheres*, 100 (D11), 23103-23113, 1995.
- Dlugokencky, E.J., B.P. Walter, K.A. Masarie, P.M. Lang, and E.S. Kasichke, Measurements of an anomalous global methane increase during 1998, *Geophysical Research Letters*, 28 (3), 499-502, 2001.
- DOE/EIA, Emissions of Greenhouse Gases in the United States, DOE/EIA-0573, Department of Energy, Washington, D.C., 2002, <http://www.eia.doe.gov/oiaf/1605/87-92rpt/>.
- Duncan, B.N., R.V. Martin, A.C. Staudt, R. Yevich, and J.A. Logan, Interannual and seasonal variability of biomass burning emissions constrained by satellite observations, *Journal of Geophysical Research-Atmospheres*, 108 (D2), 2003.
- EDGAR, EDGAR 3.0 : Emission Database for Global Atmospheric Research, National Institute of Public Health and the Environment (the Netherlands), 2002, <http://arch.rivm.nl/env/int/coredata/edgar/>
- EIA, Country Analysis Briefs: Russia, Energy Information Administration, Department of Energy, Washington, D.C., 2003, <http://www.eia.doe.gov/>.
- Enting, I.G., *Inverse Problems in Atmospheric Constituent Transport*, 392 pp., Cambridge University Press, Cambridge, 2002.
- Etheridge, D.M., L.P. Steele, R.J. Francey, and R.L. Langenfelds, Atmospheric methane between 1000 AD and present: Evidence of anthropogenic emissions and climatic variability, *Journal of Geophysical Research-Atmospheres*, 103 (D13), 15979-15993, 1998.
- Etiopie, G., and R.W. Klusman, Geologic emissions of methane to the atmosphere, *Chemosphere*, 49 (8), 777-789, 2002.
- Fan, S., M. Gloor, J. Mahlman, S. Pacala, J. Sarmiento, T. Takahashi, and P. Tans, A large terrestrial carbon sink in North America implied by atmospheric and oceanic carbon dioxide data and models, *Science*, 282, 442-446, 1998.
- Fung, I., J. John, J. Lerner, E. Matthews, M. Prather, L.P. Steele, and P.J. Fraser, Three-Dimensional Model Synthesis of the Global Methane Cycle, *Journal of Geophysical Research*, 96 (D7), 13,033 - 13,065, 1991.

- Gierczak, T., R.K. Talukdar, S.C. Herndon, G.L. Vaghjiani, and A.R. Ravishankara, Rate coefficients for the reactions of hydroxyl radicals with methane and deuterated methanes, *Journal of Physical Chemistry A*, *101* (17), 3125-3134, 1997.
- GlobalView-CH₄, Cooperative Atmospheric Data Integration Project - Methane, CD-ROM, NOAA CMDL, Boulder, Colorado [Also available on Internet via anonymous FTP to ftp.cmdl.noaa.gov, Path: ccg/ch4/GLOBALVIEW], 2001.
- GlobalView-CO₂, Cooperative Atmospheric Data Integration Project - Methane, CD-ROM, NOAA CMDL, Boulder, Colorado [Also available on Internet via anonymous FTP to ftp.cmdl.noaa.gov, Path: ccg/co2/GLOBALVIEW], 2000.
- Gloor, M., S.M. Fan, S. Pacala, and J. Sarmiento, Optimal sampling of the atmosphere for purpose of inverse modeling: A model study, *Global Biogeochemical Cycles*, *14* (1), 407-428, 2000.
- Gurney, K.R., R.M. Law, A.S. Denning, P.J. Rayner, D. Baker, P. Bousquet, L. Bruhwiler, Y.H. Chen, P. Ciais, S. Fan, I.Y. Fung, M. Gloor, M. Heimann, K. Higuchi, J. John, T. Maki, S. Maksyutov, K. Masarie, P. Peylin, M. Prather, B.C. Pak, J. Randerson, J. Sarmiento, S. Taguchi, T. Takahashi, and C.W. Yuen, Towards robust regional estimates of CO₂ sources and sinks using atmospheric transport models, *Nature*, *415* (6872), 626-630, 2002.
- Gurney, K.R., R.M. Law, A.S. Denning, P.J. Rayner, D. Baker, P. Bousquet, L. Bruhwiler, Y.H. Chen, P. Ciais, S.M. Fan, I.Y. Fung, M. Gloor, M. Heimann, K. Higuchi, J. John, E. Kowalczyk, T. Maki, S. Maksyutov, P. Peylin, M. Prather, B.C. Pak, J. Sarmiento, S. Taguchi, T. Takahashi, and C.W. Yuen, TransCom 3 CO₂ inversion intercomparison: 1. Annual mean control results and sensitivity to transport and prior flux information, *Tellus Series B-Chemical and Physical Meteorology*, *55* (2), 555-579, 2003.
- Haas-Laursen, D.E., D.E. Hartley, and T.J. Conway, Consistent sampling methods for comparing models to CO₂ flask data, *Journal of Geophysical Research-Atmospheres*, *102* (D15), 19059-19071, 1997.
- Hack, J.J., Parameterization of moist convection in the National Center for Atmospheric Research community climate model (CCM2), *Journal of Geophysical Research*, *99* (5551-5568), 5551-5568, 1994.
- Hansen, J., M. Sato, R. Ruedy, A. Lacis, and V. Oinas, Global warming in the twenty-first century: An alternative scenario, *Proceedings of the National Academy of Sciences of the United States of America*, *97* (18), 9875-9880, 2000.
- Hao, W.M., and M.H. Liu, Spatial and Temporal Distribution of Tropical Biomass Burning, *Global Biogeochemical Cycles*, *8* (4), 495-503, 1994.
- Hao, W.M., and D.E. Ward, Methane Production From Global Biomass Burning, *Journal of Geophysical Research-Atmospheres*, *98* (D11), 20657-20661, 1993.
- Hein, R., P.J. Crutzen, and M. Heimann, An inverse modeling approach to investigate the global atmospheric methane cycle, *Biogeochemistry*, *11* (1), 43-76, 1997.
- Holtslag, A.A.M., and B.A. Boville, Local versus nonlocal boundary-layer diffusion in a global climate model, *Journal of Climate*, *6*, 1825-1842, 1993.
- Houghton, R.A., J.L. Hackler, and K.T. Lawrence, The US carbon budget: Contributions from land-use change, *Science*, *285* (5427), 574-578, 1999.

- Houweling, S., F. Dentener, J. Lelieveld, B. Walter, and E. Dlugokencky, The modeling of tropospheric methane: How well can point measurements be reproduced by a global model?, *Journal of Geophysical Research-Atmospheres*, 105 (D7), 8981-9002, 2000.
- Houweling, S., T. Kaminski, F. Dentener, J. Lelieveld, and M. Heimann, Inverse modeling of methane sources and sinks using the adjoint of a global transport model, *Journal of Geophysical Research-Atmospheres*, 104 (D21), 26137-26160, 1999.
- Huang, J., Optimal Determination of Global Tropospheric OH Concentrations Using Multiple Trace Gases, Massachusetts Institute of Technology, Cambridge, 2000.
- IPCC, *Intergovernmental Panel on Climate Change, Climate Change 1994*, Cambridge University Press, 1995.
- IPCC, *Climate Change 2001: The Scientific Basis*, Cambridge University Press, Cambridge, 2001
- Janssen, L.H.J.M., J.G.J. Olivier, and A.R. van Amstel, Comparison of CH₄ emission inventory data and emission estimates from atmospheric transport models and concentration measurements, *Environmental Science & Policy*, 2 (3), 295-314, 1999.
- Jensen, C., Terrestrial Sources and Sinks of Atmospheric Methyl Bromide: Three-Dimensional Modeling of Tropospheric Abundance and Sensitivities, MS thesis, MIT, Cambridge, 1999.
- Jockel, P., Comogenic ¹⁴CO as tracer for atmospheric chemistry and transport, Rupertus Carola University of Heidelberg, Heidelberg, 2000.
- JPL, Chemical Kinetics and Photochemical Data for Use in Atmospheric Studies: Evaluation Number 14, pp. 334, JPL Publication 02-25, NASA-JPL, Pasadena, California, 2003, C:\research\library\all\jpl14.pdf.
- Kasibhatla, P., M. Heimann, P. Rayner, N. Mahowald, R. Prinn, and D. Hartley, *Inverse Methods in Global and Biogeochemical Cycles*, American Geophysical Union, Geophysical Monograph 114, Washington D.C., 2000
- Kasischke, E.S., and L.P. Bruhwiler, Emissions of carbon dioxide, carbon monoxide, and methane from boreal forest fires in 1998, *Journal of Geophysical Research-Atmospheres*, 108 (D1), 2002, doi:10.1029/2001JD000461.
- Kiehl, J.T., J.J. Hack, G.B. Bonan, B.A. Boville, B.P. Briegleb, D.L. Williamson, and P.J. Rasch, Description of the NCAR Community Climate Model (CCM3), TN-420+STR, NCAR, Boulder, CO, 1996.
- Kleiman, G., and R.G. Prinn, Measurement and deduction of emissions of trichloroethene, tetrachloroethene, and trichloromethane (chloroform) in the northeastern United States and southeastern Canada, *Journal of Geophysical Research-Atmospheres*, 105 (D23), 28875-28893, 2000.
- Kreileman, G.J.J., and A.F. Bouwman, Computing Land-Use Emissions of Greenhouse Gases, *Water Air and Soil Pollution*, 76 (1-2), 231-258, 1994.
- Kuhlmann, R.v., M.G. Lawrence, and P.J. Crutzen, A model for studies of tropospheric ozone and nonmethane hydrocarbons: Model description and ozone results, *Journal of Geophysical Research-Atmospheres*, 108 (D9, 4294), 2003, doi:10.1029/2002JD002893.
- Lassey, K.R., D.C. Lowe, and M.R. Manning, The trend in atmospheric methane delta C-13 implications for isotopic constraints on the global methane budget, *Global Biogeochemical Cycles*, 14 (1), 41-49, 2000.

- Law, K.S., and E.G. Nisbet, Sensitivity of the CH₄ growth rate to changes in CH₄ emissions from natural gas and coal, *Journal of Geophysical Research-Atmospheres*, 101 (D9), 14387-14397, 1996a.
- Law, R.M., Y.-H. Chen, K.R. Gurney, and T. modelers, TransCom3 CO₂ inversion intercomparison: 2. Sensitivity of annual mean results to data choices, *Tellus*, 55B, 580-595, 2003.
- Law, R.M., P.J. Rayner, A.S. Denning, D. Erickson, I.Y. Fung, M. Heimann, S.C. Piper, M. Ramonet, S. Taguchi, J.A. Taylor, C.M. Trudinger, and I.G. Watterson, Variations in modeled atmospheric transport of carbon dioxide and the consequences for CO₂ inversions, *Global Biogeochemical Cycles*, 10 (4), 783-796, 1996b.
- Lawrence, M.G., P.J. Crutzen, P.J. Rasch, B.E. Eaton, and N.M. Mahowald, A model for studies of tropospheric photochemistry: Description, global distributions, and evaluation, *Journal of Geophysical Research-Atmospheres*, 104 (D21), 26245-26277, 1999.
- Lawrence, M.G., P. Jockel, and R. von Kuhlmann, What does the global mean OH concentration tell us?, *Atmospheric Chemistry and Physics*, 1, 37-49, 2001.
- Lelieveld, J., P.J. Crutzen, and F.J. Dentener, Changing concentration, lifetime and climate forcing of atmospheric methane, *Tellus Series B-Chemical and Physical Meteorology*, 50 (2), 128-150, 1998.
- Lerner, J., E. Matthews, and I. Fung, Methane emission from animals: A global high-resolution data base, *Global Biogeochemical Cycles*, 2, 139-156, 1988.
- Levine, J.S., The 1997 fires in Kalimantan and Sumatra, Indonesia: Gaseous and particulate emissions, *Geophysical Research Letters*, 26 (7), 815-818, 1999.
- Lowe, D., and e. al., Concentration and ¹³C records of atmospheric methane in New Zealand and Antarctica: Evidence for changes in methane sources, *Journal of Geophysical Research*, 99 (D8), 16, 913-16, 925, 1994.
- Lucas, D., Mechanistic, Sensitivity, and Uncertainty Studies of the Atmospheric Oxidation of Dimethylsulfide, PhD thesis, MIT, Cambridge, 2003.
- Mahowald, N., Development of a 3-Dimensional Chemical Transport Model Based on Observed Winds and Use in Inverse Modeling of the Sources of CCl₃F, PhD thesis, MIT, Cambridge, 1996.
- Mahowald, N.M., R.G. Prinn, and P.J. Rasch, Deducing CCl₃F emissions using an inverse method and chemical transport models with assimilated winds, *Journal of Geophysical Research*, 102 (D23), 28,153-28,168, 1997a.
- Mahowald, N.M., P.J. Rasch, B.E. Eaton, S. Whittlestone, and R.G. Prinn, Transport of (222)radon to the remote troposphere using the model of atmospheric transport and chemistry and assimilated winds from ECMWF and the National Center for Environmental Prediction NCAR, *Journal of Geophysical Research-Atmospheres*, 102 (D23), 28139-28151, 1997b.
- Masarie, K.A., and P.P. Tans, Extension and Integration of Atmospheric Carbon-Dioxide Data into a Globally Consistent Measurement Record, *Journal of Geophysical Research-Atmospheres*, 100 (D6), 11593-11610, 1995.
- Matthews, E., and I. Fung, Methane emissions from natural wetlands: Global distribution, area, and environmental characteristics of sources, *Global Biogeochemical Cycles*, 1, 61-86, 1987.
- Matthews, E., I. Fung, and J. Lerner, Methane emission from rice cultivation: Geographic and seasonal distribution of cultivated areas and emissions, *Global Biogeochemical Cycles*, 5, 3-24, 1991.

- McCarthy, M.C., P. Connell, and K.A. Boering, Isotopic fractionation of methane in the stratosphere and its effect on free tropospheric isotopic compositions, *Geophysical Research Letters*, 28 (19), 3657-3660, 2001.
- McCulloch, A., and P.M. Midgley, The history of methyl chloroform emissions: 1951-2000, *Atmospheric Environment*, 35 (31), 5311-5319, 2001.
- Midgley, P.M., and A. McCulloch, The Production and Global Distribution of Emissions to the Atmosphere of 1,1,1-Trichloroethane (Methyl Chloroform), *Atmospheric Environment*, 29 (14), 1601-1608, 1995.
- Milkov, A.V., R. Sassen, T.V. Apanasovich, and F.G. Dadshev, Global gas flux from mud volcanoes: A significant source of fossil methane in the atmosphere and the ocean, *Geophysical Research Letters*, 30 (2), 1037, 2003, 10.1029/20002GL016358.
- Miller, J.B., K.A. Mack, R. Dissly, J.W.C. White, E.J. Dlugokencky, and P.P. Tans, Development of analytical methods and measurements of C-13/C-12 in atmospheric CH₄ from the NOAA Climate Monitoring and Diagnostics Laboratory global air sampling network, *Journal of Geophysical Research-Atmospheres*, 107 (D13), art. no.-4178, 2002, doi: 10.1029/2001JD000630.
- Mosier, A.R., J.A. Delgado, and M. Keller, Methane and nitrous oxide fluxes in an acid Oxisol in western Puerto Rico: Effects of tillage, liming and fertilization, *Soil Biology & Biochemistry*, 30 (14), 2087-2098, 1998.
- NOAA, Climate of 1998 Annual Review, National Oceanic and Atmospheric Administration, Asheville, NC, 1999, <http://lwf.ncdc.noaa.gov/oa/climate/research/1998/ann/ann98.html>.
- NOAA, CCGG Figures, National Oceanic and Atmospheric Administration (NOAA), Climate Monitoring and Diagnostics Laboratory (CMDL), Carbon Cycle Greenhouse Gases, 2003, http://www.cmdl.noaa.gov/ccgg/gallery/index.php?pageType=folder&currDir=./Data_Figures
- Novelli, P.C., K.A. Masarie, P.M. Lang, B.D. Hall, R.C. Myers, and J.W. Elkins, Reanalysis of tropospheric CO trends: Effects of the 1997-1998 wildfires, *Journal of Geophysical Research-Atmospheres*, 108 (D15), 2003.
- O'Doherty, S., P.G. Simmonds, D.M. Cunnold, H.J. Wang, G.A. Sturrock, P.J. Fraser, D. Ryall, R.G. Derwent, R.F. Weiss, P. Salameh, B.R. Miller, and R.G. Prinn, In situ chloroform measurements at Advanced Global Atmospheric Gases Experiment atmospheric research stations from 1994 to 1998, *Journal of Geophysical Research-Atmospheres*, 106 (D17), 20429-20444, 2001.
- Olivier, J.G.J., A.F. Bouwman, J.J.M. Berdowski, C. Veldt, J.P.J. Bloos, A.J.H. Visschedijk, C.W.M. van der Maas, and P.Y.J. Zandveld, Sectoral emission inventories of greenhouse gases for 1990 on a per country basis as well as on 1[deg] x 1[deg], *Environmental Science & Policy*, 2 (3), 241-263, 1999.
- Pacala, S.W., G.C. Hurtt, D. Baker, P. Peylin, R.A. Houghton, R.A. Birdsey, L. Heath, E.T. Sundquist, R.F. Stallard, P. Ciais, P. Moorcroft, J.P. Caspersen, E. Shevliakova, B. Moore, G. Kohlmaier, E. Holland, M. Gloor, M.E. Harmon, S.M. Fan, J.L. Sarmiento, C.L. Goodale, D. Schimel, and C.B. Field, Consistent land- and atmosphere-based US carbon sink estimates, *Science*, 292 (5525), 2316-2320, 2001.
- Patra, P.K., and S. Maksyutov, Incremental approach to the optimal network design for CO₂ surface source inversion, *Geophysical Research Letters*, 29 (10), 2002, doi:10.1029/2001GL013943.
- Prinn, R., Measurement Equation for Trace Chemicals in Fluids and Solution of its Inverse, in *Inverse Methods in Global Biogeochemical Cycles*, edited by P. Kashibhatla, pp. 3-18, American Geophysical Union, 2000.

- Prinn, R., D. Cunnold, P. Simmonds, F. Alyea, R. Boldi, A. Crawford, P. Fraser, D. Gutzler, D. Hartley, R. Rosen, and R. Rasmussen, Global Average Concentration and Trend for Hydroxyl Radicals Deduced from Ale Gage Trichloroethane (Methyl Chloroform) Data for 1978-1990, *Journal of Geophysical Research-Atmospheres*, 97 (D2), 2445-2461, 1992.
- Prinn, R.G., J. Huang, R.F. Weiss, D.M. Cunnold, P.J. Fraser, P.G. Simmonds, A. McCulloch, C. Harth, P. Salameh, S. O'Doherty, R.H.J. Wang, L. Porter, and B.R. Miller, Evidence for substantial variations of atmospheric hydroxyl radicals in the past two decades, *Science*, 292 (5523), 1882-1888, 2001.
- Prinn, R.G., R.F. Weiss, P.J. Fraser, P.G. Simmonds, D.M. Cunnold, F.N. Alyea, S. O'Doherty, P. Salameh, B.R. Miller, J. Huang, R.H.J. Wang, D.E. Hartley, C. Harth, L.P. Steele, G. Sturrock, P.M. Midgley, and A. McCulloch, A history of chemically and radiatively important gases in air deduced from ALE/GAGE/AGAGE, *Journal of Geophysical Research-Atmospheres*, 105 (D14), 17751-17792, 2000.
- Quay, P., S. King, D. White, M. Brockington, B. Plotkin, R. Gammon, S. Gerst, and J. Stutsman, Atmospheric (CO)-C-14: A tracer of OH concentration and mixing rates, *Journal of Geophysical Research-Atmospheres*, 105 (D12), 15147-15166, 2000.
- Quay, P., J. Stutsman, D. Wilbur, A. Snover, E. Dlugokencky, and T. Brown, The isotopic composition of atmospheric methane, *Global Biogeochemical Cycles*, 13 (2), 445-461, 1999.
- Randerson, J.T., M.V. Thompson, T.J. Conway, I.Y. Fung, and C.B. Field, The contribution of terrestrial sources and sinks to trends in the seasonal cycle of atmospheric carbon dioxide, *Global Biogeochemical Cycles*, 11 (4), 535-560, 1997.
- Rasch, P.J., J. Feichter, K. Law, N. Mahowald, J. Penner, C. Benkovitz, C. Genthon, C. Giannakopoulos, P. Kasibhatla, D. Koch, H. Levy, T. Maki, M. Prather, D.L. Roberts, G.J. Roelofs, D. Stevenson, Z. Stockwell, S. Taguchi, M. Kritz, M. Chipperfield, D. Baldocchi, P. McMurry, L. Barrie, Y. Balkansi, R. Chatfield, E. Kjellstrom, M. Lawrence, H.N. Lee, J. Lelieveld, K.J. Noone, J. Seinfeld, G. Stenchikov, S. Schwartz, C. Walcek, and D. Williamson, A comparison of scavenging and deposition processes in global models: results from the WCRP Cambridge Workshop of 1995, *Tellus Series B-Chemical and Physical Meteorology*, 52 (4), 1025-1056, 2000.
- Rasch, P.J., and M. Lawrence, Recent Development in Transport Methods at NCAR, pp. 9, National Center for Atmospheric Research, 1998, C:\research\library\all\rasch.1998.spitfire.report.pdf.
- Rasch, P.J., N.M. Mahowald, and B.E. Eaton, Representations of transport, convection, and the hydrologic cycle in chemical transport models: Implications for the modeling of short-lived and soluble species, *Journal of Geophysical Research-Atmospheres*, 102 (D23), 28127-28138, 1997.
- Rayner, P.J., R.M. Law, D.M. O'Brien, T.M. Butler, and A.C. Dilley, Global observations of the carbon budget - 3. Initial assessment of the impact of satellite orbit, scan geometry, and cloud on measuring CO₂ from space, *Journal of Geophysical Research-Atmospheres*, 107 (D21), 2002, doi:10.1029/2001JD000618.
- Redeker, K.R., N.Y. Wang, J.C. Low, A. McMillan, S.C. Tyler, and R.J. Cicerone, Emissions of methyl halides and methane from rice paddies, *Science*, 290 (5493), 966-969, 2000.
- Reilly, J., M. Mayer, and J. Harnisch, The Kyoto Protocol and non-CO₂ greenhouse gases and carbon sinks, *Environmental Modeling & Assessment*, 7 (4), 217-229, 2002.
- Reshetnikov, A.I., N.N. Paramonova, and A.A. Shashkov, An evaluation of historical methane emissions from the Soviet gas industry, *Journal of Geophysical Research-Atmospheres*, 105 (D3), 3517-3529, 2000.

- Ridgwell, A.J., S.J. Marshall, and K. Gregson, Consumption of atmospheric methane by soils: A process-based model, *Global Biogeochemical Cycles*, 13 (1), 59-70, 1999.
- Rodenbeck, C., S. Houweling, M. Gloor, and M. Heimann, Time-dependent atmospheric CO₂ inversions based on interannually varying tracer transport, *Tellus*, 55B, 488-497, 2003.
- Sagers, M.J., and T. Shabad, *The Chemical Industry in the USSR, and economic Geography*, Westview Press, Boulder, 1990.
- Sanderson, M.G., Biomass of termites and their emissions of methane and carbon dioxide: A global database, *Global Biogeochemical Cycles*, 10 (4), 543-557, 1996.
- Sass, R.L., Short Summary Chapter for Methane, in *CH₄ and N₂O Global Emissions and Controls from Rice Fields and Other Agricultural and Industrial Sources*, edited by K. Minami, A. Mosier, and R. Sass, NIAES, Tsukuba, 1994.
- Sass, R.L., J.A. Andrews, A.J. Ding, and F.M. Fisher, Spatial and temporal variability in methane emissions from rice paddies: Implications for assessing regional methane budgets, *Nutrient Cycling in Agroecosystems*, 64 (1-2), 3-7, 2002.
- Smith, I.M., and L.L. Sloss, Methane Emissions from Coal, IEAPER/04, Coal Research, London, 1992, <http://www.iea-coal.org.uk/publishing/greenhouse/ieaper04.htm>.
- Snover, A.K., and P.D. Quay, Hydrogen and carbon kinetic isotope effects during soil uptake of atmospheric methane, *Global Biogeochemical Cycles*, 14 (1), 25-39, 2000.
- Subak, S., On evaluating accuracy of national methane inventories, *Environmental Science & Policy*, 2 (3), 229-240, 1999.
- Subak, S., P. Raskin, and D.V. Hippel, National Greenhouse Gas Accounts: Current Anthropogenic Sources and Sinks, Stockholm Environment Institute (SEI), Boston, 1992.
- Sugawara, S., T. Nakazawa, Y. Shirakawa, K. Kawamura, S. Aoki, T. Machida, and H. Honda, Vertical profile of the carbon isotopic ratio of stratospheric methane over Japan, *Geophysical Research Letters*, 24 (23), 2989-2992, 1997.
- Takahashi, T., S.C. Sutherland, C. Sweeney, A. Poisson, N. Metzl, B. Tilbrook, N. Bates, R. Wanninkhof, R.A. Feely, C. Sabine, J. Olafsson, and Y. Nojiri, Global sea-air CO₂ flux based on climatological surface ocean pCO₂, and seasonal biological and temperature effects, *Deep-Sea Research Part II-Topical Studies in Oceanography*, 49 (9-10), 1601-1622, 2002.
- Tans, P.P., I.Y. Fung, and T. Takahashi, Observational constraints on the global atmospheric CO₂ budget, *Science*, 247, 1431-1438, 1990.
- Tyler, S.C., H.O. Ajie, M.L. Gupta, R.J. Cicerone, D.R. Blake, and E.J. Dlugokencky, Stable carbon isotopic composition of atmospheric methane: A comparison of surface level and free tropospheric air, *Journal of Geophysical Research-Atmospheres*, 104 (D11), 13895-13910, 1999.
- van Aardenne, J.A., F.J. Dentener, J.G.J. Olivier, C. Goldewijk, and J. Lelieveld, A 1 degrees x 1 degrees resolution data set of historical anthropogenic trace gas emissions for the period 1890-1990, *Global Biogeochemical Cycles*, 15 (4), 909-928, 2001.
- Walter, B.P., M. Heimann, and E. Matthews, Modeling modern methane emissions from natural wetlands 1. Model description and results, *Journal of Geophysical Research-Atmospheres*, 106 (D24), 34189-34206, 2001a.

- Walter, B.P., M. Heimann, and E. Matthews, Modeling modern methane emissions from natural wetlands 2. Interannual variations 1982-1993, *Journal of Geophysical Research-Atmospheres*, 106 (D24), 34207-34219, 2001b.
- Wang, J.S., M.B. McElroy, C.M. Spivakovsky, and D.B.A. Jones, On the contribution of anthropogenic Cl to the increase in delta C-13 of atmospheric methane, *Global Biogeochemical Cycles*, 16 (3), art. no.-1047, 2002a, doi:10.1029/2001GB001572.
- Wang, Y.P., and S.T. Bentley, Development of a spatially explicit inventory of methane emissions from Australia and its verification using atmospheric concentration data, *Atmospheric Environment*, 36 (31), 4965-4975, 2002b.
- WDCGG, World Data Centre for Greenhouse Gases, WMO Global Atmospheric Watch, 2003, http://www.wmo.ch/web/arep/gaw/gaw_home.html
- Worthy, D.E.J., I. Levin, F. Hopper, M.K. Ernst, and N.B.A. Trivett, Evidence for a link between climate and northern wetland methane emissions, *Journal of Geophysical Research-Atmospheres*, 105 (D3), 4031-4038, 2000.
- Worthy, D.E.J., I. Levin, N.B.A. Trivett, A.J. Kuhlmann, J.F. Hopper, and M.K. Ernst, Seven years of continuous methane observations at a remote boreal site in Ontario, Canada, *Journal of Geophysical Research-Atmospheres*, 103 (D13), 15995-16007, 1998.
- Wunsch, C., *The Ocean Circulation Inverse Problem*, Cambridge University Press, Cambridge, 1996.
- Yan, X., and Z. Cai, Methane emission from rice fields in mainland China: Amount and seasonal and spatial distribution, *Journal of Geophysical Research-Atmospheres*, 108 (D16), 2003, doi:10.1029/2002JD003182.
- Yao, H., Y.B. Zhuang, and Z.L. Chen, Estimation of methane emission from rice paddies in mainland China, *Global Biogeochemical Cycles*, 10 (4), 641-649, 1996.
- Zhang, G.J., and N.A. McFarlane, Sensitivity of climate simulations to the parameterization of cumulus convection in the Canadian Climate Centre general circulation model, *Atmos. Ocean*, 33, 407-446, 1995.

73. Estimation of Methane and Carbon Dioxide Surface Fluxes using a 3-D Global Atmospheric Chemical Transport Model, *Chen* (12/03)
72. The Equilibration of an Adjoint Model on Climatological Scales, *Bugnion & Hill* (6/03)
71. Mechanistic, Sensitivity, and Uncertainty Studies of the Atmospheric Oxidation of Dimethylsulfide, *Lucas* (6/03)
70. Box Modeling of the Eastern Mediterranean Sea, *Y. Ashkenazy & P.H. Stone* (5/03)
69. The 41 kyr World: Milankovitch's Other Unsolved Mystery, *M. Raymo & K. Nisancioglu* (9/02)
68. Reorganization of Miocene Deep Water Circulation in Response to the Shoaling of the Central American Seaway, *K.H. Nisancioglu et al.* (8/02)
67. Snowpack Model Estimates of the Mass Balance of the Greenland Ice Sheet and its Changes Over the 21st Century, *V. Bugnion & P.H. Stone* (1/02)
66. The Production of Non-Methane Hydrocarbons by Marine Plankton, *S. Shaw* (9/01)
65. Optimal Determination of Global Tropospheric OH Concentrations Using Multiple Trace Gases, *J. Huang* (1/00)
64. Measurement and Deduction of Emissions of Short-lived Atmospheric Organo-chlorine Compounds, *G. Kleiman* (9/99)
63. Construction of the Adjoint MIT Ocean GCM and Application to Atlantic Heat Transport Sensitivity, *J. Marotzke et al.* (5/99)
62. Terrestrial Sources and Sinks of Atmospheric Methyl Bromide: 3D Modeling of Tropospheric Abundance and Sensitivities, *C. Jensen* (4/99)
61. Inverse Modeling of Seasonal Variations in the North Atlantic Ocean, *L. Yu & P. Malanotte-Rizzoli* (8/98)
60. Interhemispheric Thermohaline Circulation in a Coupled Box Model, *J. Scott, J. Marotzke & P. Stone* (7/98)
59. Seasonal Measurements of Nonmethane Hydrocarbons in a Sub-tropical Evergreen Forest in Southern China, *J. Graham* (7/98)
58. Temporal Changes in Eddy Energy of the Oceans, *D. Stammer & C. Wunsch* (6/98)
57. On Convective Mixing and the Thermohaline Circulation, *J. Marotzke* (6/98)
56. The Importance of Open-Boundary Estimation for an Indian Ocean GCM-Data Synthesis, *Q. Zhang & J. Marotzke* (5/98)
55. Boundary Mixing and Equatorially Asymmetric Thermohaline Circulation, *J. Marotzke & B.A. Klinger* (4/98)
54. Impact of the Horizontal Wind Profile on the Convective Transport of Chemical Species, *C. Wang & R. Prinn* (3/98)
53. Adjusting to Policy Expectations in Climate Change Modeling, *S. Shackley et al.* (3/98)
52. Open-Ocean Convection: Observations, Theory and Models, *J. Marshall & F. Schott* (1/98)
51. Global Thermohaline Circulation: Parts I and II, *X. Wang, P. Stone & J. Marotzke* (10/97)
50. Destabilization of the Thermohaline Circulation by Atmospheric Transports: An Analytic Solution, *Y. Krasovskiy & P. Stone* (7/97)
49. The Global Ocean Circulation Estimated from TOPEX/POSEIDON Altimetry and the MIT GCM, *D. Stammer, et al.* (7/97)
48. Trapped Methane Volume and Potential Effects on Methane Ebullition in a Northern Peatland, *E. Fechner-Levy & H. Hemond* (5/97)
47. Seasonal Cycles of Meridional Overturning and Heat Transport of the Indian Ocean, *T. Lee & J. Marotzke* (3/97)
46. Analysis of the North Atlantic Climatologies Using a Combined OGCM/Adjoint Approach, *L. Yu & P. Malanotte-Rizzoli* (12/96)
45. Tracer Applications of Anthropogenic Iodine-129 in the North Atlantic Ocean, *H.N. Edmonds* (11/96)
44. Boundary Mixing and the Dynamics of 3-Dimensional Thermohaline Circulations, *J. Marotzke* (8/96)
43. The Role of Aerosols in the Troposphere: Radiative Forcing, Model Response, and Uncertainty Analysis, *W. Pan* (5/96)
42. Development of a 3D Chemical Transport Model Based on Observed Winds and Use in Inverse Modeling of CFC₃F Sources, *N. Mahowald* (4/96)
41. The Role of Vegetation in the Dynamics of West African Monsoons, *X. Zheng & E. Eltahir* (3/96)
40. Inferring Meridional Mass and Heat Transports of the Indian Ocean by Fitting a GCM to Climatological Data, *T. Lee & J. Marotzke* (2/96)
39. Analysis of Thermohaline Feedbacks, *J. Marotzke* (12/95)

38. The Iron Hypothesis: Basic Research Meets Environmental Policy, *S.W. Chisholm* (12/95)
37. Hydrostatic, Quasi-Hydrostatic and Non-Hydrostatic Ocean Modeling, *J. Marshall et al.* (9/95)
36. A Finite-Volume, Incompressible Navier Stokes Model for Studies of the Ocean on Parallel Computers, *J. Marshall et al.* (9/95)
35. A Case Study of the Adequacy of GCM Simulations for Assessing Regional Climate Changes, *J. Risbey & P. Stone* (3/95)
34. On the Role of Vegetation in Sustaining Large Scale Atmospheric Circulations in the Tropics, *E. Eltahir* (2/95)
33. Sprites, Q-Bursts and Positive Ground Strokes, *D. Boccippio, E. Williams, et al.* (2/95)
32. Subduction of Carbon in the Subtropical Gyre of the North Atlantic, *M. Follows et al.* (10/94)
31. The Growth of Convective Plumes at Seafloor Hot Springs, *K. Speer & J. Marshall* (10/94)
30. The CMPO/MIT TOPEX/POSEIDON Altimetric Data Set, *C. King, D. Stammer & C.I. Wunsch* (8/94)
29. Atmospheric Transports, the Thermohaline Circulation, and Flux Adjustments in a Simple Coupled Model, *J. Marotzke & P. Stone* (4/94)
28. Climate Dynamics and Global Change, *R. Lindzen* (3/94)
27. Effects of Atmospheric Coupling on the Stability of the Thermohaline Circulation, *M. Nakamura, P. Stone & J. Marotzke* (1/94)
26. Poleward Heat Transport in a Barotropic Ocean Model, *X. Wang, P.H. Stone & J. Marotzke* (12/93)
25. An EPV View of the Zonal Mean Distribution of Temperature and Wind in the Extra-tropical Troposphere, *D. Sun & R. Lindzen* (12/93)
24. Laboratory Experiments of Chemical Reactions on Polar Stratospheric Cloud Particles, *K. Beyer* (11/93)
23. A Model of the Ion Chemistry of Electrified Convection, *R. Boldi* (5/93)
22. Destabilization of the Thermohaline Circulation by Atmospheric Feedback, *M. Nakamura et al.* (3/93)
21. Global Circuit Response to Seasonal Variations in Global Surface Air Temperature, *E. Williams* (3/93)
20. Precipitation Recycling in the Amazon Basin, *E. Eltahir & R.L. Bras* (1/93)
19. On the Response of the Tropical Atmosphere to Large-Scale Deforestation, *E. Eltahir & R.L. Bras* (1/93)
18. On the Feasibility of Determining Surface Emissions of Trace Gases Using an Inverse Method in a 3D Transport Model, *D. Hartley & R. Prinn* (11/92)
17. Deducing Trace Gas Emissions Using an Inverse Method in 3D Chemical Transport Models, *D. Hartley* (11/92)
16. An Active Titration Method for the Local Measurement of Tropospheric Hydroxyl Radical, *M. Sprengnether* (10/92)
15. A Description of Rainfall Interception over Large Areas; and, On the Estimation of the Coverage of Rainfall in Climate Models, *E. Eltahir & R. Bras* (8/92)
14. The Schumann Resonance: A Global Tropical Thermometer, *E. Williams* (5/92)
13. The Heterogeneous Reaction $\text{HOCl} \rightarrow \text{HCl}_2 + \text{H}_2\text{O}$ on Ice and Nitric Acid Trihydrate, *J. Abbatt & M.J. Molina* (4/92)
12. Forecast Cloudy: The Limits of Global Warming Models, *P.H. Stone* (3/92)
11. The Implementation and Validation of Improved Landsurface Hydrology in an Atmospheric GCM, *K. Johnson et al.* (2/92)
10. Inferring the Annual-mean Subduction Rate Over the North Atlantic, *J. Marshall et al.* (1/92)
9. The Role of Ice in the Conditional Instability of the Tropical Atmosphere, *E. Williams & N. Renno* (11/91)
8. Nonmethane Hydrocarbon Chemistry in the Remote Marine Atmosphere, *N. Donahue* (7/91)
7. Global-Scale Sea Surface Variability from Combined Altimetric and Tide Gauge Measurements, *C. Wunsch* (1/91)
- 5/6. Non-linear Dynamics of Soil Moisture at Climate Scales: Stochastic and Chaotic Analyses, *I. Rodriguez-Iturbe, et al.* (11/90)
4. Atmospheric Emissions and Trends of Nitrous Oxide Deduced from Ten Years of ALE-GAGE Data, *R. Prinn et al.* (6/90)
3. A Scheme for Representing Cumulus Convection in Large-Scale Models, *K.A. Emanuel* (4/90)
2. On the Limitations of General Circulation Climate Models, *P.H. Stone & J. Risbey* (3/90)
1. An Annotated Bibliography on Greenhouse Effect Change, *M. Handel & J. Risbey* (4/92)